PLASMA-CATALYTIC CONVERSION OF GREENHOUSE GAS INTO VALUE-ADDED FUELS AND CHEMICALS

A THESIS
SUBMITTED TO THE UNIVERSITY OF LIVERPOOL

BY

Danhua Mei

IN PARTIAL FULFILLMENT OF THE REQUIREMENTS
FOR THE DEGREE OF
DOCTOR OF PHILOSOPHY

JUNE 2016

DEPARTMENT OF ELECTRICAL ENGINEERING AND ELECTRONICS,
THE UNIVERSITY OF LIVERPOOL

ACKNOWLEDGEMENTS

First of all, I would like to express my sincere gratitude and warmest thanks to my supervisors-Dr Xin Tu, Prof Ya-Ling He and Dr Joseph D. Yan, for their patient guidance and invaluable advice throughout the project. Their overwhelming support, larger dedication and enthusiasm as well as constructive suggestions and comments are essential and inestimable for me to complete my PhD project and help me develop well both personally and academically.

I am also thankful for the help and encouragement from Prof. Wenquan Tao, Prof. M. T. C. Fang. Their immense knowledge, rigorous scholarship attitude and great personal charisma motivate me to go further in my research life.

I would further like to express my thanks to Mr Yuxuan Zeng, Mr Alan Roby, Mr John Lynch and Miss Jill Anson for the efficient work during the construction of my experimental setup. My thanks also go especially to Dr Chunfei Wu, Dr Xinbo Zhu and Dr Shujuan Wang for the contribution in the catalyst characterisation.

In addition, I would also like to the express my gratitude to the Dual Collaborative PhD Degree Program between Xi'an Jiaotong University and the University of Liverpool and the Chinese Government Scholarship Program for Postgraduates. This thesis would not have been possible without their financial support. Thanks also go to all the members of the REU-EEU-MTF Research Group in Xi'an Jiaotong University (Dr Yubing Tao, Mr Zhexi Wen, Mr Kun Wang, etc.) and the Technological Plasma Group in the University of Liverpool (Mr Chao Xu, Miss Shiyun Liu, Miss Bryony Ashford, etc.) as well as my friends and classmates for making my time at Xi'an Jiaotong University and the University of Liverpool a great experience and a cheerful memory for my life.

The last but not least, I would like to deeply thank my parents for their devotion in raising me up. It is their firmest support, selfless giving, endless love and encouragement that give me confidence and strength to overcome the difficulties and pursue my dreams in my study.

ABSTRACT

The huge demand for energy sources in the human race's development has resulted in a great energy challenge and climate change. The latter issue is mainly induced by greenhouse gas emissions (such as CO_2) from the burning of fossil fuels - the world's primary energy sources. Investigation and development on the utilisation of CO_2 (rather than considering it as a waste) are of significant importance not only to reduce the emission of greenhouse gases, but also to provide a new approach for the use of the derived carbon fuels in an environmental friendly and carbon neutral way. This study is performed in dielectric barrier discharge (DBD) reactors to gain a better understanding on the plasma processing of CO_2, so as to help in the designing and optimisation of the plasma-catalytic system for CO_2 utilisation.

In the plasma-assisted decomposition of CO_2 without catalyst, the effects of different processing parameters, including frequency, discharge power, feed flow rate, discharge length, discharge gap and dielectric thickness have been taken into consideration. Empirical expressions are obtained to relate the reaction performance (CO_2 conversion and energy efficiency) to these different processing parameters. Through the sensitivity analysis, frequency is found to have negligible influence on both CO_2 conversion and energy efficiency in our experimental range; while discharge gap and discharge power are the most important factors affecting CO_2 conversion and energy efficiency of the process, respectively, compared with other processing parameters. Modified DBD reactors are proposed by using a screw-type inner electrode and/or an Al foil outer electrode to improve the CO_2 decomposition performance. In the modified DBD reactor with the screw-type inner electrode, the distortion of the local electric field near the electrode surface intensifies the filamentary discharge and generates more energetic electrons and reactive species, thereby enhancing the conversion of CO_2 with high energy efficiency.

In the plasma-catalytic decomposition of CO_2, the combination of plasma with $BaTiO_3$ and TiO_2 photocatalysts in the CO_2 DBD slightly increases the gas temperature of the plasma by 6-11 ^oC compared to the CO_2 discharge in the absence of a catalyst at a specific energy density (SED) of 28 kJ/l. The synergistic effect from the combination of plasma and photocatalysts ($BaTiO_3$ and TiO_2) at low temperatures contributes to a significant enhancement of both CO_2 conversion and energy efficiency by up to 250%. The UV intensity generated by the CO_2 discharge is significantly lower than that emitted from UV lamps used to activate photocatalysts in conventional photocatalytic reactions, which suggests that the UV emissions generated by the CO_2 DBD only play a very minor role in the activation of the $BaTiO_3$ and TiO_2 catalysts in the plasma-photocatalytic conversion of CO_2. The synergy of plasma-catalysis for CO_2 conversion can be mainly attributed to the

physical effect induced by the presence of catalyst pellets in the discharge and the dominant photocatalytic surface reaction driven by the plasma.

In the packed-bed DBD reactor for CO_2 conversion, both the physical and chemical effects on reaction performance have been investigated for the addition of $BaTiO_3$ and glass beads into the discharge gap. The presence of these packing materials in the DBD reactor changes the physical characteristics of the discharge and leads to a shift of the discharge mode from a typical filamentary discharge with no packing, to a combination of filamentary discharge and surface discharge with packing. Highest CO_2 conversion and energy efficiency are achieved when the $BaTiO_3$ beads are fully packed into the discharge gap. It is found that adding the $BaTiO_3$ beads into the plasma system enhances the average electric field and mean electron energy of the CO_2 discharge by 86.9% and 75.0%, respectively, which significantly contributes to the enhancement of CO_2 conversion, CO yield and energy efficiency of the plasma process. In addition, highly energetic electrons (> 3.0 eV) generated by the discharge could activate the $BaTiO_3$ photocatalyst to form electron-hole pairs on its surface, which contributes to the enhanced conversion of CO_2.

In the plasma-catalytic dry reforming of CH_4, the effect of catalyst support on the performance of the plasma-catalytic reaction over the supported Ni catalysts is firstly investigated. It is found that due to the higher specific surface area and larger amount of basic sites, Ni/γ-Al_2O_3 shows the higher conversion of reactants, the higher yield and selectivity of desired products and the higher carbon resistance compared with other catalysts (Ni/MgO, Ni/SiO_2 and Ni/TiO_2). Based on the Ni/γ-Al_2O_3 catalyst, the influence of the processing parameters (discharge power, total feed flow rate, CO_2/CH_4 molar ratio and Ni loading) and their interactions on the performance of the plasma-catalytic dry reforming reaction is evaluated using design of experiments (DoE). Quadratic polynomial regression models are established to reflect the relationships between these plasma processing parameters (different factors) and the performance of dry reforming process (different responses), in terms of the conversion of CO_2 and CH_4, the yield of CO and H_2 as well as the fuel production efficiency (FPE) of the plasma process. The results indicate that the total feed flow rate is the most important factor affecting the conversion of CO_2 and CH_4 and the yield of CO and H_2, while CO_2/CH_4 molar ratio has the most significant impact on FPE of the process. The interaction between discharge power and total feed flow rate plays a significant role in all the responses of the plasma-catalytic dry reforming process. The optimal process performance - CO_2 conversion (31.7%), CH_4 conversion (48.1%), CO yield (21.7%), H_2 yield (17.9%) and FPE (7.9%) is achieved at a discharge power of 60.0 W, a total feed flow rate of 56.1 ml/min, a CO_2/CH_4 molar ratio of 1.03 and a Ni loading of 9.5%, as the highest global desirability of 0.854 is obtained at these conditions. The reproducibility of the experimental results

successfully demonstrates the feasibility and reliability of the DoE approach for the optimisation of the plasma CO_2 conversion process.

Ni-based bimetallic catalysts have been designed and developed to further enhance the catalyst performance for plasma-catalytic dry reforming of CH_4. The 10wt.%Ni+3wt.%Co/γ-Al_2O_3 (10Ni3Co) catalyst shows the highest plasma-catalytic activity compared with other bimetallic catalysts (10wt.%Ni+3wt.%Cu/γ-Al_2O_3 (10Ni3Cu) and 10wt.%Ni+3wt.%Mn/γ-Al_2O_3 (10Ni3Mn)). This can be ascribed to the high specific surface area and larger amount of strong basic sites resulting from the interaction between Ni and Co in the Ni-Co/γ-Al_2O_3 catalyst. It is suggested that the formation of Ni-Co alloy in the Ni-Co/γ-Al_2O_3 catalysts contributes to the enhancement in the plasma-catalytic reforming performance when the Ni-Co/γ-Al_2O_3 catalysts are combined with plasma. The specific surface area of the catalyst is decreased but the amount of strong basic sites on the catalysts is increased by increasing the Co loading in Ni-Co/γ-Al_2O_3 catalyst. The compromise between the catalyst structure and the amount of basic sites on the catalyst favours the maximum enhancement in the performance of the plasma-catalytic dry reforming reaction when the 10Ni5Co catalyst is integrated with the plasma system. The maximum CH_4 conversion of 50.7% and the maximum CO_2 conversion of 30.9% are achieved for the plasma-catalytic dry reforming over the 10wt.%Ni+5wt.%Co/γ-Al_2O_3 (10Ni5Co) catalyst at a discharge power of 50 W and a total gas flow rate of 50 ml/min. Moreover, the 10Ni5Co catalyst possesses the highest carbon resistance in the plasma-catalytic reforming process. It is worthy to note that the carbon deposition on the catalyst in our plasma-catalytic dry reforming reaction is significantly lower than that in the conventional thermal catalytic dry reforming of CH_4 using similar Ni-Co/γ-Al_2O_3 catalysts at high temperatures. In addition, the maximum FPE of 12.7% is obtained in the plasma-catalytic dry reforming of CH_4 in this study, which is higher than most of the previous results obtained in the atmospheric non-thermal plasma reactors.

The high reaction rate and fast attainment of steady state in plasma processes allow rapid start-up and shutdown of the process compared to thermal treatment, whilst plasma systems can also work efficiently with a rather small and compact size. This offers flexibility for plasma-catalytic processes to be integrated with renewable energy sources (such as waste energy from wind power and solar energy), and provide a promising approach to store and transport the surplus energy in a chemical form.

TABLE OF CONTENTS

List of Figures

List of Tables

List of Abbreviations

AC	Alternating current
ANOVA	Analysis of variance
APGD	Atmospheric pressure glow discharges
BET	Brunauer-Emmett-Teller
BJH	Barrett-Joyner-Halenda
Btu	British thermal unit
CCD	Central composite design
CCS	Carbon capture and storage
CCU	Carbon capture and utilisation
CO_2-TPD	CO_2 temperature-programmed desorption
OECD	Organisation for Economic Cooperation and Development
DBD	Dielectric barrier discharge
DC	Direct current
DME	Dimethoxyethane
DoE	Design of experiments
DSC	Differential scanning calorimetry
DTA	Differential thermal analysis
EC	Energy cost
EEDF	Electron energy distribution function
ESCA	Electron spectroscopy for chemical analysis
EU	European Union
F-Gases	Fluorinated gases
F-T	Fischer-Tropsch
FID	Flame ionisation detector
FOLU	Forestry and other land use
FPE	Fuel production efficiency
GA	Gliding arc
GC	Gas chromatography
GHG	Greenhouse gas
GWP	Global warming potential
H_2-TPR	H_2-temperature programmed reduction
HFCs	Hydrofluorocarbons
ICCD	Intensified charge-coupled device

IEA	International Energy Agency
IEO	International Energy Outlook
IPCC	Intergovernmental Panel on Climate Change
LHV	Low heating value
MW	Microwave
PFCs	Perfluorocarbons
RF	Radiofrequency
RSM	Response surface methodology
RWGS	Reverse water gas shift
SED	Specific energy density
SF6	Hexafluoride
SS	Stainless steel
TCD	Thermal conductivity detector
TEM	Transmission electron microscopy
TGA	Thermo-gravimetric analysis
UNFCCC	United Nations Framework Convention on Climate Change
UNCED	United Nations Conference on Environment and Development
VOCs	Volatile organic compounds
XPS	X-ray photoelectron spectroscopy
XRD	X-ray diffraction

CHAPTER ONE INTRODUCTION

1.1 Background and Motivation

1.1.1 Energy challenge and climate change

Energy is a foundation stone of modern society's development and industrial economy. It provides essential ingredients for almost all human activities: cooking and space/water heating, lighting, health, food production and storage, education, mineral extraction, industrial production and transportation. The world's primary energy sources come from fossil fuels, which are a non-renewable energy source formed from the remains of plants and animals buried millions of years ago. Coal, oil and natural gas are the three major fossil fuel forms. **Figure 1.1**(a) shows the global energy consumption history and projections given in the International Energy Outlook (IEO2013). Clearly, high reliance on fossil fuels can be observed. For example, coal, oil and natural gas accounted for 28%, 34% and 22% of global energy consumption in 2010 [1]. Part of the dependence on fossil fuels comes from their availability. Coal is playing an important role in delivering energy access due to its wide availability, safety, and reliability as well as the relatively low cost. More than 75% of the countries all over the world have coal deposits. Recent data shows that the proved coal reserves have increased by 1% and its production by 16% compared to the 2010 survey [2]. The majority of the coal-produced energy is used in the electric power sector and the current share of coal in global power generation is over 40% [2]. The future of coal mainly depends on the advance of clean coal technologies to mitigate environmental risk factors. For oil, the current global reserves are almost 60% larger than that of 20 years ago, and its production has gone up by 25%. If the unconventional oil resources, including oil shale, oil sands, extra heavy oil and natural bitumen are taken into account, the global oil reserves will be four times larger than the current conventional reserves [2]. Oil is the premier energy resource with a wide range of possible applications and its main use will be shifted towards transport and the petrochemical sector. Natural gas, as the cleanest fossil fuel, will continue making significant contributions to the world energy economy. It is plentiful and flexible, and is increasingly used in the most efficient power generation technologies, such as combined cycle gas turbines with approximate conversion efficiencies of 60%. According to statistics, the reserves of conventional natural gas have grown by 36% and its production by 61 % over the past two decades [2]. Moreover, shale gas as a potentially major energy source has emerged and will have a serious strategic influence in geopolitics and the energy industry.

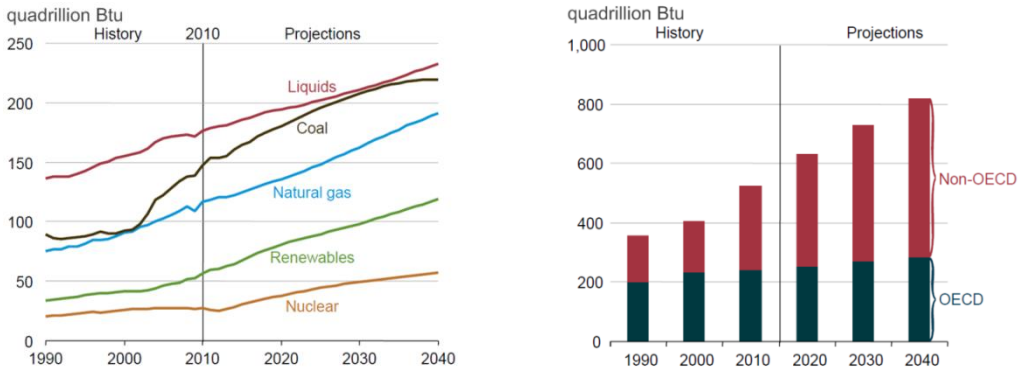

(a) (b)

Figure 1.1 World energy consumption by (a) fuel type and (b) country group (Btu: British thermal unit, a traditional unit of energy equal to about 1055 joules; OECD: Organisation for Economic Cooperation and Development) [1].

Though fossil fuels are clearly the dominant energy source, alternative and renewable energy sources contribute more and more to overall energy consumption. Alternative energy sources have been used for many years, and gradually become the focus as one of the ways to lessen the dependence on non-renewable fossil fuels. Nuclear power is one of the alternative energy sources. Total nuclear electricity production has experienced a rapid development during the past two decades; its annual output reached up to about 2600 TWh by the mid-2000s [2]. The U.S., France and Japan are the top three countries which have the highest installed nuclear power capacity and they occupied 27.2%, 17.3% and 10.4% of the global total installed capacity in 2011, respectively. Renewable energy sources have a greater appeal because they can be regenerated and sustained nearly indefinitely. The most commonly used renewable energy sources are biomass, hydropower, geothermal, wind and solar. **Figure 1.2** shows the estimated renewable energy share of global final energy consumption in 2012 [3]: more than 19% of global final energy consumption was provided by renewable energy.

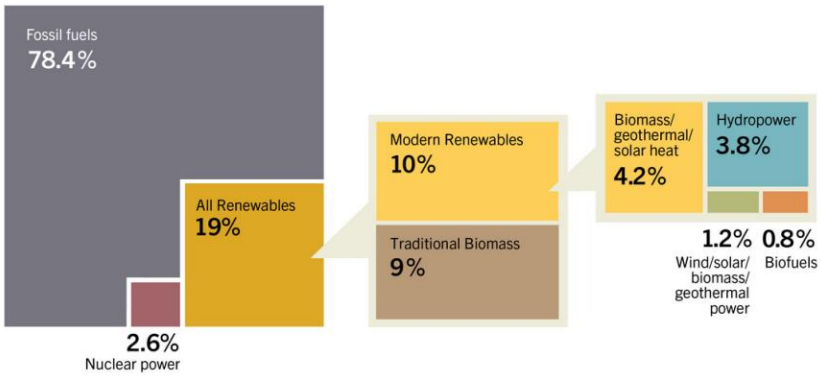

Figure 1.2 Estimated renewable energy share of global final energy consumption, 2012 [3].

As shown in **Figure 1.1**(b), the IEO2013 projects that world energy consumption will increase by 56% between 2010 and 2040. The OECD countries are expected to increase energy use by 17%; while the countries outside OECD, labelled as non-OECD, are projected to dramatically increase their energy consumption by 90% [1]. In particular, China and India are expected to make more than half of the global energy consumption growth by 2040. These two countries have been among the world's fastest growing economies during the past two decades. The prediction of the strong economic growth, together with the high populations in both countries drives an ever increasing energy demand. In order to meet this demand, energy production must increase as well. Despite that, renewable energy is predicted to be the fastest growing energy sector, as shown in **Figure 1.1**(a), China, India and other non-OECD Asian countries will still have a larger reliance on the fossil fuels, especially on coal due to the availability of coal reserves in that region and its relative low price. Global coal demand is predicted to grow by 15% by 2040, but almost two-thirds of the increase will occur over the next ten years. In the next few years, China will be the biggest coal consumer and its coal demand will plateau at just over 50% of global consumption before falling back after 2030. India is expected to overtake the U.S. as the second biggest coal consumer in the world before 2020, and soon after will surpass China as the largest importer [4]. Although the economic cost of fossil fuels may be lower than renewable sources, the environmental cost of burning fossil fuels is significantly greater. Fossil fuels are made up of hydrogen and carbon atoms, therefore named hydrocarbons. Burning the hydrocarbons will lead to the release of CO_2 (see Equation (1-1)) and other greenhouse gases (GHGs).

$$C_xH_y + \left(x + \frac{y}{4}\right)O_2 \rightarrow xCO_2 + \frac{y}{2}H_2O + \text{heat} \qquad (1\text{-}1)$$

Figure 1.3 shows the global annual anthropogenic GHG emissions between 1970 and 2010 [5]. Clearly, annual anthropogenic GHG emissions were increased by 81.5% from 1970 to 2010, and the annual increasing rate of GHG emissions in the latter ten years was much higher than that in the former thirty years during that period. In addition, energy-related CO_2 emissions accounted for 85.5% of the total anthropogenic carbon emissions in 2010. On a global scale, other key GHGs resulted from human activities include methane (CH_4), nitrous oxide (N_2O) and fluorinated gases (F-Gases). CH_4 is formed in the process of agricultural activities, waste management and energy use including oil and natural gas operations as well as coal mines. N_2O mainly comes from hydrocarbon combustion, nitrogen-containing fertiliser and other industrial processes. F-Gases, including hydrofluorocarbons (HFCs), perfluorocarbons (PFCs) and sulfur hexafluoride (SF_6), are mainly generated as by-products and emitted as leakage in industrial processes. All of these gases contribute to the warming of the planet, but CO_2 has the greatest effect because it is

produced in such a large amount due to the strong dependence of the human race's development on fossil fuel.

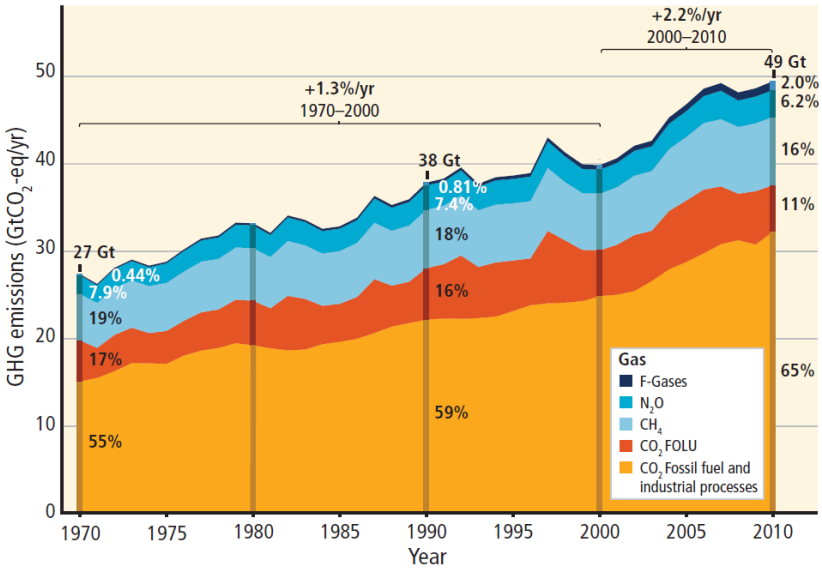

Figure 1.3 Global anthropogenic greenhouse gas emissions by gases from 1970 to 2010 ($GtCO_2$-eq/yr: gigatonne of CO_2-equivalent per year; FOLU: forestry and other land use) [5].

Increasing the concentration of GHGs by human activities has resulted in an imbalance in the natural carbon-cycle: more carbon is being emitted into the atmosphere than that can be absorbed by nature. This imbalance leads to significant changes in the local weather system, named climate change. which can be evidenced by the measurement of various climate parameters, such as surface temperature, sea level, ocean acidification, et al. **Figure 1.4** shows the estimated historical trend of the atmospheric CO_2 concentration and global temperature change [6]. The concentration of CO_2 is observed to correlate very well with the average global temperature change. The Intergovernmental Panel on Climate Change (IPCC) reported in 2015 that the globally averaged combined land and ocean surface temperature had risen about 0.85 ^oC over the period from 1880 to 2012 [5]. The warming of the climate system is considered unequivocal and many of the observed changes are unprecedented since the 1950s. Rising global temperatures resulted in the expansion of ocean water and melting of glaciers, ice caps as well as ice sheets, all of which definitely caused the sea level to climb. In the IPCC 2015 report, the global mean sea level rose by 0.19 m over the period between 1901 and 2010, and the rising rate since the mid-19th century was larger than the mean rate during the previous two millennia [5]. In addition, the excess CO_2 released by human activities breaks the balance of CO_2 exchange between the atmosphere and ocean. More CO_2 is absorbed in the ocean and reacts with water to produce a weak acid called carbonic

acid, resulting in the acidification of the oceans. The Global Biodiversity Outlook Report reported that the sea water is about 30% more acidic than that in pre-industrial times [7]. Moreover, as announced by the World Meteorological Organisation, extreme weather patterns occur more frequently than before, such as hurricanes, drought or intense rain, desertification, extreme cold weather, and super-storms [8]; therefore, agriculture has poor harvests and the population in hunger is increasing. In addition, the temperature changes around the world also have significant negative effects on the ecosystem. The extinction rates of animal and plant species have behaved significantly differently to normal expectations since the industrial revolution. The outbreaks and epidemics of diseases show an alarming increase rate throughout land and ocean based wildlife. For human beings, it was found that 40% of deaths in the world could be attributed to environmental factors [8].

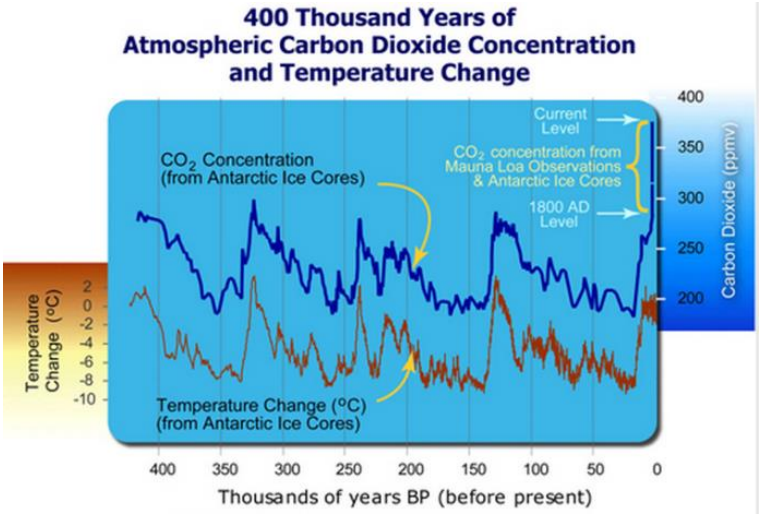

Figure 1.4 Historical trends of atmospheric CO_2 concentration and global temperature change in the past 400 thousand years [6].

1.1.2 CO_2 remediation and utilisation

The effects of the climate change are being widely investigated by individual governments and intergovernmental organisations. CO_2 emissions from the combustion of fossil fuels are believed to be the most significant contributor to global climate change. International Energy Agency (IEA) has projected that energy - related CO_2 emissions will grow by 20% by 2040, which will put the world on a path consistent with a long term global average temperature increase of 3.6 ^{o}C [4]. Therefore, it is necessary and urgent to take measures to reduce CO_2 emissions, helping lessen the threat of climate change. During the last three decades, efforts both on policy and technology have been taken to pursue possible solutions to this problem.

1.1.2.1 Policy efforts

The United Nations Framework Convention on Climate Change (UNFCCC) was open for signatures on 4 June 1992 at the United Nations Conference on Environment and Development (UNCED) and entered into force on 21 March 1994, aiming to stabilise GHG concentrations in the atmosphere at a level to prevent dangerous anthropogenic interference with the climate [9]. As an internal environmental treaty, UNFCCC itself set no binding limits on GHG emissions for individual countries and contained no enforcement mechanisms; therefore it was considered not legally binding. However, the treaty provided framework for negotiating specific international protocols which may be used to set binding limits on GHG emissions. As of 2015, UNFCCC had 197 parties [9]. Since the Conferences of the Parties in 1995, the parties of the convention have meetings every year to evaluate the progress in dealing with climate change issues. In 1997, the Kyoto Protocol was established and spelled out legally binding obligations for developed countries to reduce their GHG emissions [10]. Besides the Kyoto Protocol, further commitments have been agreed, including the Bali Action Plan (2007) [11], the Copenhagen Accord (2009) [12], the Cancún agreements (2010) [13], and the Durban Platform (2011) [14]. In the Copenhagen Accord, it was stated that global warming should be limited to below 2.0 ^{o}C compared to pre-industrial temperatures [12]. Developing countries such as China and India are included in the Durban platform for the first time in the 2011 United Nations Climate Change Conference (UNCCC) [14]. In the 2012 UNCCC, an agreement in principle that richer countries could be financially responsible to other countries for their failure to reduce carbon emissions was established [15]. The 2015 UNCCC has been held in Paris, France from 30 November to 11 December 2015. Binding and universal agreements on climate from all the nations of the world were established [16].

For the major individual government and organisation, the White House of the United States announced on 25 November 2009 that President Obama is offering a U.S. target for reducing GHG emissions in the range of 17% below 2005 level by 2020 [17]. They further promised to cut net GHG emissions by 26-28% below 2005 levels by 2025 in a U.S.-China Joint Announcement on Climate Change and Clean Energy Cooperation established during the APEC 2014 held in Beijing, China [18]. As another particular major emitter, the European Union (EU) has committed to three targets of reducing emissions for 2020. The first one is to reduce emissions by 20% on 1990 levels, the second one is to increase the renewables' share of its total energy to 20%, and the third one is to increase energy efficiency by 20% from 2007 levels. They also have endorsed an emission reduction of 80-95% by 2050 [19]. The United Kingdom participates in the EU action to tackle climate change as a member of the EU. They declared to reduce its GHG emissions by at least 80% of the 1990 baseline by 2050 in the 2008 Climate Change Act [20]. China, as the largest

developing country, positively takes part in international actions tackling climate change. They declared targets to peak CO_2 emissions around 2030, with the intention to peak early and to increase the non-fossil fuel share in total energy to around 20% by 2030 [18]. They submitted a carbon-curbing plan to the United Nations ahead of the Paris climate change summit, saying that they will cut their GHG emissions per unit of gross domestic product by 60-65% from 2005 levels and will work harder to peak emissions earlier than 2030 target [21].

1.1.2.2 Technological efforts

The technological efforts on reducing CO_2 emissions involve reducing fossil fuel consumption by boosting clean and renewable energy use, carbon capture and storage (CCS) as well as carbon capture and utilisation (CCU). The utilisation of renewable energy sources has experienced rapid development in the last two decades. They totally accounted for 11% of the global energy consumption in 2010, and this percentage has been predicted to be 15% in 2040 [1]. However, the existence of the barriers to the advancement of renewable energy from technology, market, finance and social acceptance makes it hard for it to be the main driving force in controlling and reducing CO_2 emission in the short term. This situation is especially obvious in developing countries [22].

In efforts to manage CO_2 emissions with CCS processes, captured CO_2 is designed to be stored in geological and oceanic reservoirs. Methods have been proposed to inject CO_2 into depleted oil reservoirs for enhanced oil recovery, to store CO_2 in deep underground saline formations, and to inject liquid CO_2 into the ocean at intermediate depths. Although the technologies are available for these methods, the financial cost is rather high when the energy needed to compress the captured CO_2, transport it to the storage reservoirs and pump it into the ground or ocean are taken into consideration. Moreover, there are great concerns over the potential environmental impacts of the CCS approach, associated with leakages, slow migration and accumulation, induced seismicity and ocean acidification [23].

In the CCU approaches, rather than being considered as a waste, CO_2 is regarded as a raw chemical for the production of value-added fuels and chemicals. It can be directly decomposed into CO, or can be transformed into other useful chemical in C_1 chemistry. C_1 chemistry refers to the conversion of simple carbon-containing materials that contain one carbon atom per molecule into valuable products. The feedstock for C_1 chemistry includes natural gas, CO_2, CO, methanol and syngas. The traditional feedstock for the chemical industry mainly comes from coal, oil and natural gas as well as their products. Using CO_2 as the raw materials of C_1 chemistry will not only reduce the dependence on the traditional fossil fuels, but also consume a large amount of CO_2, removing the negative effects of the greenhouse effect. Common CO_2 conversion approaches include photocatalytic

reduction, electrochemical reduction, thermal-catalytic conversion and plasma-assisted conversion.

(1) Photocatalytic reduction of CO_2

The photocatalytic reduction of CO_2 is completed by the radicals or electrons generated on the photocatalysts irradiated with UV and/or visible light radiations. In photocatalytic processes, light radiations which have energy equal to or greater than the band gap energy of a semiconductor strikes its surface, electrons are excited from the valence band to the conduction band and an equal numbers of holes are generated in the conduction band simultaneously. The generated electron-hole pairs separate from each other and move to catalytically active sites on the surface of the semiconductor, where CO_2 is reduced by the electrons into carbon-containing fuels such as CO, CH_3OH and/or CH_4 with the presence of H_2O; meanwhile, the oxidation of H_2O occurs due to the oxidation ability of holes, as shown in **Figure 1.5** [24].

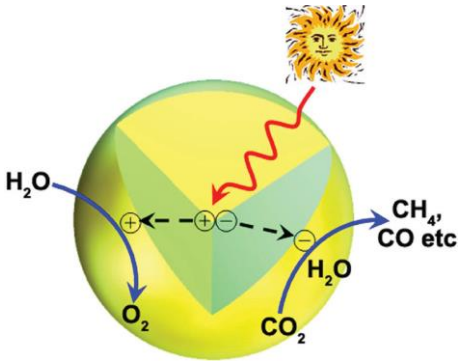

Figure 1.5 Schematic illustration of the photocatalytic reduction process of CO_2 at semiconductor surface [24].

The first study related to the photcatalytic reduction of CO_2 was reported by Inoue et al. in 1979. They used both oxide and non-oxide photocatalytsts, such as TiO_2, WO_3, ZnO, GaP, CdS and SiC. In their work, CO_2 was photoreduced into various organic compounds, such as CH_3OH, HCOOH, CH_4 and HCHO with H_2O as the reducing agent [25]. Subsequently, many researches on the photocatalytic CO_2 reduction to fuels have been performed under UV and/or visible light irradiations. It has been found that CH_4, CH_3OH and CO are the major products and TiO_2 based photocatalysts are more efficient than other photocatalysts [26]. In order to enhance the response of TiO_2 to visible light, a variety of strategies have been proposed, including doping TiO_2 with metals and non-metals, sensitisation and using nanocarbons, graphene, and enzymes [26]. Currently, the efficiency of CO_2 photocatalytic reduction is very low and far from practical application. More efforts should be made to improve the efficiency of the photoreduction process, including the development of the novel heterostructured photocatalysts with considerable

activity, high reaction selectivity for CO_2 reduction and stability, further understanding of the mechanism in the photochemical process and establishing efficient photoreactor and reaction systems [27]. Detailed information about the research status and the future recommendation can be found in the recently published reviews [24, 26, 27].

(2) Electrochemical reduction of CO_2

The electrochemical reduction of CO_2 has a long history dating from the 19th century and has attracted interest in the last three decades [28]. One common device for the electrochemical reduction of CO_2 is H-type cells with metal plate electrodes. CO_2 can be converted into various products directly at the surface of solid electrodes. A homogeneous catalyst is incorporated into the system to participate in the electron transfer reaction from solid electrodes. The cells consist of two compartments connected through a diaphragm. The diaphragm ensures ionic conductivity through the cell parts, but prevents the oxidation of the CO_2 cathodic products on the anode electrocatalyst and the oxygen contamination (from anodic water oxidation) in the cathodic compartment [29]. The over-voltages are required to provide the electrons for the direct electrochemical reduction of CO_2. This is one of the major differences between electrochemical and photocatalytic reduction; in the latter case, the electrons come from the interaction between the semiconductor and exposed light radiation [30]. **Figure 1.6** shows a representative example of an H-type cell described by Lee et al. in 2001, in which the anodic and cathodic cell compartments were separated by an anion-exchange polymer membrane [31]. The electrochemical reduction can proceed in gaseous, aqueous and non-aqueous phases at both low and high temperatures, and the major reduction products include CO, formic acid (HCOOH) or formate ($HCOO^-$) in basic solution, oxalic acid ($H_2C_2O_4$) or oxalate ($C_2O_4^{2-}$) in basic solution, formaldehyde (HCHO), methanol, CH_4, C_2H_4, ethanol, as well as others [30].

The research topics related to the electrochemical reduction of CO_2 mainly focus on the development of the electrocatalysts and the prototype systems. The most commonly studied electrocatalysts are transition metal elements and their associated compounds - metal alloys, metal oxides and metal complexes. Other metals, such as aluminium, gallium, indium, thallium, tin and lead, as well as alkaline metals and alkaline earth metals, are considered as well. Besides these metals and metal complexes, organic catalysts are also investigated, including conducting polymers, aromatic amine catalysts, radical anion catalysts, ionic liquid, enzyme catalysts and others [30]. The effects of the electrode potential, solution-electrolyte type and composition, temperature, pressure and other conditions on the performance of the catalysts have also been widely explored. However, challenges still remain, such as the slow kinetics of CO_2 electrochemical reduction, even when the high electrode

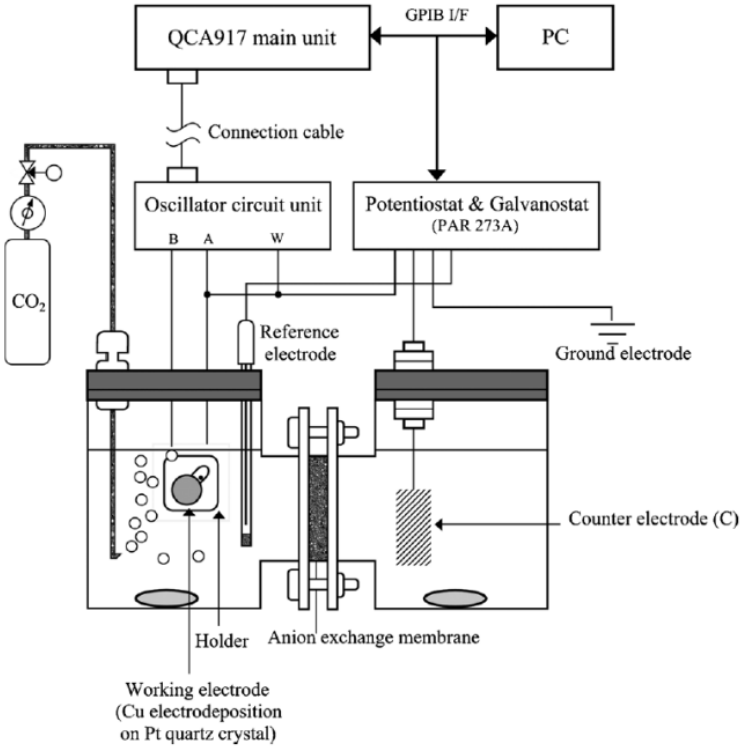

Figure 1.6 Schematic diagram of H-type cell for the electrochemical reduction of CO_2 [31].

reduction potentials are applied in the presence of the electrocatalysts; the low process energy efficiency due to the parasitic energy consumption or decomposition of the solvent at high reduction potential; the low product selectivity due to the complicated reactions involved in the electrochemical reduction; the short life-time of the metal-based catalyst compared with the requirements for practical commercialisation, and high energy consumption [29, 30]. Therefore, substantial advances in the electrode, electrolyte, system stability, electrocatalysts and the overall process costs are required for the development of the commercial processes [28, 29].

(3) Thermal catalytic conversion of CO_2

Thermal catalytic conversion of CO_2 mainly refers to the CO_2 conversion into chemicals driven by homogeneous, heterogenised, heterogeneous and enzymatic catalytic systems [32]. Several reviews have reported the research progress in this field [32-34]. Here, only the thermal catalytic decomposition of CO_2 and syngas production from CO_2 reforming of CH_4 in the heterogeneous catalytic system will be described.

Since Tamaura et al. reported that CO_2 could be reduced to carbon with an efficiency of nearly 100% at 290 ^oC on the oxygen-deficient magnetite (Fe_3O_4) in 1990 [35], different catalysts have been studied in the thermally direct decomposition of CO_2, such as binary oxygen-deficient ferrites, expressed as $M(II)Fe(III)_2O_{4-\delta}$ (M =

Ni, Zn, Co, Cu, Fe, Mn, etc.), where δ is the degree of the oxygen-deficiency. A high δ in the ferrites results in increased Fe(II) reduction potential and enhanced decomposition efficiencies [36]. The ferrites have stable spinel structures, which can accommodate interchanges between stoichiometry and non-stoichiometry. The reactions with the spinel ferrites involve lattice oxygen in two different ways: oxidation reactions, in which oxygen atoms are transferred from the ferrites to the gas, and reduction reactions, in which the oxygen vacancies on the ferrites are replenished by oxygen from the gas. In the CO_2 decomposition process, the non-stoichiometric forms are required, which can be obtained with a reducing agent such as H_2 [37]. Later, ternary ferrites, such as (Ni-Zn)Fe_2O_4, (Ni-Cu)Fe_2O_4, (Mn-Zn)Fe_2O_4, and (Mn-Ni)Fe_2O_4 were proposed for the decomposition of CO_2 [38]. In these reactions, CO_2 is decomposed into CO, carbon, or both.

In the thermal-catalytic conversion of CO_2, the Boudouard reaction has also been used to activate CO_2 through the reaction with carbon to produce CO, as shown in Equation (1-2), which is usually involved in the gasification of coal and other carbon-rich sources. However, it is highly endothermic and a high temperature (> 700 ^oC) is favourable for CO formation. This reaction only plays an important role in high temperature (> 900 ^oC) gasification and melting processes [39]. Hunt et al. reported that the utilisation of microwave radiation could result in a dramatic change in the thermodynamics of the reaction and shift the temperature favouring CO production to around 400 ^oC, lower than that in the conventional heating effect [39].

$$C + CO_2 \rightarrow 2CO \qquad \Delta H^0 = 172\,kJ/mol \tag{1-2}$$

Another form of thermal catalytic decomposition of CO_2 is that using concentrated solar radiation energy. Chueh et al. proposed a two-step thermochemical cycle to dissociate CO_2 using metal oxide redox reaction in a solar cavity-receiver reactor, as shown in **Figure 1.7**. The entire cycle include the oxygen evolution and CO_2 decomposition processes, as described in Equations (1-3) and (1-4), respectively, where A is Ce or a combination of Ce and a dopant element. The cerium oxide was partially reduced at higher temperatures (around 1600 ^oC), releasing O_2 under concentrated solar radiation, and then re-oxidised again by reacting with CO_2 at a lower temperature of about 900 ^oC. The temperature in the reactor was controlled by adjusting the solar radiation concentrated in the reactor. Their results indicated that a near 100% selectivity towards CO was achieved without appreciable amount of carbonaceous species being deposited on ceria [40].

$$\frac{1}{\delta}AO_2 \rightarrow \frac{1}{\delta}AO_{2-\delta} + \frac{1}{2}O_2 \tag{1-3}$$

$$CO_2 + \frac{1}{\delta}AO_{2-\delta} \rightarrow \frac{1}{\delta}AO_2 + CO \tag{1-4}$$

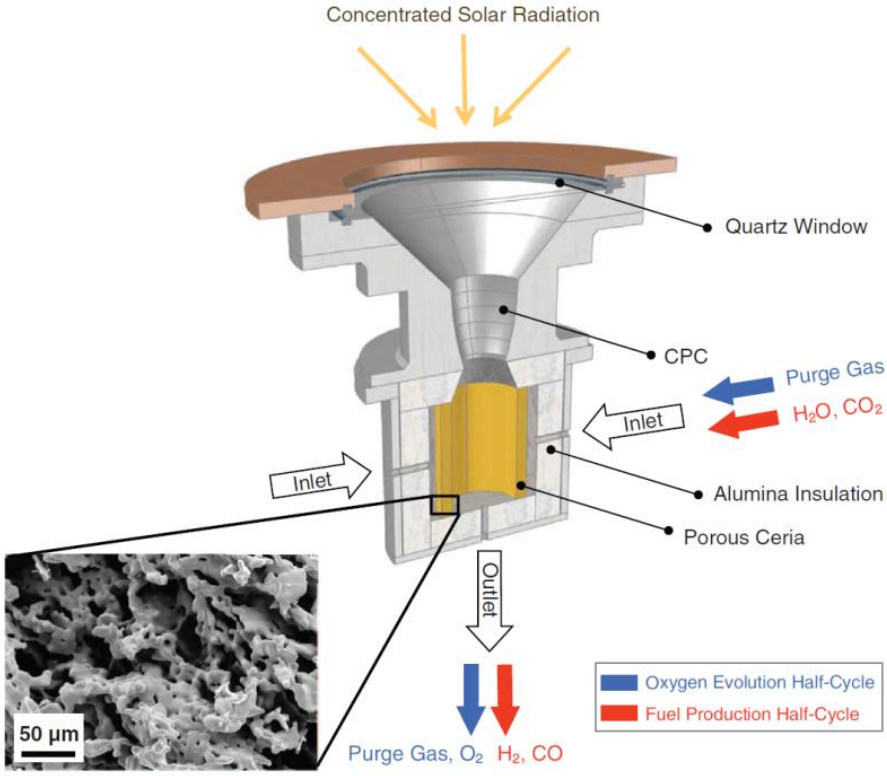

Figure 1.7 Schematic diagram of the solar reactor for the two-step, solar-driven thermochemical production of fuels (CPC: compound parabolic concentrator) [40].

CO_2 conversions in the above thermocatatytic reduction processes are usually higher than those in the photocatalytic and electrocatalytic processes discussed before, but the requirement of high temperatures will incur high operation costs.

In the thermal catalytic conversion of CO_2, CO_2 reforming of CH_4 (also named dry reforming of CH_4) to produce syngas (CO + H_2) has been considered as one of the most promising technologies as well. CH_4, on the one hand, is the second major greenhouse gas (see **Figure 1.3**); while on the other hand, it is also the main constituent of natural gas, biogas, coal bed gas and shale gas. Up to now, the conversion of CH_4 to useful products is mainly involved in indirect processes, where CH_4 is firstly to be converted to syngas. Syngas can be directly used as a fuel: combustion in a gas turbine, internal combustion engine or boiler, in the same way as natural gas. As shown in **Figure 1.8**, a wide range of other applications of syngas have been found in synthetic chemical industries [41]. H_2 and CO in the syngas can be separated and applied individually for synthesis of various chemicals, such as ammonia (NH_3) in the case of H_2, or acids and other carbonylation products with the presence of CO. Syngas gas can be directly used to reduce iron oxides in industrial steel manufacture. In addition, the mixture of H_2 and CO can be used directly in the synthesis processes with a suitable catalyst and an elevated temperature, such as Fischer-Tropsch (F-T) process, oxy-synthesis, methanol synthesis, etc.

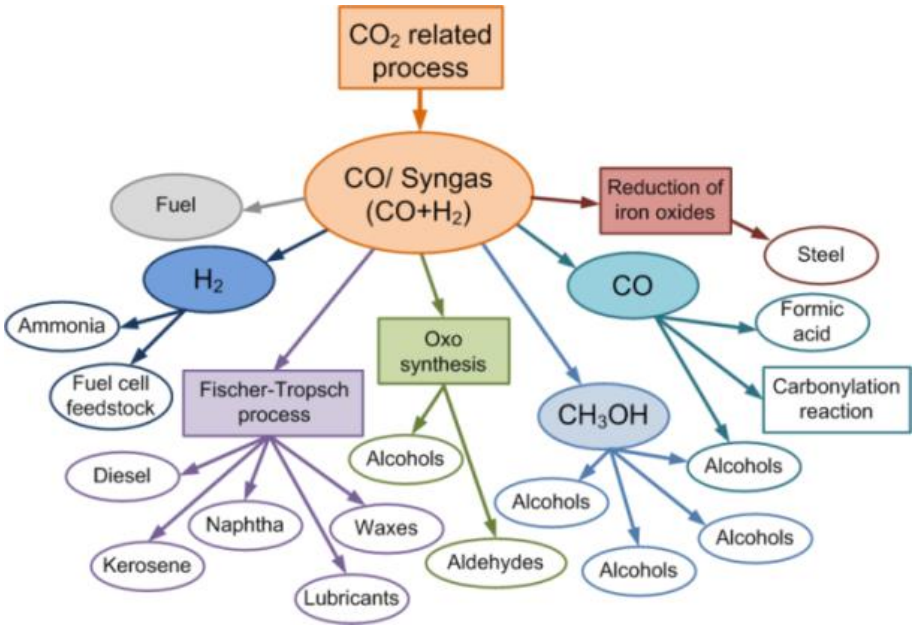

Figure 1.8 Schematic diagram of the main applications of syngas [41].

The principal routes for the conversion of CH_4 to syngas include steam reforming (Equation (1-5)), partial oxidation (Equation (1-6)) and dry reforming (Equation (1-7)). Steam reforming is a mature conventional process for syngas production. It is a highly endothermic reaction, which results in a relatively energy-intensive generation of syngas with a high cost. The main challenge to the steam reforming process is to reduce the cost for syngas production and coke formation. Although using a large excess of steam could help prevent the deposition of carbon on the catalyst, it would decrease the thermal efficiency and negatively affect the economics of the process. Moreover, the resulting H_2/CO molar ratio in the syngas would be in the range of 3.4-5.0, much higher than the ratio required for many synthesis processes [42]. Adjustment of the H_2/CO molar ratio is therefore needed, which would lead to a high capital cost. Partial oxidation of CH_4 can be achieved both with and without the catalysts. In the absence of a catalyst, CH_4 is mixed with excess O_2 and ignited. High temperatures (1200 -1500 ^oC) are required for the higher conversion of CH_4 [43]. Catalysts including supported transition and noble metal oxides as well as various transition metal carbides have been investigated for partial oxidation of CH_4, which lower the operating temperature to 727-927 ^oC [41]. The major advantage of this process is less external heating is required due to its slightly exothermic characteristics. In addition, this process produces syngas with a CO/H_2 molar ratio close to 2, which is suitable for the F-T synthesis and methanol synthesis [42]. However, the cost to separate O_2 from air results in a high operating cost [41]. In addition, the fast reaction of CH_4 with O_2 leads to complete oxidation of the reactants, producing H_2O and CO_2, which is not desirable because valuable H_2 is converted to water [44].

$$CH_4 + H_2O \rightarrow CO + 3H_2 \qquad \Delta H^0 = 206\ \text{kJ/mol} \qquad (1\text{-}5)$$

$$CH_4 + 0.5O_2 \rightarrow CO + 2H_2 \qquad \Delta H^0 = -36\ \text{kJ/mol} \qquad (1\text{-}6)$$

$$CH_4 + CO_2 \rightarrow 2CO + 2H_2 \qquad \Delta H^0 = 247\ \text{kJ/mol} \qquad (1\text{-}7)$$

The dry reforming of CH_4 is also strongly endothermic, like the steam reforming process. However, the dry reforming process stoichiometrically produces syngas with a H_2/CO molar ratio close to 1. The H_2/CO molar ratio in the syngas can also be easily controlled by adjusting CO_2/CH_4 molar ratio in the feed gas to meet the requirements of different end use. Most importantly, this process has received considerable attention as it involves the conversion of two major GHGs from the view point of environmental protection. Moreover, from the perspective of resource utilisation, the successful realisation of the process would enable the direct use of the low-grade biogas, natural gas, coal bed gas and/or shale gas containing different amounts of CO_2 and CH_4. Both of these two factors make it an applicable route to control CO_2 emission.

As dry reforming of CH_4 is a highly endothermic reaction, a temperature higher than 640 ^oC is required to achieve reasonable reactant conversions [45]. However, two side reactions: CH_4 decomposition (Equation (1-8)) and CO disproportionation (Equation (1-9)) favour the formation of carbon at a temperature range of 560 to 700 ^oC. Therefore, dry reforming of CH_4 is usually performed at temperatures higher than 750 ^oC to minimise the effect of these side reactions, including the catalyst deactivation and reactor blockages due to the carbon deposition and sintering under the severe reaction conditions [45]. Several reviews have been conducted to discuss the catalytic aspects of CO_2 reforming of CH_4 [46-48].

$$CH_4 \rightarrow C(s) + 2H_2 \qquad \Delta H^0 = 75\ \text{kJ/mol} \qquad (1\text{-}8)$$

$$2CO \rightarrow C(s) + CO_2 \qquad \Delta H^0 = -172\ \text{kJ/mol} \qquad (1\text{-}9)$$

(4) Plasma-assisted conversion of CO_2

Due to the non-equilibrium property and the capacity to induce physical and chemical reactions at relatively low temperatures, non-thermal plasmas provide an alternative approach to convert CO_2 into high grade gas products, as the highly energetic electrons in the plasma have the ability to efficiently active the gas molecules. Several reviews have discussed the applications of plasma processing in CO_2 conversion [49-52]. The basic principle of plasma and the current state of the plasma-assisted CO_2 conversion will be given in the following sections.

1.2 Plasma Systems

1.2.1 Basic principle and classification of plasma technology

Plasma is a term used to describe an ionised gas containing a mixture of particles: electrons, ions, radicals as well as neutral gas atoms and molecules. It was firstly introduced by Irving Langmuir in 1928 to describe the inner region of a glowing ionised gas phase produced through electric discharge in a tube. Actually, Sir Williams Crooks was the first person to identify plasma in a so called Crooks tube in 1879 and named it 'radiant matter'. He also referred to it as the 'fourth sate of matter'. As shown in **Figure 1.9** [53], when heat or another energy is exerted, the temperature of a substance will increase, and molecules will become more energetic; consequently, the matter is transformed in the sequence of solid, liquid, gas and finally plasma, which exactly justifies the concept "fourth sate of matter". Compared with other states of matter, on one hand, plasma is like gas, which does not have a definite shape or a definite volume unless it is enclosed in a container; on the other hand, it is not like the normal neutral gas, as it is strongly influenced by electromagnetic fields due to the presence of a non-negligible number of charge carriers. This is the main property to distinguish plasma from neutral gas.

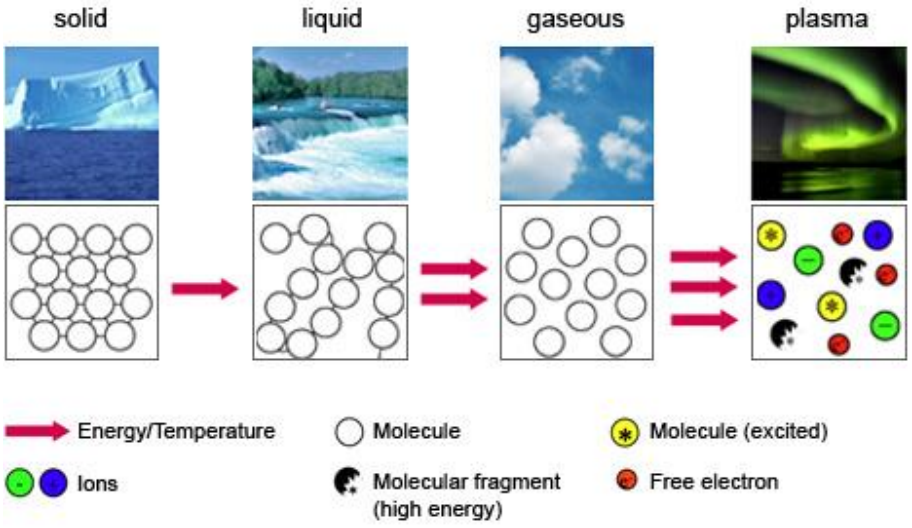

Figure 1.9 The four states of matter [53].

Just like the other states of matter, plasmas occur naturally as well. Much of the visible matter in the universe is in the state of plasma, such as stars and the visible interstellar matter. Due to the continuous cosmic radiation, there exist electron-ion pairs even in ambient air at normal temperature and pressure. The ionisation rate in the air is in the order of 10^6 $m^{-3}s^{-1}$ ion-electron pairs (1 ion per $cm^{-3}s^{-1}$) when only the cosmic radiation is considered [54]. Thus, dry air is electrically insulating. Lightning and Auroras are the two typical examples of naturally occurring

plasma. In a laboratory setting, plasma can be generated for practical application. As shown in **Figure 1.10**, various types of energy can be applied to generate plasma: thermal energy , magnetic fields or electric fields [55]. The most common approach to generate and sustain plasma is exerting an external electric field to the neutral gas, which results in the formation of a variety of new species, such as electrons, ions, radicals, excited atoms and molecules, as well as the UV photons. The newly formed free charged particles are accelerated by the electric field and collide with other atoms, molecules and/or the electrode surfaces, and then new charged particles are created. This leads to an avalanche of the charged particles; meanwhile, annihilation of part of the charge carriers also occurs, and eventually a balance is created to develop the steady-state plasma. This man-made plasma is often referred to as 'discharges'. The electrical discharges in gases are obtained with high applied voltage and the typical *U* vs *i* plot is independent of the gas types (shown in **Figure 1.11**) [55]. Townsend discharge is a self-sustained discharge created at low discharge current. The transition to a sub-normal glow discharge and to a normal glow discharge is characterised by a decrease in the voltage and an increase in the current. Further increasing the current develops an abnormal glow discharge. Finally, at very high currents, the discharge undergoes an irreversible glow-to-arc transition [55].

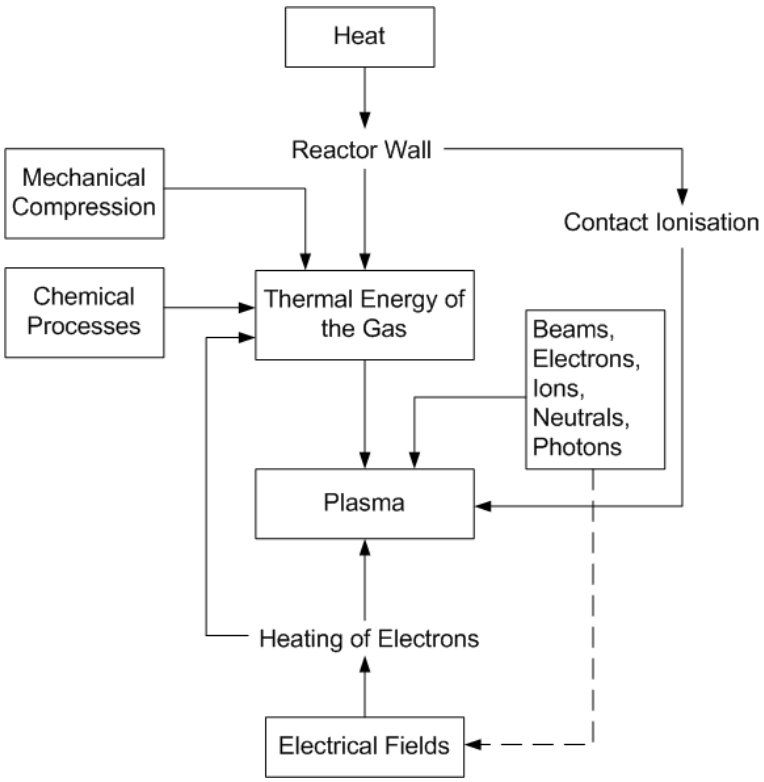

Figure 1.10 Principles of plasma generation [55].

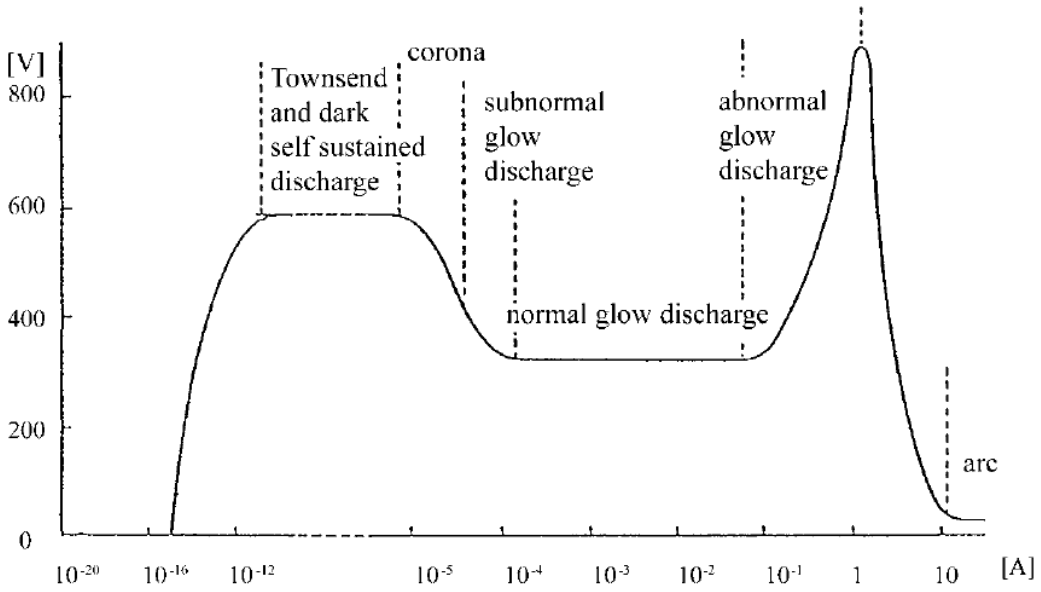

Figure 1.11 The dependence of voltage upon current for various kinds of discharges [55].

Plasmas possess various configurations and characteristics, depending on the approaches used for plasma generation, as presented in **Figure 1.12** [56]. The differences in plasma appearance mainly result from the differences in plasma characteristics, including gas temperature, discharging gas species as well as degree of ionisation. The diverse characteristics of plasmas can be related to the parameters such as electron temperature and density, and ion temperature, which can be altered by discharge types, power supply and/or operating temperature and pressure. In general, different electric fields are used to form direct current (DC) or alternating current (AC) discharges. The DC discharges can be maintained with a constant current (e.g. arc and glow) or be sustained in a pulsed-periodic regime (e.g. pulsed corona). In DC discharges, external ballast is usually applied in series with plasma to restrict the current through the circuit, which will significantly limit the electron density, and thus effectively restrict excessive neutral heating by electrons. The AC discharges can be generated with both low and high frequency. AC dielectric barrier discharge (DBD) is typical example of low frequency AC discharge operated at kHz frequency ranges; while the electrodeless induced radiofrequency (RF) discharges between 1-100 MHz and microwave (MW) discharges commonly generated at 24.5 GHz are classified as high frequency AC discharges.

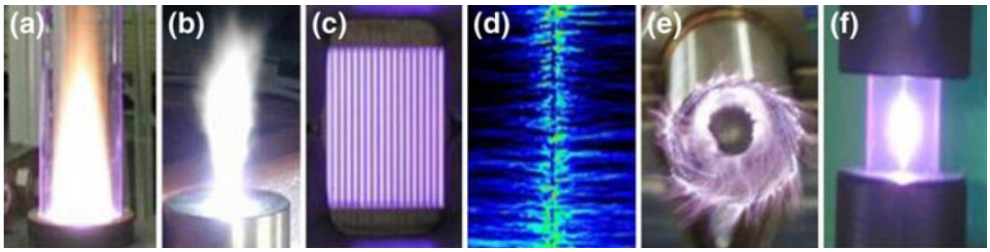

Figure 1.12 Diverse plasma configurations: (a) Microwave (MW); (b) DC torch; (c) dielectric barrier discharge (DBD); (d) pulsed corona discharge (PCD); (e) rotating gliding arc (RGA); (f) Spark discharge [56].

Depending on the required applications, plasmas can be generated over a wide range of pressures and temperatures. Gas pressure is one of the most important characteristic parameters. At a given gas temperature, the pressure defines the total density of gas particles and consequently the probability of mutual collisions among particles, namely, the collision frequency. In low pressure plasmas (10^{-4} to 10^{-2} kPa), the inelastic collisions between electrons and the heavy particles are excitative or ionising. These collisions do not raise the temperature of heavy particles, leaving it lower than those electronic ones. By increasing the pressure, more collisions take place, and therefore a more efficient energy transfer is achieved, leading to the increase in the temperature of the heavy particles and the formation of the steady-state of energy equilibrium in the plasma [57]. **Figure 1.13** shows the variation of the electron temperature (T_e) and the gas temperature (T_g) in a mercury-vapour discharge as a function of the mercury-vapour pressure at a constant current. Clearly, the gas temperature is only 300 K at 1 mtorr, while the corresponding electron temperature is up to 10,000 K (1 eV = 11,600 K); these two temperatures tend to be an average value of 5000 K when the pressure is above 5 torr [58].

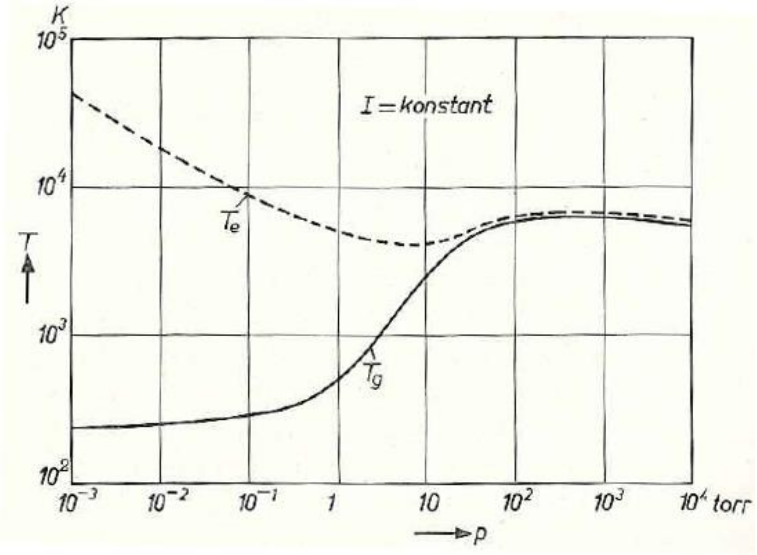

Figure 1.13 Schematic of the electron temperature (T_e) and gas temperature (T_g) as a function of pressure in a plasma discharge at a constant current [58].

In general, plasma can be categorised as thermal or non-thermal plasma based on the relationship between different particle temperatures. In the electric discharges, electrons firstly gain energy from the electric field and then transfer it to the heavy particles during collisions, losing only a small fraction of their own energy. At this stage, electron temperatures are higher than that of heavy particles. If sufficient time and energy is provided, subsequent collisions of electrons with the other heavy particles can equilibrate their temperature [59]. The kinetic energy (temperature) of the charged particles and the kinetic energy (temperature) of the background gas are similar under these conditions. This plasma is called thermal plasma and may be characterised by a single temperature at each point in space. Since all the particles are in a state of thermal equilibrium, thermal plasma is also known as equilibrium plasma [59]. By contrast, in non-thermal plasmas, also called non-equilibrium plasmas, plasma species have different temperatures; electrons generally have a kinetic energy in the range between 10^4 K and 10^5 K, 2-3 orders of magnitude greater than that corresponding to the background gas molecules [60]. **Table 1.1** compares the properties of thermal and non-thermal plasma [61, 62]. Basically, the temperature in the thermal plasma can reach up to 10^4 ~ 10^5 K; this high temperature makes it more powerful and can achieve high specific productivity. Thermal plasma is suitable for the pyrolysis processes and has applications in metallurgy, high temperature chemistry, solid waste treatment, thermal spraying, etc. The first plasma-assisted reformer with thermal plasma was the DC plasma torch; however, such devices are not effective in terms of energy consumption [63]. Moreover, due to the extremely high temperatures attained in the thermal plasma reactors, much more energy is required to cool the electrodes.

Table 1.1 Comparison of the general properties of thermal and non-thermal plasma [61, 62].

Properties	Thermal plasma	Non-thermal plasma
Gas temperature (K)	$(1\text{-}5)\times10^4$	300-1000
Ionisation degree (n_e/n)	$>10^{-3}$	$< 10^{-6}$
Electron temperature (eV)	1-5 ($T_e \approx T_n$)	1-10 ($T_e \gg T_n$)
Ionisation mechanism	Step-wise	Direct
Cathode current density (A/cm^2)	10^4-10^7	10-10^2

Figure 1.14 shows the comparison of the energy cost for H_2 production from CH_4 and diesel using thermal and non-thermal plasmas, in which new plasmatron and old plasmatron refer to the non-thermal plasma and thermal plasma assisted reformers, respectively [64]. Clearly, comparable H_2 yields can be achieved is both kinds of plasma reactors, but significantly lower energy consumption is observed in the case of non-thermal plasma.

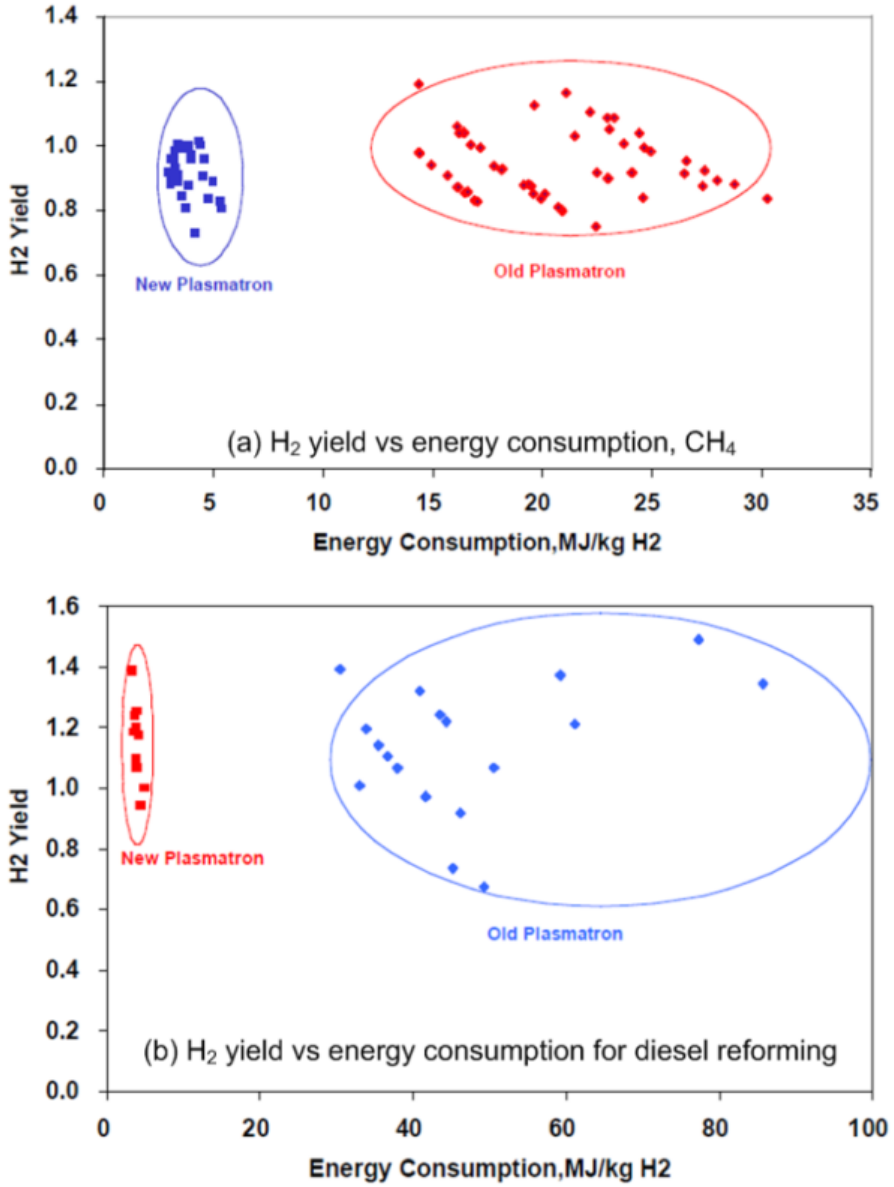

Figure 1.14 Comparison of energy costs for H_2 yield by thermal and non-thermal plasma [64].

1.2.2 Non-thermal plasma and its generation methods

Non-thermal plasmas present some advantages on the high selectivity and energy efficiency in plasma chemical reactions along with effective operation at relatively low temperatures, compared with thermal plasma. This basic feature is mainly due to the fact that most of the input power is used to produce the energetic electrons, rather than heating the bulk gas. As mentioned in Section 1.2.1, the most common method of plasma generation is by using an external electric field. Electrical breakdown will occur when the electric field exceeds a certain value at which a conductive gas channel is formed. In non-thermal plasma, most of the breakdown mechanisms start with an electron avalanche, which is a multiplication of primary

electrons in cascade ionisation. Compared with thermal plasma, the ionisation degree is rather lower, usually $n_e/n \leq 10^{-6}$ and the electron density is relatively low (see **Table 1.1**). This restriction in the electron density enables the electrons to gain more energy from the electric field between successive collisions and decreases the probability of electron-neutral interaction, thereby reducing the gas heating effect. The temperatures of the background gas in non-thermal plasma are often at or near room temperature. However, they can become excited and/or store energy in their thermodynamic energy modes by the collisions between energetic electrons and neutral particles, which will produce electronic, vibrational and rotational excitation of the neutral gas, ionisation, fragmentation of molecules, and lead to the formation of active chemical species that act as aggressive oxidising and reducing agents. In addition to the non-equilibrium property, non-thermal plasma technology is characterised by lower energy consumption and electrode erosion, significant reduction of the electrode cooling problems as well as compactness and low weight with relatively simple power supplies, which makes them potentially applicable for a wide range of purposes [63]. The first investigation on non-thermal plasma can be traced back to Simens' experiment for ozone generation using DBD in the 1850's [65]. Later, non-thermal plasma is being widely used in the volatile organic compounds (VOCs) abatement [66], NO_x treatment [67], water purification [68], hydrogen production [69], surface treatment as well as the catalysts preparation and activation [70, 71].

In non-thermal plasma, in addition to the highly energetic electrons, highly reactive species are produced, including free radicals, excited atoms, ions and molecules, etc., the plasma chemistry is rather complex. **Table 1.2** lists the main reactions occurring in the non-thermal plasma [65]. In the plasma gas processing, each of the plasma species plays different roles in the plasma chemistry. Electrons firstly obtain energy from the external electric field, and then distribute the energy through collisions and generate other new reactive species. Excited molecular states from vibrational excitation can transfer a significant proportion of energy into gas heating, which would accelerate the chemical reaction in the plasma. Ions and radicals contribute significantly to the plasma chemical synthesis because they have the ability to react in the plasma at lower temperatures than those required in thermal reactions [41]. By selecting the appropriate gases, plasma types and operating conditions, the complex chemical processes in the plasma can be controlled, which would favour the selective synthesis of the desired end products [59].

Table 1.2 Main reactions in the non-thermal plasma (A, B stand for atoms, A_2, B_2 for molecules; e represents an electron; M is a temporary collision partner; * marks the excited species and the species marked by + or – are ions) [65].

	Reaction Type	Reaction Formula
Electron/ Molecular Reactions	Excitation (rotational, vibrational, electronic)	$e + A_2 \rightarrow A_2^* + e$
	Dissociation	$e + A_2 \rightarrow 2A + e$
	Attachment	$e + A_2 \rightarrow A_2^-$
	Dissociation attachment	$e + A_2 \rightarrow A + A^-$
	Ionisation	$e + A_2 \rightarrow A_2^+ + 2e$
	Dissociation ionisation	$e + A_2 \rightarrow A^+ + A + 2e$
	Recombination	$e + A_2^+ \rightarrow A_2$
	Detachment	$e + A_2^- \rightarrow A_2 + e$
Atomic/Molecular Reactions	Penning dissociation	$M^* + A_2 \rightarrow 2A + M$
	Penning ionisation	$M^* + A_2 \rightarrow A_2^+ + M + e$
	Charge transfer	$A^\pm + B \rightarrow B^\pm + A$
	Ion recombination	$A^- + B^+ \rightarrow AB$
	Neutral recombination	$A + B + M \rightarrow AB + M$
Decomposition	Electronic	$e + AB \rightarrow A + B + e$
	Atomic	$A^* + B_2 \rightarrow AB + B$
Synthesis	Electronic	$e + A_2 \rightarrow A_2^* + e$ $A^* + B \rightarrow AB$
	Atomic	$A + B \rightarrow AB$

Until now, several different types of plasma have been used for CO_2 utilisation, including corona discharge, microwave discharge, gliding arc, DBD, and packed-bed reactors. In the following sections, a brief introduction of each discharge as well as their characteristics will be presented. Although the non-thermal plasma can also be generated at low gas pressures, expensive vacuum systems and pumps are required in these plasma technologies. Over the last two decades, a growing interest has been aroused to replace these low pressure systems with atmospheric non-thermal plasmas [54]. Therefore, the discussions on the non-thermal plasma generated under low gas pressure are not considered in this study.

1.2.2.1 Corona discharge

The corona discharge is a relatively low power electrical discharge that takes place in regions of high electric field strength near sharp edges, points, or thin wires near atmospheric pressure. It can be frequently observed at high voltage transmission lines, lightning rods, and its name 'crown' was taken from the mariner's observation of discharges from their ships' masts during electrical storms [72]. **Figure 1.15** (a) shows an example of corona discharge. Man-made corona discharge can be generated by either continuous or pulsed DC voltage between two electrodes. The electrodes are generally arranged as a grounded cylindrical outer electrode with a concentric high voltage wire or rod inner electrode, or as point-to-point, or point-to plate electrode configurations. The volume between the electrodes is occupied by a static or continuous flow gas. The non-uniform electric field is formed in the vicinity of the sharps edges or points of its electrodes where the radius of the curvature is small. **Figure 1.15** (b) shows a typical positive corona discharge between a needle and a plate. The ionisation of neutral gas occurs when the electric field is greater than a certain critical value. The non-uniform electric field is only formed in the vicinity of the sharp corona source, where the ionisation of gas molecules occurs; therefore, this region is called the ionisation zone and the corona discharge is considered as locally ionised plasma. Further away from the corona needle, the electric field magnitude drops and when it is below the required threshold value, no ionisation occurs. With the aid of the electrode, the ions created in the ionisation zone drift through the region outside the ionisation zone and towards the collecting electrode; the space outside the ionisation zone is therefore called the drift zone. In the drift zone, electron attachment reactions are favourable, producing negative ions.

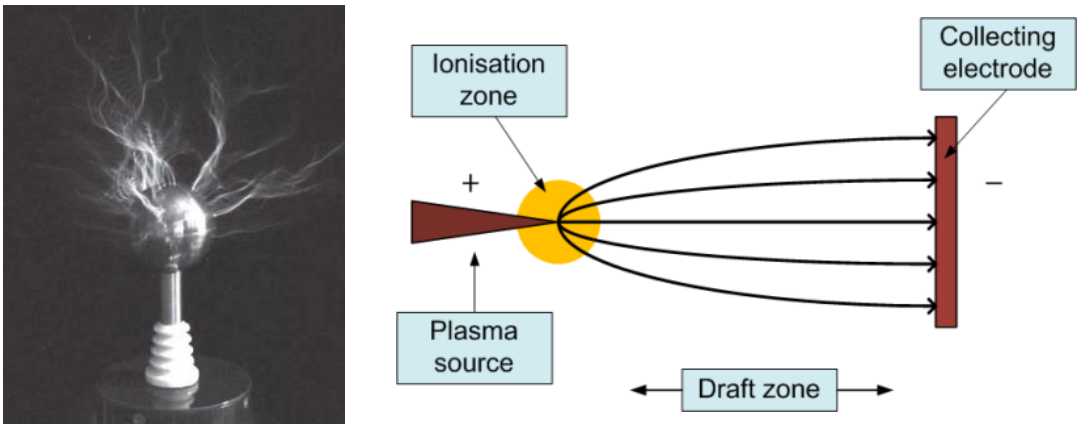

(a) (b)

Figure 1.15 (a) Image of a corona plasma discharge; (b) schematic of a positive corona discharge.

The corona discharge can be controlled depending on the polarity of the DC voltage applied to the electrode. As described above, a positive corona can be formed when the high electric field is centred on the anode. When the high electric field is centred on the cathode, a negative corona is produced as well. In the corona discharge, the strong electric field, ionisation and luminosity are only located close to one electrode; the electric current is transferred to the other electrode by the drift of the charged particles in the relatively low electric field [73]. Therefore, a low current and, as a result, low discharge power are achieved, which will limit the application of the continuous corona discharge. Increasing the applied voltage can enable the active corona to reach the opposite electrode, forming a spark [72]. However, spark channels will result in the local overheating and plasma non-uniformity, which is not favourable for practical application. The pulsed-periodic voltage can be used to deliver fast and effective power transfer into the non-thermal plasma discharge without the spark formation as long as the pulse width is shorter than the duration range (on the order of 100-300 nanoseconds with electrode distance of about 1-3 cm), which is necessary for the development of electron avalanches, avalanche-to-streamer transition, and streamer propagation between electrodes [61].

1.2.2.2 Radio frequency (RF) and microwave (MW) discharges

Radio frequency (RF) and microwave (MW) discharges are the two forms of discharges which are sustained with high frequency electromagnetic fields without electrodes. In RF discharges, electromagnetic fields generated by the power supply interact with the plasma through the inductive or capacitive coupling processes, with the former one generating thermal discharges and the latter one non-thermal discharges. The coupling of the electromagnetic field to the plasma discharge is mainly to maintain the plasma by the energy absorbed from the field. Poor coupling will result in the low efficiency of the power supply and the overall circuit. The frequencies to generate RF plasma are typically in the range of 0.1- 100 MHz, with the most used frequency being 13.56 MHz [59]. In the RF discharge, the wavelength is within the range of 3-300 meters.

For MW discharges, the operating frequency ranges between 300 MHz to 10 GHz with the most commonly used frequency being 2.45 GHz, much higher than that of RF discharges. **Figure 1.16** shows the typical configuration of a MW discharge [62]. In these reactors, the MWs are generated by a magnetron and guided by a wave guide to the process chamber. A dielectric tube (usually quartz tube), transparent to MW radiation, is passed through the wave guide. The electrons in the processing gas absorb the MW energy, which leads to an increase in kinetic energy, and thus the ionisation reactions are ignited by the inelastic collisions [74]. The plasma is formed at the interaction region of the wave guide and the dielectric tube, as the highest electric field is achieved at that point. Depending on the consumed

MW power, the bulk gas temperature can be at room temperature or reach up to several thousand kelvin [75]. In MW plasmas, the wavelengths are very small, which are on the order of centimetres and approach the dimensions of the reactor itself.

The electrode-less operation of RF discharge and MW discharge render them favourable for the conditions where extremely high temperatures are required, as complicated electrode cooling devices can be eliminated. However, initiating the high frequency plasma is much more challenging than DC plasmas because complex and somewhat more expensive power supplies as well as a high frequency generator are required. Moreover, the plasma must be coupled and matched as a load in the power circuit [76].

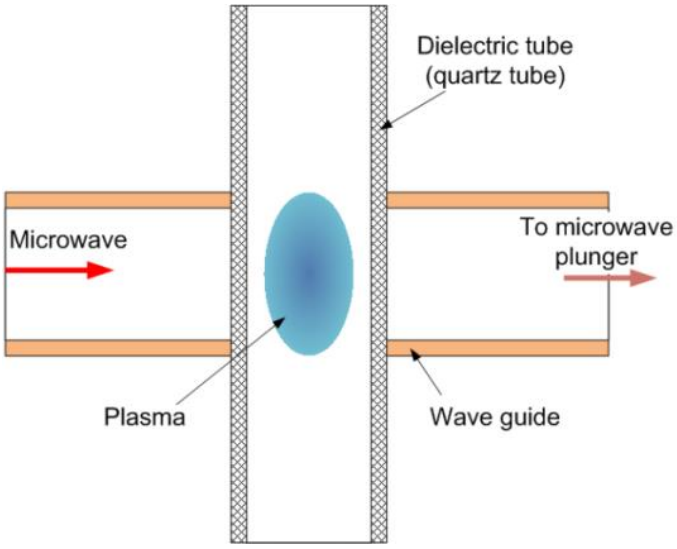

Figure 1.16 Schematic diagram of microwave plasma reactor [62].

1.2.2.3 Gliding arc discharge (GA)

Gliding arc (GA) discharge is an oscillating phenomenon developing between at least two diverging electrodes placed in a fast laminar or turbulent gas flow. The typical quasi-two-dimensional bi-electrode GA discharge device is shown in **Figure 1.17** (a). A high voltage generator provides the appropriate electric field to initially breakdown the gas at the shortest distance between these two electrodes and creates a plasma arc column. With the aid of the convective gas flow from the upstream injection port, the arc is pushed downstream along the electrode axis and its length is elongated until it can no longer sustain itself by the supplied power. Then the arc extinguishes, but immediately the new arc is generated at the narrowest gap. Through this ignition-evolution-extinction cycle, as shown in **Figure 1.17** (b) [77], GA discharge region is formed.

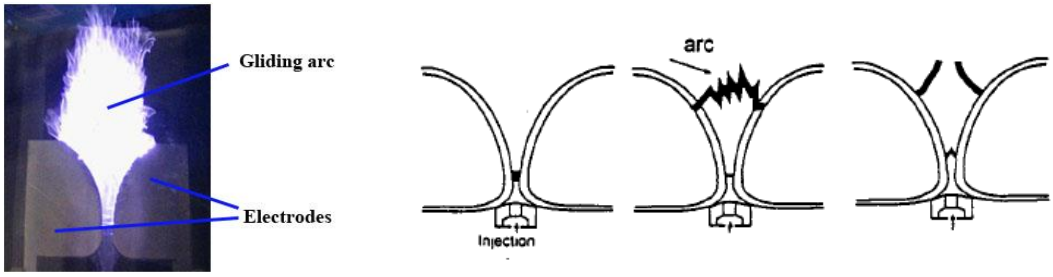

(a) (b)

Figure 1.17 Phenomenon of GA discharge: (a) photograph of GA discharge; (b) ignition, evolution and extinction of GA discharge [77].

Since the traditional GA discharge (i.e. plate GA discharge) device was designed by A. Czernichowski [77], it has been widely used in the fields of environment and energy, due to its unique characteristics of simple configurations and strong capacity of inducing chemical reactions. Several new types of GA reactors have been developed based on the configuration and basic characteristics of the traditional reactors. **Figure 1.18** shows the development of the GA discharge reactors, including multi-electrode GA discharge reactor [78], cone-shaped rotating GA reactor [79], magnetic GA reactor [80], and reverse vortex GA reactor [81].

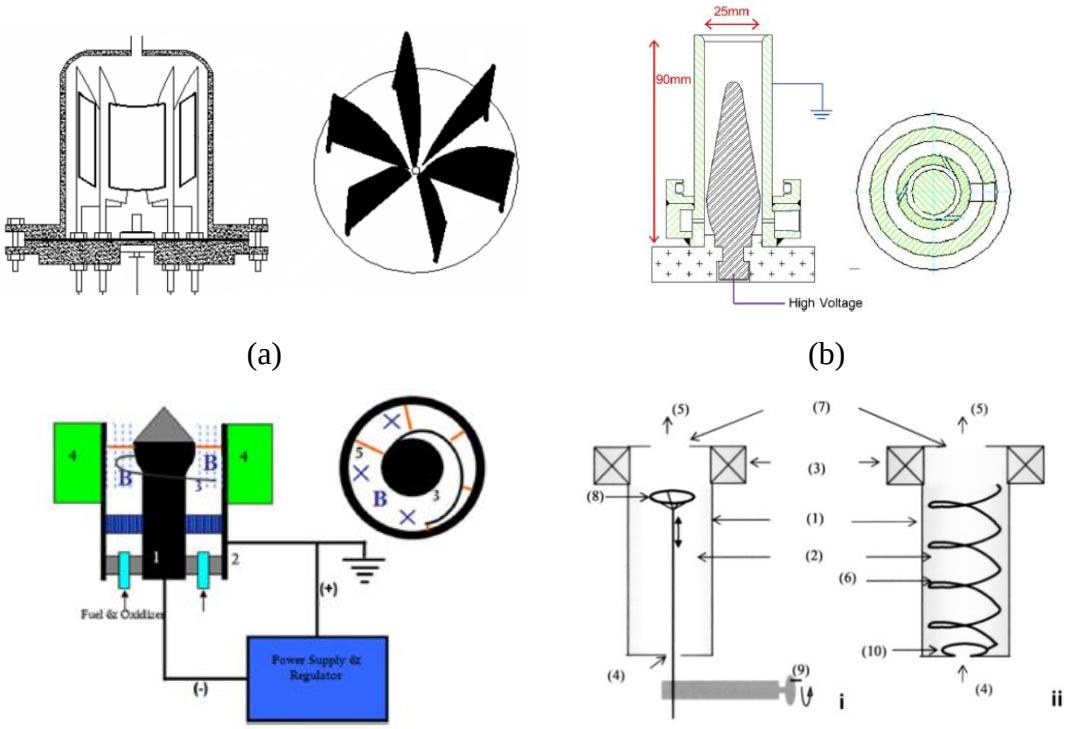

(a) (b)

(c) (d)

Figure 1.18 Development of different GA discharge configurations: (a) multi-electrode GA discharge reactor [78]; (b) cone-shaped rotating GA reactor [79]; (c) magnetic GA reactor [80]; (d) reverse vortex GA reactor [81].

1.2.2.4 Dielectric barrier discharge (DBD)

Dielectric barrier discharges (DBDs) are also named silent discharges as they were originally known due to the prevention of spark formations, which generated noise. There are two major discharge modes in DBDs: filamentary mode and homogeneous or glow mode. The filamentary mode has been a hot topic for investigation in the past several years, and most industrial applications of DBD use the filamentary mode [73]. Therefore, we mainly consider the filamentary mode in our study. A DBD reactor consists of two planar or cylindrical electrodes with one or more dielectric barriers positioned in the discharge gap as shown in **Figure 1.19** (a) and (b). The dielectric barrier acts to limit current flow once the discharge is ignited. It enables the microdischarges to distribute over the entire electrode area; and no spark or arc occurs in the discharge gap with an intact dielectric barrier [82]. The dielectric constant and thickness of the dielectric barrier determine the amount of displacement current passing through the dielectric. Preferred materials for the dielectric barrier are glass or silica glass. Ceramic materials and thin layers of enamel and polymer can be used in some special cases. Moreover, additional protective or functional coatings are applied in some applications [83]. For an atmospheric pressure DBD reactor, the distance between the two electrodes ranges from micrometres up to centimetres depending on the used processing gas and the applied voltage [74].

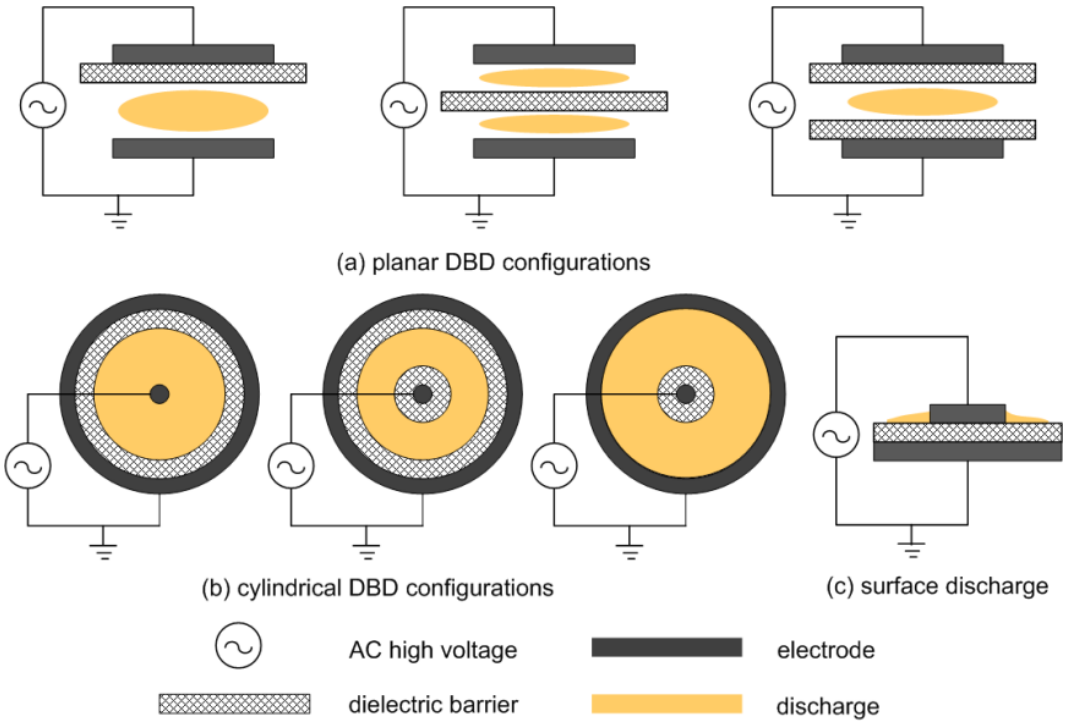

Figure 1.19 Different configurations of DBD reactors [84].

DBD reactors can be operated in a wide range of pressures (mbar up to atmospheric pressure) and the frequency can range between 50 Hz to 1 MHz [55]. Applying a strong electric field across the discharge gap, a large number of separate and short-lived current filaments, also known as microdischarges, are formed when the local electron density at certain locations in the discharge gap reaches a critical value. These bright, thin filaments are statistically distributed in space and time and are formed by channel streamers with nanosecond durations. When a microdischarge reaches the dielectric, it spreads into a surface discharge and the accumulation of the transferred charge on the surface of the dielectric barrier reduces the electric field. As the electric field further reduces, electron attachment prevails over the ionisation and the microdischarges are extinguished. As the polarity of the electrodes is rapidly changing, the microdischarges are re-formed at the point where the electron density reaches the critical value necessary for electrical breakdown. This leads to the continuous formation of nanosecond microdischarges at a frequency which is twice of the applied frequency [60]. The microdischarges appear as spikes on the current waveform and in appearance, they are randomly distributed over the surface of the dielectric. In reality, the position of the microdischarge is dependent on the residual charge distribution on the dielectric surface due to the memory effect [85]. In the microdischarges, the total transferred charge is closely related to the gas properties and can be influenced by the discharge gap width and the properties of the dielectric barriers [82].

Surface discharge, as shown in **Figure 1.19** (c), is another configuration of DBD [86]. A series of strip electrodes are attached to the surface of the dielectric barrier; while a film like counter electrode is embedded inside the dielectric barrier base and serves as the induction electrode. The dielectric barrier can be either planar or cylindrical. By applying an AC voltage between the strip and embedded counter electrodes, a surface discharge starts from the peripheral edges of each electrode and stretches out along the dielectric barrier surface. Many nanosecond surface streamers are contained in the surface discharge.

1.2.2.5 Packed-bed DBD reactor

The packed-bed reactor is a variation of the typical DBD system, which consists of packing pellets between the electrodes, as shown in **Figure 1.20**. The packing pellets could be either catalytic or non-catalytic. Glass beads, quartz, aluminate and ferroelectrics are the generally used packing pellets. $BaTiO_3$ is the most widely used ferroelectric material, which has a dielectric constant of 2000-10000 [84]. In addition to the packing pellets, one dielectric barrier layer (two or none in some cases) may be inserted between the electrodes. In the cylindrical packed-bed reactor, the dielectric barrier layer could be adhered to the inner and/or

outer electrodes; the inner electrode could be in the shape of a wire, rod, screw or a tube. The materials of the dielectric barrier and packing pellets could be different.

The major characteristic of the packed-bed reactor is the presence of the contact point between the packing pellets and between the packing pellets and the electrodes or the reactor wall. Applying a high voltage to the electrodes leads to a spontaneous polarisation of the ferroelectric material in the direction of the external electric field, generating a strong local electric field at the contact points [87]. This intense electric field results in gas breakdown and the production of partial discharges in the vicinity of each contact point. The presence of ferroelectric pellets in the discharge volume is favourable for a uniform gas distribution and electrical discharge. Packing pellets with a high dielectric constant will reduce the breakdown voltage and this generally leads to a higher discharge power. Therefore, packed-bed reactors could be considered as high electron energy but low plasma density devices [88]. Despite the low electron density, the packed-bed reactor could function as an alternative approach to enhance the energy efficiency due to the high mean electron energy resulting from the increase in the electric field. For the packed-bed reactor, the most important parameters are the material, dielectric constant, as well as the size and shape of the packing pellets [59, 88].

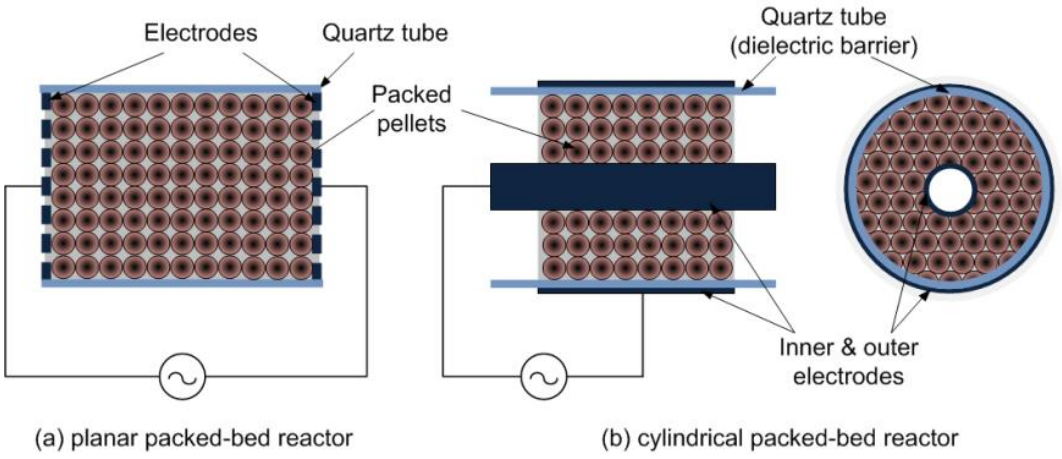

Figure 1.20 Different configurations of packed-bed reactors.

1.2.3 Plasma-catalysis systems

1.2.3.1 Plasma-catalysis system configurations

As mentioned above, the chemistry in non-thermal plasma is rather complex. The selectivity of the desired products is typically low. The combination of non-thermal plasma and catalysts has attracted high interest as an alternative in increasing the energy efficiency and optimising the by-product distribution, as it combines the low temperature activity, fast response and compactness of the plasma reactor with the high selectivity of the catalytic reactions. The non-thermal plasma can be

combined with the catalysts in either single-stage or two-stage configurations, as shown in **Figure 1.21**, depending on the position of the catalyst. In the single-stage configuration, the catalyst could be completely or just partially placed in the plasma zone, which enables the plasma and the catalyst to interact directly with each other. Reactions in this configuration involve short-lived active species, such as excited atoms and molecules, radicals, electrons and photons [89].

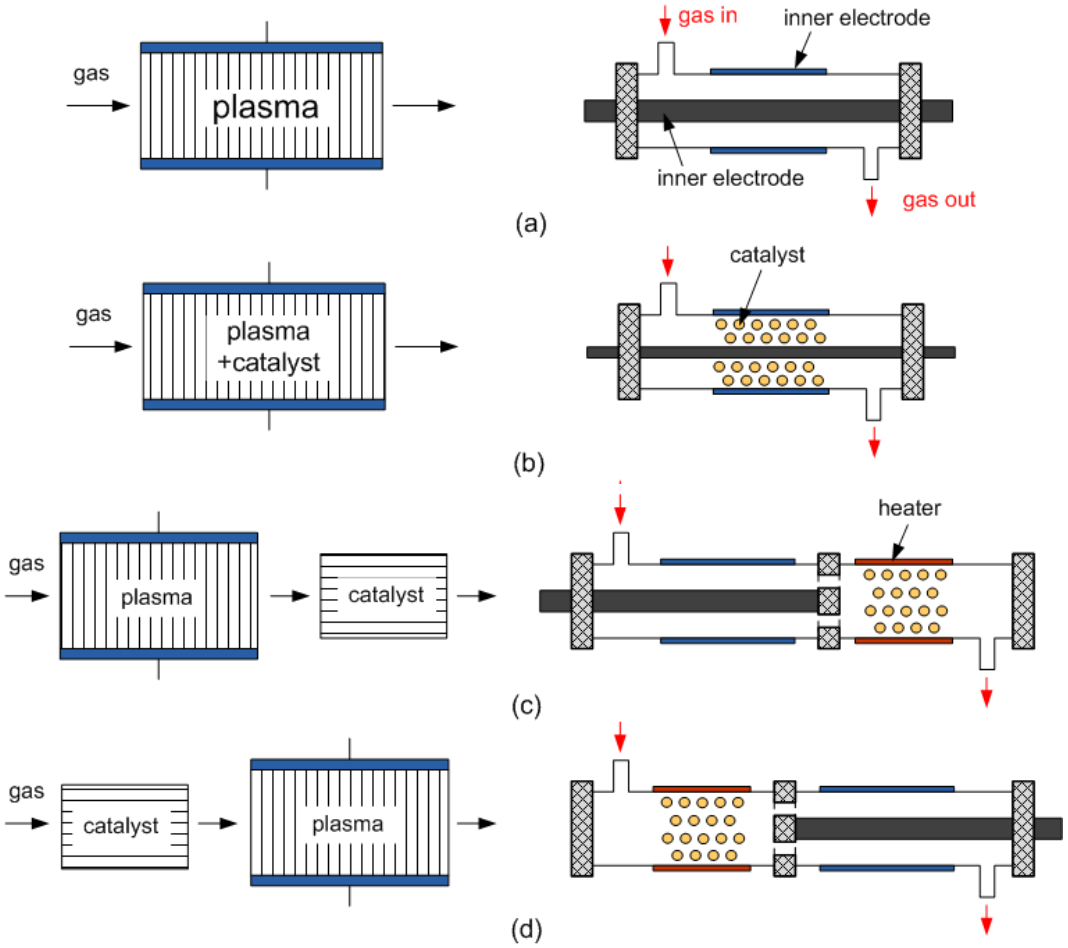

Figure 1.21 Schematic diagram of different plasma-catalysis configurations: (a) plasma-only system; (b) single-stage arrangement; (c) two-stage arrangement with plasma pre-processing; (d) two-stage arrangement with plasma post-processing.

Figure 1.22 shows the common heterogeneous catalyst arrangement in the single-stage plasma-catalysis systems [90]. Tu et al. found that the fully packing configuration (**Figure 1.22** (b)) strongly changes the discharge mode from a typical filamentary microdischarge to a combination of spatially limited microdischarges and a predominant surface discharge on the catalyst surface. While in the partially packing configuration (**Figure 1.22** (c)), strong filamentary discharges were still clearly observed and the physical and chemical interactions between the plasma and catalysts were significantly enhanced, which resulted in much higher performance in

the plasma-catalytic dry reforming of CH_4 than the fully packed reactor [91]. In the two-stage configuration, the plasma zone can be located either upstream or downstream of catalyst bed, which is termed as plasma pre-processing and plasma post-processing, respectively. In the former case, the plasma provides chemically reactive species for further catalysis or pre-converts reactants into easier converted products to accelerate the catalysis, which makes it the most adopted configuration for the two-stage plasma catalysis; while in the latter case, the plasma is generally applied to convert the residual reactants and destroy the undesired by-products generated by the thermal catalysis [92]. From the comparison of these two two-stage systems for autothermal reforming of C_8H_{18}, the plasma pre-processing gave better performance for H_2 production [93]. In this thesis, the plasma-catalysis refers to the single-stage process, where the catalyst is packed directly into the discharge gap of a coaxial DBD reactor.

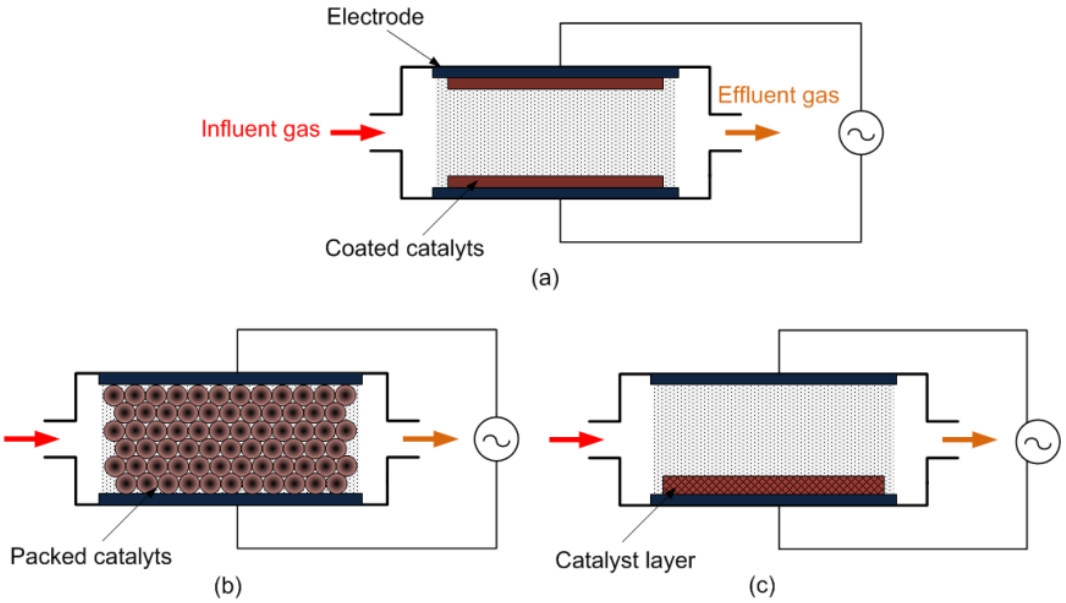

Figure 1.22 Common catalyst arrangement methods for the single-stage plasma-catalysis systems: (a) catalysts coated on the surface of the reactor wall and/or electrodes; (b) catalysts inserted as a packed-bed reactor (granulates, coated fibres, pellets); (c) catalysts placed as a layer at the bottom of the reactor (powers, pellets, granulates, coated fibres) [90].

1.2.3.2 Plasma-catalyst interactions

The interactions between the plasma and catalysts in the two-stage configuration are relatively simple as almost all of the generated short-lived active species (excited species, radicals and ions) in the plasma extinguish before they reach the catalysts. In such systems, the plasma mainly serves to change the gas composition fed into the catalytic reactor for the pre-processing configuration or to

convert the residual reactants and the undesired by-products from the thermal-catalytic reactions for the post-processing configuration [92].

For the single-stage plasma-catalysis system, the interactions between the plasma and the catalysts become rather complicated, which has been discussed in detail in the reviews [90, 94-96]. The interactions can be elucidated from two aspects: (1) the influence of packing catalysts on plasma characteristics and (2) the influence of plasma discharge on the catalysis. **Figure 1.23 (a)** represents some the plasma-catalysis effects reported in the literatures and **Figure 1.23 (b)** summarises the possible plasma-catalyst interactions resulting in the plasma-catalysis synergism [95]. The principles of these mechanisms are briefly described as follows.

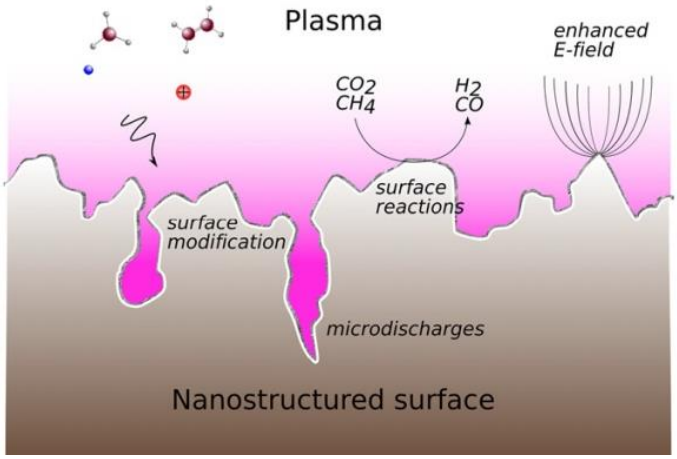

(a)

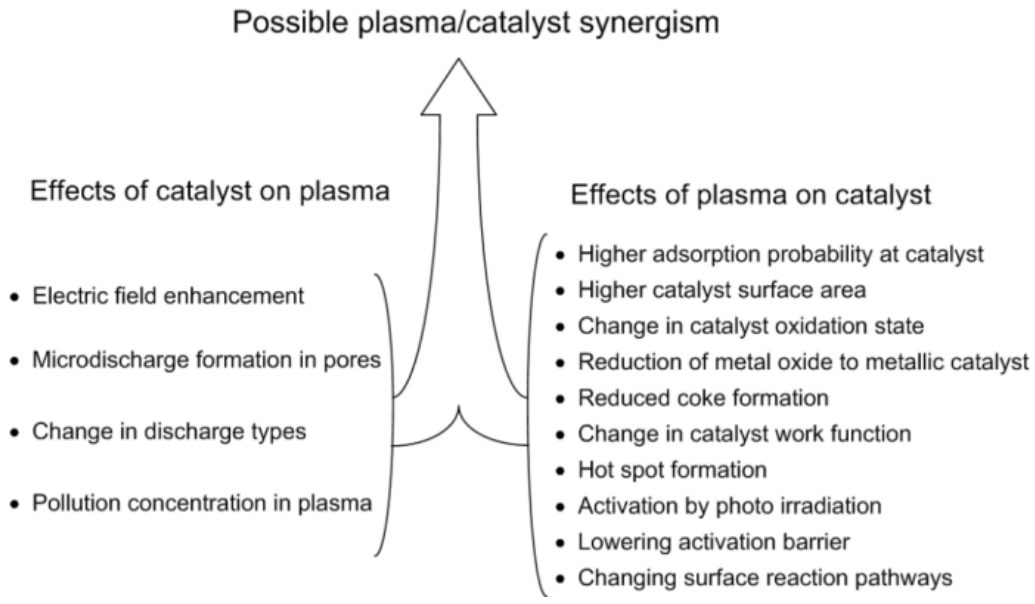

(b)

Figure 1.23 (a) Schematic representation of the factors active in plasma catalysis; (b) possible plasma-catalytic synergism caused by the effects of catalyst on plasma and of plasma on catalyst [95].

(1) Effect of catalyst on plasma

With the presence of catalysts in the discharge volume, the electric field will be enhanced due to the large curvature of the local surface of the catalyst, just like the non-catalytic materials packing in the plasma reactor, causing the packed-bed effect. Although the electric field enhancement is a physical effect, the modified electric field directly influences the electron energy distribution function as well as the electron impact dissociation and ionisation rates, which will vary the chemical composition in the plasma [95]. Moreover, the electric field enhancement results in the formation of microdischarges in the volume of catalyst pores, which is rather strong and make the discharge characteristics quite different from the discharge in the bulk gas [97-99]. This will in turn lead to the different production and loss rates of various plasma species. In addition, packing catalyst pellets in the discharge area will propagate the streamer along the catalyst surface, resulting in the expansion of the discharge region and a more intensive discharge around the contact points [90, 100]. With this so-called surface discharge, the electron impact ionisation and dissociation rates are enhanced significantly. All of these phenomena contribute to the change in the chemistry. The porous structures of the catalyst enable the gas reactant species to be adsorbed on the surface, leading to a longer retention time in the reactor and therefore a higher reaction efficiency of the plasma-catalytic process than that in the plasma process without catalysts [90].

(2) Effect of plasma on catalyst

When the applied voltage across the catalyst bed exceeds a specified value, gas discharge will be formed, and it will greatly affect the adsorption-desorption equilibrium of molecules on the surface of the porous catalyst due to the electric surface properties changed by the discharge [101]. A higher adsorption probability at the catalyst surface has been observed in the case of plasma than in the thermal catalysis, which will affect the concentration of the gas reactant species, and therefore the reaction efficiency. The adsorption probability at the catalyst surface is also increased with the surface area of the catalyst. It has been reported that plasma discharge favours the formation of the smaller active metal nanoparticles, leading to higher dispersion and thus, a larger total surface area [102]. The surface area can also be modified by the discharge induced changes in the overall catalyst morphology [103]. Moreover, the plasma generated small nanoparticles typically possess a less ordered surface structure, containing defects, vacancies, under-coordinated sites, edges and corners, all of which will additionally enhance the catalytic activity of the catalyst [104]. In addition, in the presence of the plasma, the coke formation on the catalyst surface is reduced and therefore, the deactivation of the catalyst is prevented, which has been demonstrated to result from increasing the active metal dispersion [105].

Exposing the catalyst to a plasma discharge will change the oxidation state of the catalysts, due to the influence of the high voltages or through the interaction with reactive oxygen species (ozone, atoms and radicals) [103, 106]. It has been reported that a change in the oxidation state of a surface layer of Cu, Ag and Au supported on ZrO_2 occurred after the O_2 plasma treatment; and the O_2 plasma reduced catalysts led to the increase in the activity towards butanol dehydrogenation [106]. Plasma can also reduce the catalyst, turning oxide phases into the metallic phase [107, 108]. Tu el al has shown the reduction of NiO to metallic Ni in an atmospheric DBD reaction for the dry reforming of CH_4 reaction [107].

In the plasma-catalysis system, the presence of the voltage and current (or charge accumulation) on the catalyst surface could lead to the changes in the work function of the metal catalyst, resulting from the change in the electron extraction potential of the catalyst due to the plasma induced polarisation [109, 110]. It is stated that a higher work function will enhance the reduction of the active metals and promote the oxidation reaction [111].

In the plasma discharge, photons can be generated for the activation of the catalyst. This process is therefore called photocatalysis. The most commonly used photocatalyst is anatase phase TiO_2 with a bandgap of 3.2 eV. Photons with wavelengths below 387 nm will promote the electrons from the valence band to the conduction band, thereby activating the catalyst for redox reactions [95]. However, the plasma generated UV radiation is not always the factor inducing the activation of the photocatalyst [112].

When catalysts are placed into the discharge volume, strong microdischarges are formed in the vicinity of structures with high curvature, leading to the high temperature in these regions, which is beneficial to the formation of the hot spots on the catalyst surface [90]. These hot spots can then modify the local plasma chemistry or perhaps even locally activate the catalyst [97].

Plasma typically consists of a large fraction of species in vibrationally excited states, which can lower the activation barrier for the surface reactions due to the increased energy state of the reactants compared to the ground state and the non-adiabatic barrier crossing (e.g. a barrier crossing which is not accessible from the ground state) [95]. Furthermore, plasma treatment can also lower the activation barrier of the catalyst [113].

As mentioned above, plasma is a complex mixture of ions, electrons, electronically and vibrationally excited species, and stable molecules, atoms, radicals as well as photons. This makes the plasma chemistry quite different from that in the thermal-catalytic reaction system. Consequently, the reaction path for the formation of the desired products from the reactants in the plasma-catalysis process will also be different [95].

(3) Synergistic effect between the plasma and catalyst (plasma-catalysis)

In plasma-catalysis, the synergistic effect between the plasma and the catalyst may occur, and consequently improved process performances are achieved in terms of reactant conversion, product selectivity and/or energy efficiency, compared with the catalysis only and the plasma-only process or their sum. This has been demonstrated in the VOC removal and the NH_3 synthesis process [89, 114, 115]. For the dry reforming process, Zhang et al. also reported the synergistic effect generated by the combination of the DBD reactor and Cu-Ni/Al_2O_3 catalyst, as shown in **Figure 1.24** [116]. The conversion of CO_2 and CH_4 in the plasma-catalytic reaction was higher than the sum of the catalysis only and the plasma-only. The selectivity of CO and H_2 were also enhanced in the plasma-catalysis process.

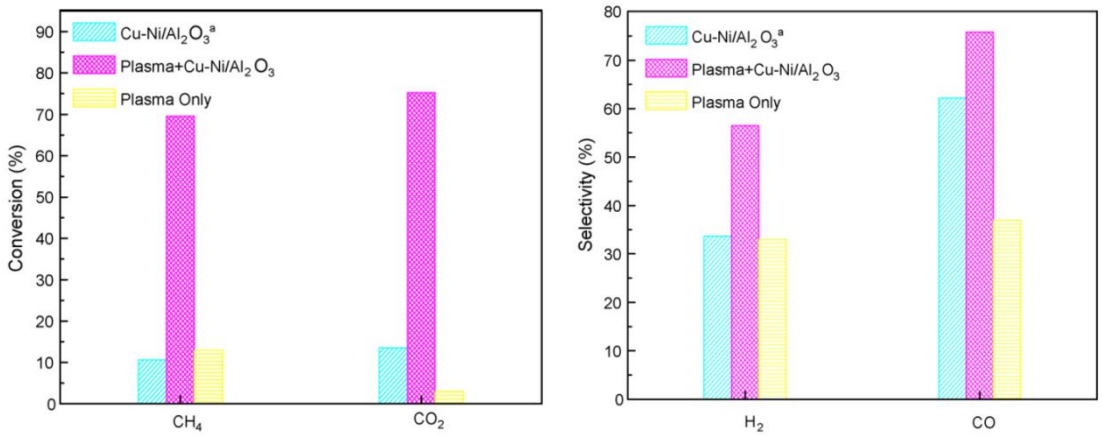

Figure 1.24 Synergistic effect of a DBD and catalyst in dry reforming of CH_4 from the work of Zhang et al.: (a) reactant conversion; (b) product selectivity [116].

1.3 Review of the Application of Non-thermal Plasma in CO_2 Decomposition

Based on the generation methods for the non-thermal plasma, different types of non-thermal plasma reactors have been applied for CO_2 decomposition, including corona, DBD, MW and GA. In this section, the performance of different non-thermal plasma reactors in CO_2 decomposition will be described, except for those processes operated at low pressure, such as MW and RF discharges [117, 118], as they may be incompatible with the economic requirements for chemical synthesis at a commercial scale.

In the early stage, when global warming was not yet an issue, applications of CO_2 decomposition mainly focused on the emission control of automobile exhaust gas and the development of CO_2-detectors, where highly diluted CO_2 was investigated [119]. Since CO_2 was considered as one of the major contributors to the

GHG effect, decomposition of GHGs from industrial and energy production exhausts have been attracting increasing attention. From the view point of large scale applications, dilution cannot be considered as an optimal option; therefore, pure CO_2 decomposition using non-thermal plasma technology has become a hot research topic.

For the corona discharge, both the positive and the negative corona discharges have been used [120-122]. In these studies, CO_2 conversion was around 10% with CO as the carbonaceous products. O_2 or O_3 were also observed in different reactors. Horvath et al. reported that CO_2 conversion in the negative polarity discharges was slightly higher than that in the positive discharges [122]. In the DBD reactor for pure CO_2 decomposition, the effects of frequency, input/discharge power, feed flow rate, feed gas temperature, discharge gap and dielectric materials have been studied [123, 124]. The specific energy density (SED) has been demonstrated to play the most significant role in CO_2 conversion and energy efficiency. Aerts et al. reported that a lower discharge power with a lower gas flow rate could result in a higher conversion and energy efficiency [124]. In their work, a maximum CO_2 conversion of 35% with an energy efficiency of 1.9% was obtained in a DBD reactor at a feed flow rate of 10 ml/min and a discharge power of 40 W [124]. In the experiments performed by Brehmer et al., an almost stoichiometric CO/O_2 molar ratio of 2:1, along with a strongly temperature dependent O_3 production of up to 0.075%, was observed in the CO_2 decomposition products from a DBD reactor [125]. GA discharge seems to be very promising for CO_2 decomposition, in which high energy efficiencies are possible due to high feed flow rate under atmospheric conditions. Nunally et al. reported a maximum energy efficiency of 43% for CO_2 decomposition in a non-equilibrium GA plasmatron; however, the corresponding CO_2 conversion was quite low. In their experiments, CO_2 conversion to CO was observed in the range of 2-9% for a specific energy input (SEI) variation from 0.1 to 1.0 eV/molecule and a flow rate variation from 14 to 40 l/min [126]. Therefore, it can be deduced that high energy efficiency is achieved at the expense of low CO_2 conversion. Indarto et al. also obtained similar results in their work of CO_2 decomposition in a GA discharge reactor [127].

In order to improve the CO_2 decomposition performance, the combination of plasma and catalyst (i.e. plasma-catalysis) was introduced, however, most researches focused on the effect of the electrode materials. Matsumoto et al. investigated the CO_2 decomposition process in a DBD reactor with Cu, Ni, and Fe rods as the inner electrode for a mixture of 10% CO_2 in Ar. They found that CO_2 conversion increased with the increase in the heat of formation for the corresponding metal oxides, i.e. CO_2 conversion increased in the order of Cu<Ni<Fe. No obvious difference was observed in the selectivity to the produced O_2 and CO [128]. In order to study the effect of the electrode materials, active metal could be coated on the electrode

surface. Brock et al. investigated CO_2 decomposition in a fan-type AC glow discharge reactor coated with Au, Cu, Pt, Pd, Rh and mixed rotor/stator systems (Au/Rh and Rh/Au) for a mixture of 2.5% CO_2 in He. The trend in the activity of these metals in both conversion and efficiency was observed in the order: Rh > Pt ≈ Cu > Pd > Au/Rh ≈ Rh/Au ≈ Au. In the Rh-coated reactor, a conversion as high as 30.5% was obtained [129].

The modification of the plasma reactor by using a packed-bed reactor or developing new dielectric materials is applied for the enhancement in the CO_2 decomposition performance. For the packed-bed plasma reactors, Wen et al. performed pure CO_2 decomposition in a corona reactor packed with porous Al_2O_3 pellets (α-Al_2O_3, γ-Al_2O_3). It was found that the high surface area and strong CO_2 adsorption capacity of γ-Al_2O_3 played a positive role in CO_2 decomposition; meanwhile, the presence of γ-Al_2O_3 also suppressed the reaction of CO and O to form CO_2 again. Therefore, the decomposition of CO_2 was greatly enhanced by packing γ-Al_2O_3 [130]. Yu et al. used silica gel, quartz, α-Al_2O_3, γ-Al_2O_3, and $CaTiO_3$ as packing materials in a packed-bed DBD reactor to investigate the roles of dielectric properties and morphology of packing dielectric pellets in the decomposition of CO_2. $CaTiO_3$ was found to exhibit the best promotional effect on CO_2 decomposition with a maximum CO_2 conversion about of 20% [131]. Similarly, quartz wool, quartz sand, γ-Al_2O_3, MgO and CaO were utilised as the packing materials in a DBD microplasma reactor for CO_2 decomposition. CO_2 conversion and energy efficiency achieved the highest value of 41.9% and 7.1% in a CaO-packed reactor due to the higher dielectric constant and basicity of CaO [132].

For the modification of the dielectric materials, Li et al. prepared a series of $Ca_{1-x}Sr_xTiO_3$ ($0.1 \leq x \leq 0.4$) with 0.5 wt% $Li_2Si_2O_5$ by liquid phase sintering and used them as dielectric barriers in the DBD reactor for CO_2 decomposition. $Ca_{0.8}Sr_{0.2}TiO_3$ with 0.5wt.% $Li_2Si_2O_5$ led to a maximum CO_2 conversion of 18.9%, much higher than those obtained in commercial SiO_2 and Al_2O_3. This optimal $SrTiO_3$ concentration was resulted from two competitive effects caused by the high permittivity of dielectric barrier: the increase in the transported charges within a single microdischarge channel and the rapid accumulation of the charges on the surface of the dielectric barrier [133, 134]. Wang et al. prepared $Ca_{0.8}Sr_{0.2}TiO_3$ ceramic barriers with the addition of CaO-B_2O_3-SiO_2 (CBS) glass in the range of 0.5%-5% and investigated their effect on the conversion of CO_2. They found that CO_2 conversion and conversion efficiency reached their maximum values of 48.7% and 1.1 W/% with the addition of 5.0 wt% CBS when 10% CO_2 in N_2 was used as the reactant. They suggested that increasing the CBS amount would lead to the increases of the surface resistance and the capacitance of the grain boundaries; moreover, the grain boundaries on the dielectric barrier surface could serve as charge-trapping sites, so that a more homogeneous discharge would be generated, all

of these factors would result in the enhancement of both CO_2 conversion and energy efficiency [135].

1.4 Review of the Application of Non-thermal Plasma in Dry Reforming of CH_4

Several types of non-thermal plasmas have been investigated for dry reforming of CH_4, including glow discharge [136, 137], corona discharge [138, 139], MW discharge [140, 141], GA discharge [142, 143] and DBD [144, 145]. The state of the art for dry reforming of CH_4 is summarised in the following sections from the perspectives of plasma-only and plasma-catalytic processes.

1.4.1 Non-thermal plasma dry reforming of CH_4 without catalyst

Atmospheric pressure glow discharges (APGDs) have been investigated for dry reforming due to their high electron energy and electron density as well as the proper temperature during the plasma process. Ghorbanzadeh et al. studied syngas production in an atmospheric pulsed glow discharge reactor sustained by the corona pre-ionisation. The energy efficiency was within 15%-40% for different experimental conditions with syngas as the main products. Hydrocarbons up to C_4 were also detected with C_2H_2 showing the highest selectivity [146]. The advantage of APGD for the dry reforming process is mainly due to the higher electron density; however, the enlargement of the process is the biggest challenge for its industrial application [147].

Using corona discharge, the dry reforming process has been investigated in different discharge forms, including pulsed, positive, negative and AC corona discharges [138, 148, 149]. Dai et al. found that in a pulsed corona plasma at ambient conditions, CO_2 and CH_4 were respectively transformed into CO and C_2 hydrocarbons; the pulse voltage and the repeated frequency had a positive influence on the conversion of the feed gases [148]. Li et al. found that the conversion of CO_2 and CH_4 increased in the order of negative corona < AC corona < positive corona, whereas the H_2/CO molar ratio in the products exhibited the opposite order [138, 149]. Although high electron density can be obtained in corona discharge, it is an inhomogeneous discharge with low current density. High electron density mainly occupies the region around the high curvature electrode, which makes it difficult to achieve a large treatment capacity for dry reforming of CH_4.

For dry reforming of CH_4 in the atmospheric MW discharge reactor, Zhang et al. reported that syngas together with C_2H_4 and C_2H_2 were obtained as the major products in a pulsed MW reactor [141]. Jasinski et al. proposed two types of atmospheric pressure MW plasma sources (namely, a nozzleless waveguide supplied coaxial-line-based and a nozzleless wave guide-supplied metal cylinder-based) for

hydrogen production via CH_4 conversion. Their results indicated that the nozzleless waveguide-supplied metal-cylinder-based MW plasma source showed better performance in terms of hydrogen production rate and energy efficiency [140]. MW discharge seems to be a promising plasma form for dry reforming of CH_4 due to the high conversions, product selectivity and large treatment capacity as well as high energy efficiency. However, the equipment necessary for MW discharge is more complicated and bulky, which increases the project difficulty and operating cost for industrial application.

For the utilisation of GA discharge in dry reforming of CH_4, the quasi-two-dimensional gliding arc discharges were mainly applied. Bo et al. investigated the effect of the feed gases proportion on the dry reforming performance using GA discharges. Their results showed that syngas as well as C_2H_2 and C_2H_4 were the main reforming products; increasing the CH_4/CO_2 molar ratio, both CH_4 and CO_2 conversion and consequently the formation of each main by-product were enhanced. They also found that a CH_4/CO_2 molar ratio larger than 2:1 resulted in serious coke deposition, especially in the relatively high applied voltage condition [142]. Tu et al. emphasised the production of carbon nanomaterials from the dry reforming of CH_4 in a GA discharge reactor. They found that different carbon materials (including spherical carbon nanoparticles, multi-wall carbon nanotubes and amorphous carbon) were obtained as by-products of syngas generation in the plasma dry reforming ptocess [143]. In a GA discharge, high feed flow rates were required to maintain the arc evolution during the discharge process. The relatively higher energy efficiencies were obtained at the expense of low reactant conversions due to the higher total feed flow rate.

DBD reactors have been investigated for dry reforming of CH_4 for nearly three decades, including both the plasma-only and the plasma-catalysis processes. In the plasma-only process, syngas was the targeted products in the early stage [44, 150]. Later, higher hydrocarbons and oxygenates were also considered. Liu et al. reported that besides syngas, gaseous and liquid hydrocarbons, plasma-polymerised film as well as oxygenates could be directly synthesised in the plasma dry reforming reactions [151]. Li et al. developed three different DBD reactors for synthesis of oxygenates and higher hydrocarbons directly from the dry reforming of CH_4. The first reactor had a larger discharge gap while the second one had a smaller gap; based on the configuration of the second reactor, the high voltage electrode in the third reactor was divided into five parts with equal length to form an after-glow zone between each part. Their results indicated that smaller discharge gap favoured the formation of liquid hydrocarbons and acid; while much higher concentrations of methanol and ethanol were generated with a larger discharge gap. For the production of acetic acid, the smaller discharge gap was favourable, especially in the presence of

after-glow zones [152]. They also demonstrated that there existed an optimum CH_4/CO_2 molar ratio for the maximum selectivity of the objective oxygenates [153].

Several modifications of the DBD reactor have been performed to improve the reactant conversion and/or the distribution, yield and selectivity of the products. Wang et al. proposed the multi-stage ionisation design to enhance the reactant conversion and to reduce the output of by-products. It was found that the multi-stage ionisation favoured a higher conversion of CO_2, but lowered the conversion of CH_4. Meanwhile, the selectivity to CO and H_2 was increased, while the selectivity to the by-products (C_2-C_6) was decreased by the multi-stage ionisation [154]. Rico et al. compared two different DBD plasma configurations for the dry reforming of CH_4. In the first plasma device, attention was paid to the influence of the surface roughness of the electrodes on the conversion yields; the effect of the different filling dielectric materials (i.e. Al_2O_3 or $BaTiO_3$) was evaluated in the second packed configuration. It was found that the maximum efficiency yield was observed in the packed - bed reactor configuration containing Al_2O_3 for the dry reforming of CH_4 (~ 1 mol H_2 per kilowatt hour) [155]. The effect of the packing materials on the plasma dry reforming performance was also investigated by Gallon et al. They used quartz wool, Al_2O_3 and zeolite 3A as the packing materials in their DBD reactor. Quartz wool was found to enhance the conversion of CH_4 and improve H_2 yield because it induced an increase in the intensity of the microdischarge filament; while in the presence of Al_2O_3 and zeolite 3A, the discharge intensity was reduced and consequently the conversions of CH_4 and CO_2 were decreased compared with the condition without packing [156]. Ozkan et al. developed a new geometry of a DBD reactor with multiple electrodes for the treatment of high gas flow rates in the dry reforming of CH_4. In their work, the main products were syngas, C_2H_4 and C_2H_6 when Ar or He was used as the carrier gas [157].

1.4.2 Non-thermal plasma-catalytic dry reforming of CH_4

Generally, the product distribution in the plasma-only process is rather complex, including syngas, higher hydrocarbons (≥ 2), oxygenates and polymers. In addition, the selectivities towards target products (e.g. syngas) are typically low. The combination of non-thermal plasma and heterogeneous catalysts has the potential to improve reactant conversions and product selectivities at low temperatures. In plasma-catalytic processes, the synergistic effect may be generated by the combination of plasma and catalysts, which will enhance the energy efficiency of the plasma processes and improve the catalyst stability by reducing poisoning, coking and sintering. Up to now, the investigations on plasma-catalytic dry reforming have reported using plasma jet, corona and DBD reactors. The plasma-catalytic dry reforming of CH_4 using DBD reactors has attracted the most significant attention.

In the early stage of the research on the plasma-catalytic dry reforming of CH_4 in the DBD reactors, different zeolites were used as the catalysts. Eliasson et al. demonstrated the direct formation of higher hydrocarbons from dry reforming of CH_4 when zeolite NaX was used. They found that the presence of zeolite NaX in the discharge zone reduced the overall conversion but increased the concentrations of C_2 to C_4 compounds in the products [158]. Zhang et al. compared the effects of quartz fleece, zeolite X, zeolite HY, and zeolite NaY on the reaction of CH_4 and CO_2 at ambient conditions. Zeolite NaY was found to be the most promising catalyst for producing syngas and liquid hydrocarbonss (C_{5+}) with high CH_4 and CO_2 conversions [42]. Comparatively, Zeolite HY showed the best performance in producing syngas and C_4 hydrocarbons (C_4H_8, *n*-C_4H_{10}, *i*-C_4H_{10}) with high selectivity, compared with quartz fleece, zeolite NaA and zeolite NaY [159]. Jiang et al. reported that the application of zeolite A inhibited the formation of carbon black and plasma polymers and resulted in a higher selectivity towards valuable hydrocarbons (C_2-C_4) [160].

In the same period, the catalytic effects from different electrode materials were also taken into consideration. Li et al. investigated the effect of the electrode materials (Ti, Al, Fe and Cu) on the cogeneration of syngas and higher hydrocarbons from dry reforming of CH_4 in the DBD reactor. They found the Ti electrode exhibited the highest activity for reactant conversions, while the other three materials showed a similar performance [161].

Later, supported metal catalysts were applied in the plasma-catalytic dry reforming of CH_4 in DBD reactors, such as Ni/γ-Al_2O_3 [91, 107, 162-168], Ag/Al_2O_3 [169], Pd/Al_2O_3 [169, 170], Cu-Ni/Al_2O_3 [116], Cu/Al_2O_3 [166, 170], Co/γ-Al_2O_3 [166], Mn/γ-Al_2O_3 [166], Fe/Al_2O_3 [171], La_2O_3/γ-Al_2O_3 [172], $LaNiO_3$@SiO_2 [173, 174], etc. Song et al. reported that the presence of Ni/γ-Al_2O_3 in the discharge volume led to enhancement in CO selectivity and CO_2 conversion, but the Ni loading had no obvious effects on reactant conversion and product distribution [168]. However, different phenomenon in the effect of the Ni loading was observed in the study of Mahammadunnisa et al. They stated that the 20 wt.% Ni/Al_2O_3 catalyst showed higher reactant conversion, syngas selectivity and H_2/CO molar ratio in the gas product than those in the catalyst with a higher (30 wt.%) and lower (10 wt.%) Ni loading [162]. Zeng et al. compared the influence of different supported metal catalysts M/γ-Al_2O_3 (M = Ni, C_O, Cu and Mn) on the performance of the plasma reforming process. They found that the combination of plasma with the Ni/γ-Al_2O_3 and Mn/γ-Al_2O_3 catalysts significantly enhanced the conversion of CH_4, while no enhancement in CO_2 conversion was observed with any catalyst. Moreover, the integration of plasma and Ni/γ-Al_2O_3 exhibited the highest activity for syngas production [166]. In the study of Zheng et al., $LaNiO_3$@SiO_2 core-shell nanoparticle catalysts showed better catalytic performance with higher reactant conversion,

product selectivity and catalytic stability, compared to the traditional Ni-based catalysts (Ni/SiO_2, $LaNiO_3/SiO_2$ and $LaNiO_3$) [173, 174].

For the interaction between the catalyst and the plasma in the plasma-catalytic system at different conditions, Lee et al. studied the heating effect on the syngas production from dry reforming of CH_4 in a DBD reactor packed with Ni/γ-Al_2O_3. The heating zone was added downstream of the plasma zone with a partially overlapped part. In this case, the conversion of CH_4 was 97.5 % and that of CO_2 was almost 100% with an input power of 80 W and a heating temperature of 573 K. Such high conversions in the pure thermal catalytic reforming could only be obtained when the temperature reached more than 1073 K. They suggested that the synergetic effect between the plasma and catalyst resulted in high conversion and selectivity at lower temperatures [165]. Wang et al. used three different contact modes of catalyst and plasma to investigate their synergetic effect on the dry reforming process, as shown in **Figure 1.25** (a). In mode A, the catalyst was placed 15 mm away from the discharge zone; for mode B, the catalyst was placed at the end of the discharge zone; and in mode C, the catalyst was fully packed in the annular discharge gap. They found that the synergetic effect was only achieved when the catalyst was fully filled in the annular discharge gap (mode C). In addition, with the increase of temperature, the synergetic effect appeared to be evident from 673 K [163]. Similarly, Tu et al. compared the effect of three different packing methods for Ni/γ-Al_2O_3 in the single stage DBD plasma-catalysis system on the physical properties of the DBD and the performance in the plasma-catalytic dry reforming process, see in **Figure 1.25** (b). In packing method A, the supported Ni catalyst pellets were fully packed into the entire discharge gap; in packing method B, Ni catalyst pellets (1 g) were partially packed into the discharge gap along the radial direction; and in the packing method C, several pieces of the Ni/γ-Al_2O_3 catalyst (1 g) in flake form were placed along the bottom of the quartz tube. It was found that the fully packed reactor strongly changed the discharge mode due to a significant reduction in the discharge volume, while partially packing the Ni/γ-Al_2O_3 catalyst either in a radial or axial direction into the discharge gap still showed strong filamentary discharge and significantly enhanced the physical and chemical interactions between the plasma and catalyst, which consequently results in the synergistic effect [91]. In their study, the effect of the calcination temperature on the plasma-catalytic performance was also investigated. The low calcination temperature (300 ^oC) was reported to result in higher synergy of plasma-catalysis [91]. Wang et al. studied the synergistic effect of catalyst and non-thermal plasma on dry reforming of CH_4 in plasma fluidised bed and packed-bed reactors with Ni/γ-Al_2O_3 catalyst. They concluded that both contact modes between plasma and catalytic particles could promote the catalyst activity at low temperatures (e.g. 673 K) and the plasma fluidised bed behaved better than the plasma packed-bed within a certain temperature range [164]. Moreover, Goujard et al. investigated the

influence of the plasma power supply nature on the plasma-catalytic synergy for dry reforming of CH_4. Their experiments were performed in a DBD reactor packed with cordierite honeycomb monolith and excited by two different power supplies: a pulsed excitation and a sinusoidal excitation. In the absence of the Ni catalyst, the plasma discharges generated by the pulsed power supply were more efficient for higher CO_2 and CH_4 conversion. Nevertheless, when a 2 wt.% Ni catalyst was deposited in the packed-bed, the active species generated by the AC power supply resulted in more promotion of the reactant activation on the Ni catalysts, therefore leading to a sharp increase of CH_4 and CO_2 conversion [175].

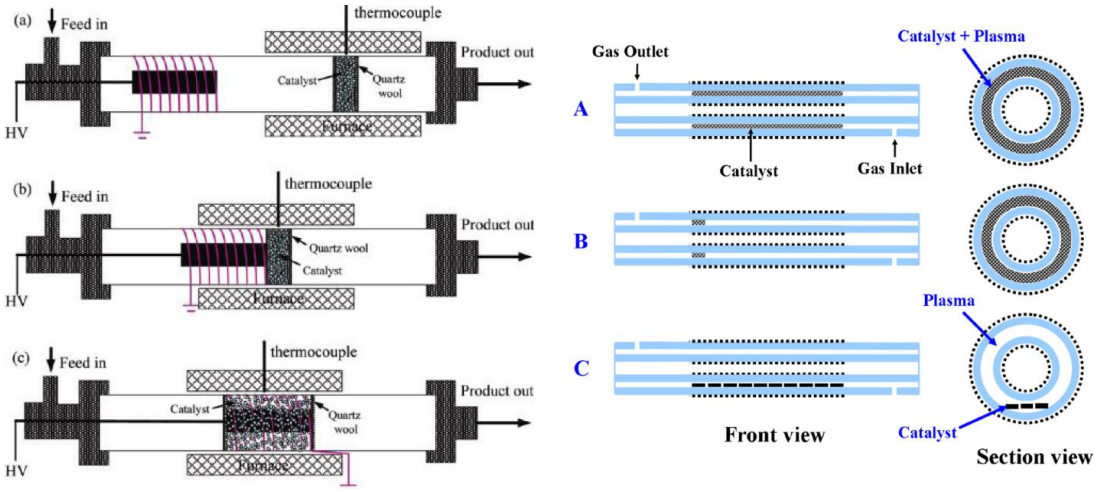

(a) (b)

Figure 1.25 Different catalyst packing methods in a DBD reactor: (a) the work of Wang et al. [163]; (b) the work of Tu et al. [91].

1.5 Thesis Outline

As mentioned above, the energy challenge and global climate change caused by the increasing consumption of fossil fuels have become one of the greatest threats to humankind's sustainable development, and make it more and more urgent to research and develop effective renewable, alternative energy sources. CO_2, as one of the GHGs, has little value itself, but it contributes most to the man-made greenhouse effect among all the GHGs. Any successful CO_2 utilisation method will not only alleviate GHG emissions but also provide promising approaches for energy production through better utilisation of carbon sources. For CO_2 utilisation, the current methods, including photocatalytic reduction, electrochemical reduction and thermal catalytic conversion of CO_2, usually have the drawbacks of low efficiency, low selectivity towards the target product and/or high energy consumption as well as low ability for treatment of the gas with a high flow rate.

In the last three decades, non-thermal plasma technology has been widely investigated in the field of energy production and environmental protection due to

convenient operation at low temperatures with high activity of energetic electrons, ions, excited atoms and molecules, radials and other reactive species as well as compactness and flexibility of the plasma system. The feasibility of the non-thermal plasma technology in an industrial scale application has been demonstrated in ozone generation, gas cleaning and water purification. In the plasma-only process, the reactant conversions and selectivity towards the target product is usually low and/or the production distribution is complex. This drawback can be compensated for by combining the non-thermal plasma with the catalysts, namely, plasma-catalysis.

Both the plasma-only and the plasma-catalysis processes have been used in the field of CO_2 utilisation. From the above reviews on the current status of plasma-assisted CO_2 utilisation (mainly CO_2 decomposition and CO_2 reforming of CH_4), the following problems are observed:

(1) The systematic study of the influences of the different processing parameters on the performance of the plasma-assisted process and the search for effective reactor designs with high efficiency is very limited;

(2) Few investigations focus on the relationship between the discharge characteristics (e.g. discharge behaviour, electric field, mean electron energy and etc.) and the reactant conversion and energy efficiency in the plasma process;

(3) For the direct decomposition of CO_2, lack of catalyst investigation in the plasma process makes it a great challenge to find a suitable and cost-effective catalyst for this reaction to enhance the efficiency of the process; while for the plasma-catalytic dry reforming of CH_4, the involved catalysts are mainly zeolites and unitary supported Ni catalysts, which is still suffered from carbon deposition; in addition, the energy efficiency is still low although some new catalysts are utilised.

Based on these problems, this thesis aims to develop the effective plasma processes for the conversion and utilisation of greenhouse gases (plasma-assisted CO_2 decomposition and CO_2 reforming of CH_4). Emphasis will be given to the effects of the processing parameters and their relative importance on the plasma process, the development of the new plasma reactor, the relationship between the discharge mode and plasma reaction performance, the exploration of catalysts with high activity and stability for plasma reactions as well as the identification of the mechanism of plasma-catalysis synergy. The experiments will be mainly performed in a coaxial DBD reactor, due to its straightforward scaling up with industrial application experience. The study in this thesis is expected to be beneficial to the future industrial scale application of the plasma-assisted CO_2 conversion and utilisation process, and consequently contributes to the development of new energy technologies to reduce the negative effects of climate change caused by carbon emissions and to ensure global energy security based on sustainable and renewable energy sources.

The contents of this thesis are arranged as 8 chapters. The first chapter primarily describes the current status of the energy challenge and climate change from the high consumption of fossil fuels and the different efforts made for CO_2 remediation and utilisation. Then, the basic principle and generation methods of non-thermal plasma are described, followed by the reviews of the research progress and the remaining problems in plasma-assisted CO_2 conversion, mainly for direct decomposition of CO_2 and dry reforming of CH_4. The research scope of this thesis is given in the last part of Chapter 1.

Chapter 2 describes the experimental equipment and system setup for plasma reactions, measurement methods of electrical signals, calculation of the discharge power, catalyst preparation and characterisation methods and their basic principles as well as the reactant and product gas analysis methods involved in this thesis.

In Chapter 3, the direct decomposition of CO_2 is investigated in a coaxial DBD reactor. The effects of different processing parameters (frequency, discharge power, feed flow rate, discharge length, discharge gap and dielectric thickness) are systematically studied. Empirical expressions relating the CO_2 decomposition performance (i.e. CO_2 conversion and energy efficiency) to these processing parameters are derived to evaluate the relative importance of these parameters. Modified DBD reactors with a screw-type inner electrode and/or an Al foil outer electrode are proposed to enhance the efficiency of the plasma process. The effects of the photocatalysts ($BaTiO_3$ and TiO_2) on the CO_2 decomposition performance and the detailed reaction mechanisms are analysed as well.

Chapter 4 performs the CO_2 decomposition in a packed-bed DBD reactor. A simplified model for the calculation of the gas electric field is proposed. The variations in the discharge behaviour, gas electric field and the mean electron energy due to the presence of the packing pellets ($BaTiO_3$ and glass beads) in the discharge volume are analysed. The relationships between the changes in the discharge characteristics and the enhancement in CO_2 decomposition performance are discussed in detail. The possible chemical effect introduced by the packing pellets is included as well. In the last part, comparison of the energy efficiency in the plasma-assisted CO_2 decomposition process using different atmospheric non-thermal plasma systems is carried out.

In Chapter 5, firstly, thermodynamic equilibrium calculation for the dry reforming of CH_4 is carried out. Then the dry reforming of CH_4 in the plasma-only process is performed in a similar coaxial DBD reactor. The influences of discharge power, total feed flow rate and CO_2/CH_4 molar ratio in the feed gas on the dry reforming process are investigated in terms of the conversion of reactants, the yield and selectivity of target products, the energy cost (EC) and the fuel production efficiency (FPE) of the plasma process.

Chapter 6 firstly investigates the effect of supports on the performance of the supported Ni catalysts in the plasma-catalytic reforming process and the optimal support is selected. In the second part, design of experiments (DoE) is utilised to study the effects of different processing parameters (discharge power, total feed flow rate, CO_2/CH_4 ratio, and Ni loading) and their interactions on the performance in plasma-catalytic reforming; an optimisation study is performed to obtain the optimum processing parameters for maximum reactant conversions, product yield and FPE.

Chapter 7 aims to develop catalysts with higher plasma-catalytic activity and carbon-resistance based on the optimum catalyst 10 wt.% $Ni/\gamma\text{-}Al_2O_3$ in Chapter 6. Investigations are firstly emphasised on the Ni-Co, Ni-Cu, Ni-Mn bimetallic catalyst and the optimum bimetallic catalyst is determined. After the performance evaluation on the individual bimetallic catalyst, further studies are carried out to obtain the optimum loading of the metal additive on the optimum bimetallic catalyst. In the last part, comparisons on the performance of plasma dry reforming of CH_4 in both plasma-only and plasma catalysis processes are given as well.

Finally, in chapter 8, appropriate conclusions are summarised and possible future work is discussed.

CHAPTER TWO EXPERIMENTAL SETUP AND ANALYTICAL TECHNIQUES

2.1 Experimental System

Figure 2.1 shows the experimental system for plasma conversion of greenhouse gas. It is consisted four parts: a gas-supplying unit, a high voltage power supply, a DBD plasma reactor and a product analysis unit. The reactant gases (CO_2 and CH_4) are supplied by the gas cylinders. The gas pressure from the gas cylinder is adjusted by the gas regulator and the flow rates are controlled by the mass flow controllers (MFC).

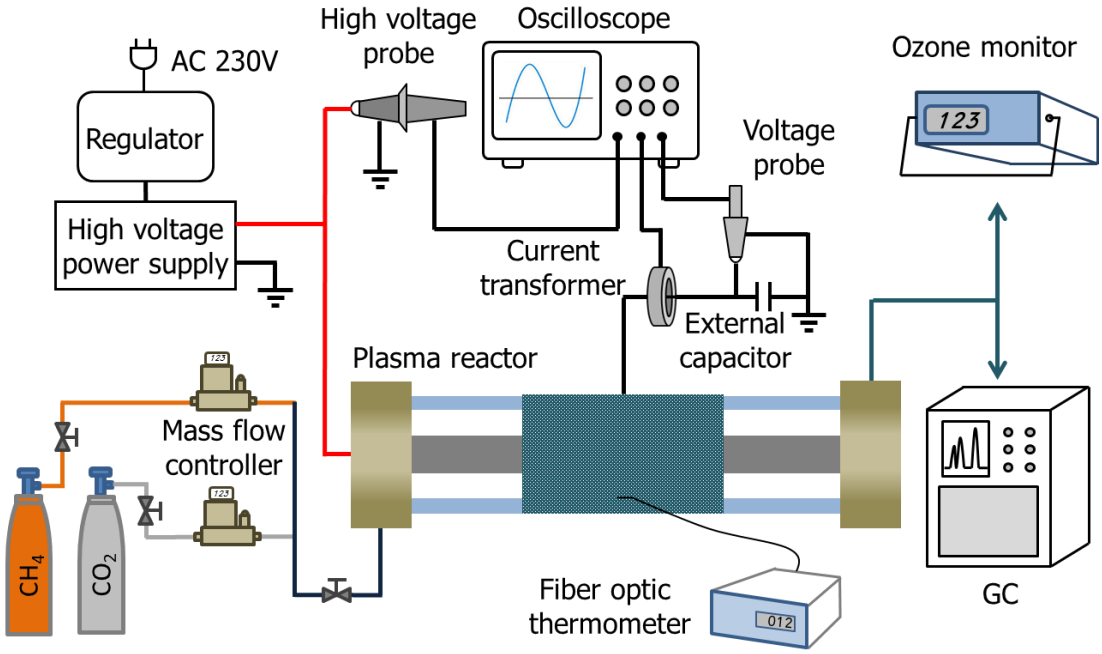

Figure 2.1 Schematic diagram of the experimental setup.

Two kinds of home-made plasma reactors are used: coaxial DBD and packed -bed DBD, which have the similar appearance and structure. In the coaxial DBD reactor (**Figure 2.2** (a)), a quartz tube is used as the dielectric material. A smooth stainless steel (SS) or screw-type rod (see in Chapter 3) is placed in the centre of the quartz tube and used as the inner high voltage electrode, which is connected to the high voltage output of the power supply. The SS mesh or Al foil (see in Chapter 3), used as the outer electrode, is wrapped over the quartz tube and grounded via an external capacitor. In the plasma-catalytic reaction, catalyst particles are placed along the bottom of the quartz tube. Based on the configuration of the coaxial DBD reactor, a packed-bed DBD reactor is formed when packing materials are fully packed in the discharge volume, shown in **Figure 2.2** (b). In these two reactors, quartz wool is

used to support the catalysts or packing materials. To avoid the effect of quartz wool on the plasma chemical reactions, it is placed outside the plasma region.

The DBD reactors are supplied by an AC high voltage power supply (CTP-2000K) with a maximum peak voltage of 30 kV and a frequency of 5-20 kHz.

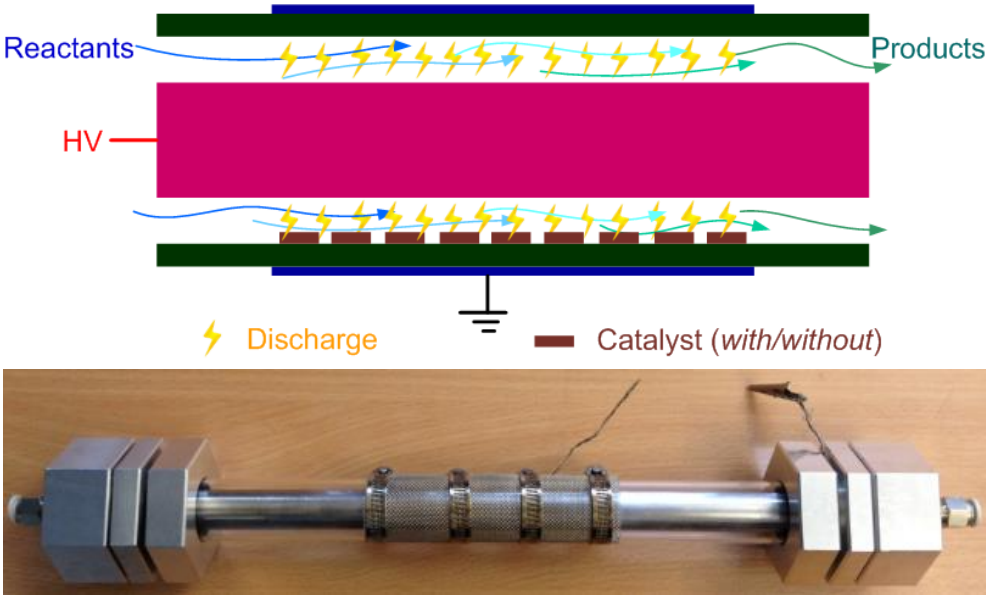

(a)

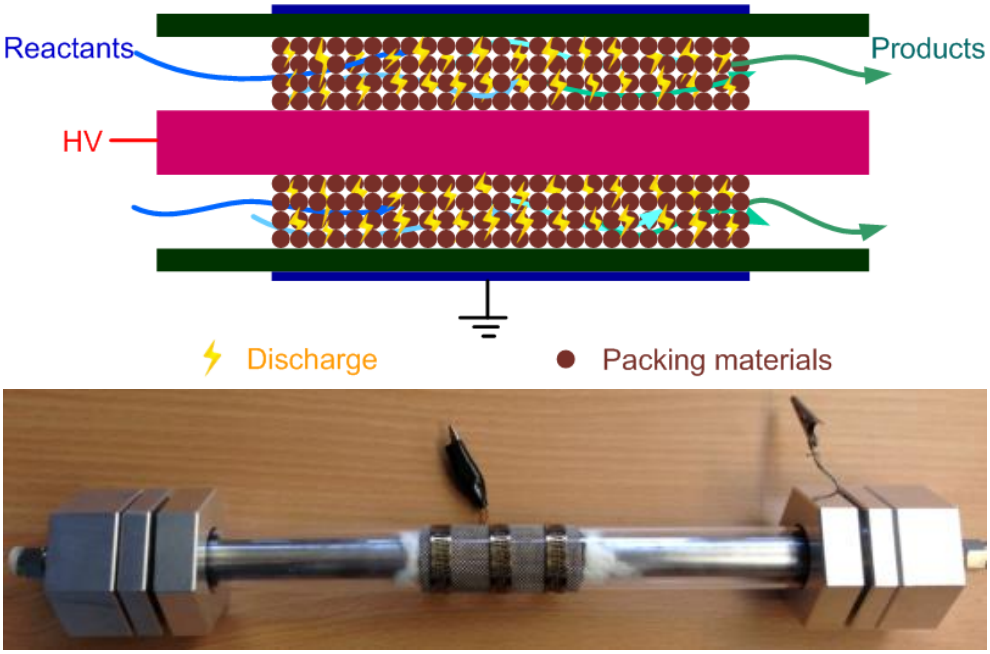

(b)

Figure 2.2 Schematic diagram and picture of the plasma reactor: (a) coaxial DBD; (b) packed-bed DBD.

2.2 Catalyst Preparation

In this study, the monometallic catalysts are prepared by impregnation of aqueous solution of nitrate salts (e.g. $Ni(NO_3)_2 \cdot 6H_2O$), as shown in **Figure 2.3** (a). The aqueous precursors are prepared and stirred by the magnetic stirrer for 2 h at room temperature, and then the support particles with a diameter of roughly 1 mm are added into the solution and impregnated for 12 h. The solutions with the catalyst supports are then evaporated in a water bath at 80 ^oC for 4 h and dried at 110 ^oC in the chamber furnace overnight. All the dried samples are calcined at 400 ^oC for 5 h.

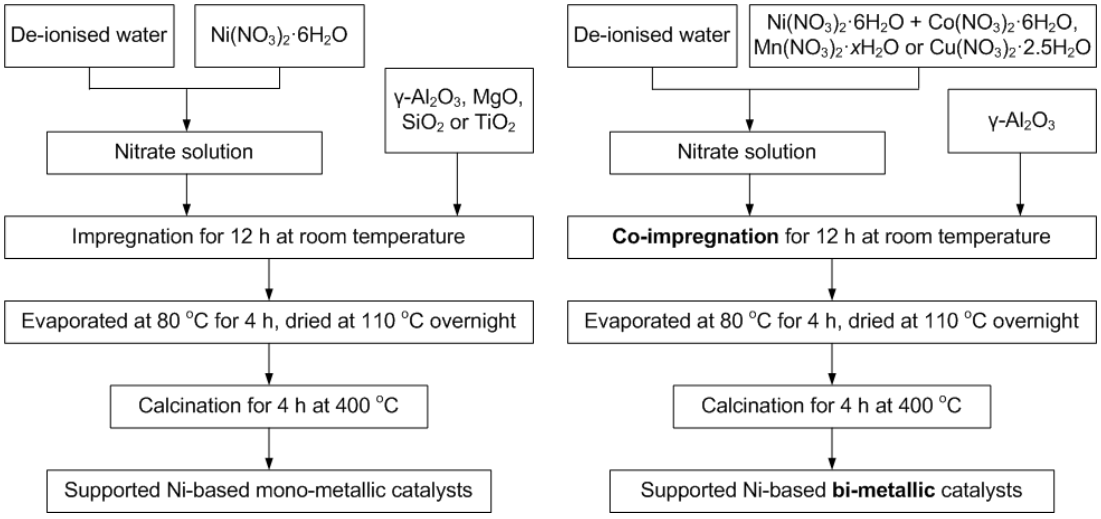

Figure 2.3 Schematic flow chart for the preparation steps of Ni-based (a) mono-metallic catalysts and (b) bimetallic catalysts.

The bimetallic catalysts are prepared by co-impregnating the nitrate salts of Ni and another metal (Co, Cu and Mn) with support particles using the same procedures mentioned above (shown in **Figure 2.3** (b)).

2.3 Analytic Methods

2.3.1 Measurement and analysis of electrical signals

In the experiments, the Tektronix digital oscilloscope (Tektronix, MDO 3024, **Figure 2.4** (a)) is used to collect the voltage and current signals in the discharge process. The applied voltage is measured by a high voltage probe (Testec, TT-HVP15 HF, **Figure 2.4** (b)), while the voltage on the external capacitor is measured by a voltage probe (Tektronix, P6109, **Figure 2.4** (c)) to obtain the charge generated in the discharge process. The current transformer (Magnelab, CT-E 0.5-BNC, **Figure 2.4** (d)) is used to record the current in the discharge.

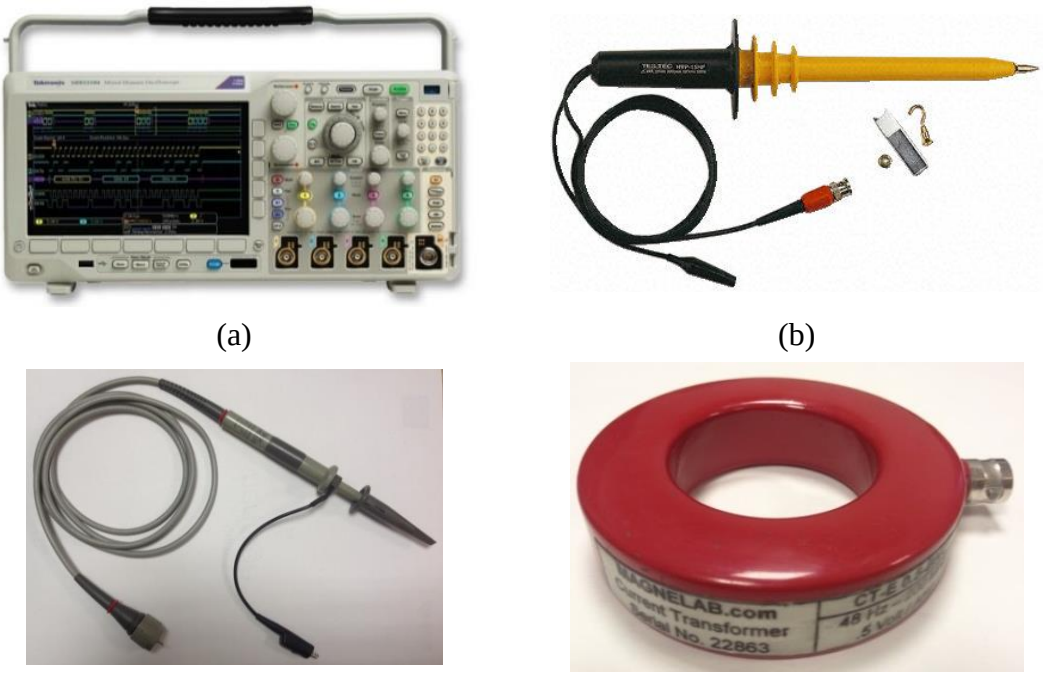

(a) (b)

(c) (d)

Figure 2.4 (a) Four-channel digital oscilloscope; (b) High voltage probe; (c) Voltage probe; (d) Current transformer.

The discharge power is determined by the Lissajous method, which was first introduced by Manley in 1943 [176]. **Figure 2.5** shows a typical circuit layout for the measurement of the discharge power of a DBD reactor [177] and the *Q*-*U* Lissajous figure [107, 178]. The principle of this method can be found in the related reference [41]. The specific energy density (SED) into the plasma reactor can be determined by

$$\mathrm{SED}\left(\mathrm{kJ/L}\right)=\frac{60\times P\left(\mathrm{W}\right)}{q\left(\mathrm{ml/min}\right)} \tag{2-1}$$

where P and q are the discharge power and total feed flow rate, respectively.

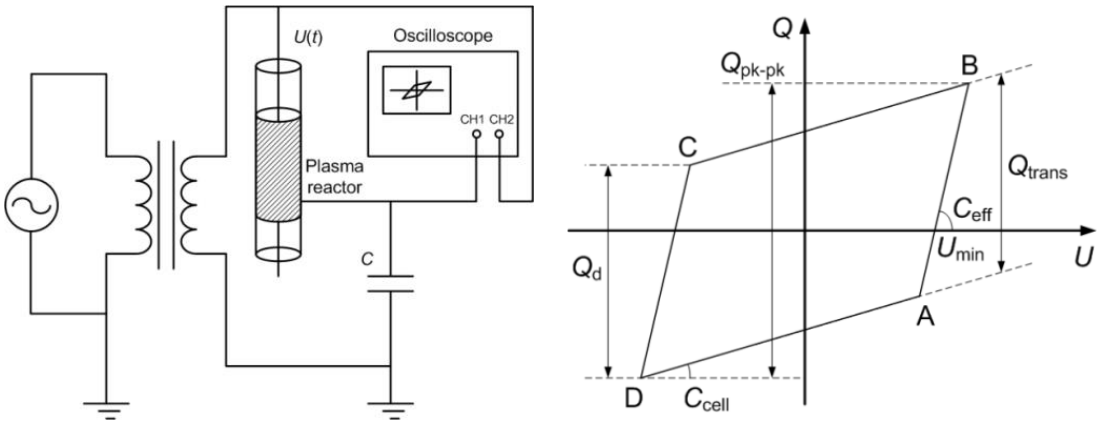

(a) (b)

Figure 2.5 (a) Circuit for measuring the discharge power of a plasma reactor [177]; (b) typical Lissajous figure of a DBD [107, 178].

Figure 2.6 (a) shows an equivalent electrical circuit of a DBD reactor, which contains two capacitors in series [107]. The capacitor C_d stands for the capacitance of the dielectric material and the other is the capacitance of the gap, C_{gap}. When the plasma is generated, a resistive channel appears in parallel to C_{gap}. The switch 'K' on the equivalent electrical circuit is fictional. The equivalent capacitance of the dielectric material is calculated according to the topology of a coaxial capacitor, shown in Equation (2-2) [179]:

$$C_d = \frac{2\pi\varepsilon_0\varepsilon l}{\ln\left((d+x)/d\right)} \tag{2-2}$$

where ε_0 is the dielectric constant of the vacuum (8.854 $\times 10^{-12}$ F/m); ε is the relative dielectric constant of the dielectric material; l is the discharge length; d and x are the inner diameter and wall thickness of the dielectric material, shown in **Figure 2.6** (b).

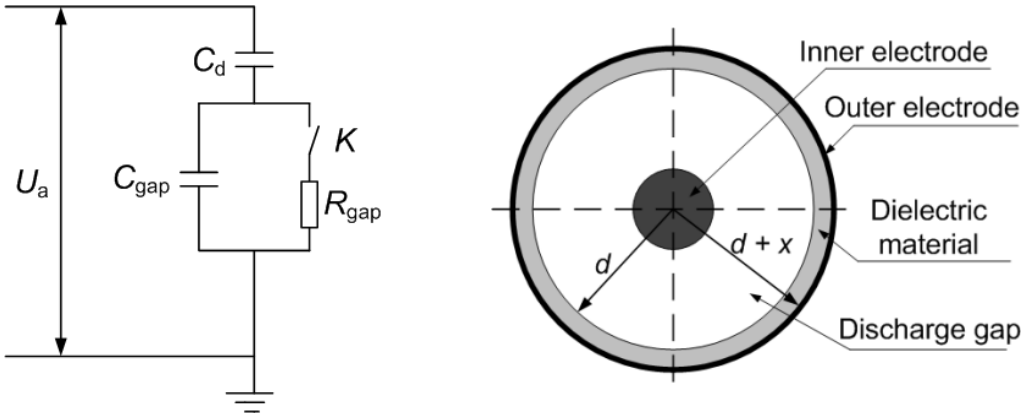

(a) (b)

Figure 2.6 (a) Equivalent electrical circuit of the DBD reactor; (b) Transversal section of the DBD reactor without packing.

In the typical *Q-U* Lissajous figure for a DBD reactor shown in **Figure 2.5** (b), lines BC and AD represent the discharge-off phase when there is only displacement current, and their slopes correspond to the C_{cell} in the plasma-off period, which is formed by the dielectric capacitance C_d and the capacitance of the gap C_{gap}, as expressed in Equation (2-3). Then, C_{gap} in the discharge-off phase is calculated in Equation (2-4). Lines AB and CD represent the discharge-on phase when gas breakdown occurs in the gap and the plasma is ignited. The slope of Lines AB and CD is the effective capacitance C_{eff}, which should equal C_d for a fully bridged gap [180].

$$\frac{1}{C_{cell}} = \frac{1}{C_d} + \frac{1}{C_{gap}} \tag{2-3}$$

$$C_{gap} = \frac{C_d \times C_{cell}}{C_d - C_{cell}} \tag{2-4}$$

The charge Q flowing through the DBD reactor can be obtained from the voltage across the external capacitor (C_{ext} = 470 nF in this study) by

$$Q = C_{ext} \times U_c \tag{2-5}$$

Then the voltage on the dielectric material U_d can be determined by the following relation [181]

$$U_d = \frac{Q}{C_d} = \frac{C_{ext} \times U_c}{C_d} \tag{2-6}$$

Therefore, the voltage across the gap U_{gap} is given as

$$U_{gap} = U - U_d \tag{2-7}$$

The breakdown voltage U_B is the voltage across the gap at which the plasma is ignited, which can be calculated by the following equation [70, 83]:

$$U_B = \frac{U_{min}}{1 + \left(C_{gap} / C_d\right)} \tag{2-8}$$

Moreover, the peak-to-peak charge ($Q_{pk\text{-}pk}$), charge discharged (Q_d) and charge transferred per half-cycle (Q_{trans}) can also be obtained from the Lissajous figure, as plotted in **Figure 2.5**(b) [181].

2.3.2 Catalyst characterisation

In this study, the following catalyst characterisation approaches are utilised to investigate the physical structure, surface element valence, the amount of the basic sites and carbon resistance of the catalysts: N_2 physisorption, X-ray diffraction (XRD), CO_2 temperature-programmed desorption (CO_2-TPD), X-ray photoelectron spectroscopy (XPS) and thermo-gravimetric analysis (TGA). The principles of these methods are briefly described as follows.

2.3.2.1 N_2 physisorption

Gas adsorption is an effective approach to analyse the specific area, pore structure and pore distribution of a catalyst. In general, inert gases (mostly N_2) are used as the adsorbate to avoid chemical adsorption. The adsorption isotherms are obtained by measuring the adsorbed gas amount at a constant temperature with different relative pressure p/p_0 (p is the real gas pressure; while p_0 is the saturated vapour pressure at a constant temperature). The adsorption and desorption branches are contained in the adsorption isotherms; and the shape of the isotherms is dependent on the pore structure of the solid materials.

In this study, the N_2 physisorption is carried out at 77 K using a surface area analyser (Quantachrome NOVA 4200e) to measure the pore size and the specific surface area of the catalyst. Before each measurement, the samples are outgassed at 300 ^{o}C for 2 h under a vacuum to remove any moisture and other adsorbed gases.

The specific surface area is calculated via the Brunauer-Emmett-Teller (BET) method, while the pore size distribution is determined using the Barrett-Joyner-Halenda (BJH) model from the data of the desorption branch of the N_2 isotherm.

2.3.2.2 XRD

XRD is a technique primarily used to characterise crystal structure at atomic level, based on the constructive interference between the monochromatic X-rays and the crystalline samples. The X-rays are generated by a cathode ray tube, filtered to produce monochromatic radiation, collimated to concentrate and directed to the sample. Constructive interference will occur when the interaction between the incident rays and the sample satisfies the Bragg's Law [182], expressed by

$$2d\sin\theta = n\lambda \tag{2-9}$$

where d is the spacing between diffracting planes, θ is the incident angle, n is any integer, and λ is the wavelength of the beam. In this condition, a reflection spot is produced in the diffraction pattern, where an X-ray is reflected from the specimen surface at an angle of θ (equal to the angle of the incident radiation) [183], as illustrated in **Figure 2.7**. These diffracted X-rays are then detected. For XRD, the samples are prepared by grinding the solid materials into a fine homogeneous powder, which is then pressed into a sample holder and smoothed. This procedure produces a sample with the crystallites distributed at random orientations, which enables all possible diffraction directions of a lattice to be attained by scanning the sample through a range of 2θ angles. Then the identification of the crystal structure can be completed through conversion of the diffraction peaks to d-spacings, as each crystal structure has a set of unique d-spacing, resulting in a characteristic XRD pattern.

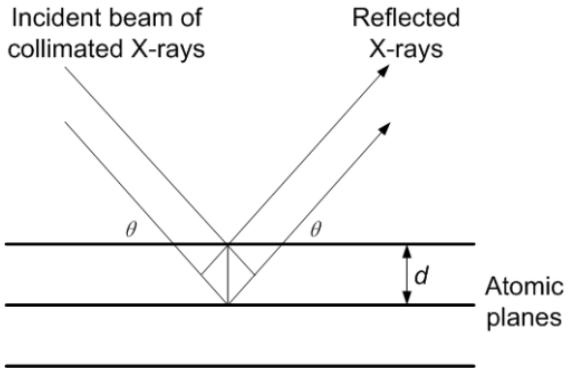

Figure 2.7 Reflection of X-rays at an angle (θ) from two planes of atoms with separation distance (d) in a crystalline solid.

In this study, the crystallinity of the catalyst is identified through XRD analysis using an X-ray diffractometer (Rigaku, SmartLab) equipped with Cu-Kα

radiation (40 kV tube voltage and 40 mA tube current) in the scanning range 2θ between 10^o and 80^o with a scanning rate of 4 ^{o}/min and a scanning step size of 0.02^o.

2.3.2.3 CO_2-TPD

TPD is one of the most powerful tools to elucidate the strength of interfacial chemical bonds, which can be used to investigate the surface acidic/basic sites, the adsorbate species, as well as the surface activity of the catalysts. In TPD, the solid samples are saturated by the adsorbate after pre-treatment. Then the samples are heated linearly, and desorption will occur when the adsorbate is activated by the heat, which is sufficient to help it overcome the desorption activation energy to escape the samples. In general, weakly bonded adsorbates require less heat to break the substrate-adsorbate bonds, and desorb at a low temperature; while more strongly boned adsorbates require more energy to break their bonds, and thus they desorb at a higher temperature.

In this study, CO_2-TPD measurement is applied to investigate the amount of the basic sites on the catalyst. It is performed on a fully automated chemisorption analyser (AutoChem II 2920) with a thermal conductivity detector (TCD). The CO_2 adsorption is carried out at room temperature for 30 min by passing a CO_2/He gas mixture (V/V, 10/90) with a flow rate of 50 ml/min. Afterwards, CO_2-TPD signal is recorded with the temperature rising to 700 ^{o}C at a rate of 10 ^{o}C/min.

2.3.2.4 XPS

XPS, also known as electron spectroscopy for chemical analysis (ESCA), is an analysis method for electron spectroscopy based on the photoelectric effect. In general, any material can emit electrons when it is irradiated by photoelectrons; the information of kinetics, intensity and angular distribution related to the electrons is obtained by detecting these electrons, resulting in the understanding of components of the material as well as the electronic structures of atoms and molecules; this is so-called photoelectron spectroscopy [184]. XPS spectra are obtained by irradiating a material with a beam of X-rays, while simultaneously measuring the kinetic energy and the number of the electrons that escape from the top 0 to 10 nm of the material being analysed [185]. The kinetic energy of these emitted electrons is characteristic of the element from which the electron originated. A typical XPS spectrum is a plot of the intensity of the XPS peaks (Y-axis, ordinate) versus the binding energy of the detected electrons (X-axis, abscissa). Each element produces a characteristic set of XPS peaks at its characteristic binding energy values, through which the element that exists in or on the surface of the material can be directly identified. The position and intensity of the peaks in the energy spectrum provide the desired information for the identification of the elemental composition on the surface, the relative amount of these constituents in the surface region, as well as the valence band structure.

In this study, XPS measurements are carried out on a Perkin-Elmer PHI-5400 XPS system with mono-chromatic Mg Kα (1253.6 eV) X-rays with a data acquisition system. The spectra are referenced to C1s peak at 284.5 eV.

2.3.2.5 TGA

TGA is an analytical technique to examine the thermal stability of a material and its fraction of volatile components by monitoring the weight change when it is heated. In general, the measurement is performed in air or in an inert atmosphere, such as helium or argon, and the weight is recorded and plotted against temperature or time to illustrate thermal transitions in the material - such as loss of solvent and plasticisers in polymer, water hydration in inorganic materials and finally decomposition of the material. In addition to weight changes, the temperature difference between the material being analysed and the reference material (differential thermal analysis, or DTA) or the heat flow into the material being analysed compared to that of the reference one (differential scanning calorimetry, or DSC) can also be recorded. The latter one can be used to monitor the energy released or absorbed via chemical reactions during the heating processes.

In this work, the coke deposition on the spent catalyst is analysed via TGA in air atmosphere using TA Instruments SDT-Q600 (simultaneous TGA/DSC). The spent catalyst (20 mg) is heated from 30 to 800 ^{o}C at a heating rate of 10 ^{o}C/min with an air flow of 30 ml/min.

2.3.3 Analysis of gas products

Gas chromatography (GC) is used for the analysis of the gas mixtures during the experiments in this study. Essentially, chromatography requires a ‘mobile phase’ (containing the mixture to be separated) and a ‘stationary phase’ through which the mobile phase will be eluted. In GC, the mobile phase is a carrier gas, usually an inert gas such as helium or argon, or an unreactive gas such as nitrogen. The GC column originally consists of a piece of glass or metal tube containing an inert solid support with a microscopic layer of liquid or polymer (called stationary phase). The separation process is based upon the different partitioning between the mobile and stationary phases. When the gas mixture is injected into the column, different gas species pass through it at different rates according to the strength of the electrostatic interactions with the column walls. This enables the gas mixture to be separated and individual gas components to elute at different times, known as the retention time. The gas component can be identified by comparing its retention time with chromatograms for known species. The retention time is sensitively affected by the gas concentration, carrier gas flow rate and pressure as well as the column material and operating temperature [186]; therefore, the selection of an appropriate column and the operating conditions is critical for the high performance of GC.

When each gas reaches the detector, one characteristic peak for that gas is produced on the chromatogram. The peak area is proportional to the gas concentration. Before gas separation, calibration for the components in the gas mixture should be conducted by using the standard gas with a known gas component and amount. The gas calibration is only valid for constant operating conditions. Re-calibration is required once any of the following is changed: flow rate and pressure of the carrier gas, the temperatures of the injection, the column and the detectors.

The most commonly used detectors are TCD and flame ionisation detector (FID). Both detectors are sensitive to a variety of components and can work over a wide range of concentrations. TCD is used to detect any component other than the carrier gas, as long as their thermal conductivities are different from that of the carrier gas at the detector temperature, while FID is primarily sensitive to organic compounds.

In this study, the feed and product gases are analysed by a two-channel gas chromatograph (Shimadzu GC-2014) equipped with a FID and a TCD. The first channel contains a Molecular Sieve 5A (60-80 mesh) column for the separation of H_2 and CO, while the second channel is equipped with a HayeSep N (60-80 mesh) column for the measurement of CO_2, CH_4 and C_2-C_4 hydrocarbons. The GC is calibrated for a wide range of concentrations for each gaseous component using standard gas mixtures (Air Liquid) and other calibrated gas mixtures.

The temperature inside the plasma reactor is measured by a fibre optic thermometer (Omega, FOB102). The fibre is inserted into the catalyst bed to contact with the catalysts for the measurement of the temperature on the catalyst surface. The ozone concentration is measured by an ozone monitor (2B, Model 106-M).

Preliminary experiments are performed to decide the processing time to reach a stable discharge. The gas products are collected when the discharge is stable using a sampling bag for further analysis by the GC mentioned above. For the plasma CO_2 decomposition process, the discharge becomes stable when the plasma is on for 20 min. The conversion of CO_2 (C), the selectivity of CO (S), the carbon balance (B_{Carbon}) and oxygen balance (B_{Oxygen}) as well as the energy efficiency (η) are defined as follows:

$$C_{\text{CO}_2}(\%) = \frac{\text{CO}_2 \text{ converted } (\text{mol/s})}{\text{CO}_2 \text{ input } (\text{mol/s})} \times 100 \tag{2-10}$$

$$S_{\text{CO}}(\%) = \frac{\text{CO produced } (\text{mol/s})}{\text{CO}_2 \text{ converted } (\text{mol/s})} \times 100 \tag{2-11}$$

$$B_{\text{Carbon}}(\%) = \frac{\text{CO}_2 \text{ unconverted } (\text{mol/s}) + \text{CO produced } (\text{mol/s})}{\text{CO}_2 \text{ input } (\text{mol/s})} \times 100 \tag{2-12}$$

$$B_{\text{Oxygen}}(\%) = \frac{\begin{pmatrix} 2\times \text{CO}_2 \text{ unconverted } (\text{mol/s}) \\ +\text{CO produced } (\text{mol/s}) + 2\times \text{O}_2 \text{ produced } (\text{mol/s}) \end{pmatrix}}{2\times \text{CO}_2 \text{ input } (\text{mol/s})} \times 100 \quad (2\text{-}13)$$

$$\eta(\%) = \frac{\text{CO}_2 \text{ converted } (\text{mol/s}) \cdot \Delta H\,(\text{kJ/mol})}{\text{Discharge power } (\text{kW})} \times 100 \quad (2\text{-}14)$$

where ΔH is the reaction enthalpy of CO_2 decomposition, 280 kJ/mol.

For the plasma dry reforming of CH_4, the stable discharge is obtained around 1 h after igniting the plasma. In the plasma-catalytic dry reforming of CH_4, each experiment is run for another 90 min after the gas products are collected to investigate the carbon deposition on the spent catalyst. The definition of CO_2 conversion is the same as that in CO_2 decomposition (shown in Equation (2-10)). CH_4 conversion and the total carbon conversion are determined by

$$C_{\text{CH}_4}(\%) = \frac{\text{CH}_4 \text{ converted } (\text{mol/s})}{\text{CH}_4 \text{ input } (\text{mol/s})} \times 100 \quad (2\text{-}15)$$

$$C_{\text{TC}}(\%) = x_{\text{CO}_2} \times C_{\text{CO}_2} + x_{\text{CH}_4} \times C_{\text{CH}_4} \quad (2\text{-}16)$$

where x_{CO_2} and x_{CH_4} are the percentage concentration of CO_2 and CH_4 in the feed gas, respectively.

The selectivities (S) and yields (Y) of the main reforming products are calculated by

$$S_{\text{H}_2}(\%) = \frac{\text{H}_2 \text{ produced } (\text{mol/s})}{2\times \text{CH}_4 \text{ converted } (\text{mol/s})} \times 100 \quad (2\text{-}17)$$

$$S_{\text{CO}}(\%) = \frac{\text{CO produced } (\text{mol/s})}{\text{CH}_4 \text{ converted } (\text{mol/s}) + \text{CO}_2 \text{ converted } (\text{mol/s})} \times 100 \quad (2\text{-}18)$$

$$S_{\text{C}_x\text{H}_y}(\%) = \frac{x\times \text{C}_x\text{H}_y \text{ produced } (\text{mol/s})}{\text{CH}_4 \text{ converted } (\text{mol/s}) + \text{CO}_2 \text{ converted } (\text{mol/s})} \times 100 \quad (2\text{-}19)$$

$$Y_{\text{H}_2}(\%) = \frac{\text{H}_2 \text{ produced } (\text{mol/s})}{2\times \text{CH}_4 \text{ input } (\text{mol/s})} \times 100 \quad (2\text{-}20)$$

$$Y_{\text{CO}}(\%) = \frac{\text{CO produced } (\text{mol/s})}{\text{CH}_4 \text{ input } (\text{mol/s}) + \text{CO}_2 \text{ input } (\text{mol/s})} \times 100 \quad (2\text{-}21)$$

The H_2/CO ratio and carbon balance (B) of the plasma dry reforming process are determined as follows:

$$\frac{\text{H}_2}{\text{CO}} = \frac{\text{H}_2 \text{ produced } (\text{mol/s})}{\text{CO produced } (\text{mol/s})} \quad (2\text{-}22)$$

$$B_{\text{Carbon}}(\%) = \frac{\begin{pmatrix} [\text{CH}_4 + \text{CO}_2] \text{unconverted } (\text{mol/s}) \\ +[\text{CO} + 2\times \text{C}_2 + 3\times \text{C}_3 + 4\times \text{C}_4] \text{produced} (\text{mol/s}) \end{pmatrix}}{[\text{CH}_4 + \text{CO}_2] \text{input } (\text{mol/s})} \times 100 \quad (2\text{-}23)$$

To evaluate the performance of the plasma dry reforming process, the energy cost (EC) for CO_2 conversion (EC_{CO_2}), CH_4 conversion (EC_{CH_4}) and total carbon conversion (EC_{TC}), the EC for H_2 production (EC_{H_2}) and syngas production (EC_{Syngas}), and the fuel production efficiency (FPE) are defined as follows:

$$EC_{CO_2}\left(\text{MJ/mol}\right)=\frac{\text{Discharge power}\left(\text{kW}\right)}{1000\times \text{CO}_2\text{ input}\left(\text{mol/s}\right)\times C_{CO_2}\left(\%\right)} \tag{2-24}$$

$$EC_{CH_4}\left(\text{MJ/mol}\right)=\frac{\text{Discharge power}\left(\text{kW}\right)}{1000\times \text{CH}_4\text{ input}\left(\text{mol/s}\right)\times C_{CH_4}\left(\%\right)} \tag{2-25}$$

$$EC_{TC}\left(\text{MJ/mol}\right)=\frac{\text{Discharge power}\left(\text{kW}\right)}{1000\times\left(\text{CH}_4\text{ input}\left(\text{mol/s}\right)+\text{CO}_2\text{ input}\left(\text{mol/s}\right)\right)\times C_{TC}\left(\%\right)} \tag{2-26}$$

$$EC_{H_2}\left(\text{MJ/mol}\right)=\frac{\text{Discharge power}\left(\text{kW}\right)}{1000\times \text{H}_2\text{ produced}\left(\text{mol/s}\right)} \tag{2-27}$$

$$EC_{Snygas}\left(\text{MJ/mol}\right)=\frac{\text{Discharge power}\left(\text{kW}\right)}{1000\times\left(\text{H}_2\text{ produced}\left(\text{mol/s}\right)+\text{CO produced}\left(\text{mol/s}\right)\right)} \tag{2-28}$$

$$\text{FPE}\left(\%\right)=\frac{\sum\text{fuel produced}\left(\text{mol/s}\right)\times\text{LHV}\left(\text{kJ/mol}\right)}{\left(\begin{matrix}\text{CH}_4\text{ converted}\left(\text{mol/s}\right)\times\text{LHV of CH}_4\left(\text{kJ/mol}\right)\\+\text{Discharge power}\left(\text{kW}\right)\end{matrix}\right)}\times 100 \tag{2-29}$$

where LHV is the low heating value of the fuel.

The reproducibility is demonstrated in the preliminary experiments. The experiment under the same condition is repeated for 3 times. The relative error of the reactant conversions and product yields (selectivities) under one experimental condition is less than 5%. The uncertainty in the measurement of the gas concentration is less than 2%, whilst the uncertainty in the calculation of conversion, selectivity and yield is less than 3%.

CHAPTER THREE CARBON DIOXIDE DECOMPOSITION IN A COAIXAL DBD REACTOR

3.1 Introduction

CO_2 has been recognised as one of the major contributors to the greenhouse gas effect and its concentration in the atmosphere is continuously increasing due to the use of fossil fuels. Great efforts have been devoted to the development of effective strategies to deal with the global challenge of CO_2 emissions. Undoubtedly, CO_2 conversion and utilisation could be one of the attractive and sustainable solutions for the mitigation of CO_2 emissions, by turning CO_2 from a waste gas into an integral part of industrial processes. Various processes have been used to convert CO_2 into value-added fuels and chemicals, such as CO_2 reforming of CH_4 for hydrogen production and CO_2 hydrogenation for the synthesis of methanol, methane, formaldehyde, dimethyl ether, etc [52, 187]. Direct splitting of CO_2 into CO has also attracted great interest [36], as CO is a useful chemical feedstock which can be used as a reactant to produce higher energy products. However, due to the high stability of CO_2, a large amount of energy is required for its activation in the conventional CO_2 conversion process (see Equation (3-1)).

$$CO_2 \rightarrow CO + \frac{1}{2}O_2 \qquad \Delta H = 280\ \text{kJ} \cdot \text{mol}^{-1} \tag{3-1}$$

Non-thermal plasma technology has been considered as an attractive alternative to the conventional thermal or catalytic route for gas purification and energy conversion due to its non-equilibrium character, low energy cost and unique ability to initiate both physical and chemical reactions at low temperatures [91, 107]. In non-thermal plasma, the overall gas kinetic temperature remains low, while the electrons are highly energetic with a typical electron temperature of 1-10 eV, which can breakdown most chemical bonds in inert molecules (e.g. CO_2) and generate a large number of reactive species for chemical reactions. The non-equilibrium character of such plasma could overcome thermodynamic barriers in chemical reactions (e.g. direct CO_2 decomposition) and enable thermodynamically unfavourable chemical reactions to occur at atmospheric pressure and low temperatures [91]. Non-thermal plasma technology has been widely investigated and applied in the energy and environmental sectors, such as for hydrogen generation, gas cleaning [84, 90, 188, 189] and carbon dioxide utilisation [49, 52]. DBD is one of the most effective and most studied non-thermal plasma technologies due to its success originating from ozone synthesis. With the presence of one or two dielectric barriers in the discharge gap, unstable spark or arc plasma can be inhibited while numerous filamentary microdischarges are generated. In addition, the reactor

configuration has great flexibility as it can be constructed from inexpensive materials (e.g. glass and polymers) and different materials (catalytic or non-catalytic) can easily fill the discharge volume.[190]. The efficiency of the DBD reactor is closely related to its configurations and operating parameters. It has been reported that the synergistic effect may be generated when the DBD plasma is combined with catalyst, which leads to higher plasma process performance, compared to the sum of the individual processes (i.e. the plasma-only process and the catalysis only process) [91].

In the first part of this chapter, the thermodynamic equilibrium calculation of CO_2 decomposition is carried out to provide a reference to demonstrate the synergistic effect of the plasma-catalytic process for the conversion of CO_2.

In the latter part, the plasma decomposition of CO_2 is performed in a coaxial DBD reactor. For the plasma-only process, the effect of the processing parameters (frequency, feed flow rate, discharge power, discharge length, discharge gap and dielectric material thickness) on the performance of CO_2 decomposition are studied in terms of CO_2 conversion and energy efficiency. The empirical formulas are established to indicate the relationship between CO_2 decomposition performance and these processing parameters. The relative importance of these processing parameters on the plasma process performance is discussed based on the established formulas. Moreover, modified reactors are designed and manufactured by replacing the SS mesh outer electrode with Al foil and/or using a SS screw type inner electrode. In the plasma-catalytic process, $BaTiO_3$ and TiO_2 pellets are used as photocatalytsts and packed into the discharge gap along the bottom of the quartz tube to investigate the synergistic effect introduced by the combination of plasma and photocatalysts, from both physical and chemical perspectives. A possible mechanism for the plasma-photocatalytic process is illustrated.

3.2 Thermodynamic Equilibrium Calculation of CO_2 Decomposition

3.2.1 Description of thermodynamic equilibrium calculation

The thermodynamic equilibrium calculation of CO_2 decomposition has been carried out using the method based on minimisation of Gibbs free energy in a closed system. Different from that in the equilibrium constant method, which requires the exact knowledge of the chemical species and the independent reactions occurring in the system, the Gibbs free energy minimisation-based method considers only the chemical species in the calculations. Therefore, the application of this approach is quite simple especially for complex systems involving a large number of reactions. The Gibbs free energy minimisation-based method has been widely used to perform thermodynamic analysis [191, 192]. The basic principle of this method can be found elsewhere [191].

In this study, the thermodynamic equilibrium calculation for the CO_2 decomposition process is conducted by the software HSC Chemistry 5, which is a thermochemical software designed for various chemical reactions and equilibria calculations [108]. In each calculation, it is supposed that 1 mol of CO_2 is injected into the closed system. The products are assumed to be O_2 and CO only. The definition of CO_2 conversion in this calculation is the same as that in the experimental studies, shown in Equation (2-10).

3.2.2 Calculation results

The results of the thermodynamic equilibrium calculation for CO_2 conversion are shown in **Figure 3.1**. We can see that CO_2 begins to decompose into CO and O_2 near 2000 K, but the conversion of CO_2 is very low (< 1%). Reasonable conversion of CO_2 (~60%) can only be obtained at extraordinarily high temperatures (3000-3500 K), which leads to high energy cost for thermal conversion of CO_2. Moreover, CO_2 conversion drops significantly by increasing the operating pressure. Thus, it is crucial to perform CO_2 decomposition at atmospheric pressure to attain high CO_2 conversion.

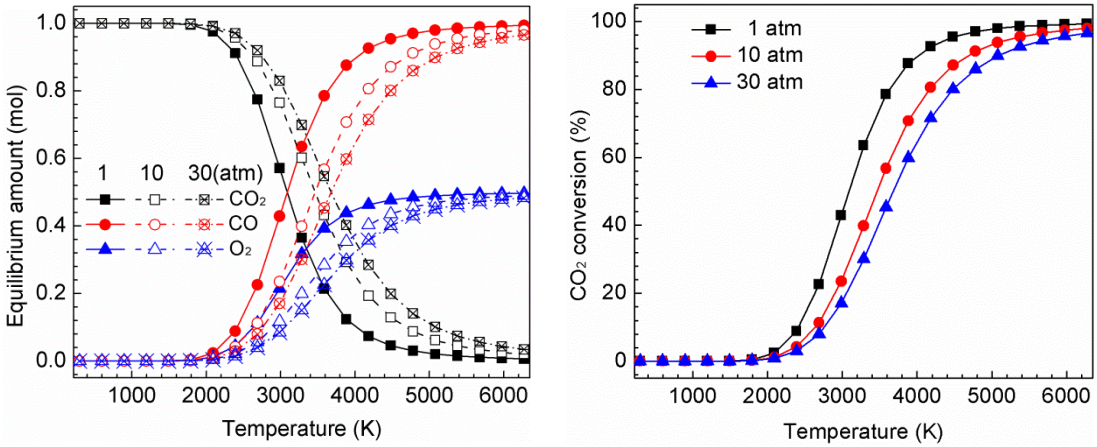

(a) (b)

Figure 3.1 Thermodynamic equilibrium calculation of CO_2 conversion as a function of temperature and pressure (a) gas equilibrium amount; (b) CO_2 conversion.

3.3 Experimental Study of Plasma-Assisted CO_2 Decomposition in a Coaxial DBD Reactor

3.3.1 Experimental section

3.3.1.1 Experimental setup

CO_2 decomposition is performed in a coaxial DBD reactor, as shown in **Figure 3.2** (a). A SS mesh is wrapped over a quartz tube with an external diameter

(D_o) of 25 mm and an inner diameter (D_i) of 20-22 mm. The length of SS mesh varies from 60 mm to 140 mm in order to adjust the discharge length (L). A SS rod with an outer diameter (d_o) of 15-17 mm is placed in the centre of the quartz tube and acts as an inner electrode. In the modified reactor, an Al foil outer electrode with a length of 100 mm and a screw-type SS inner electrode with a diameter of 17 mm (shown in **Figure 3.2** (b)) are utilised for comparison. In the plasma-catalytic CO_2 decomposition, different catalyst pellets $BaTiO_3$ (TCU) and TiO_2 (*Alfa Aesar*) with a diameter of 1 mm were packed into the discharge gap along the bottom of the quartz tube, as shown in **Figure 3.2** (c). XRD and XPS measurements are performed to investigate the surface structure and element valance and further reveal their effects on the reaction performance of plasma-catalytic CO_2 decomposition.

The experimental setup is illustrated in **Figure 2.1**. The inner electrode of the DBD reactor is connected to a high voltage output of the power supply and the outer electrode is grounded via an external capacitor C_{ext} (0.47 μF). The applied voltage (U_a) is measured by a high voltage probe, while the current (I_t) is recorded by a current monitor. The voltage (U_c) on the external capacitor is measured to obtain the charge generated in the discharge. All the electrical signals are sampled by a four-channel digital oscilloscope. A homemade control system is used for the online measurement of the discharge power through the area calculation of the *Q*-*U* Lissajous figure. Pure CO_2 is used as the feed gas with a flow rate of 25-125 ml/min. The temperature inside the DBD reactor is measured by a fibre optic temperature probe. The temperature probe is inserted into the catalyst bed to contact the catalyst for the measurement of the temperature on the catalyst surface. The gas products are analysed by a two-channel GC. The details of the measurement equipment are described in Section 2.3.

3.3.1.2 Parameter calculation

CO_2 conversion, CO selectivity, carbon balance, oxygen balance and energy efficiency are defined in Section 2.4.3 to evaluate the performance of the plasma process.

Mathematical models are established using the statistical experimental design and analysis method to state the relationships between CO_2 decomposition performance and the processing parameters, expressed as:

$$y = f(x_1, x_2, x_3, ...) \tag{3-2}$$

where y is the dependent variable and x_1, x_2, x_3, ……are the independent variables. In this study, the dependent variables are CO_2 conversion (C_{CO_2}) and energy efficiency (η); and the independent variables are frequency (f), discharge power (P), feed flow rate (q), discharge length (L), discharge gap (G) and dielectric material thickness (T). The relationships between C_{CO_2}, η and f, P, q, L, G, and T are linked as follows:

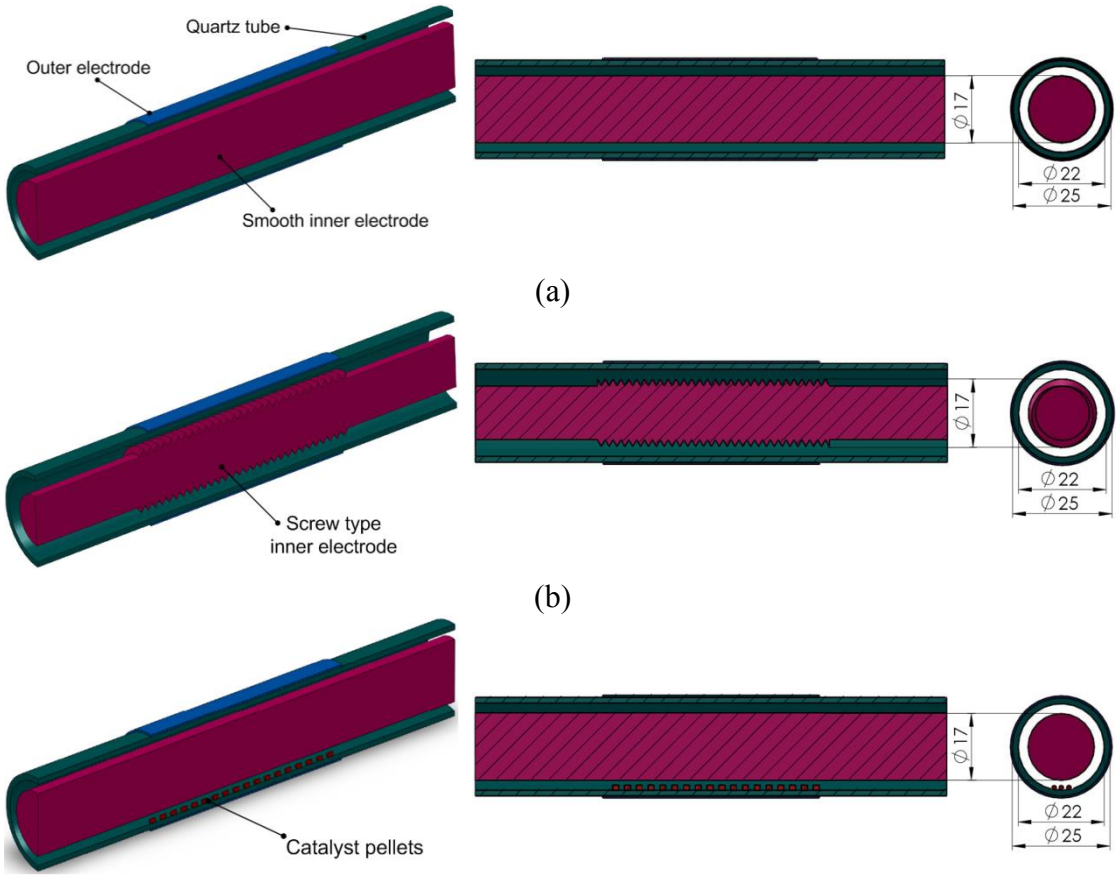

Figure 3.2 Schematic diagrams of (a) the smooth electrode reactor, (b) the screw-type electrode reactor and (c) plasma-catalytic DBD reactor.

$$C_{CO_2} = K_1 [f]^{a_1} [P]^{b_1} [q]^{c_1} [L]^{d_1} [G]^{e_1} [T]^{f_1} \quad (3\text{-}3)$$

$$\eta = K_2 [f]^{a_2} [P]^{b_2} [q]^{c_2} [L]^{d_2} [G]^{e_2} [T]^{f_2} \quad (3\text{-}4)$$

where K_1, K_2 are constants that correlate CO_2 conversion and energy efficiency with these processing parameters; a_i, b_i, c_i, d_i, e_i, and f_i (i=1, 2) are the exponents of the terms related to each processing parameter. The value of these constants and indexes are calculated using the multiple regression analysis method.

3.3.2 Experimental results

3.3.2.1 Effect of frequency

Figure 3.3 (a) shows the effect of frequency on CO_2 conversion and the energy efficiency of the plasma process. Clearly, CO_2 conversion and energy efficiency are almost independent of the frequency when it increases from 8 kHz to 11 kHz at a constant SED of 96 kJ/l. This phenomenon is possibly due to the slight variation in frequency. Similar results have been reported in previous studies [123, 124]. Aerts et al. reported that more filamentary discharges were observed when

increasing the frequency from 6 kHz to 75 kHz in an AC CO_2 DBD reactor at a constant input power and gas flow rate; however, they also found that the variation of frequency had a weak influence on the plasma reaction performance [124]. Liu et al. demonstrated that frequency is the least important parameter affecting the plasma process performance for nonoxidative conversion of CH_4 in an AC power supplied DBD reactor [193]. They found that the conversion of CH_4 slightly decreased (by 10%) when the frequency was increased from 20 kHz to 50 kHz at a discharge power of 45 W and a gas flow rate of 100 ml/min [193].

The effect of frequency on the selectivity of CO and the carbon balance is shown in **Figure 3.3** (b). Increasing the frequency from 8 kHz to 11 kHz has negligible effect on the CO selectivity. The selectivity of CO based on the carbon atoms at each frequency almost reaches 100%, which indicates that CO is the major product from CO_2 conversion and that the stoichiometric conversion of CO_2 into CO is achieved. Moreover, the carbon balance is also independent of the frequency and changes between 98.7% and 99.2%. This can be confirmed by the fact that almost no carbon deposition is observed during the plasma process. It is noticeable that in addition to frequency, CO selectivity and carbon balance are also independent of the other processing parameters (e.g. discharge power, feed flow rate, discharge gap, discharge length and dielectric material thickness). Therefore, the influence of other parameters on the CO_2 splitting performance will only be discussed in terms of CO_2 conversion and energy efficiency in the following sections.

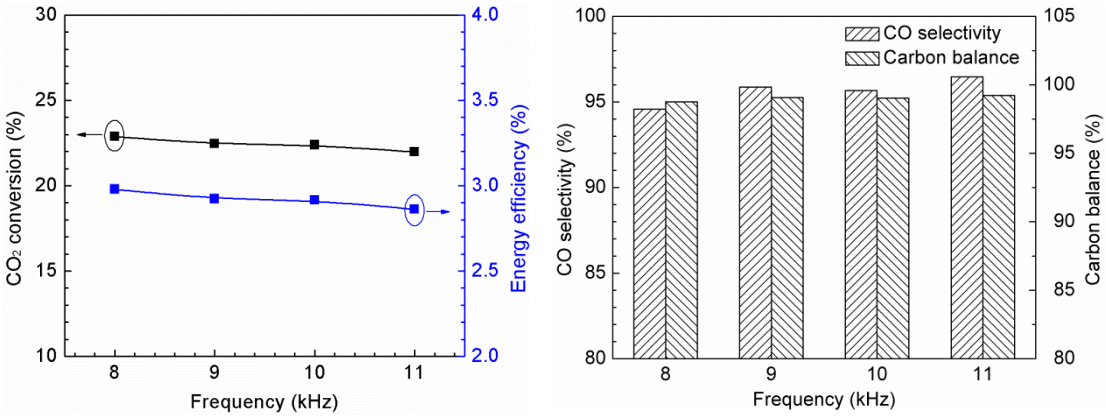

(a) (b)

Figure 3.3 Effect of frequency on: (a) CO_2 conversion and energy efficiency; (b) CO selectivity and carbon balance (SED: 96 kJ/l; feed flow rate: 25 ml/min; discharge length: 100 mm; discharge gap: 2.5 mm).

3.3.2.2 Effect of discharge power and feed flow rate

Figure 3.4 (a) presents the effect of discharge power on CO_2 conversion and energy efficiency. Increasing the discharge power leads to an increase in the conversion of CO_2, and a decrease in the energy efficiency; but the increasing rate in

CO_2 conversion and the decreasing rate in energy efficiency become moderate at higher discharge powers. CO_2 conversion rises from 17.4% to 22.4% when the discharge power increases from 10 W to 50 W. In this study, the CO_2 DBD can be characterised as a typical filamentary discharge. The discharge power is changed by adjusting the applied voltage at a fixed frequency. Increasing the discharge power by only changing the applied voltage does not change the average electric field of the plasma, since the gas voltage and breakdown voltage of the CO_2 DBD is almost constant (calculated from the Lissajous figure [107]) with the increase in discharge power. This also means that the change in the average electron energy in the CO_2 discharge is negligible when changing the discharge power at a constant frequency, which can be shown from Einstein's equation, $k_B T_e/e=D_e/\mu_e$ (k_B is the Boltzmann constant, 1.38×10^{-23} J/K; D_e and μ_e are the diffusion constant and the drift mobility of electrons related to the reduced electric field, respectively) [194]. In contrast, we find that the number and amplitude of the current pulses in the electrical signals in the CO_2 DBD increase with the rise in discharge power or applied voltage, as shown in **Figure 3.4** (b), which indicates the number of microdischarges is increased by increasing discharge power or applied voltage. This phenomenon has been confirmed by Kim et al. using an intensified charge-coupled device (ICCD) camera [195]. They found that more microdischarges were formed in the packed-bed DBD reactor by increasing the applied voltage. Dong et al. also reported that the number of filaments on the per unit area of dielectric surface in a DBD reactor increases with an increase in the applied voltage [196]. The increased number of microdischarges in the CO_2 DBD suggests the formation of more reaction channels and electrons in the plasma, both of which contribute to the enhancement in CO_2 conversion. The energy efficiency of the plasma process is decreased from 9.0% to 2.3% when the discharge power is raised from 10 to 50 W.

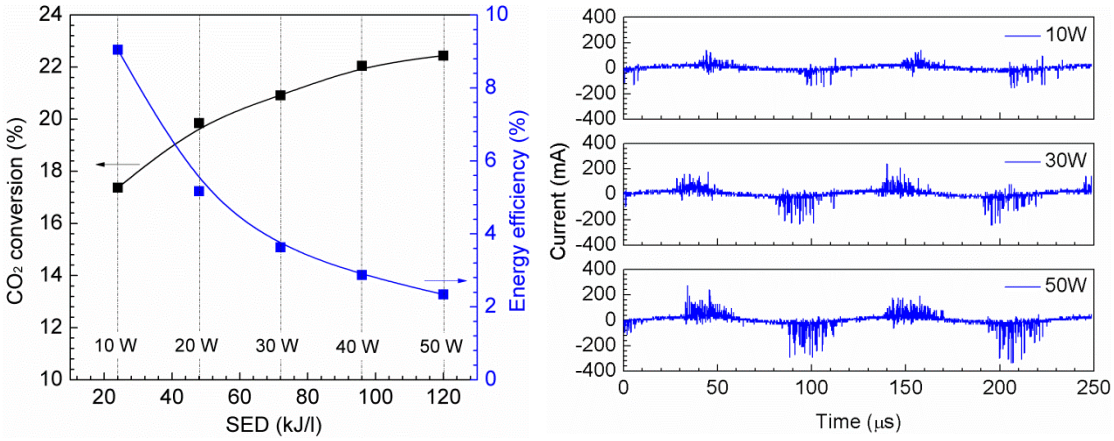

(a) (b)

Figure 3.4 Effect of discharge power on: (a) CO_2 conversion and energy efficiency; (b) current signal characteristics (feed flow rate: 25 ml/min; discharge length: 100 mm; discharge gap: 2.5 mm).

The influence of the feed flow rate on CO_2 conversion and energy efficiency of the plasma process is shown in **Figure 3.5**. Clearly, a maximum CO_2 conversion of 22.4% has been obtained at the minimum CO_2 flow rate of 25 ml/min. With the other processing parameters fixed, increasing the feed flow rate reduces the residence time of the reactants in the discharge region, which decreases the possibility for activation of the reactants through collisions with energetic electrons and reactive species. The residence time of CO_2 in the discharge volume decreases from 36.8 s to 7.4 s when feed flow rate increases from 25 ml/min to 125 ml/min, which decreases the conversion of CO_2 from its maximum value to 12.6%. Similar results have been obtained in the previous studies [123, 124]. Paulussen et al. reported that the conversion of CO_2 decreased from 28.8% to 3.6% when the gas flow rate increased from 50 to 500 ml/min at an input power of 150 W and a frequency of 30 kHz [123]. However, the energy efficiency in this study is increased from 2.3% to 6.6% when increasing feed flow rate from 25 ml/min to 125 ml/min.

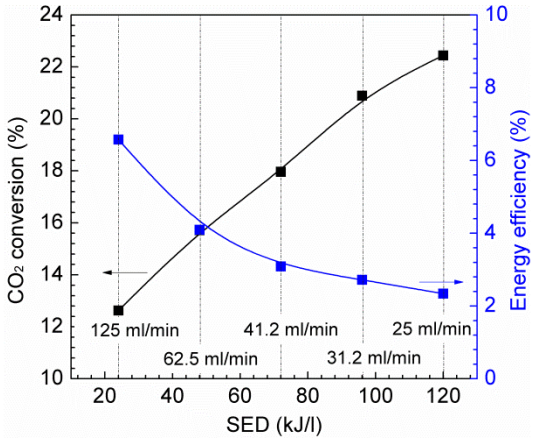

Figure 3.5 Effect of feed flow rate on CO_2 conversion and energy efficiency (discharge power: 50W; discharge length: 100 mm; discharge gap: 2.5 mm).

From the definition of SED (Equation (2-1)), variation of SED can be achieved by adjusting the discharge power and/or feed flow rate. In **Figure 3.4** (a) and **Figure 3.5**, increasing SED from 24 kJ/l to 120 kJ/l is obtained by two approaches: (1) increasing the discharge power from 10 W to 50 W at a feed flow rate of 25 ml/min; (2) decreasing the feed flow rate from 125 ml/min to 25ml/min at a discharge power of 50 W. In the former approach, CO_2 conversion is increased by 28.7% (from 17.4% to 22.4%), whilst in the latter approach, it is increased by 77.8% (from 12.6% to 22.4%). Obviously, the residence time of CO_2 in the discharge region is quite different in these two approaches. The former approach has a constant residence time of 36.8 s, but the residence time is increased by a factor of 4 by reducing the gas flow rate in the latter one. Although the discharge power in the former approach is also enhanced 4 times, the higher enhancement in CO_2

conversion in the latter approach suggests that the variation in SED obtained by changing the feed flow rate has a more pronounced influence on CO_2 conversion. By contrast, higher decrease in the energy efficiency in the former approach is observed, which indicates that the change in SED obtained by adjusting the discharge power plays a more important role in energy efficiency. Therefore, both discharge power and feed flow rate should be considered when pursuing a suitable SED for high CO_2 conversion and energy efficiency simultaneously.

3.3.2.3 Effect of discharge gap and discharge length

Figure 3.6 shows the effect of discharge gap on CO_2 conversion and energy efficiency as a function of SED. At a specified SED, both CO_2 conversion and energy efficiency are decreased by increasing the discharge gap. The decreasing rate of these two performance parameters becomes more significant at the larger discharge gap. For example, at a SED of 96 kJ/l, CO_2 conversion slightly decreases from 22.1% to 20.5% when the discharge gap increases from 2.5 to 3.0 mm, whereas CO_2 conversion is decreased by 18.1% (from 20.5% to 16.8%) by increasing discharge gap from 3.0 mm to 3.5 mm. The energy efficiency of the plasma process is decreased by 7.0% and 18.0% when the discharge gap is increased from 2.5 mm to 3 mm and from 3 mm to 3.5 mm, respectively.

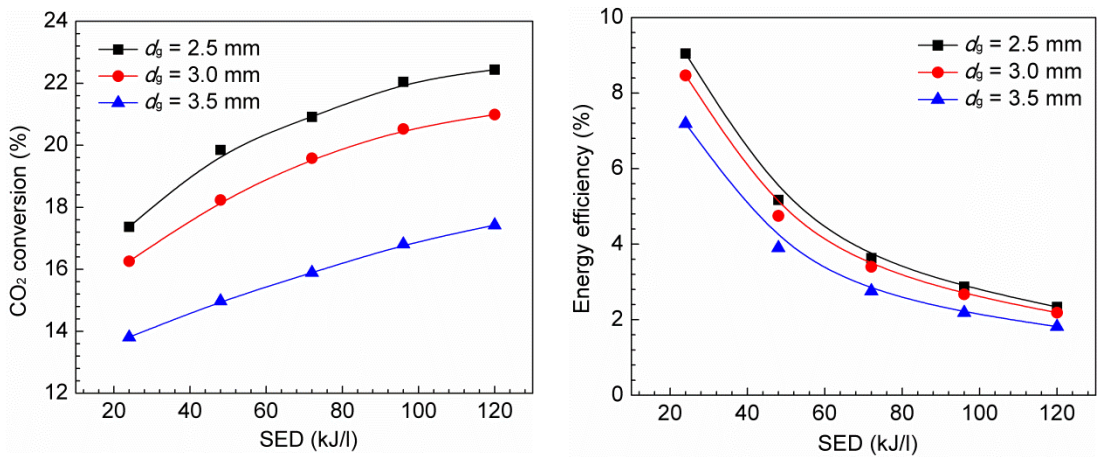

(a) (b)

Figure 3.6 Effect of discharge gap on CO_2 conversion and energy efficiency (feed flow rate: 25 ml/min; discharge length: 100 mm).

Increasing the discharge gap increases the residence time of the reactant molecules in the discharge region. In this study, the residence time of CO_2 in the plasma increases from 36.8 s to 48.8 s as the discharge gap is increased from 2.5 mm to 3.5 mm, which seems to be beneficial to the plasma processing of CO_2. However, increasing the discharge gap increases the discharge volume, which results in a decline in the power density at a constant discharge power. Previous work of Aerts et

al. has demonstrated that the plasma volume (i.e. the volume occupied by the discharge streamers) is much smaller than the total volume of the plasma reactor, especially for the large discharge gap, by comparing the effective capacitance C_{eff} with the capacitance of the dielectric materials C_d [124]. **Figure 3.7** shows the Lissajous figures of the CO_2 DBD with different discharge gaps at a SED of 96 kJ/l. Increasing the discharge gap decreases the transferred charge (i.e. the transferred charge is 0.51, 0.49 and 0.47 μC for discharge gaps of 2.5, 3.0 and 3.5 mm, respectively). It is reported that the transferred charge is positively correlated with the electron density [197]. The increase in the discharge gap decreases the electron density in the discharge, and therewith, the density of reactive species. The effect of discharge gap on CO_2 decomposition performance is reflected by the combined effect of residence time and power density together with electron density. In our DBD reactor, the positive effect from the longer residence time cannot compensate the negative effect from the decrease in the power density and the electron density. Additionally, this negative effect is more significant at higher discharge gap, which results in the higher decrease in both CO_2 conversion and energy efficiency.

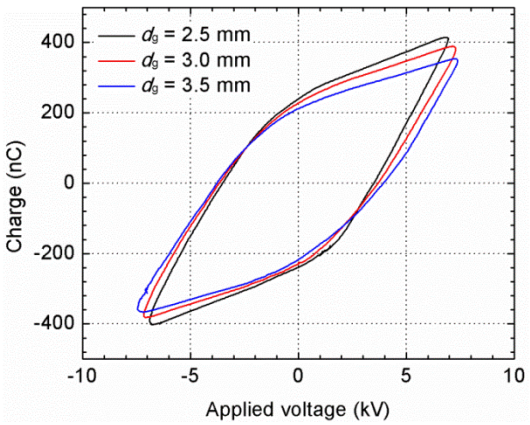

Figure 3.7 Lissajous figures of the CO_2 DBD with different discharge gaps (SED: 96kJ/l; discharge length: 100 mm; frequency: 9 kHz).

The influence of discharge length on CO_2 conversion and energy efficiency as a function of SED is displayed in **Figure 3.8**. Both CO_2 conversion and energy efficiency are increased by around 27% when the discharge length increases from 60 mm to 140 mm at a SED of 120 kJ/l. The effect of discharge length on the CO_2 decomposition performance can be reflected by two competing effects. On the one hand, the residence time of CO_2 in the discharge region is increased by 133.3% when discharge length increases from 60 to 140 mm, which increases the probability of the CO_2 molecules colliding with the highly energetic electrons and reactive species, thereby improving the conversion of CO_2. On the other hand, the barrier volume is increased from 6.6 cm^3 to 15.5 cm^3 when the discharge length increases from 60 mm to 140 mm, which consumes more energy to heat the dielectric material.

Correspondingly, the surface area of the discharge regions increases from 47.1 cm^2 to 110.0 cm^2, leading to an increase in the energy loss by the heat dissipation [198]. Moreover, longer discharge length lowers the power density due to the increase in the discharge volume (from 9.2 cm^3 to 21.4 cm^3), and consequently decreases the mean energy to each CO_2 molecule [198], which decreases the conversion of CO_2. The results in **Figure 3.8** suggest that the change in the residence time obtained by increasing the discharge length has a much more significant impact on the conversion of CO_2 in our DBD reactor.

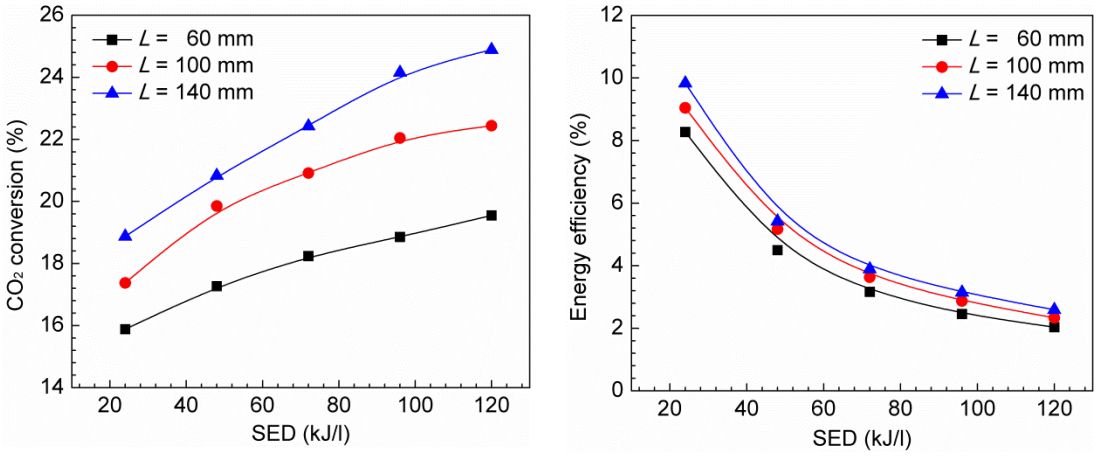

(a) (b)

Figure 3.8 Effect of discharge length on CO_2 conversion and energy efficiency (feed flow rate: 25 ml/min; discharge gap: 2.5 mm).

3.3.2.4 Effect of dielectric material thickness

Figure 3.9 shows the effect of the dielectric material thickness on the CO_2 decomposition performance as a function of SED. Clearly, increasing the thickness of the quartz tube decreases CO_2 conversion and energy efficiency at a fixed SED. For example, CO_2 conversion and energy efficiency are decreased by 14.7% and 15.0%, respectively, when the thickness of the dielectric material increases from 1.5 mm to 2.5 mm at a SED of 120 kJ/l. In DBD, the transferred charge Q is approximately proportional to the parameter ε_r/d ratio (ε_r and d are the relative permittivity and the thickness of the dielectric material, respectively) when the other parameters are fixed [197]. Therefore, increasing the relative permittivity and/or decreasing the thickness of the dielectric material will increase the transferred charge Q, and consequently increase the electron density in the discharge. In this study, as only the quartz tube is used as the dielectric material, decreasing its thickness will increase the transferred charge and hence the density of the highly energetic electrons and reactive species for CO_2 decomposition. **Figure 3.10** shows the Lissajous figures of the CO_2 DBD with different dielectric material thicknesses at a SED of 96 kJ/l. It can be found that increasing the thickness of the quartz tube from

1.5 to 2.5 mm decreases the transferred charge Q by 19.9% (from 0.51 μC to 0.41 μC), resulting in a decrease in both CO_2 conversion and energy efficiency.

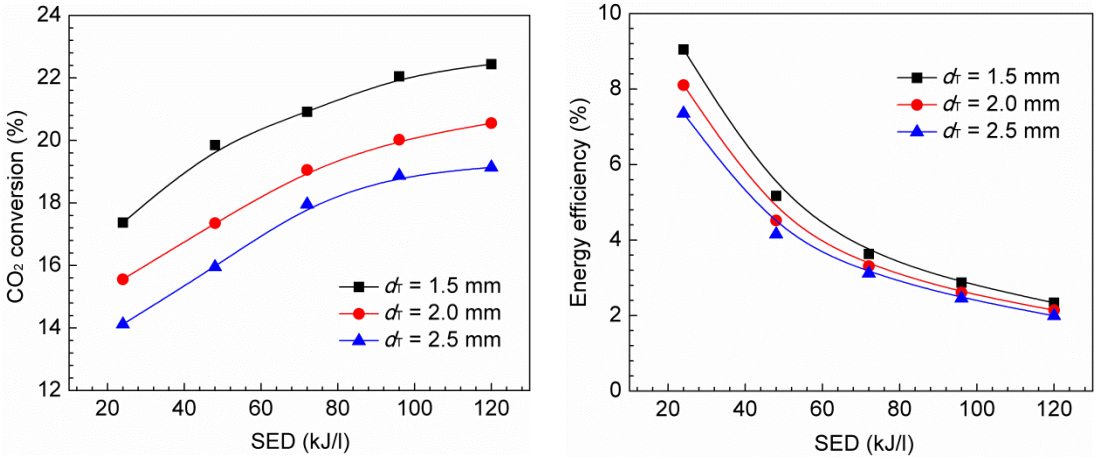

(a) (b)

Figure 3.9 Effect of dielectric material thickness on CO_2 conversion and energy efficiency (feed flow rate: 25 ml/min; discharge gap: 2.5 mm; discharge length: 100 mm).

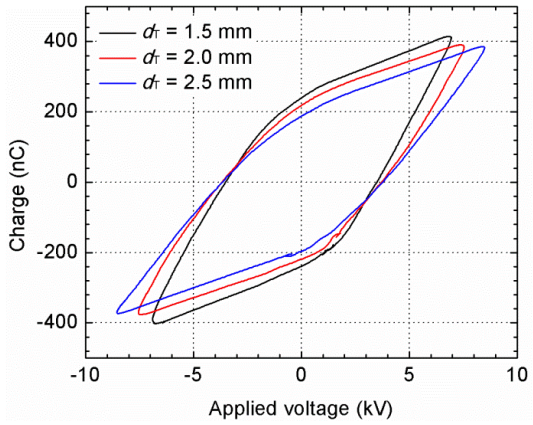

Figure 3.10 Lissajous figures of the CO_2 DBD with different dielectric material thicknesses (SED: 96kJ/l; discharge gap: 2.5 mm; discharge length: 100 mm; frequency: 9 kHz).

3.3.2.5 Sensitivity analysis of the processing parameters

The empirical formulas are derived to describe the relationships between the plasma processing parameters and plasma reaction performance (e.g. CO_2 conversion and energy efficiency), as shown in Equations (3-5) and (3-6).

$$C_{CO_2} = 34.3401 \times [f]^{-0.0448} [P]^{0.1634} [q]^{-0.3839} [L]^{0.2527} [G]^{-0.6999} [T]^{-0.3593},$$
$$R^2 = 0.9872 \quad (3\text{-}5)$$

$$\eta = 6.4876 \times [f]^{-0.0415} [P]^{-0.8367} [q]^{0.6158} [L]^{0.2531} [G]^{-0.7004} [T]^{-0.3605},$$
$$R^2 = 0.9947 \quad (3\text{-}6)$$

It is important to note that these two models are obtained on the experimental data under the following conditions: f = 8-11 kHz, P = 10-50 W, q = 25-125 ml/min, L = 60-140 mm, G = 2.5-3.5 mm and T = 1.5-2.5 mm. There is a relatively good agreement between the experimental results and the predicted data using the established models with an error of within 5.8% (e.g. 5.8% and 5.7% for CO_2 conversion and energy efficiency, respectively).

The model sensitivity analysis has also been performed to gain a better understanding on the relative importance of the processing parameters for CO_2 conversion and energy efficiency. In each sensitivity analysis, only one parameter is changed from +10% increase or -10% decrease, and all other parameters are fixed at their respective initial values (f = 9 kHz, P = 30 W, q = 41.2 ml/min, L =100 mm, G = 3 mm, T = 2 mm). **Figure 3.11** shows the sensitivity analysis of processing parameters for CO_2 conversion and energy efficiency. $\delta\lambda/\lambda$ is the change of each parameter divided by the initial value, whilst $\delta S/S$ is the change in CO_2 conversion or energy efficiency divided by the corresponding value at initial conditions.

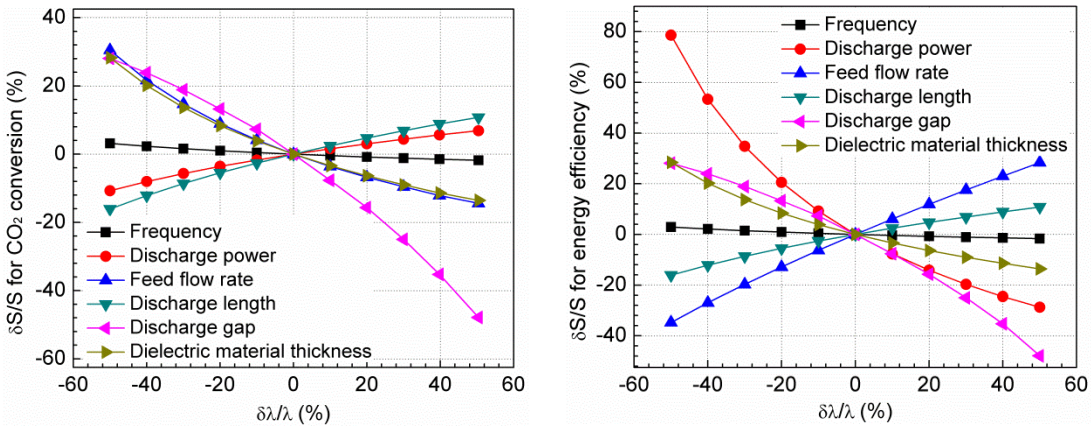

(a) (b)

Figure 3.11 Sensitivity analysis of parameters for (a) CO_2 conversion and (b) energy efficiency.

Figure 3.11 (a) shows the sensitivity analysis of operating parameters for CO_2 conversion. Obviously, discharge gap significantly affects the conversion of CO_2, especially at higher discharge gap. A decrease of $\delta\lambda/\lambda$ from 0 to -50% results in a moderate increase of $\delta S/S$ from 0 to 28.1%, but an increase of $\delta\lambda/\lambda$ from 0 to 50% significantly decreases $\delta S/S$ from 0 to -47.9%. This phenomenon is inconsistent with the results shown in **Figure 3.6** (a). Feed flow rate and dielectric material thickness have a similar negative effect on CO_2 conversion. Their $\delta S/S$ decrease roughly from 30% to -14% when $\delta\lambda/\lambda$ is increased from -50% to 50%. CO_2 conversion is positively correlated with discharge power and discharge length. For discharge power, an increase of $\delta\lambda/\lambda$ from -50% to 50% leads to a nearly linear enhancement of $\delta S/S$ from -10.7% to 6.8%. Frequency is observed to weakly affect the conversion of

CO_2. In general, the relative significance of these processing parameters for CO_2 conversion decreases in the following order: $G > q > T > L > P > f$.

It is clear from **Figure 3.11** (b) that discharge power has a more significant effect on energy efficiency of the plasma process compared with other processing parameters. The $\delta S/S$ for energy efficiency is decreased from 78.6% to -28.8% by increasing the $\delta\lambda/\lambda$ of discharge power from -50% to 50%. Energy efficiency is positively correlated with feed flow rate and discharge length, but negatively correlated with discharge gap and dielectric material thickness. The effect of frequency on energy efficiency is negligible. Briefly, the relative significance of the sensitivity of these processing parameters to energy efficiency is $P > G > q > T > L > f$.

3.3.2.6 CO_2 decomposition in a modified DBD reactor

Figure 3.12 shows the influence of different types of inner and outer electrodes on the conversion of CO_2 as a function of SED. The SS rod acts as the inner high voltage electrode and the SS mesh as the outer electrode in the reference DBD reactor. When the SS mesh outer electrode is replaced by the Al foil, higher CO_2 conversion and energy efficiency are obtained compared to these in the reference reactor; e.g. CO_2 conversion and energy efficiency increase by 10.8% and 10.7%, respectively, at a SED of 120 kJ/l. When the SS mesh is used as the outer electrode, the effective discharge area is less than the coverage area, and the mesh cannot uniformly cover the quartz tube. However, when the Al foil is used as the outer electrode, it covers the outer surface of the quartz tube more uniformly and larger effective discharge area is obtained, which increases the number of the microdischarges, and consequently contributes to the improvement in both CO_2 conversion and energy efficiency.

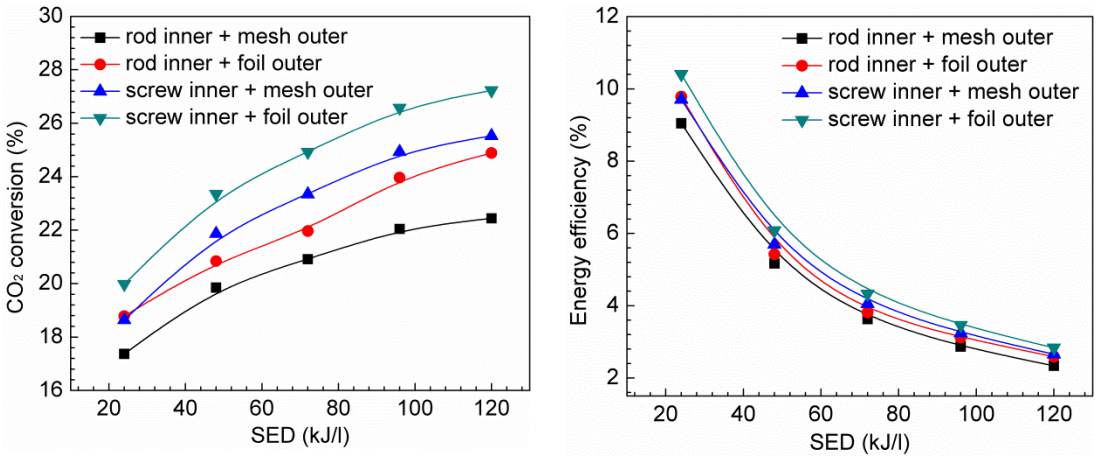

(a) (b)

Figure 3.12 Effect of electrode forms on CO_2 conversion and energy efficiency (feed flow rate: 25 ml/min; discharge gap: 2.5 mm; discharge length: 100 mm).

Compared to the reference reactor, CO_2 conversion and energy efficiency are increased by 13.8% and 11.8%, respectively, when using the screw-type inner electrode at a SED of 120 kJ/l (**Figure 3.12**). As discussed before, increasing SED results in the increase of CO_2 conversion, but this phenomenon is more remarkable in the case of the screw inner electrode. CO_2 conversion is increased by 29.2% and 37.0% in the case of the rod and screw electrodes, respectively, when SED increases from 24 kJ/l to 120 kJ/l. The difference between the effect of the screw and rod inner electrodes on CO_2 decomposition is possibly ascribed to the sharp edge of the screw electrode, which can enhance the local electric field near the electrode surface [199]. As shown in **Figure 3.13**, the filaments are distributed randomly in the discharge volume when the SS rod is used as the inner electrode; while in the case of the screw-type inner electrode, the filaments are significantly intensified near the sharp edge of the screw. This generates more reaction channels as well as more energetic electrons and reactive species, resulting in higher CO_2 conversion and energy efficiency of the plasma process.

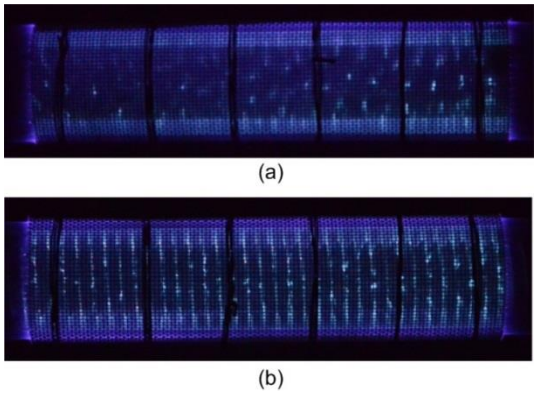

Figure 3.13 Images of pure CO_2 DBD plasma (exposure time: 25 ms): (a) SS rod inner electrode; (b) SS screw-type inner electrode (discharge power: 40 W; discharge gap: 2.5 mm, discharge length: 100 mm; CO_2 feed flow rate: 25 ml/min; frequency: 9 kHz).

It is interesting to note that the combination of the screw-type inner electrode and Al foil outer electrode can further increase the CO_2 conversion and energy efficiency in the DBD reactor. At a SED of 120 kJ/l, CO_2 conversion and energy efficiency are 27.2% and 2.8%, respectively, in a DBD reactor with screw-type inner electrode and Al foil outer electrode. The maximum energy efficiency of 10.4% is achieved at a SED of 24 kJ/l in the DBD reactor with these two modified electrodes. **Figure 3.14** presents the electrical signals of the pure CO_2 discharge with different electrode forms at a SED of 96 kJ/l. Clearly, the current waveforms are quasi-sinusoid with numerous superimposed current pulses per half cycle of the applied voltage. These current pulses are assigned to the transient filamentary microdischarges. When the outer electrode is changed from the SS mesh to the Al

foil, the microdischarge filaments extend across the discharge gap due to the higher effective covered area when using the Al foil, reflected by the enhanced number and amplitude of the current pluses (**Figure 3.14** (b)). When the screw-type inner electrode is used, the current pulses are also intensified due to the higher local electric field resulting from the sharp edge of the screw electrode (**Figure 3.14** (c)). The number and amplitude of the current pulses (and therefore the intensity of the microdischarges) are further enhanced by the combination of the Al foil outer electrode and the screw-type SS inner electrode in the DBD reactor (**Figure 3.14** (d)), which results in the maximum CO_2 conversion. This variation in the number and amplitude of the current pulses in CO_2 discharge with different electrodes can be confirmed by the corresponding transferred charge, as shown in **Figure 3.15**. By integrating the screw-type inner electrode and the Al foil outer electrode into the DBD reactor, the transferred charge is increased from 0.51 μC to 0.60 μC, compared with the reference reactor.

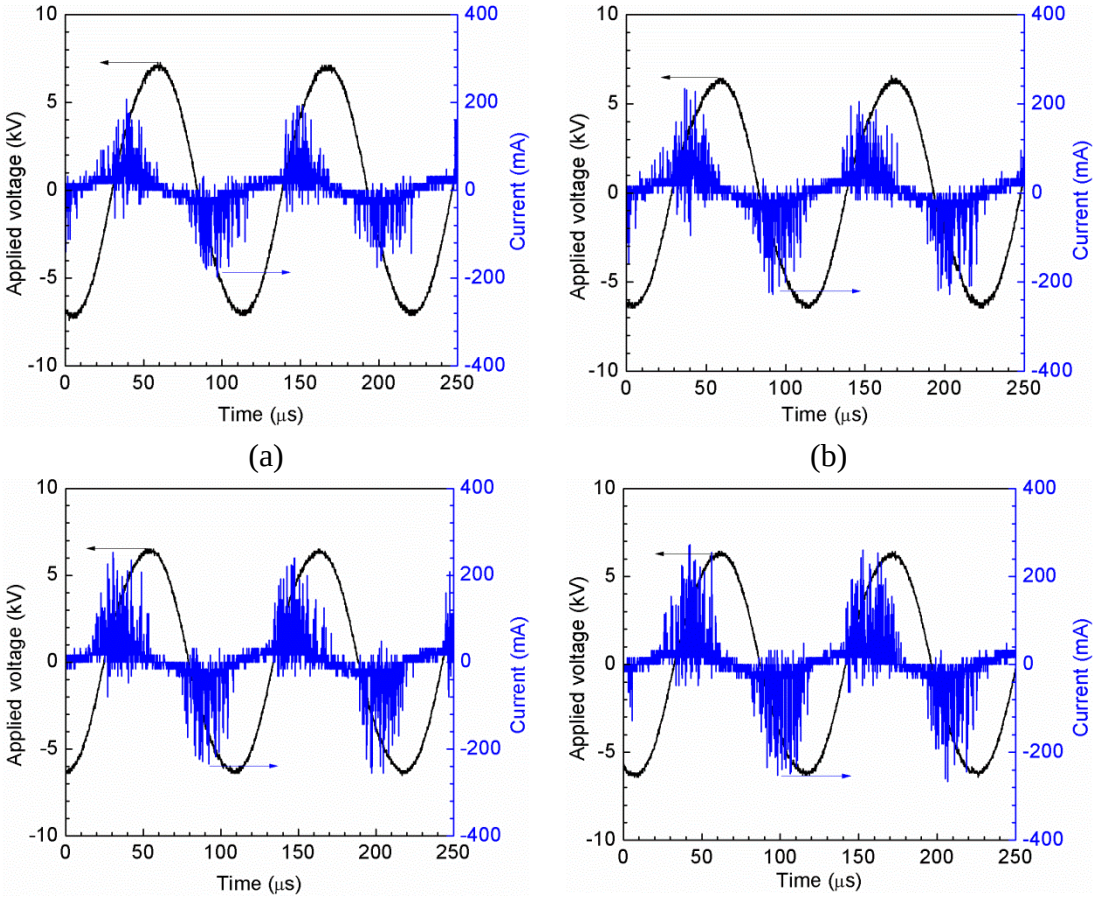

Figure 3.14 Electrical signals of the CO_2 DBD: (a) mesh outer electrode and rod inner electrode; (b) foil outer electrode and rod inner electrode; (c) mesh outer electrode and screw-type inner electrode; (d) foil outer electrode and screw-type inner electrode (SED: 96k J/l; discharge gap: 2.5 mm; discharge length: 100 mm; frequency: 9 kHz).

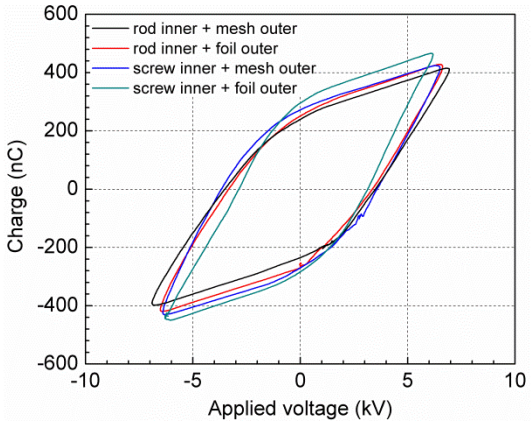

Figure 3.15 Lissajous figures of the CO_2 DBD with different electrodes (SED: 96 kJ/l; discharge gap: 2.5 mm; discharge length: 100 mm; frequency: 9 kHz).

3.3.2.7 CO_2 decomposition in the plasma-catalytic DBD reactor

The effect of $BaTiO_3$ and TiO_2 photocatalysts on the conversion of CO_2 is shown in **Figure 3.16**. It is clear that the presence of both $BaTiO_3$ and TiO_2 in the discharge significantly enhances the CO_2 conversion and energy efficiency. Packing $BaTiO_3$ pellets into the discharge gap exhibits exceptional performance with a remarkable enhancement of both CO_2 conversion (from 15.2% to 38.3%) and energy efficiency (from 6.8% to 16.7%), which are enhanced by a factor of 2.5 at a SED of 28 kJ/l.

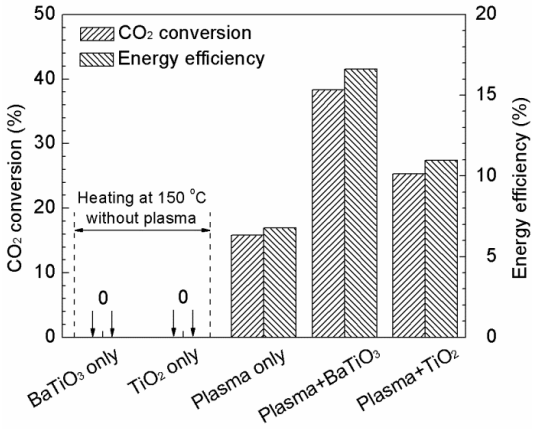

Figure 3.16 Demonstration of the synergistic effect of plasma-catalysis for the conversion of CO_2 (SED = 28 kJ/l).

The plasma gas temperature and the temperature on the catalyst surface in the plasma conversion of CO_2 have been measured in the DBD reactor at a SED of 28 kJ/l, as shown in **Figure 3.17**. Clearly, the plasma gas temperature of the CO_2 DBD without a catalyst significantly increases from 23.3 ^oC to 123.5 ^oC in the first 15 min after igniting the plasma, after which it rises slowly and becomes almost constant

(~138 ^{o}C) at 25 min when the plasma reaches a stable state. Similar evolution behaviour of the temperature can also be observed in the plasma-catalysis system.

In the CO_2 DBD reactor partially packed with the $BaTiO_3$ and TiO_2 catalysts, we note that the plasma temperature in the gas phase and the temperature on the catalyst surface are almost the same. Thus, only one temperature (the temperature on the catalyst surface) is shown in **Figure 3.17** to present the temperature in the plasma-catalytic system. It is interesting to note that the combination of plasma with the $BaTiO_3$ and TiO_2 catalysts slightly increases the gas temperature (TiO_2: ~144 ^{o}C and $BaTiO_3$: ~149 ^{o}C) of the CO_2 discharge by 6-11 ^{o}C compared to the CO_2 DBD in the absence of a catalyst at the same SED (28 kJ/l). This phenomenon might be attributed to inelastic electron-molecule collisions in the plasma-catalytic processes [90, 200, 201].

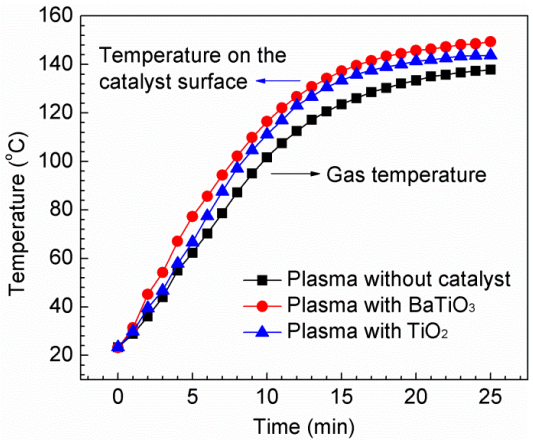

Figure 3.17 Plasma gas temperature and the temperature on the surface of $BaTiO_3$ and TiO_2 catalysts in the CO_2 DBD reactor (SED = 28 kJ/l).

To understand the role of plasma in the reaction, a purely thermal experiment has been carried out by heating both photocatalysts in a pure CO_2 flow at 150 $^{\circ}$C. No conversion or adsorption of CO_2 was observed. Thermodynamic equilibrium calculation of CO_2 decomposition (shown in **Figure 3.1**) has confirmed that the conversion of CO_2 is almost zero at 150 $^{\circ}$C, suggesting that low CO_2 conversion is expected using thermal catalytic reduction of CO_2 at the same temperature as that measured in the plasma reaction. The results clearly show that the exceptional reaction performance has been achieved by using plasma-catalysis, which is much higher than the sum of plasma-only and catalysis only processes, indicating the formation of a synergistic effect when combining plasma with photocatalysts at low temperatures.

Catalysts can be integrated into a DBD system in different ways. The presence of the catalyst pellets in part of the gas gap still leads to predominantly filamentary discharges and surface discharges on the catalyst surface, which induces effective interactions between the plasma and catalysts for CO_2 activation. In this

work, the dielectric constants of $BaTiO_3$ and TiO_2 are 10000 and 85, respectively. Previous experimental [202, 203] and simulation [204, 205] studies have shown that packing catalyst pellets, especially pellets with high dielectric constant (e.g. $BaTiO_3$), into the discharge gap can generate a non-uniform electric field, with enhanced electric field strength near contact points between the pellets and the pellet - dielectric wall. The maximum local electric field near these contact points can be 10 – 10^4 times higher than that in the void in a plasma-catalytic reactor, depending on the contact angle, curvature and dielectric constant of the materials [88]. The space (including the space filled with pellets) averaged electric field in a plasma reactor fully packed with packing pellets is initially increased by a factor of 1.4 with increasing dielectric constant of the materials from 10 to 1000; above this the change in the electric field becomes negligible [88]. We have reported that the interaction between plasma and TiO_2 exhibited a strong effect on the electron energy distribution in the discharge, with an increase in both highly energetic electrons and electric field [185]. This phenomenon is also confirmed by previous work, showing that the presence of TiO_2 in the plasma leads to a significant increase in the reduced electric field [206]. These results suggest that the presence of the catalyst pellets in the plasma gap play a crucial role in inducing physical effects, which in turn lead to chemical effects and contribute to the conversion of CO_2.

In this study, the electric field of the discharge (breakdown voltage/electrode gap) and the electron energy for different experimental conditions are calculated through Lissajous figure and BOLSIG$^+$ code based on electron energy distribution function (EEDF), respectively [107, 207] and the results are shown in **Figure 3.18**.

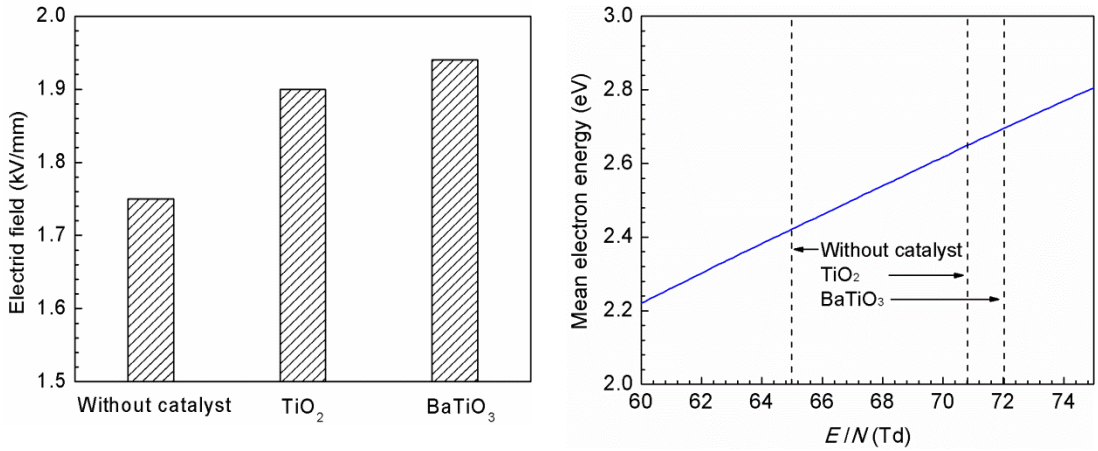

(a) (b)

Figure 3.18 (a) Average electric field and (b) mean electron energy in the three reactor conditions (SED = 28 kJ/l).

It can be observed that the average electric field is increased by 10.9% and 9.0% with the presence of $BaTiO_3$ and TiO_2 in the discharge gap, respectively; while

the corresponding mean electron energy increases by 11.3% and 9.4%. Both of these effects contribute to the enhancement of CO_2 conversion. However, the enhancement of the reaction performance in terms of CO_2 conversion and energy efficiency is found be more significant than the change in plasma physical parameters (e.g. average electric field). This suggests that in addition to the plasma physical effect, the contribution of the plasma-activated photocatalytic reaction to the synergy of plasma-catalysis cannot be ruled out. The XRD patterns of the samples show that the $BaTiO_3$ catalyst has the tetragonal phase, while TiO_2 exhibits a crystal structure of anatase (see **Figure 3.19**). TiO_2 is a widely used photocatalyst with a wide band gap of 3.2 eV for anatase phase, while $BaTiO_3$ is a perovskite semiconductor photocatalyst with a band gap of 2.8-3.0 eV for tetragonal phase. It is well known that photocatalysts can be activated through the formation of electron-hole (e^--h^+) pairs with the aid of sufficient photonic energy ($h\nu$) with appropriate wavelength to overcome the band-gap between the valence band and conductive band [208]:

$$TiO_2 + h\nu \rightarrow e^- + h^+ \quad (3\text{-}7)$$

$$BaTiO_3 + h\nu \rightarrow e^- + h^+ \quad (3\text{-}8)$$

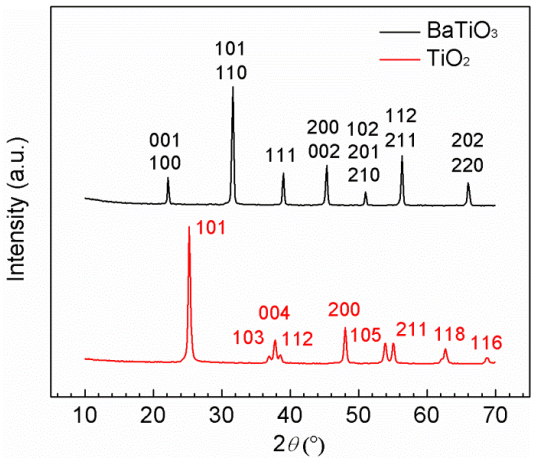

Figure 3.19 XRD patterns of $BaTiO_3$ and TiO_2.

Plasma discharges can generate UV radiation without using any extra UV sources (e.g. UV lamps). This has been confirmed by the dominant N_2 (C-B) bands (between 300 nm and 400 nm) in a CO_2 DBD in our previous works [91, 209]. However, UV radiation generated by plasma discharges is not always the controlling factor for activating photocatalysts due to its low intensity compared to that emitted by an UV lamp [210]. In this work, we have measured the UV intensity generated by the CO_2 DBD with and without a catalyst, as shown in **Figure 3.20**.

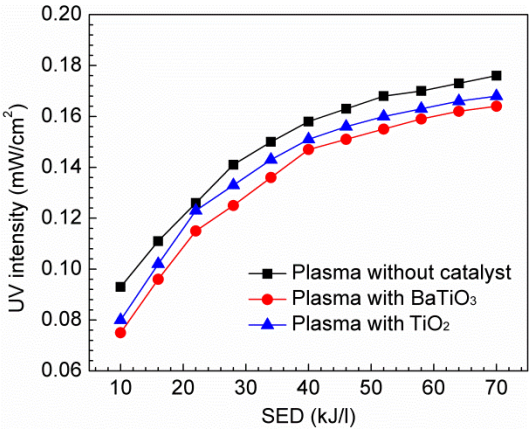

Figure 3.20 UV intensity generated by the CO_2 DBD with and without a catalyst as a function of SED.

In the absence of a catalyst in the DBD reactor, the UV intensity produced by the CO_2 discharge is about 0.141 mW/cm^2 at a SED of 28 kJ/l. When the $BaTiO_3$ and TiO_2 photocatalysts are placed in the plasma zone, the UV intensity of the CO_2 discharge is decreased to 0.115 mW/cm^2 and 0.123 mW/cm^2, respectively. Note that these values are significantly lower than the UV intensity (~20-60 mW/cm^2) produced from UV lamps to activate photocatalysts in conventional photocatalytic reactions [211-213], which suggests that the UV emissions generated by the CO_2 discharge only play a minor role in the activation of the $BaTiO_3$ and TiO_2 photocatalysts. Similar results have been reported in previous papers [214, 215]. Assadi et al. found that the UV light generated by a surface DBD was too weak to activate a TiO_2 photocatalyst for the removal of 3-methylbutanal (3MBA) [214]. Sano et al. reported that the UV intensity emitted by a N_2/O_2 surface discharge was only 2.5 μW/cm^2 at an input power of 5 W. The contribution of the plasma UV activated photocatalytic reaction to the overall performance of acetaldehyde decomposition was less than 0.2% [215].

Whitehead has suggested that electron-hole pairs can be created by electron impact upon the photocatalyst surface since part of the electrons generated by the DBD have an energy over 3 eV [89, 216], as shown in Equations (3-9)-(3-10). Nakamura et al. have also reported that photocatalysts can be activated by plasma and the electrons can be trapped on the formed oxygen vacancies (V_o) to enhance the photoexcitation process [217].

$$TiO_2 + e^- (> 3.2\,eV) \rightarrow h^+ + e^- \quad (3\text{-}9)$$

$$BaTiO_3 + e^- (> 3.0\,eV) \rightarrow h^+ + e^- \quad (3\text{-}10)$$

In this work, the exceptional performance of the plasma-catalytic CO_2 conversion has been achieved through the combination of plasma and photocatalysts. However, the significant enhancement of the reaction performance in terms of CO_2 conversion and energy efficiency cannot only be attributed to the changes in plasma

physical parameters (e.g. increased average electric field), as the estimated average electric field and mean electron energy in the CO_2 DBD are only increased by around 10% when the $BaTiO_3$ and TiO_2 catalysts are placed in the plasma zone. Furthermore, we find that the UV radiation generated by the CO_2 DBD is significantly weak compared to that produced from UV lamps, which suggests that it may only play a minor role in the activation of photocatalytic CO_2, and its contribution to the exceptional performance of the plasma-catalytic reaction and the synergy of plasma-photocatalysis could be very weak or negligible. Therefore, the highly energetic electrons generated by plasma are considered as the main driving force to activate the photocatalysts for CO_2 conversion.

Previous investigation has shown that the photocatalytic conversion of CO_2 is a multistep process, which involves the adsorption and subsequent activation of CO_2 molecules on the surface of photocatalysts and the subsequent dissociation of the C-O bond. The key step is the activation of CO_2 molecules through the transfer of trapped electrons to the adsorbed CO_2 molecules in the V_o [218].

However, the recombination rate of electron-hole pairs is 2 or 3 orders of magnitude faster than that of charge separation and transfer in the defect-free photocatalysts, which will limit the efficiency of CO_2 conversion [218]. The defect disorders in photocatalysts, such as V_o, play an important role in CO_2 photoreduction processes. V_o has been considered as the active site for the adsorption and activation of reactants in the photocatalytic reaction [219]. In this study, XPS measurement has been performed to investigate the surface structure and the element valence of the photocatalysts. **Figure 3.21** (a) shows the deconvolution of the spectra of Ti 2p in $BaTiO_3$. Two components (Ti $2p_{3/2}$ and Ti $2p_{1/2}$) are contained and can be deconvoluted into 4 peaks, two of which at higher binding energy (459.88, 465.57 eV) are assigned to the formal valence of Ti (4+) in $BaTiO_3$; while the other two peaks, located at around 457.85 eV and 463.67 eV, are consistent with the Ti $2p_{3/2}$ and Ti $2p_{1/2}$ peaks of Ti^{3+} in $BaTiO_3$. The presence of Ti^{3+} demonstrates the formation of V_o on the catalyst surface through the following reaction [220, 221]:

$$2Ti^{4+} + O^{2-} \rightarrow V_o + 2Ti^{3+} + 1/2\,O_2 \qquad (3\text{-}11)$$

where O^{2-} is the lattice oxygen. Clearly, the formation of V_o is accompanied by the change in the oxidation state of the vicinal Ti atoms from Ti^{4+} to Ti^{3+} to retain the local charge balance. Similarly, the Ti $2p_{3/2}$ and Ti $2p_{1/2}$ peaks of Ti^{3+} can also be detected in the XPS profile of TiO_2, as shown in **Figure 3.21** (b). Interestingly, from the fitted results of Ti 2p XPS profiles of $BaTiO_3$ and TiO_2, there are more Ti^{3}+ species in $BaTiO_3$ (60.9%) than TiO_2 (49.9%), which implies more active sites (V_o) are contained in $BaTiO_3$, resulting in the higher CO_2 conversion.

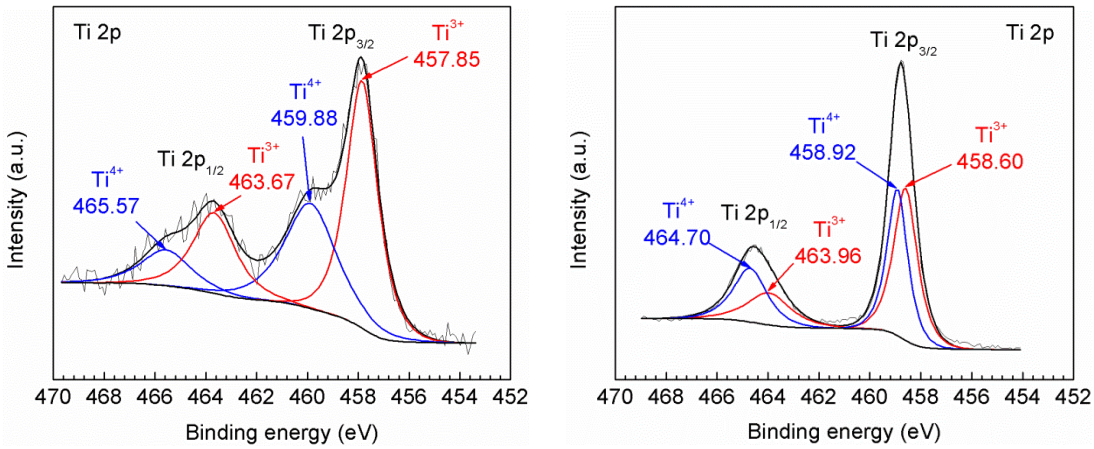

(a) (b)

Figure 3.21 XPS spectra of Ti 2p peaks for (a) $BaTiO_3$; (b) TiO_2.

Moreover, the combination rate of electron-hole pairs can also be significantly reduced in a plasma-photocatalysis system due to the high electric field and strong interactions between plasma and photocatalysts [222]. In this study, the process of the plasma-assisted photocatalytic CO_2 decomposition can be described by **Figure 3.22**. The electron (e^-) - hole (h^+) pairs are generated with the aid of highly energetic electrons from the gas discharge, and are moved in the opposite direction by the electric field, which can reduce the probability of recombination. In the electron transfer process, CO_2 adsorbed in the V_o is reduced to the anion radical $CO_2^{\bullet -}$ by electrons from e^--h^+ pairs (Equation (3-12)), followed by the decomposition of $CO_2^{\bullet -}$ into CO and the occupation of one oxygen atom in the V_o site. The overall reaction is expressed in Equation (3-13) [218, 223], where [Photocatalyst + V_o] and [Photocatalyst] represent the defective and defect-free photocatalysts, respectively.

$$CO_2 + e^- \rightarrow CO_2^{\bullet -} \quad (3\text{-}12)$$

$$CO_2 + [\text{Photocatalyst} + V_o] \rightarrow CO + [\text{Photocatalyst}] \quad (3\text{-}13)$$

$$4h^+ + 2O^{2-} \rightarrow O_2 \quad (3\text{-}14)$$

$$e^- + Ti^{4+} \rightarrow Ti^{3+} \quad (3\text{-}15)$$

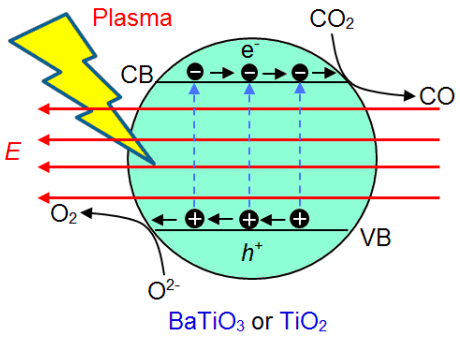

Figure 3.22 Reaction mechanisms of plasma-photocatalytic conversion of CO_2 on the surface of photocatalysts.

In addition, the V_o can be regenerated by oxidising the surface O^{2-} anions using holes, followed by the releasing of O_2, shown in Equation (3-14). To balance the charge, the Ti^{4+} in the vicinity of the regenerated V_o are reduced to Ti^{3+} by the electrons [218, 224, 225]. This cyclic healed-regeneration of the oxygen vacancies maintains the equilibrium of the active sites in the photocatalysts and accelerates the decomposition of CO_2, which is confirmed by our experimental results as CO_2 conversion did not change much when the plasma discharge was on for nearly two hours.

Therefore, we find that the synergistic effect resulting from the integration of DBD and photocatalysis for CO_2 conversion at low temperatures (without extra heating) can be attributed to the physical effect induced by the presence of photocatalysts in the discharge and the dominant photocatalytic surface reaction driven by the discharge.

3.4 Conclusions

In this chapter, the thermodynamic equilibrium calculation for the CO_2 decomposition process is firstly carried out. It is found that reasonable conversion of CO_2 (~60%) can only be obtained at an extraordinarily high temperature. Then, the plasma decomposition of CO_2 is performed in a coaxial DBD reactor. The results indicate that CO_2 is stoichiometrically decomposed into CO and O_2. In the plasma-only process, higher CO_2 conversion can be obtained by increasing discharge power and/or decreasing feed flow rate; while the decrease in discharge power and/or the increase in feed flow rate contribute to the higher energy efficiency. Moreover, decreasing the discharge gap and the dielectric material thickness and/or enlarging the discharge length have a positive influence on both CO_2 conversion and energy efficiency. From the sensitivity analysis, it is found that the frequency has a weak effect on CO_2 decomposition; while discharge gap and discharge power play the most significant role in CO_2 conversion and energy efficiency, respectively. In addition, the introduction of the Al foil outer electrode and the screw-type inner electrode intensifies the microdischarges in the discharge volume, which can further enhance the CO_2 decomposition performance. The maximum CO_2 conversion of 27.2% is achieved at a SED of 120 kJ/l while the maximum energy efficiency of 10.4% is obtained at a SED of 24 kJ/l when the Al foil outer electrode and the screw-type inner electrode are utilised in the DBD reactor.

In the plasma-catalytic reaction, the combination of plasma with the $BaTiO_3$ and TiO_2 photocatalysts in the CO_2 DBD slightly increases the gas temperature of the plasma by 6-11 ^oC compared to the CO_2 discharge in the absence of a catalyst at a SED of 28 kJ/l. The plasma temperature in the gas phase is almost the same as the temperature on the surface of the photocatalysts ($BaTiO_3$ and TiO_2) in the plasma-catalytic DBD reactor. The combination of plasma with $BaTiO_3$ and TiO_2 catalysts

has resulted in a synergistic effect, which significantly enhances the conversion of CO_2 and energy efficiency by a factor of 2.5 compared to the plasma reaction in the absence of a catalyst. The presence of the catalyst pellets in the plasma gap is found to play a dominant role in inducing plasma physical effects, such as the enhancement of the electric field and production of more energetic electrons and reactive species, which in turn leads to chemical effects and contributes towards the conversion of CO_2. We find that the intensity of UV emissions generated in the CO_2 DBD is significantly lower than that emitted from external UV sources (e.g. UV lamps) that are commonly used to activate photocatalysts in conventional photocatalytic reactions. This phenomenon suggests that the UV emissions generated by the CO_2 DBD only play a minor role in the activation of the $BaTiO_3$ and TiO_2 catalysts in the plasma-photocatalytic conversion of CO_2, and its contribution to the achieved exceptional performance of this reaction and the synergy of plasma-photocatalysis could be very weak or negligible. In this study, the highly energetic electrons generated by plasma have been considered as the main driving force to activate the photocatalysts for CO_2 conversion. The overall synergistic effect resulting from the integration of DBD with photocatalysis for CO_2 conversion at low temperatures (without extra heating) can be attributed to both the physical effect induced by the presence of the catalyst in the discharge and the dominant photocatalytic surface reaction driven by energetic electrons from the CO_2 discharge.

CHAPTER FOUR CARBON DIOXIDE DECOMPOSITION IN A PACKED-BED DBD REACTOR

4.1 Introduction

Packed-bed DBD is another type of non-thermal plasma, which is constructed by inserting the dielectric pellets within the discharge volume inside the plasma reactor. The materials with different dielectric constants (e.g. glass, quartz, Al_2O_3, ceramic, ferroelectrics, etc.) can be used as the dielectric pellets. The enhanced local electric field can be achieved in the vicinity of the contact points between pellets and pellets/electrodes, which results in the generation of highly energetic electrons. This unique characteristic of the packed-bed DBD reactor enables it to have higher energy efficiency in the plasma process than that in the conventional non-thermal plasma reactor, which has been demonstrated in the plasma processes for ozone generation and pollutant removal [88]. The packed-bed DBD reactors have also been applied in the CO_2 decomposition process [131, 135, 226]. In these invetigations, the high permittivity of the dielectrics led to an increasing in the plasma power with very dense and strong microdischarges, which significantly enhances the conversion of CO_2. These findings suggest that the interactions between plasma and packing materials play an important role in the plasma conversion of CO_2. However, a fundamental understanding of the interaction between plasma and packing materials, from both a physical and chemical perspective, is still very patchy. In particular, the influence of packing materials on the physical characteristics (e.g. electric field, mean electron energy) of the discharge and consequent plasma chemical reactions is still not clear and has been paid less attention.

In this study, direct conversion of undiluted CO_2 into CO and O_2 is carried out in a cylindrical DBD reactor with and without packing at low temperatures. The effect of glass and $BaTiO_3$ beads on the physical characteristics of the discharge and chemical reaction performance is investigated to get a better understanding of plasma interactions with packing materials in CO_2 conversion.

4.2 Experimental Section

4.2.1 Experimental setup

The experiment is carried out in a packed-bed DBD reactor, as shown in **Figure 2.2** (b). A 6 cm long SS mesh is wrapped over a quartz tube with an external diameter of 25 mm and an inner diameter of 22 mm. A SS rod with an outer diameter of 16 mm is placed in the centre of the quartz tube and acted as an inner electrode. As a result, the discharge gap is 3 mm with a discharge volume *V* of 10.1 ml in the

absence of the packing material. Different packing materials ($BaTiO_3$ and glass beads) of 1 mm in diameter are fully packed into the discharge volume. In this case, the reactor can be considered as a typical packed-bed DBD system. For comparison, CO_2 conversion is also carried out in the DBD reactor with no packing. CO_2 is used as the feed gas without dilution and the flow rate is fixed at 50 ml/min. The experimental setup is the same as those in Section 3.3.

4.2.2 Parameter calculation

The equivalent electrical circuit model of the DBD reactor has been described in Section 2.3.1. The equivalent capacitance of the quartz tube C_d is 96.6 pF, calculated by Equation (2-2), where the relative dielectric constant of dielectric material ε is 3.7 for quartz tube. The detailed calculation for the capacitance of the gap C_{gap} in the discharge-off phase, the charge Q flowing through the DBD cell, the voltage on the dielectric materials U_d, the voltage across the gap U_{gap} and the breakdown voltage U_B can be found in Section 2.4.1. The peak-to-peak voltage ($Q_{pk\text{-}pk}$), charge discharged (Q_d) and charge transferred per half-cycle (Q_{trans}) can be obtained from the Lissajous figure, shown in **Figure 2.5** (b).

In the presence of packing pellets in the discharge gap, C_{gap} represents the capacitance of gas-solid integration in the gas gap; and U_{gap} is the sum of the voltage on the gas (U_g) and packing material (U_p). In this study, the beads are tightly packed into the discharge gap. The void fraction (α) of the DBD reactor in the presence of packing materials is defined as $1\text{-}V_p/V$ (V_p is the total volume of packing beads), which is about 0.283 for the fully packing of glass or $BaTiO_3$ beads into the DBD reactor. To understand the effect of packing materials on the physical characteristics of the discharge, a simplified model has been established to determine the voltage across the gas and solid, respectively. The region of solid beads and gas is equivalently considered as two parallel plate capacitors, as shown in **Figure 4.1**.

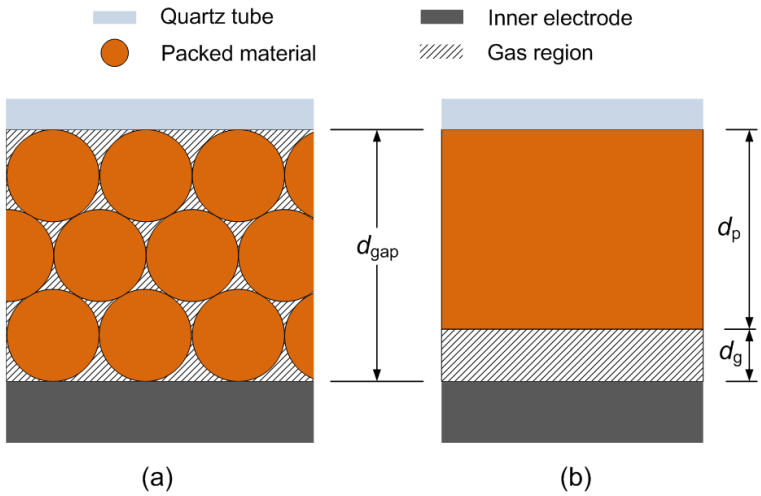

Figure 4.1 Simplified model for the determination of the gas gap.

The equivalent gap thicknesses in the gas (d_g) and solid (d_p) region are determined by Equations (4-1) and (4-2):

$$d_g = \frac{2V \times \alpha}{\pi (D+d) l} \tag{4-1}$$

$$d_p = d_{gap} - d_g \tag{4-2}$$

where D is the outer diameter of the inner electrode.

The equivalent capacitances of the gas (C_g) and solid (C_p) regions are calculated in the form of a parallel plate capacitor:

$$C_g = \frac{\varepsilon_g \cdot \varepsilon_0 \cdot S}{d_g} \tag{4-3}$$

$$C_p = \frac{\varepsilon_p \cdot \varepsilon_0 \cdot S}{d_p} \tag{4-4}$$

where ε_g is the relative dielectric constant of CO_2 (ε_g =1.6); ε_p is the relative dielectric constant of the packing materials (3.9 for glass bead and 10000 for $BaTiO_3$); S is the surface area of the outer electrode.

The gas voltage U_g can be obtained from the following equation:

$$U_g = \frac{Q}{C_g} = \frac{U_p \cdot C_p}{C_g} = \frac{(U_{gap} - U_g) \cdot C_p}{C_g} \tag{4-5}$$

By introducing Equations (4-3) and (4-4) into Equation (4-5), we obtain:

$$U_g = \frac{U_{gap}}{\frac{\varepsilon_g}{\varepsilon_p} \times \frac{d_p}{d_g} + 1} \tag{4-6}$$

To evaluate the performance of the plasma process, CO_2 conversion, CO yield and selectivity as well as the energy efficiency are defined in Section 2.4.3.

4.3 Experimental Results

4.3.1 Effect of different packing materials on discharge characteristics

Figure 4.2 presents the electrical signals of the CO_2 discharge with and without packing materials. In the discharge with no packing, a typical filamentary discharge can be clearly observed, which can also be confirmed by the numerous peaks in the current signal. In contrast, packing $BaTiO_3$ or glass beads into the entire discharge area generates a typical packed-bed effect and leads to a transition in the discharge behaviour from a filamentary discharge to a combination of surface discharge and filamentary discharge. The addition of $BaTiO_3$ or glass beads into the DBD reactor is found to significantly reduce the amplitude of the current peaks. In a packed-bed DBD reactor, filaments can only be generated in the small gap between the pellet-pellet and the pellet-quartz wall, while surface discharge can be formed on

the surface of pellets near contact points between pellets. Similar findings were reported in our previous works where fully packing Ni/Al_2O_3 or TiO_2 catalyst pellets into a DBD reactor significantly changes the discharge mode and inhibits the formation of filamentary discharges due the decrease of the discharge volume [107, 185]. However, intense filamentary discharges were still formed when quartz wool was placed in the discharge area due to the porosity of this material and strong interactions between the plasma and quartz wool [91].

Note that the gap voltage of the CO_2 discharge in the packed-bed DBD reactor is much lower than that of the discharge with no packing. The breakdown voltage (U_B) of the discharge significantly decreases from 3.43 kV without packing to 1.56 kV (packed with glass beads) and 1.03 kV (packed with $BaTiO_3$), respectively. This phenomenon can be ascribed to the reduced electrode gap and reduced pressure due to the packing of solid materials into the discharge gap. Such changes were also observed in previous studies where packing a series of materials (Ni/Al_2O_3, Al_2O_3, TiO_2, and zeolite 3A) into the discharge gap showed that the influence of dielectric constant of the packing materials on the reduction of breakdown voltage was weak [107, 156, 194].

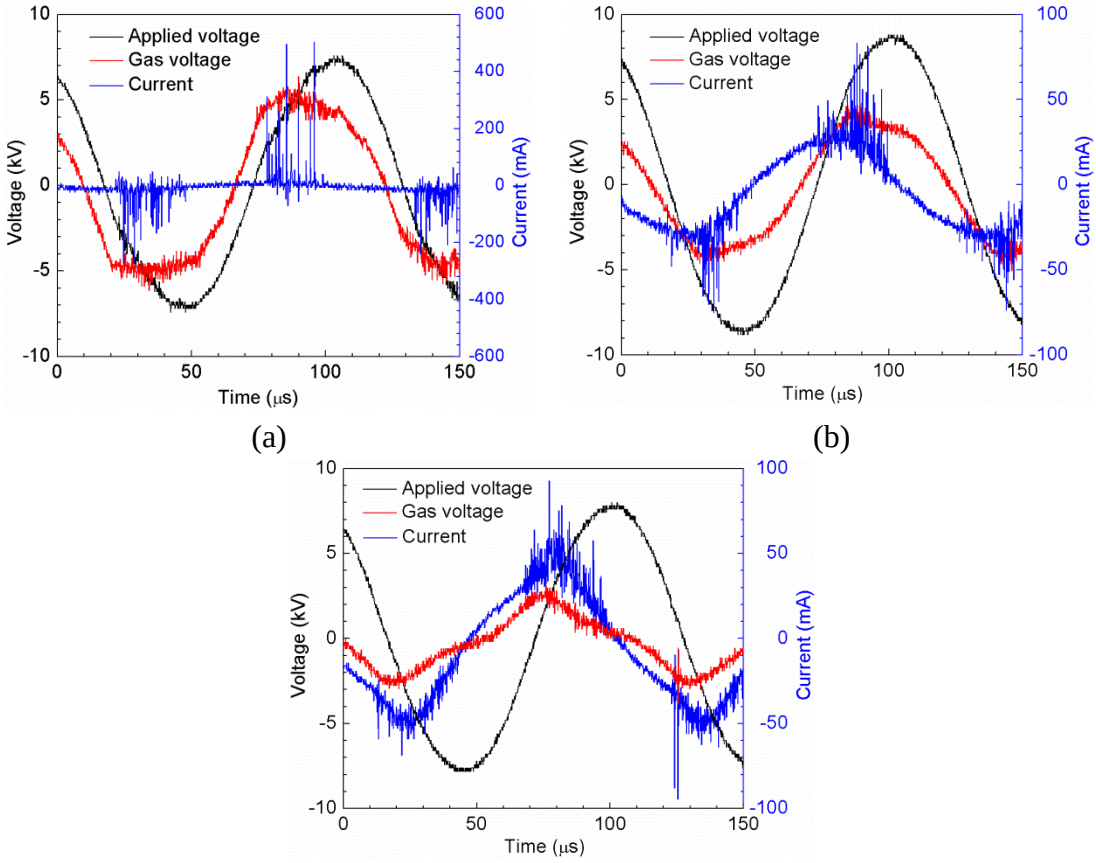

Figure 4.2 Electrical signals of the CO_2 DBD: (a) with no packing; (b) packed with glass beads; (c) packed with $BaTiO_3$ beads (discharge power: 40W; feed flow rate: 50 ml/min; frequency: 9 kHz).

Figure 4.3 shows the Lissajous figures of the CO_2 discharge with and without packing material at the same discharge power of 40 W. The shape of the Lissajous figure changes from parallelogram to oval shape when either $BaTiO_3$ or glass beads are fully packed in the DBD reactor. This also indicates the change in the discharge characteristics. At the same discharge power, the applied voltage of the DBD increases from 14.1 kV_{pk-pk} without packing to 15.3 kV_{pk-pk} with the $BaTiO_3$ packing and 16.9 kV_{pk-pk} with the glass beads packing, while the current in the discharge with no packing is much higher than that in the presence of packing beads, as shown in **Figure 4.2**.

In the discharge-off phase, the total equivalent capacitance of the DBD reactor with no packing is about 13.6 pF. Adding the glass or $BaTiO_3$ beads to the plasma system significantly increases the value of this parameter to 43.8 pF and 54.4 pF, respectively. Similarly, the gap capacitance is also increased from 14.5 pF without packing to 80.2 pF and 124.6 pF when the discharge gap is fully packed with the glass or $BaTiO_3$ beads.

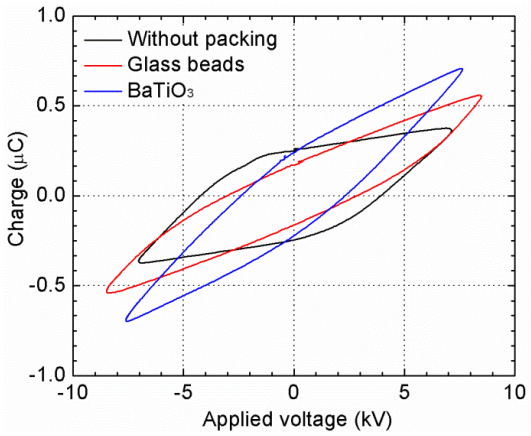

Figure 4.3 Lissajous figures of the CO_2 DBD without and with different packing materials at a constant discharge power of 40 W (feed flow rate: 50 ml/min; frequency: 9 kHz).

The influence of the packing solids on the effective capacitance of the DBD at different discharge powers is plotted in **Figure 4.4**. Increasing the discharge power or SED enhances the effective capacitance irrespective of the use of packing materials. For example, the effective capacitance of the discharge without packing increases from 25.5 pF to 58.6 pF when the discharge power varies from 20 W to 50 W. This can be clearly seen from the slope of the lines AB and CD in the Lissajous figure. In the discharge with no packing, the effective capacitance is much lower than the capacitance of the quartz tube (96.6 pF). This phenomenon might be caused by the incomplete formation of microdischarge in the whole discharge gap under the experimental conditions. Similar observation was reported in a CH_4/CO_2 DBD [107].

In addition, it is also suggested that C_{eff} depends on the spatial distribution of the discharge across the discharge gap over a half-period of the applied voltage. When the packing materials are placed in the reactor, the C_{eff} increases compared with that of the discharge with no packing. Interestingly, the maximum C_{eff} of 91.5 pF can be obtained when the $BaTiO_3$ beads are fully packed into the discharge gap at a discharge power of 50 W. This value is very close to the capacitance of the quartz tube. It is expected the effective capacitance should be equal to C_d for a fully bridged gap [37]. This can demonstrate that the presence of $BaTiO_3$ beads in the discharge leads to the expansion of the discharge across the gap, and might consequently affect the plasma chemical reactions.

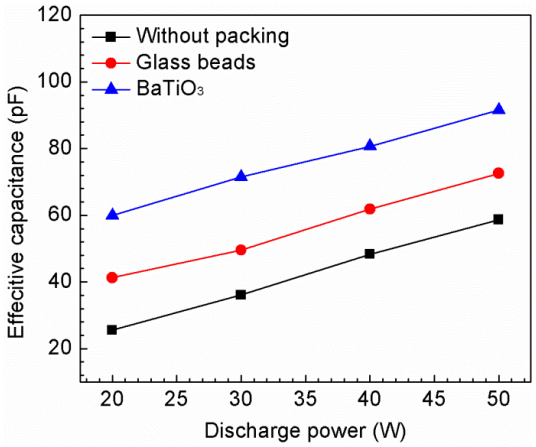

Figure 4.4 Effect of packing materials on the effective capacitance of the CO_2 discharge (feed flow rate: 50 ml/min; frequency: 9 kHz).

Figure 4.5 shows the influence of the packing materials on the charge characteristics of the CO_2 DBD at different discharge powers. It is found that the peak-to-peak charge increases with the increase in the discharge power. Both charge generated and transferred per half-cycle of the applied voltage also increase with the discharge power. Similar evolution was observed in previous studies where these charge parameters increased with the discharge power in a plasma methane reforming process [107]. The addition of the packing materials to the DBD reactor has a significant effect on the charge characteristics of the CO_2 discharge. Both packing materials are found to bridge the gap between the electrodes and enhance the charge transfer between them.

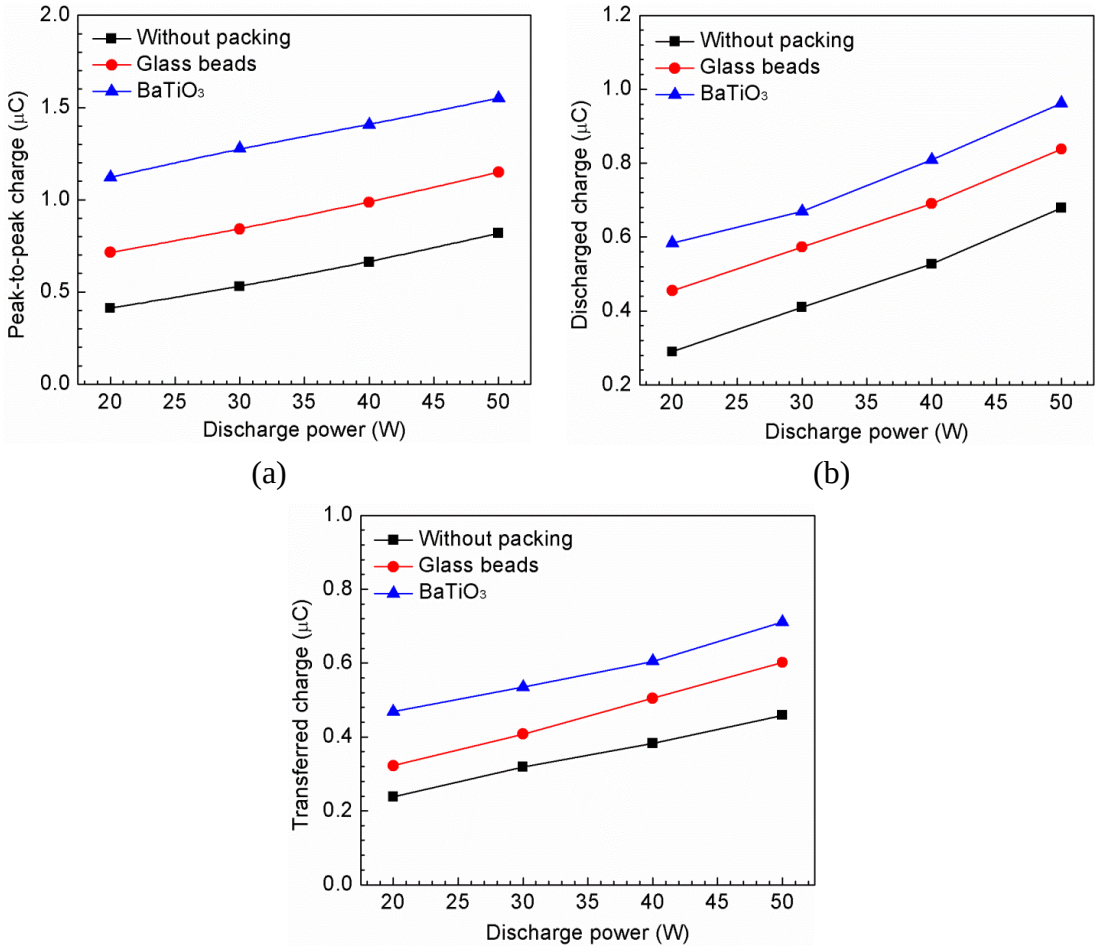

Figure 4.5 Effect of packing materials on the charge generation and transfer in the pure CO_2 DBD: (a) peak-to-peak charge; (b) charge generated per half-cycle; (c) charge transferred per half-cycle (feed flow rate: 50 ml/min; frequency: 9 kHz).

4.3.2 Effect of packing materials on electric field and electron energy

The effect of the packing materials on the average electric field strength of the discharge is shown in **Figure 4.6**. Clearly, the presence of the packing materials in the discharge significantly improves the average electric field strength. The material ($BaTiO_3$) with a higher dielectric constant has a more significant effect on the electric field of the discharge. For example, the average electric field strength (3.27 kV/mm) in the DBD reactor fully packed with the $BaTiO_3$ beads is almost doubled compared to that of the discharge with no packing (1.75 kV/mm) at the same discharge power of 40 W. A similar finding was reported in [206] where the presence of TiO_2 pellets in a nitrogen DBD led to a significant increase of the electric field. Previous experimental [202, 203] and simulation studies [204, 227] showed that packing solid pellets especially the pellets with a high dielectric constant (e.g. $BaTiO_3$) into the discharge gap significantly enhanced the local electric field strength near contact points between the pellets and the pellet - dielectric wall. The maximum

local electric field near these contact points can be 10 - 10^4 times higher than that in the void in a plasma-catalysis system, depending on the properties of the packing materials such as contact angle, shape and dielectric constant, while the averaged electric field in an argon plasma fully packed with packing pellets was increased by a factor of 1.4 with increasing the dielectric constant of the packing materials from 10 to 1000, above this the change in the electric field became negligible [88]. Our results also show that the electric field of the CO_2 discharge is not a function of dielectric constant when the packing materials with different constants (3.9 and 10000) are fully packed in the DBD reactor. **Figure 4.6** also presents the effect of the packing materials on the reduced electric field strength. Similarly, the presence of the glass or $BaTiO_3$ beads in the plasma system leads to a higher reduced electric field.

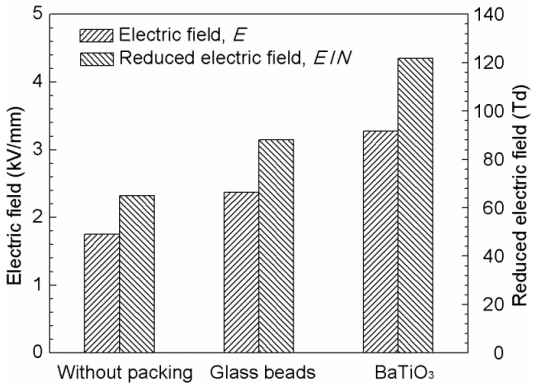

Figure 4.6 Effect of packing materials on the average electric field and reduced electric field strength (discharge power: 40 W; feed flow rate: 50 ml/min; frequency: 9 kHz).

The EEDF of the CO_2 discharge under our experimental conditions is calculated by BOLSIG+ [228]. **Figure 4.7** shows the effect of the packing solids on the mean electron energy of the discharge. Clearly, packing the $BaTiO_3$ pellets in the discharge gap almost results in an increase of 75.0% in the mean electron energy at the discharge power of 40 W, while the mean electron energy of the discharge with glass beads is increased by around 34.6%. In our previous study, we reported that the integration of plasma and TiO_2 strongly affected the electron energy distribution in a N_2 discharge with an increase in both highly energetic electrons and electric field strength [185]. These results suggest that the presence of solid pellets in the discharge gap play a crucial role in inducing physical effects, such as the enhancement of electric field and mean electron energy, which in turn produces more energetic electrons and chemically reactive species for plasma reactions and consequently contributes to the conversion of CO_2.

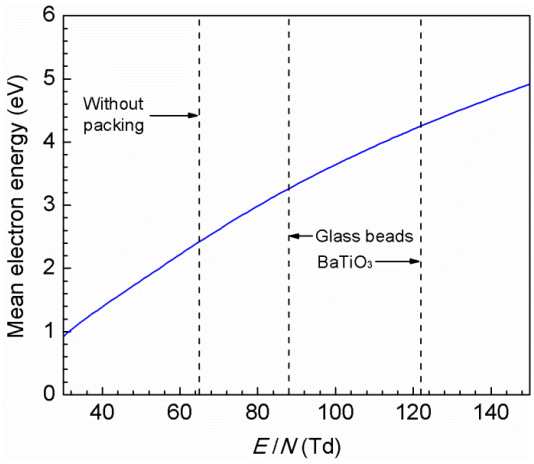

Figure 4.7 Effect of packing materials on the mean electron energy in the CO_2 DBD (discharge power: 40 W; feed flow rate: 50 ml/min; frequency: 9 kHz).

4.3.3 Effect of packing materials on CO_2 conversion

Plasma conversion of CO_2 is carried out in the DBD reactor with and without packing material. CO_2 conversion increases with the increase of the discharge power, as shown in **Figure 4.8**. The presence of the packing materials in the discharge gap makes the reactor more effective for CO_2 conversion, even though fully packing these packing beads into the discharge gap significantly decreases the residence time of CO_2 molecules in the discharge area from 12.9 s with no packing to 3.7 s with packing. It is worth noting that plasma-induced adsorption and desorption of CO_2 on the $BaTiO_3$ surface may prolong the retention time of CO_2 in the discharge and partly compensate the reduced of CO_2 residence time due to the decrease of the discharge volume. Compared to the plasma reaction with no packing, the addition of $BaTiO_3$ and glass beads to the plasma system increases the conversion of CO_2 by around 75.0% and 35.0%, respectively. It is found that the conversion of CO_2 is not a function of dielectric constant when the packing pellets with different dielectric constants are placed in the plasma reactor. The enhancement of CO_2 conversion is mainly attributed to the changes in the discharge characteristics, such as the increase of the average electric field and mean electron energy when solid pellets are packed into the discharge volume, as shown in **Figure 4.6** and **Figure 4.7**. However, with the $BaTiO_3$ packing, the contribution of plasma photocatalytic surface reaction to the enhancement of CO_2 conversion cannot be ruled out [208]. It is believed that plasma discharges can generate strong UV radiation without using extra UV sources (e.g. UV lamps) to activate photocatalysts such as $BaTiO_3$. Previous works reported that UV radiation generated by plasma discharges is not always the controlling factor to activate photocatalysts [50, 51]. In contrast, the electrons with a high energy (> 3.0 eV for $BaTiO_3$) generated by the CO_2 discharge can trigger electron impact activation of $BaTiO_3$ photocatalysts to form electron-hole pairs, as discussed in Chapter 3, which contributes to the enhanced conversion of CO_2.

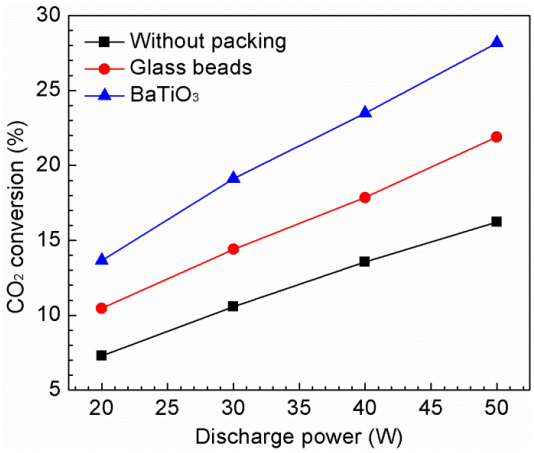

Figure 4.8 Effect of packing materials on CO_2 conversion (feed flow rate: 50 ml/min; frequency: 9 kHz).

Figure 4.9 shows the effect of the packing materials on the energy efficiency of the plasma processing of CO_2 as a function of the discharge power. The energy efficiency is defined as the ratio of the dissociation enthalpy of CO_2 and the energy for converting per unit CO_2 molecules (Equation (2-14)). Compared to the plasma reaction with no packing, the presence of $BaTiO_3$ and glass beads in the gas gap significantly enhances the energy efficiency of the plasma process. Packing the $BaTiO_3$ into the discharge leads to an increase in the energy efficiency of the process by 73.5% compared to the reaction with no packing at the same discharge power of 50 W. The maximum energy efficiency of 7.1% is achieved when the $BaTiO_3$ pellets are fully packed into the discharge volume at a discharge power of 20 W and a feed flow rate of 50 ml/min.

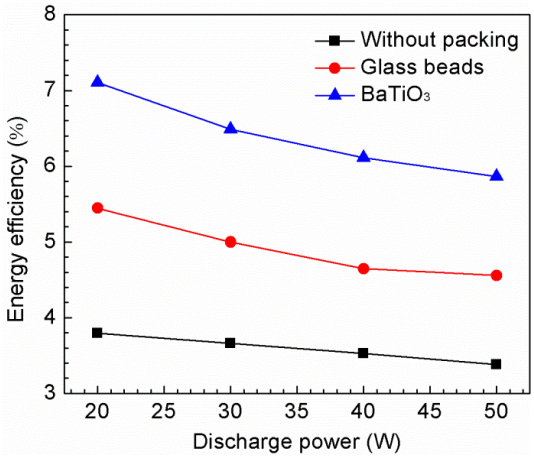

Figure 4.9 Effect of discharge power on energy efficiency (feed flow rate: 50 ml/min; frequency: 9 kHz).

The influence of the packing solids on CO selectivity and CO yield at different discharge powers is plotted in **Figure 4.10**. CO selectivity is almost independent of the discharge power and packing materials, while CO yield increases with the increase of the discharge power. The presence of the $BaTiO_3$ in the

discharge gap significantly enhances the yield of CO by 72.9%. The selectivity of CO based on carbon atom (Equation (2-12)) is close to 100%, which suggests that stoichiometric conversion of CO_2 to CO is achieved in this study. This can be confirmed by the linear relationship between the CO_2 conversion and CO yield (see **Figure 4.11**), which suggests that the production of CO mainly comes from the dissociation of CO_2. The electron impact dissociation of CO_2 will most likely result in CO in its ground state ($^1\Sigma$) and O atoms in both the ground state (^3P) and the metastable state (^1D). However, previous work reported that CO can also be formed in excited state since CO electronic bands were observed [91]. The stoichiometric conversion of CO_2 to CO can be further demonstrated by the fact that no carbon deposition and ozone are detected in the plasma reactions. In contrast, Horvath et al. found that CO and ozone were the main gas products in the decomposition of pure CO_2 by a corona discharge [122]. Mikoviny et al. reported that adding trace oxygen into pure CO_2 significantly increased the concentration of ozone and CO in the CO_2 splitting using a negative corona discharge reactor [120].

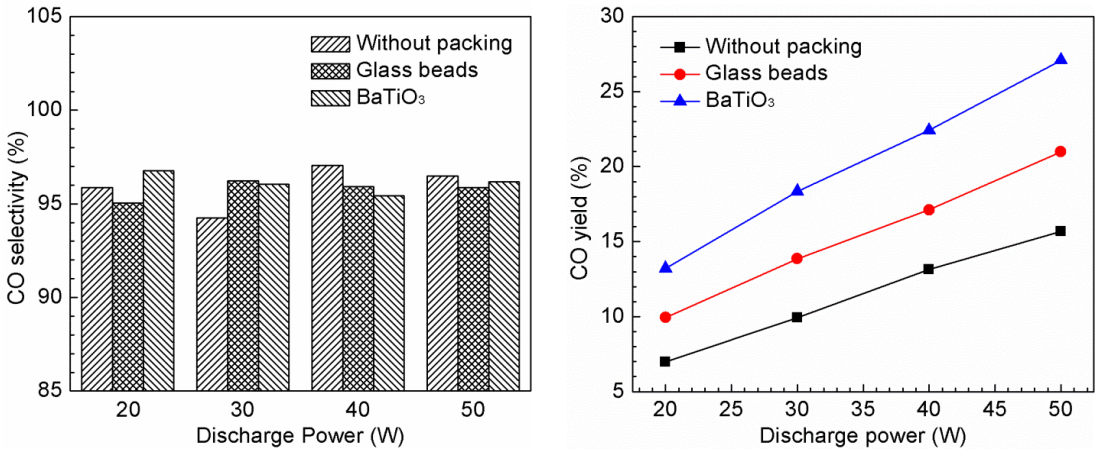

Figure 4.10 Effect of packing materials on (a) CO selectivity and (b) CO yield (feed flow rate: 50 ml/min; frequency: 9 kHz).

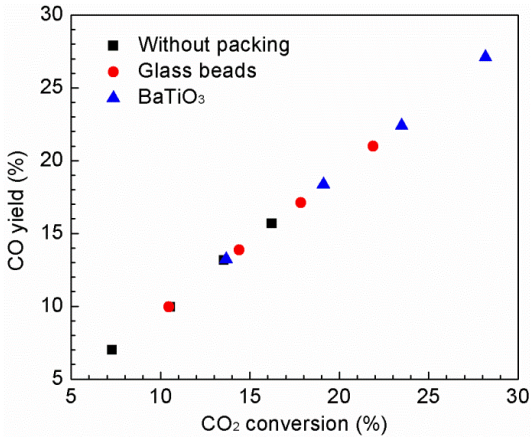

Figure 4.11 CO yield vs. CO_2 conversion (feed flow rate: 50 ml/min; frequency: 9 kHz).

4.3.4 Energy efficiency of the plasma process

Table 4.1 compares the CO_2 conversion and energy efficiency of the CO_2 decomposition process using different atmospheric plasma sources. It is worth noting that in each plasma reactor, the maximum CO_2 conversion and energy efficiency cannot be achieved simultaneously. In general, higher power and/or lower feed flow results in higher CO_2 conversion but lower energy efficiency, while higher energy efficiency can be obtained at lower power and/or higher feed flow rate but with lower CO_2 conversion. This phenomenon calls for the further optimisation of these processing parameters in the future investigation of the plasma-assisted CO_2 decomposition process. The energy efficiency of the plasma-assisted CO_2 decomposition process achieved in this work is higher than those obtained in the decomposition processes using similar DBDs regardless of the packing materials. The combination of the Al outer electrode and screw-type SS inner electrode are introduced into the atmospheric DBD reactor to improve CO_2 conversion and energy efficiency, and a maximum energy efficiency of 10.4% for the plasma decomposition process is achieved at a discharge power of 10 W and a feed flow rate of 50 ml/min. As shown in Table 4.1, a maximum energy efficiency of 19.3% was achieved when the pure CO_2 decomposition was performed in an AC gliding arc discharge at a feed flow rate of 1.31 l/min. However, the corresponding conversion of CO_2 in this process was only 15.1%, which is significantly lower than that (27.2%) obtained in this work at the condition without catalysts (Chapter 3). A balance between CO_2 conversion and energy efficiency in the plasma processing of CO_2 is significantly important for the development and deployment of an efficient and cost-effective plasma process for CO_2 conversion and utilisation [229].

In the DBD reactor, the dielectric layer placed between the electrodes is of significant importance in the discharge process. Arc formation during the discharge process is inhibited with the aid of the dielectric layer, and non-thermal and homogeneous plasma is generated. It has been reported that the dielectric materials with higher permittivity lead to an increase in the density of the energetic electrons and therefore the improvement in the reactivity of the DBD reactor. Li et al. used a series of $Ca_{0.7}Sr_{0.3}TiO_3$ as the dielectric materials in the DBD reactor for CO_2 decomposition [133, 226, 230]. Due to the high permittivity, much denser microdischarges characterised by the stronge current pulses are generated when the $Ca_{0.7}Sr_{0.3}TiO_3$ ceramic is applied, thereby leading to much higher CO_2 conversion than that with using alumina and silica glass. Similar studies are performed by Wang et al. [135], where $Ca_{0.8}Sr_{0.2}TiO_3$ added with $CaO\text{-}B_2O_3\text{-}SiO_2$ (CBS) glass was used as the dielectric material and a maximum CO_2 conversion of 48.7% was achieved with a CBS addition of 5%.

Table 4.1 Comparison of CO_2 conversion and energy efficiency of CO_2 decomposition process using different atmospheric plasma sources.

Plasma type	Feed gas (vol/vol)[a]	Power (W)	Total flow rate (ml/min)	Catalysts/ dielectric	CO_2 conversion (%)	η (%)	Ref
DBD Screw	Pure CO_2	50	25	-	27.2	2.8	Chapter 3
		10	25	-	20.0	10.4	
DBD	Pure CO_2	24	50	TiO_2	25.3	11.0	Chapter 3
		24	50	$BaTiO_3$	38.3	16.6	
Packed DBD	Pure CO_2	50	50	$BaTiO_3$	28.2	5.9	Chapter 4
		20	50		13.7	7.1	
DBD	Pure CO_2	40	10	-	33.8	1.9	[124]
		15	50	-	13.1	9.1	
DBD	Pure CO_2	200	50	-	30.0	1.6	[123]
		150	200	-	14.0	3.9	
Packed DBD	Pure CO_2	35	40	$CaTiO_3$	20.5	4.8	[131]
		22	40		15.8	6.1	
DBD	CO_2/Ar (3/197)	25	2000	-	9.5	2.3	[231]
		7.5	2000	-	6.5	5.3	
Packed DBD	CO_2/N_2 (1/9)	42	200	CST+ CBS[b]	48.7	4.8	[135]
Corona	Pure CO_2	40	30	-	10.9	1.7	[121]
		8	90	-	3.1	7.5	
GA	Pure CO_2	219	857	-	17.4	14.1	[127]
		229	1380	-	15.1	19.3	
Glow	CO_2/He (1/99)	0.506	40	Cu	21.2	3.5	[232]
	CO_2/He (1/24)	0.019	40		1.1	19.7	
Glow	CO_2/He (1/39)	2.85	30	Rh	30.5	1.7	[129]
		0.714	100		5.8	4.2	
Glow	CO_2/He (1/39)	8.21	30	Rh	36.4	0.8	[233]
		1.79	60	Pt	14.1	2.5	

[a] vol/vol: the feed flow rate ratio of CO_2 and the auxiliary gas in the feed gas;
[b] CST: $Ca_{0.8}Sr_{0.2}TiO_3$; CBS: CaO-B_2O_3-SiO_2.

For the packed-bed DBD reactor, it can significantly improve CO_2 conversion and energy efficiency due to the energetic electrons generated by the high electric field near the contact points between the packing pellets as well as between the packing pellets and the dielectric tube. This enhancement is closely related to the

relative permittivity of the packing pellets. The enhancement of CO_2 conversion performance in the packed-bed DBD reactor has been reported in the work of Yu et al. [131]. They reported that a maximum energy efficiency of 6.1% was obtained with a CO_2 conversion of 15.8% when $CaTiO_3$ was used as the packing material. In this work, a relative higher CO_2 conversion of 7.1% is obtained when $BaTiO_3$ is used as the packing pellets in this chapter.

Another advantage of DBD technology is its ability to be combined with other technologies such as heterogeneous catalysis, known as hybrid plasma-catalysis. Up to now, limited work related to the plasma catalysis CO_2 decomposition has been reported. Metal coated electrodes using Cu, Rh, Pt, Au and Pd were applied in the glow discharge for CO_2 decomposition [129, 232, 233]; a maximum CO_2 conversion of 36.4% was obtained with the Rh coated electrode [233]. But these metal coated electrodes were used in the highly diluted CO_2 by He, Ar or N_2, their feasibility in the treatment of gas stream with large amount of CO_2 has not been reported yet. Moreover, the utilisation of inert gases as dilution is not favourable for industrial applications due to the cost of these gases, especially for He.

In Chapter 3, the integration of plasma and photocatalysts ($BaTiO_3$ and TiO_2) shows a synergistic effect in the reduction of CO_2 into CO and oxygen, which significantly enhances the conversion of CO_2 and the energy efficiency of the process, as well as a balance between them. An energy efficiency (16.6%) of the plasma CO_2 conversion in the presence of $BaTiO_3$ (Chapter 3), increased by up to 250% compared to that obtained in the plasma-only condition, is much higher than most of the other plasma processes regardless of the catalyst used. It is also interesting to note that the energy efficiency obtained in the plasma-catalytic process using $BaTiO_3$ as photocatalyst is much higher than that of similar chemical reactions using a conventional packed-bed DBD reactor where materials and/or catalysts are fully packed into the discharge gap [178]. Previous works have demonstrated that packing catalysts into the entire discharge zone led to a strong packed-bed effect and was found to shift the discharge mode from a typical strong filamentary microdischarge across the gap to a combination of surface discharge and weak microdischarge due to a significant reduction in the discharge volume [91, 107, 156]. As a result, only limited surface discharge can be generated on part of the catalyst surface and spatially limited microdischarges generated in the void space between pellet-pellet and pellet-quartz wall [107, 203]. The formation of strong filamentary discharges in a DBD reactor without a catalyst is strongly suppressed when the solid catalysts are fully packed into the discharge gap. It is well known that a packed-bed effect can enhance the electric field in the plasma, which contributes to the enhancement of the reaction performance to some extent. This phenomenon has also been observed in our CO_2 decomposition experiments in the fully packed-bed DBD reactor in this chapter. However, such a significant transition in behaviour of the

discharge mode induced by the strong packed-bed effect (fully packed) could substantially reduce the performance of plasma-catalytic conversion or reforming processes for energy and fuel production, as catalysts placed in the plasma area cannot be fully interacted and activated by the spatially limited discharges and weak interactions between the plasma and catalyst [91, 107]. This may be one of reasons for the phenomenon that CO_2 conversion and energy efficiency in the fully packed DBD reactor (Chapter 4) are lower than those obtained in the DBD reactor partially packed with the same photocatalyst $BaTiO_3$ (Chapter 3). It has been reported that how to pack catalysts in a DBD reactor is of primary importance to induce strong physical and chemical interactions between the plasma and catalyst, which consequently affects the generation of the synergistic effect of the plasma-catalytic reaction, especially for the conversion of undiluted reactants to valuable fuels and chemicals [91].

One may argue that as packed-bed DBD reactors have been demonstrated to be effective at removing a wide range of low concentration (10-1000 ppm) environmental gas pollutants [88], they could also be beneficial in the conversion of undiluted reactants. However, the major reaction mechanisms involved in the removal of dilute and low concentration gas pollutants and in the conversion of undiluted reactants (e.g. CO_2 or a mixture of CO_2 and CH_4) are significantly different due to different concentrations of reactants in the plasma chemical reactions. In the former reactions, highly energetic electrons mainly collide with carrier gas (e.g. air) to generate chemically reactive species (e.g. O, O_3, OH and N_2 (A)), which play dominant roles in the stepwise decomposition and oxidation of low concentration (ppm level) pollutants into CO, CO_2, H_2O and other by-products [234]. In contrast, electron impact reactions with reactants (e.g. CO_2) make significant contributions to the conversion of undiluted reactants in the latter reactions as carrier gases (e.g. N_2 and Ar) are not preferable. The transition behaviour of the discharge mode resulting in weak interactions of plasma and catalyst induced by the packed-bed effect might not be so important in the former reactions since the increased electric field in the packed-bed DBD reactor might be sufficient to produce reactive species for the removal of pollutants of ppm level. In addition, even a catalyst support (e.g. γ-Al_2O_3 and SiO_2) placed in a packed-bed DBD reactor could absorb or decompose some gas pollutants of low concentration [235, 236], leading us to think that the negative effect caused by the weak interaction between the plasma and packing catalysts (or supports) might be insignificant in the removal of dilute gas pollutants.

Compared with the thermal catalytic CO_2 decomposition, CO_2 conversion obtained in the DBD reactor is rather lower and there is still much room for improvement [37]. Considering the heterogeneous catalysts used in the thermal catalytic decomposition of CO_2, series of ferrite catalysts MFe_2O_4 (M = Ni, Cu, Co and Zn) and iron oxides were widely used [38, 237-239]. The oxygen-deficient sites

on these catalysts are the major contributor to the high performance of CO_2 decomposition. This mechanism for CO_2 decomposition on oxygen-deficient sites of the catalyst is much similar with that on the plasma-photocatalytic CO_2 decomposition, as discussed in Chapter 3. It is therefore expected that exploration and development of the catalysts with high redox ability and low-temperature activity, which can be activated in the non-thermal plasma reactor, can further enhance CO_2 conversion and energy efficiency in the plasma-assisted CO_2 decomposition. Additionally, previous simulation work has suggested that the energy efficiency of a plasma reactor can be enhanced by a factor of 4 when using rectangular pulses instead of a sinusoidal voltage [240]. Further improvement in the energy efficiency of this process can also be expected from the optimisation of the plasma power.

4.4 Conclusions

Plasma-assisted conversion of undiluted CO_2 into CO and O_2 has been carried out in a cylindrical DBD reactor with and without packing materials. The influence of the packing materials ($BaTiO_3$ and glass beads) on the CO_2 discharge characteristics and CO_2 conversion has been investigated. The presence of $BaTiO_3$ and glass beads in the DBD reactor changes the discharge behaviour and shows a transition from a typical filamentary discharge with no packing to a combination of filamentary discharge and surface discharge at the same discharge power. The addition of $BaTiO_3$ into the plasma system significantly enhances the average electric field and mean electron energy by 86.9% and 75.0%, respectively, which also affects the plasma chemical reactions. The use of packing materials ($BaTiO_3$ and glass beads) in the discharge gap is found to make the DBD reactor more effective for CO_2 conversion even though the residence time of CO_2 in the discharge is reduced due to the decrease of the discharge volume at the same gas flow rate. Compared to the plasma CO_2 conversion with no packing, the presence of $BaTiO_3$ beads in the DBD reactor significantly increases the conversion of CO_2 by 75 %. These results indicate that the change of the discharge properties (e.g. electric field and mean electron energy) significantly enhances CO_2 conversion, CO yield and energy efficiency of the plasma process. In addition, highly energetic electrons (> 3.0 eV) generated by the discharge could activate photocatalyst ($BaTiO_3$) to form electron-hole pairs on the surface of $BaTiO_3$, which also contributes to the enhanced conversion of CO_2.

From the comparison of the CO_2 decomposition performance in different plasma reactors and in the conventional thermal-catalytic reactors, the development of the catalyst with high redox ability and low-temperature activity would favour the enhancement of CO_2 conversion and energy efficiency in the plasma-assisted CO_2 decomposition process.

CHAPTER FIVE DRY REFORMING OF METHANE IN A COAXIAL DBD REATOR WITHOUT CATALYST

5.1 Introduction

Aside from CO_2, CH_4 is the second major greenhouse gas, and its global warming potential (GWP) is approximately 25 times higher than that of CO_2 although its concentration in the atmosphere is lower [241, 242]. The conversion of CO_2 with CH_4 (dry reforming of CH_4) for the generation of synthesis gas (syngas) has attracted significant interest as this reaction uses two major greenhouse gases simultaneously. This process generates syngas with a H_2/CO molar ratio of ~ 1:1, which is preferable for the further synthesis of long-chain hydrocarbons or oxygenated hydrocarbons. Moreover, this reaction can be carried out using feedstock in the form of natural gas, biogas or shale gas with differing amounts of CO_2, which maximises the energy utilisation and minimises the negative environmental impact. However, dry reforming of CH_4 using conventional catalytic methods still faces two major challenges that limits the use of this process on a commercial scale: firstly, high reaction temperatures (> 700 ℃) are required to obtain reasonable conversions of reactants and yields of syngas, since this is a highly endothermic reaction and both reactants (CO_2 and CH_4) are very stable molecules, which incurs high energy cost; secondly, the formation of carbon deposition on the catalyst surface results in rapid deactivation of the catalyst, especially for the transition metal catalyst [91, 166].

Non-thermal plasma is considered as an attractive alternative for converting greenhouse gases (CO_2 and CH_4) into syngas and other value-added chemicals, as it can be carried out at atmospheric pressure and low temperatures, resulting from its non-equilibrium characteristics. In this thesis, the plasma dry reforming of CH_4 will be performed in a coaxial DBD reactor with and without a catalyst.

In this chapter, the thermodynamic equilibrium calculation for dry reforming of CH_4 is firstly carried out, in which the effects of operating temperature and CO_2/CH_4 molar ratio in the feed gas are taken into consideration. Secondly, dry reforming of CH_4 in the plasma-only process are performed to investigate the effects of discharge power, total feed flow rate and CO_2/CH_4 molar ratio on the performance of the plasma process. The results presented in this chapter will be compared with the plasma-catalytic dry reforming reaction in the following chapters.

5.2 Thermodynamic Equilibrium Calculation for Dry Reforming of CH_4

5.2.1 Thermodynamic equilibrium calculation method

The thermodynamic equilibrium calculation for dry reforming of CH_4 is carried out using the Gibbs free energy minimisation-based method in a closed system. The main reactions which may occur in the dry reforming process are listed in Equations (5-1) to (5-7) [191, 192]. Dry reforming of CH_4 (Equation (5-1)) is an intensively endothermic reaction, which consumes a large amount of energy. In addition, the occurrence of side reactions (Equations (5-2) to (5-7)) lowers the conversion of reactants and the yields of products.

$$CH_4 + CO_2 \rightarrow 2H_2 + 2CO \qquad \Delta H^0_{298K} = 247\ \text{kJ/mol} \qquad (5\text{-}1)$$

$$CO_2 + H_2 \rightarrow CO + H_2O \qquad \Delta H^0_{298K} = 41\ \text{kJ/mol} \qquad (5\text{-}2)$$

$$CH_4 + H_2O \rightarrow CO + 3H_2 \qquad \Delta H^0_{298K} = 206\ \text{kJ/mol} \qquad (5\text{-}3)$$

$$CH_4 + 2H_2O \rightarrow CO_2 + 4H_2 \qquad \Delta H^0_{298K} = 165\ \text{kJ/mol} \qquad (5\text{-}4)$$

$$CO + H_2O \rightarrow CO_2 + H_2 \qquad \Delta H^0_{298K} = -41\ \text{kJ/mol} \qquad (5\text{-}5)$$

$$CO_2 + 4H_2 \rightarrow CH_4 + 2H_2O \qquad \Delta H^0_{298K} = -165\ \text{kJ/mol} \qquad (5\text{-}6)$$

$$CO + 3H_2 \rightarrow CH_4 + H_2O \qquad \Delta H^0_{298K} = -206\ \text{kJ/mol} \qquad (5\text{-}7)$$

The calculation results are reported in terms of the thermodynamic equilibrium amount of each species as well as the conversion of the reactants (CO_2 and CH_4). The definitions of the conversion of reactants have been provided in Section 2.4.3.

5.2.2 Thermodynamic equilibrium calculation results

5.2.2.1 Effect of operating temperature

Figure 5.1 shows the thermodynamic equilibrium calculation results for dry reforming of CH_4 at 1 atm. The major products from the dry reforming process are CO, H_2 and H_2O with a trace of C_2 hydrocarbons, methanol and dimethoxyethane (DME). Due to their small amount, C_2 hydrocarbons, methanol and DME are not considered in the calculation. The performance of dry reforming of CH_4 process is strongly dependent on the temperature, since it is an intensively endothermic reaction. Clearly, the reforming reaction starts to take place only when the temperature is higher than 600 K. The amounts of produced CO and H_2 increase sharply as the temperature is increased up to 1000 K. Afterward, the amount of these two produced gases rises smoothly before reaching a constant value. From the Equation (5-1), it is expected that an equal conversion of CO_2 and CH_4 with a unity H_2/CO molar ratio

would be obtained. However, CO_2 conversion is higher than that of CH_4 in the equilibrium system, and more CO is produced. A small amount of water can be seen to form in the higher temperature range, with its value peaking at 900 K; this phenomenon indicates that the unfavourable reactions involving water formation have a pronounced influence on both reactant conversions and product yields.

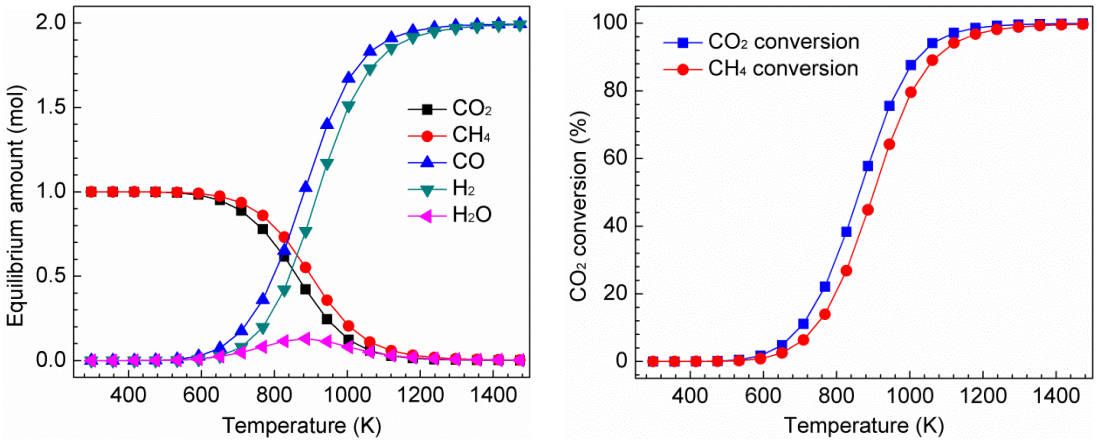

(a) (b)

Figure 5.1 Thermodynamic equilibrium calculation for dry reforming of CH_4 as a function of operating temperature at 1 atm (a) gas composition; (b) reactant conversions (total feed gas: 2 mol, CO_2/CH_4: 1:1).

5.2.2.3 Effect of CO_2/CH_4 molar ratio

The effect of the CO_2/CH_4 molar ratio on the conversion of CO_2 and CH_4 at 1 atm is presented in **Figure 5.2**. We can see that a lower CO_2/CH_4 molar ratio is beneficial to CO_2 conversion, whilst a higher CO_2/CH_4 molar ratio is preferred for a higher CH_4 conversion. This phenomenon indicates that CO_2 as a weak oxidant has a positive effect on CH_4 conversion; adding more CO_2 into the reaction system will

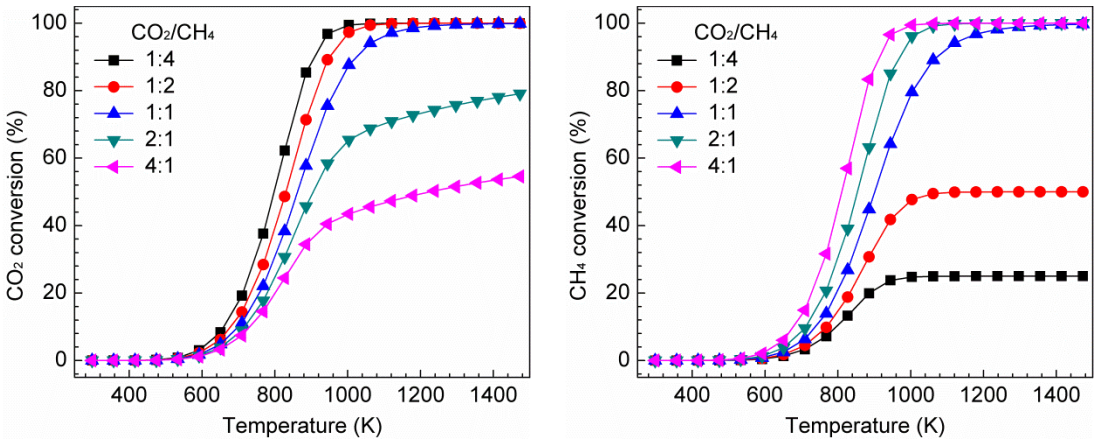

(a) (b)

Figure 5.2 Effect of CO_2/CH_4 molar ratio on the thermodynamic equilibrium conversion of (a) CO_2 and (b) CH_4 (total feed gas: 2 mol, pressure: 1 atm).

enhance the activity of CH_4 and lead to higher CH_4 conversion. When the CO_2/CH_4 molar ratio is lower than 1:1, CO_2 is the limiting reactant and will be consumed to the maximum extent within the investigated temperature range, but CH_4 cannot be converted completely. Therefore, CO_2 conversion is nearly 100% at higher temperature (e.g. 1023 to 1473 K) with a CO_2/CH_4 molar ratio of lower than 1:1. Conversely, the conversion of CO_2 will be limited when CO_2/CH_4 molar ratio is higher than 1:1, as CH_4 plays the role of the limiting reactant in such conditions.

Figure 5.3 depicts the thermodynamic equilibrium mole number of CO, H_2 and H_2O at different CO_2/CH_4 molar ratios. When the CO_2/CH_4 molar ratio is less than 1:1, increasing CO_2/CH_4 molar ratio enhances the thermodynamic equilibrium mole number of CO. As mentioned above, CO_2 is the limiting reactant at this condition; any incremental addition of CO_2 would be largely consumed, leading to a higher equilibrium mole number of CO. However, when the CO_2/CH_4 molar ratio is larger than 1:1, CH_4 becomes the limiting reactant; addition of CO_2 inhibits the conversion of CO_2, resulting in a decline in the equilibrium mole number of CO. Similarly, the CO_2/CH_4 molar ratio exhibits a positive impact on H_2 yield with a ratio lower than 1:1 and a negative impact with a ratio higher than 1:1. Contrary to the increasing trend in the equilibrium mole number of CO versus temperature (> 885 K) at a specified CO_2/CH_4 molar ratio (> 1:1), H_2 yield is suppressed due to the RWGS reaction, in which H_2 is consumed by reacting with CO_2 to produce CO and H_2O. This can be confirmed by the reliance of the equilibrium mole number of H_2O on temperatures when the CO_2/CH_4 molar ratio is higher than 1:1 (see **Figure 5.3** (c)).

5.3 Dry Reforming of CH_4 in a Coaxial DBD Reactor without Catalyst

5.3.1 Experimental section

The experiments are performed in a coaxial DBD reactor, as shown in **Figure 2.2** (a). A 10 cm long SS mesh is wrapped over a quartz tube with an external diameter of 25 mm and an inner diameter of 22 mm. A SS rod with an outer diameter of 17 mm is placed in the centre of the quartz tube and acts as an inner electrode. As a result, the discharge gap is 2.5 mm with a discharge volume (V) of 15.3 ml. The power supply (including the calculation of discharge power) and gas analysis methods are the same as those in Section 3.3.1.1. CO_2 and CH_4 are used as the feed gas.

To evaluate the performance of the plasma process, the reactant conversions, product yields and selectivities as well as the EC and FPE have been defined in Section 2.3.3.

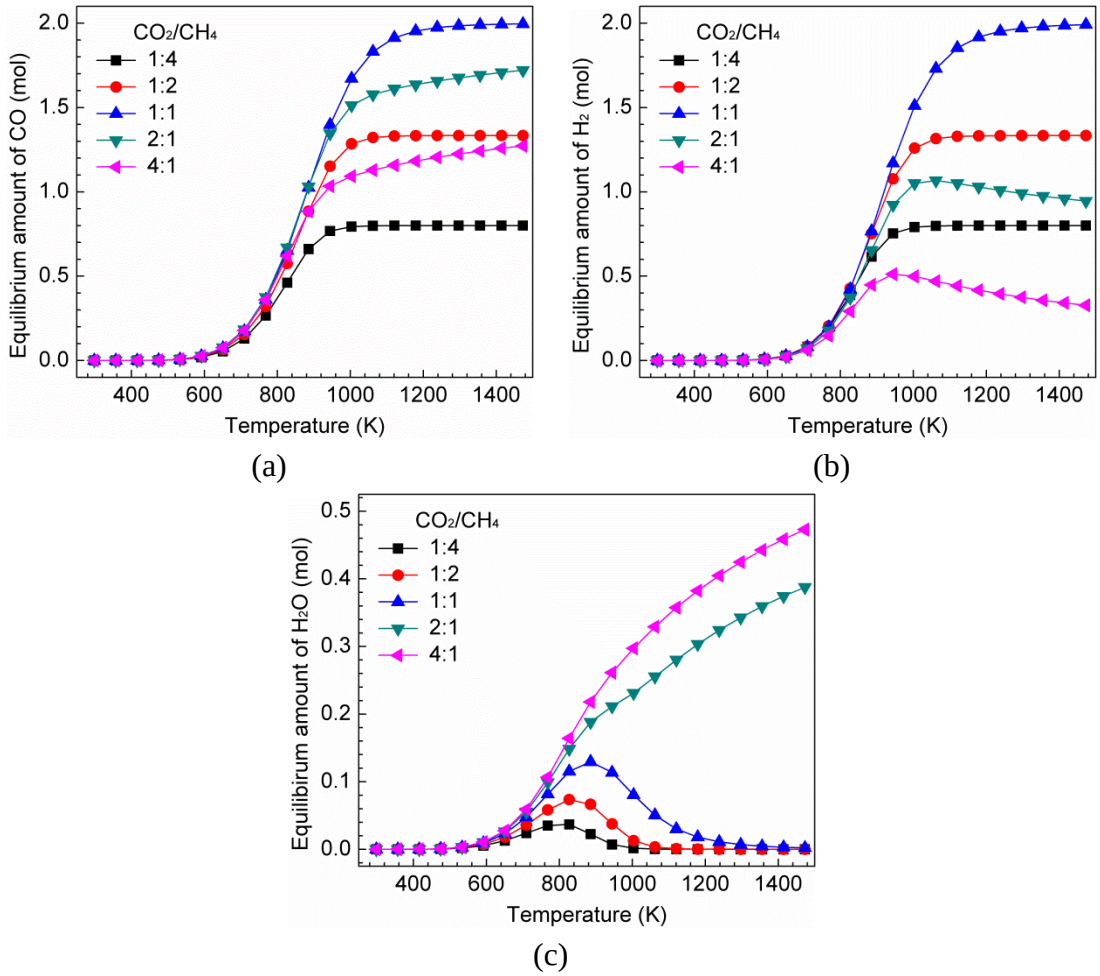

Figure 5.3 Effect of CO_2/CH_4 molar ratio on the thermodynamic equilibrium mole number of (a) CO, (b) H_2 and (c) H_2O (total feed gas: 2 mol, pressure: 1 atm).

5.3.2 Experimental results

5.3.2.1 Effect of discharge power

The influence of discharge power on the performance of plasma dry reforming of CH_4 is displayed in **Figure 5.4**. Both CO_2 and CH_4 conversion increases with increasing discharge power. The conversions of CO_2 and CH_4 increase up to 23.8% and 41.8%, respectively, at a discharge power of 60 W. Similar results have been reported in previous studies [91, 243]. In this study, the discharge power is changed by adjusting the applied voltage at a fixed frequency. As discussed in Section 3.3.2.2, increasing the discharge power by only changing the applied voltage results in the increase in the number of microdischarges and the current intensity in the DBD reactor, which indicates that more reaction channels and electrons are formed to activate and convert the reactant molecules; both of these two factors contribute to the enhancement in the conversion of CO_2 and CH_4.

The conversion of CO_2 is always lower than that of CH_4 under our experimental conditions. This phenomenon is different from that in the conventional

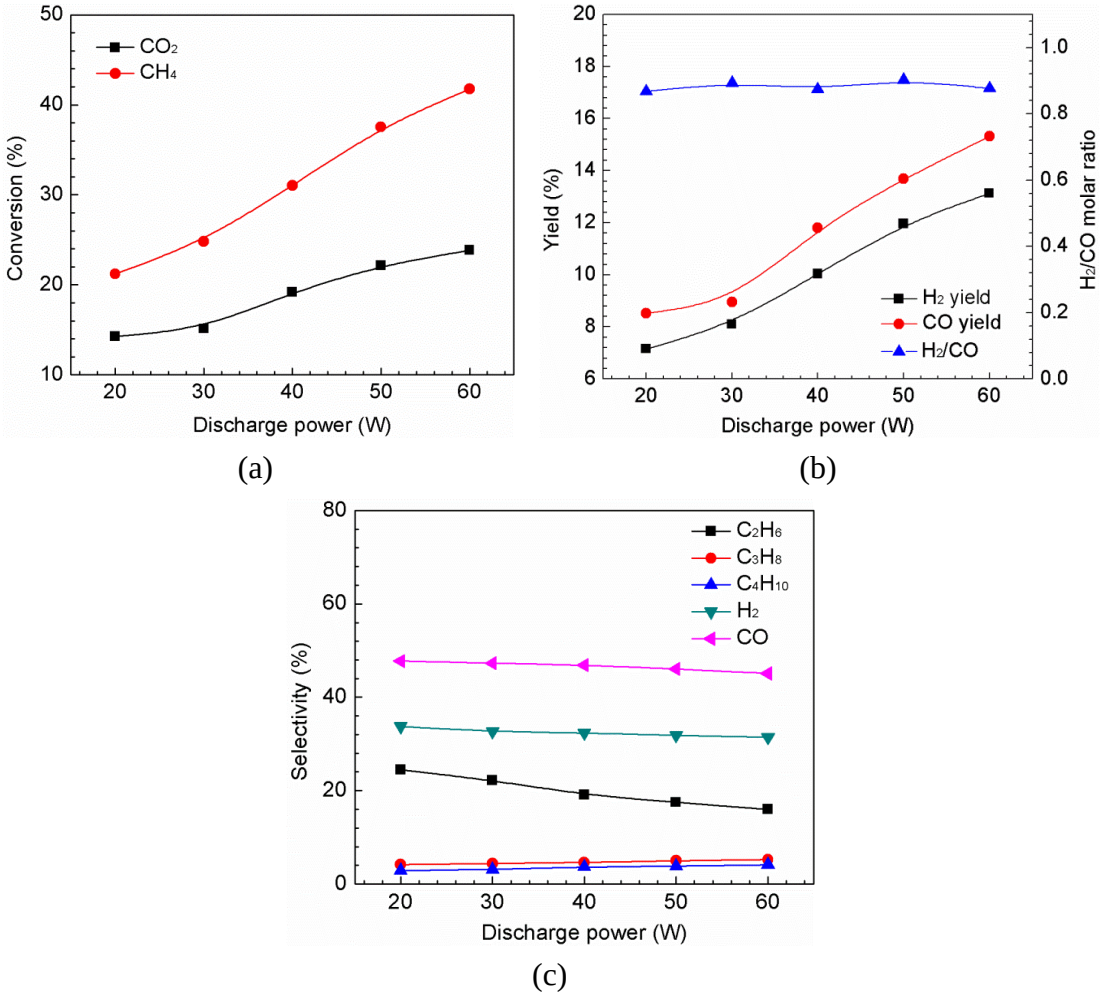

Figure 5.4 Effect of discharge power on the performance of plasma dry reforming reaction without catalyst: (a) conversion of CO_2 and CH_4; (b) yield of CO and H_2 and H_2/CO molar ratio; (c) selectivities of syngas and C_2-C_4 hydrocarbons (total feed flow rate: 50 ml/min; CO_2/CH_4: 1:1).

thermal catalytic dry reforming of CH_4, in which the conversion of CH_4 is usually lower than that of CO_2 due to the occurrence of the RWGS reaction, as shown in Equation (5-2). This higher conversion of CO_2 is also observed in our thermodynamic equilibrium calculation. These results indicate that CO_2 and CH_4 conversions occur through different pathways in the conventional thermal catalytic and plasma-assisted processes. Pyrolysis of the gas molecules is dominant in the thermal dry reforming process, whilst reactions of electrons, radicals and excited species play important roles in the plasma process [41]. More specifically, in the plasma dry reforming of CH_4, the initial reaction steps for the conversion of CO_2 and CH_4 are mainly driven by electron-impact dissociation (Equations (5-8) and (5-9)). Moreover, more reaction pathways exist for CH_4 conversion to generate CH_3, CH_2 and CH (Equations (5-9) to (5-11)), followed by the radical recombination reactions to form higher hydrocarbons or further electron-impact dissociation of radicals.

$$CO_2 + e \rightarrow CO + O + e \quad (5\text{-}8)$$

$$CH_4 + e \rightarrow CH_3 + H + e \quad (5\text{-}9)$$

$$CH_4 + e \rightarrow CH_2 + H_2 + e \quad (5\text{-}10)$$

$$CH_4 + e \rightarrow CH + H + H_2 + e \quad (5\text{-}11)$$

CO_2 and CH_4 can promote the conversion of each other when they are co-fed to the plasma reactor, compared to the decomposition of pure CO_2 or CH_4 [44]. The excited atomic oxygen species from the dissociation of CO_2 can easily break C-H bond in CH_4 as shown in Equation (5-12), while hydrogen atoms from CH_4 dissociation can facilitate the conversion of CO_2 according to Equation (5-13). However, the rate coefficient of Equation (5-12) is several orders of magnitude higher than that of Equation (5-13) in the temperature range of 300-2500 K [44]. This may be one of the reasons for the less pronounced CO_2 conversion compared to that of CH_4 in the plasma dry reforming of CH_4.

$$CH_4 + O \rightarrow CH_3 + OH,\ k = 8.75\times10^{-12} \times (T/298)^{1.5} \exp(-4330/T)\ [44] \quad (5\text{-}12)$$

$$CO_2 + H \rightarrow OH + CO,\ k = 2.5\times10^{-10} \exp(-13300/T)\ [44] \quad (5\text{-}13)$$

In addition, recent simulation has shown that the following reaction plays a dominant role in the production of CO_2 in the plasma dry reforming reaction in a DBD reactor, leading to a lower CO_2 conversion [244].

$$CO_2^+ + CH_4 \rightarrow CH_4^+ + CO_2 \quad (5\text{-}14)$$

The plasma dry reforming processes are performed without extra heating. When the discharge power increases from 20 W to 60 W, the temperature inside the reactor in the plasma-only process is increased from 150 ^oC to 225 ^oC. From the thermodynamic equilibrium calculations in the above section, the equilibrium conversion of CO_2 and CH_4 under such temperature (150 ~ 225 ^oC) is very low (<1%). This phenomenon demonstrates that the DBD plasma can induce the dry reforming reaction at lower temperature.

Figure 5.4 also shows that increasing the discharge power results in an increase in the yield of CO and H_2 but slightly decreases their selectivity. At a higher discharge power of 60 W, the maximum yield of CO and H_2 is 15.3% and 13.1%, respectively. However, discharge power has weak influence on the H_2/CO ratio, which only changes between 0.87 and 0.90 in the discharge power range of 20-60 W.

Noticeably, increasing the discharge power significantly decreases the selectivity of C_2H_6. Previous simulation has shown that the reaction (Equation (5-9)) is responsible for 79% of the total electron impact dissociation of CH_4 [245], which generates CH_3 as the main radical. C_2H_6 is mainly formed from the recombination of CH_3 radicals through the neutral-neutral reaction, shown in Equation (5-15). Meanwhile, C_2H_6 can be consumed by the reactions with CH radicals to form C_3 hydrocarbons, electron ionisation to form $C_2H_4^+$, and/or dissociation to form C_2H_4 or

C_2H_5 [246]. The produced radicals favour the formation of other hydrocarbons, such as C_3H_8 and C_4H_{10} from the neutral-neutral reaction (Equations (5-16) and (5-17)). This suggests that increasing the discharge power results in the decomposition of C_2H_6 to form other hydrocarbons, confirmed by the slight increase in the selectivity of C_3H_8 and C_4H_{10} (see **Figure 5.4** (c)).

$$CH_3 + CH_3 \rightarrow C_2H_6 \quad (5\text{-}15)$$

$$C_2H_5 + CH_3 \rightarrow C_3H_8 \quad (5\text{-}16)$$

$$C_2H_5 + C_2H_5 \rightarrow C_4H_{10} \quad (5\text{-}17)$$

Figure 5.5 shows the effect of the discharge power on the EC and FPE of the plasma dry reforming process. Clearly, increasing the discharge power increases EC for both reactant conversion and gas production. Although the mole numbers of converted CO_2 and CH_4, as well as the mole numbers of generated CO and H_2, are

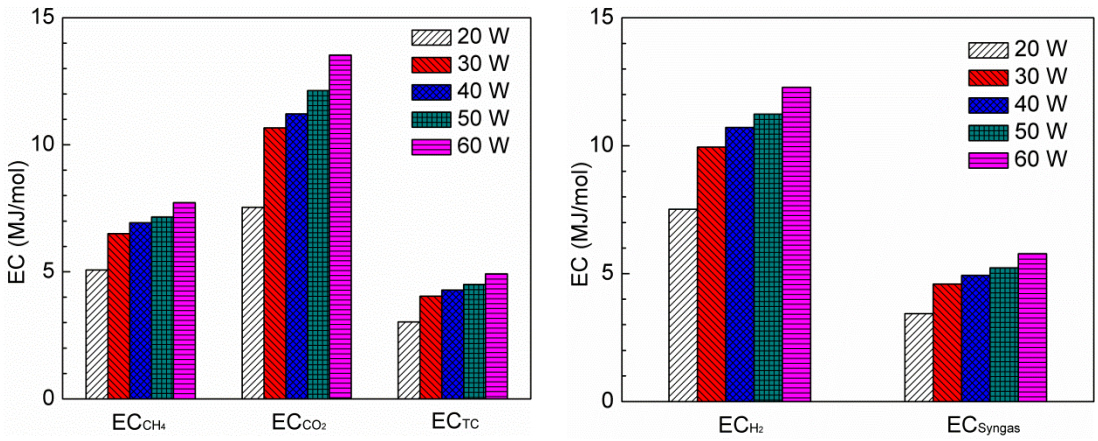

Figure 5.5 Effect of discharge power on (a) the EC for CH_4 conversion, CO_2 conversion and total carbon conversion; (b) the EC for H_2 and syngas production; (c) the FPE of plasma dry reforming without catalyst (total feed flow rate: 50 ml/min; CO_2/CH_4: 1:1).

increased by increasing the discharge power, the energy consumed to convert a unit amount of reactant and to generate a unit amount of syngas is also increased due to the increase in discharge power. The EC for CO_2 and CH_4 conversion is 7.5 MJ/mol and 5.1 MJ/mol at a discharge power of 20 W, respectively, and increases to 13.5 MJ/mol and 7.7 MJ/mol when the discharge power is increased to 60W. Correspondingly, the EC for total carbon conversion increases from 3.0 MJ/mol to 4.9 MJ/mol; meanwhile, the EC for H_2 and syngas production increases by 63.4% and 68.0%, respectively.

Figure 5.4 (c) shows that the selectivity towards C_3H_8 and C_4H_{10} is slightly increased by increasing discharge power, which leads to an increase in the mole numbers of the generated C_3H_8 and C_4H_{10}. Although increasing discharge power decreases the selectivity to C_2H_6, the mole number of the produced C_2H_6 is still increased due to the increase in the mole numbers of the converted CO_2 and CH_4. It therefore can be concluded that increasing discharge power increases the mole numbers of all the produced fuels (H_2, CO, C_2H_6, C_3H_8 and C_4H_{10}). However, increasing discharge power decreases the FPE (see **Figure 5.5** (c)), due to the higher increasing rate in the discharge power compared to that in the total low heating value (LHV) of the generated fuels. A maximum FPE of 13.0% is achieved at a discharge power of 20 W, which decreases to 7.4% when the discharge power is increased to 60 W.

5.3.2.2 Effect of feed gas flow rate

Figure 5.6 shows the influence of total feed flow rate on the plasma dry reforming at a constant discharge power of 50 W and a CO_2/CH_4 molar ratio of 1:1. Increasing the total feed flow rate decreases the conversion of CO_2 and CH_4 due to the decline of the residence time of the reactants in the discharge region, which reduces the possibility of the reactant molecules colliding with energetic electrons and reactive species. When total feed flow rate is increased from 25 ml/min to 150 ml/min, the residence time of CO_2 and CH_4 in the plasma zone is significantly decreased from 36.7 s to 6.1 s; therefore, CO_2 and CH_4 conversion decreases from 34.1% and 50.5% to 9.1% and 16.1%, respectively. In addition, increasing total feed flow rate results in a remarkable decrease in the yield of CO and H_2 but only slightly decreases their selectivity. **Figure 5.6** (b) shows that the yield of CO and H_2 is decreased by about 75% when total feed flow rate increases from 25 ml/min to 150 ml/min. However, the selectivity of CO and H_2 is only decreased by approximately 11.0% when the total feed flow rate increases to 50 ml/min, and remains nearly constant afterwards, as shown in **Figure 5.6** (c). This suggests that a lower total feed flow rate is beneficial in improving the conversions of CO_2 and CH_4 and producing more syngas. Moreover, a maximum H_2/CO molar ratio of 0.90 is achieved at a total

flow rate of 50 ml/min, which decreases to 0.84 when the total flow rate is increased up to 150 ml/min.

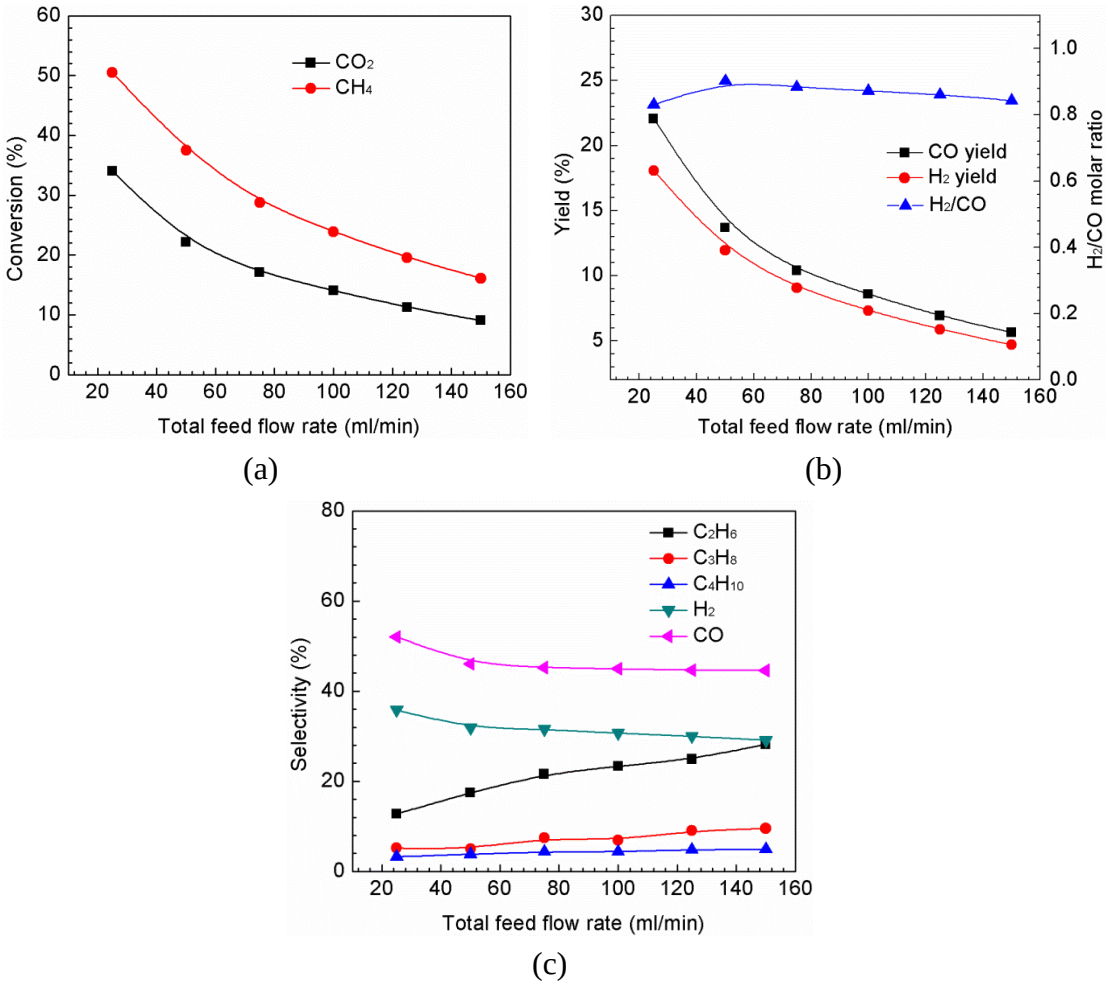

Figure 5.6 Effect of total feed flow rate on the performance of plasma dry reforming without catalyst: (a) conversion of CO_2 and CH_4; (b) yield of CO and H_2 and H_2/CO molar ratio; (c) selectivities of syngas and C_2-C_4 hydrocarbons (discharge power: 50 W; CO_2/CH_4 : 1:1).

In **Figure 5.6** (c), we can see that increasing the total feed flow rate increases the selectivity of C_2-C_4 hydrocarbons, especially C_2H_6 and C_3H_8, which is in accordance with previous studies [158]. The decline in the residence time resulting from an increase in the feed gas flow rate reduces the chance for C_2-C_4 hydrocarbons to be dissociated in an electron avalanche and converted to free radicals to form other carbon-containing chemicals, such as CO [243]. This explanation can be clearly confirmed by the decreasing trend in CO selectivity with the increase of total feed flow rate. Therefore, a high total feed flow rate is preferred for the production of C_2-C_4 hydrocarbons.

The dependence of the EC and FPE of the plasma process on total feed flow rate is shown in **Figure 5.7**. The EC for reactant conversion decreases significantly when the total feed flow rate increases from 25 ml/min to 100 ml/min, beyond which the EC becomes stable or starts to increase slightly. The EC for CO_2 and CH_4 conversion reaches their respective minimum value of 9.5 MJ/mol and 5.5 MJ/mol at a total feed flow rate of 125 ml/min, which results in the minimum EC for total carbon conversion as well (3.5 MJ/mol). This phenomenon is mainly caused by the increased mole number of converted CO_2 and CH_4 resulting from the increase in the total feed flow rate, although the conversions of CO_2 and CH_4 decrease (see **Figure 5.6** (a)).

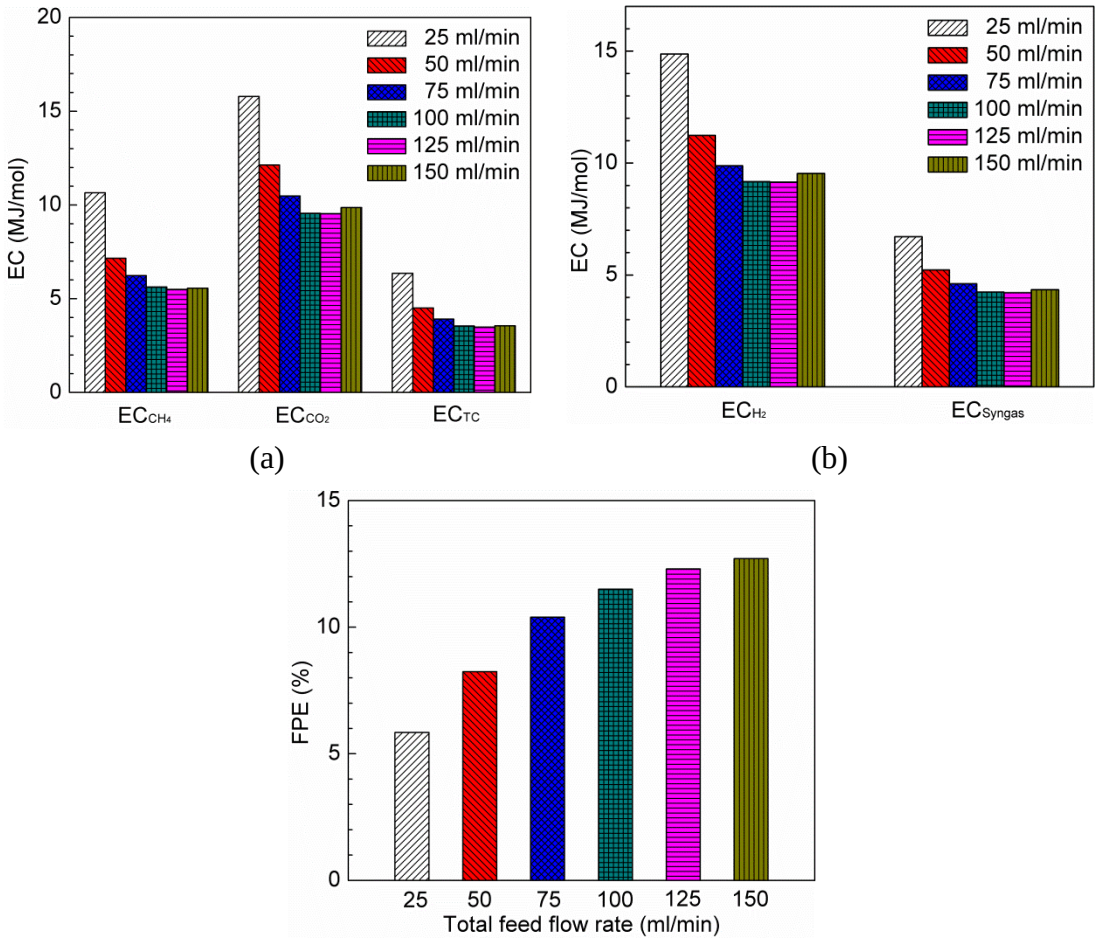

Figure 5.7 Effect of total feed flow rate on (a) the EC for CH_4 conversion, CO_2 conversion and total carbon conversion; (b) the EC for H_2 and syngas production; (c) the FPE of plasma dry reforming without catalyst (discharge power: 50 W; CO_2/CH_4: 1:1).

The EC for both H_2 and syngas production is also decreased by increasing the total feed flow rate. In **Figure 5.6** (b), we can see that increasing the total feed flow rate decreases the yield of CO and H_2, but the mole number of produced CO and H_2

is increased due to the large amount of CO_2 and CH_4 in the feed gas, which decreases the EC for both. At the total feed flow rate of 125 ml/min, the minimum EC for H_2 production and syngas production is 9.1 MJ/mol and 4.2 MJ/mol, respectively.

The FPE increases gradually with the total feed flow rate. The maximum FPE of 12.7% is achieved at a total feed flow rate of 150 ml/min. The mole numbers of C_2H_6, C_3H_8 and C_4H_{10} are all increased by increasing the total feed flow rate, due to the increase in their selectivities, as shown in **Figure 5.6** (c). Therefore, the mole numbers of the different produced fuels are all increased by increasing the total feed flow rate, which results in the increase in the FPE at a constant discharge power.

5.3.2.3 Effect of CO_2/CH_4 molar ratio

Figure 5.8 presents the effect of different CO_2/CH_4 molar ratios on performance of the plasma dry reforming process. The conversion of CH_4 increases significantly with the increase of the CO_2/CH_4 molar ratio, which suggests that a higher content of CO_2 in the reactant gas mixture favours the conversion of CH_4. A maximum CH_4 conversion of 51.5% is achieved at a CO_2/CH_4 molar ratio of 4:1. In contrast, the conversion of CO_2 is slightly decreased from 24.2% to 21.1% when the CO_2/CH_4 ratio is changed from 1:4 to 4:1. As discussed above, active oxygen from CO_2 decomposition favours the conversion of CH_4 through Equation (5-12). More oxygen is produced and therefore the rate of Equation (5-12) is increased by increasing the CO_2/CH_4 molar ratio, which results in the enhancement in CH_4 conversion. By contrast, the effect of Equation (5-13) on the conversion of CO_2 becomes weaker by increasing the CO_2/CH_4 molar ratio, which leads to the decline in CO_2 conversion.

Figure 5.8 (b) shows that the CO_2/CH_4 molar ratio significantly affects the yield of CO and H_2. When the CO_2/CH_4 molar ratio increases from 1:4 to 4:1, the yield of H_2 is more than doubled, and the yield of CO is enhanced 2.8 times. These results are in good agreement with those obtained in previous studies [44, 116]. Zhang et al. reported that increasing the CO_2/CH_4 molar ratio from 2:3 to 3:1 increased the H_2 yield from 11.4% to 20.4% and the CO yield from 7.3% to 31.3% in a non-catalytic DBD reactor [116]. The variation of CO_2/CH_4 molar ratio plays a significant role in determining the H_2/CO molar ratio in the produced syngas. Thus we could expect that syngas with a desired H_2/CO molar ratio for further synthesis can be produced by adjusting the CO_2/CH_4 molar ratio. For example, when the CO_2/CH_4 molar ratio is lower than 1:2, a H_2/CO molar ratio of 2:1 can be obtained, which is desirable for catalytic synthesis of methanol [44].

In addition, increasing the CO_2 content in the feed gas significantly increases the selectivity of H_2 and CO. We can see that the selectivity of H_2 increases by 35.9% (from 29.5% to 40.1%), while the CO selectivity is increased by a considerable factor of 2.9 when the CO_2/CH_4 molar ratio changes from 1:4 to 4:1. By contrast,

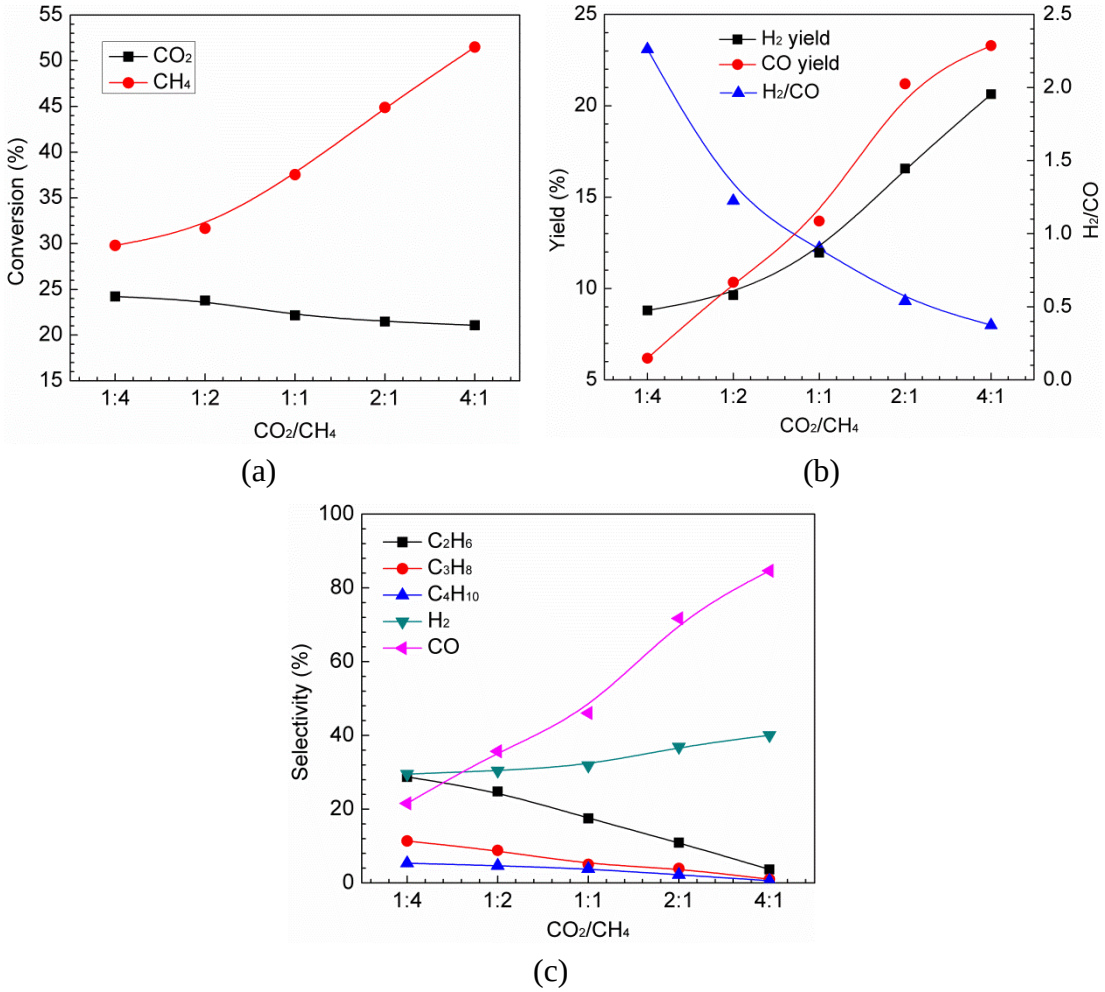

Figure 5.8 Effect of CO_2/CH_4 molar ratio on the performance of plasma dry reforming without catalyst: (a) conversion of CO_2 and CH_4; (b) yield of CO and H_2 and H_2/CO molar ratio; (c) selectivities of syngas and C_2-C_4 hydrocarbons (discharge power: 50 W; total feed flow rate: 50 ml/min).

lower content of CO_2 in the feed gas leads to a higher selectivity of C_2-C_4 hydrocarbons, especially to C_2H_6, as shown in **Figure 5.8** (c). Zhang et al. suggested that lower CO_2 content in the feed gas decreased the availability of oxygen in the reaction system, which enhanced the possibility of the active CH_4 species (CH_3, CH_2, CH) reacting with each other to form other hydrocarbons (C_2, C_3, etc.) compared with that of CH_4 oxidation to form CO [116]. This explanation is in consistent with the decreasing trend in CO selectivity as a result of decreasing the CO_2 content in the feed gas (see **Figure 5.8** (c)). The highest selectivity to C_2H_6 (28.8%) is obtained at a CO_2/CH_4 molar ratio of 1:4, which nearly reaches that of H_2 and is increased by a factor of 6.8 compared with that obtained at a CO_2/CH_4 molar ratio of 4:1.

Figure 5.9 shows the effect of CO_2/CH_4 molar ratio on the EC and FPE of the plasma process. Increasing the CO_2/CH_4 molar ratio decreases the EC for CO_2 conversion, but increases that for CH_4 conversion. This is mainly due to the fact that

increasing the CO_2/CH_4 molar ratio results in an increase in the mole number of converted CO_2 but a decrease in that of converted CH_4. When the CO_2/CH_4 molar ratio is less than 2:1, the EC for CO_2 conversion is higher than that for CH_4 conversion. The maximum EC for CO_2 conversion of 27.7 MJ/mol is obtained at a CO_2/CH_4 molar ratio of 1:4, but the corresponding EC for CH_4 conversion approaches its minimum value (5.6 MJ/mol). The EC for CH_4 conversion peaks (13.0 MJ/mol) at a CO_2/CH_4 molar ratio of 4:1. The EC for total carbon conversion is independent of the variation in CO_2/CH_4 molar ratio.

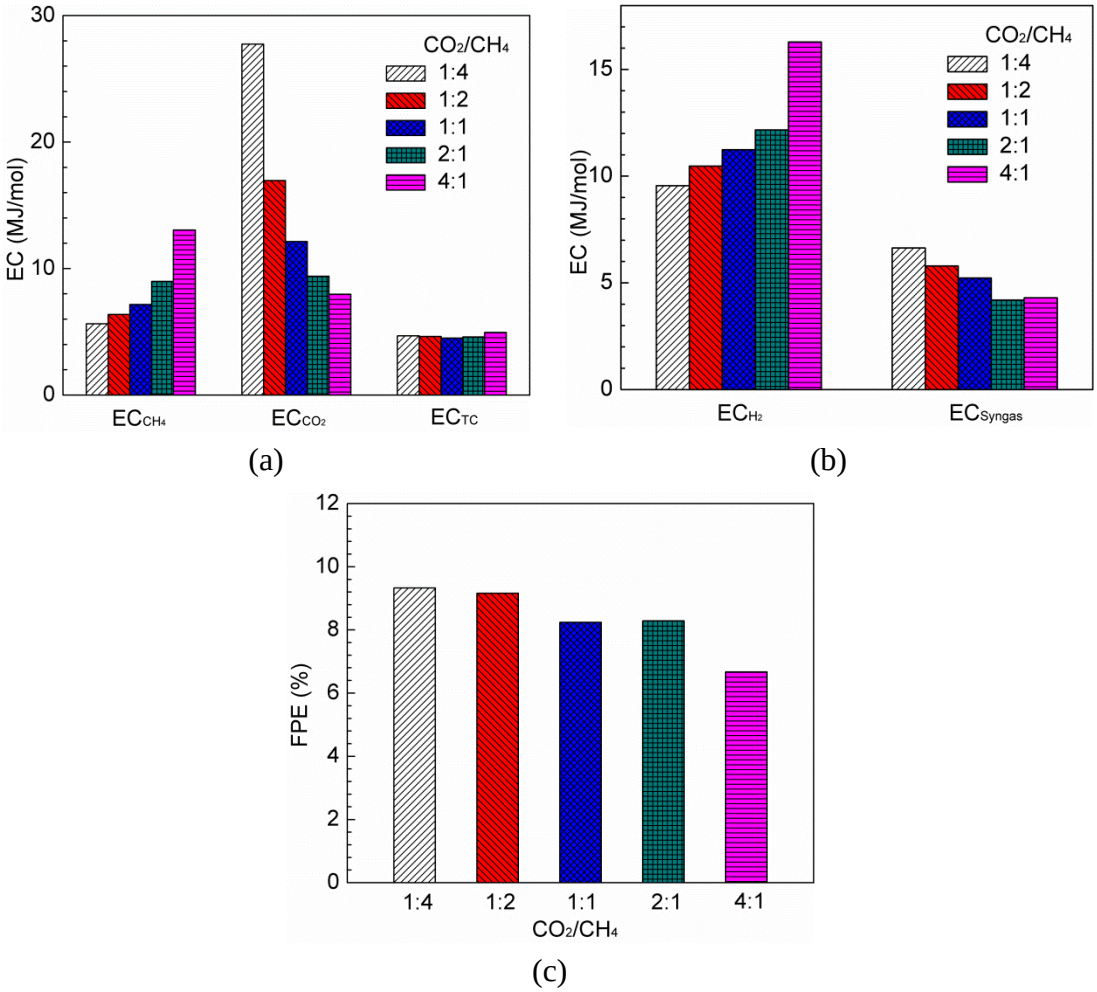

Figure 5.9 Effect of CO_2/CH_4 molar ratio on (a) the EC for CH_4 conversion, CO_2 conversion and total carbon conversion; (b) the EC for H_2 and syngas production; (c) the FPE of plasma dry reforming without catalyst (discharge power: 50 W; total feed flow rate: 50 ml/min).

The yield of H_2 is increased by increasing the CO_2/CH_4 molar ratio, but the mole number of the produced H_2 is decreased, which leads to the increase in the EC for H_2 production, as shown in **Figure 5.9** (b). A maximum EC of 16.3 MJ/mol for H_2 production is obtained at a CO_2/CH_4 molar ratio of 4:1. However, the

corresponding EC for syngas production is decreased, resulting from the increase in the mole number of produced syngas (mainly CO) via the plasma reaction.

In **Figure 5.9** (c), we can see the FPE is slightly decreased by increasing the CO_2/CH_4 molar ratio. The maximum FPE is 9.3%, obtained at a CO_2/CH_4 molar ratio of 1:4. Increasing the CO_2/CH_4 molar ratio decreases the mole numbers of the produced C_2H_6, C_3H_8 and C_4H_{10}, due to the decline in their selectivities, as shown in **Figure 5.8** (c). Although the mole number of the produced CO is increased, the total LHV of the generated fuels is decreased by increasing the CO_2/CH_4 molar ratio, which leads to the decrease in the FPE.

5.4 Conclusions

In this chapter, the thermodynamic equilibrium calculation for dry reforming of CH_4 and the experiments of the plasma dry reforming of CH_4 without catalyst, have been performed. From the thermodynamic equilibrium calculation, it is known that the reaction is significantly sensitive to the operating temperature due to the endothermic character of the reaction. In the reaction system with CO_2/CH_4 molar ratio of 1:1, the conversion of CO_2 is always higher than that of CH_4, due to the occurrence of the RWGS reaction. Furthermore, increasing the amount of CO_2 in the feed gas favours the conversion of CH_4 but limits the conversion of CO_2. In addition, increasing the CO_2/CH_4 molar ratio results in a higher thermodynamic equilibrium mole number of CO than that of H_2, especially when the CO_2/CH_4 molar ratio is larger than 1 due to the formation of water by the RWGS reaction.

In the plasma dry reforming of CH_4 without catalyst, increasing discharge power favours the conversions of CO_2 and CH_4, but increases EC for reactant conversion and gas production and decreases FPE of the plasma process. By contrast, the increase in total feed flow rate has a negative influence on the reactant conversions, but decreases EC for both reactant conversion and gas production and increases FPE. Different from the reaction mechanism in the thermal process for dry reforming, the reactions related to electrons, radicals and other reactive species are of great importance in the plasma process, which results in higher conversions of CH_4 than those of CO_2 at a CO_2/CH_4 molar ratio of 1:1 in the feed. Moreover, the variation in CO_2/CH_4 molar ratio has the opposite effect on CO_2 and CH_4 conversion. It was also found that H_2/CO molar ratio in the product gas is significantly affected by the CO_2/CH_4 molar ratio in the feed gas, but almost independent on the other reaction condition parameters (e.g. discharge power and total feed flow rate); high H_2/CO molar ratios (>1) are obtained in the plasma reaction when CO_2/CH_4 molar ratio is less than 1. The dependence of H_2/CO molar ratio on CO_2/CH_4 molar ratio can be manipulated to adjust the composition of syngas, making it suitable for the production of different desired chemical products. The variation in CO_2/CH_4 molar ratio also plays an opposite role in EC for CO_2 conversion and CH_4 conversion as

well as in EC for H_2 production and syngas production. Due to the decreased amount of generated fuels, an increasing CO_2/CH_4 molar ratio leads to a decrease in FPE of the plasma process.

CHAPTER SIX DRY REFORMING OF METHANE IN A COAXIAL DBD REACTOR USING NI-BASED CATALYSTS

6.1 Introduction

In the thermal catalytic dry reforming of CH_4, catalysts based on both noble (Rh, Ru, Pt and Pd) and transition metals (Fe, Co and Ni) have been extensively investigated [48, 247]. Although the noble metal catalysts have been demonstrated to show high activity and carbon-resistance, their inherent rarity and high costs limit their widespread application in industry [46]. Alternatively, Ni-based catalysts have been extensively investigated in the reforming process due to their high initial activity and availability in large scale, lending them great potential for industrial application [248]. Nevertheless, high temperatures are required in the dry reforming process to obtain reasonable conversions of CO_2 and CH_4 due to the strong endothermic character of this reaction, which leads to the sintering of the active metal component and the supportive phases and/or coke formation over the catalyst surface; all of these factors result in catalyst deactivation and reactor blocking, thereby hinder its long-term application in industrial practices [248]. In order to overcome these drawbacks, several approaches have been applied to improve the activity and stability of the Ni-based catalyst, including exploring effective supports with high resistance against Ni particle sintering and coke formation, incorporating promoters (alkali, alkali earth and rare earth metal oxides) to modify the existing supports [249], adding modifiers to form Ni-based bimetallic catalysts [250], and selecting the catalyst preparation methods [247].

As mentioned in Chapter 5, the non-equilibrium character of non-thermal plasma could overcome the thermodynamic barriers in the dry reforming reaction and enable it to occur at a lower temperature than that required in the conventional thermal catalytic process. However, in the plasma dry reforming of CH_4 without catalyst, the conversions of reactants and the selectivities towards the target products such as CO and H_2 are rather low. It has been reported that the efficiency and the selectivity of desired products in the plasma process can be improved when a suitable catalyst is involved in the plasma reaction [171]. The synergistic effect generated by the combination of plasma and different catalysts has also been demonstrated by previous studies [91, 116]. In the early stage, the catalysts used in the plasma-catalytic dry reforming of CH_4 were mainly focused on the zeolites [42, 158-160]; later on, the Ni-based catalysts have attracted increasing interest [91, 107, 162, 163, 166, 243]; however, these catalysts were mainly supported on limited supports (e.g. Al_2O_3). The limitation in the exploration of low cost and active catalysts cannot

satisfy the development of the plasma-catalytic dry reforming process. In addition, the deactivation of the Ni-based catalysts in the discharge zone due to carbon deposition and the sintering of active metals has also been reported [162], but very few works have been devoted to the further modification of the Ni catalysts to enhance their catalytic activity in the plasma-catalytic dry reforming process. Therefore, it is of great importance to find cost-effective Ni-based catalysts with high activity and carbon-resistance suitable for the plasma-catalytic dry reforming conditions.

Supports have been reported to play a key role in the enhancement of catalytic activity and the suppression of carbon deposition in the process of dry reforming of CH_4 [46]. The primary role of supports is mainly determined by their surface area, acid-base properties and ability to disperse the supported phase. Different supports (e.g. γ-Al_2O_3, MgO, SiO_2, TiO_2, etc.) are commonly employed in the conventional thermal-catalytic dry reforming of CH_4 [46, 247]. In this chapter, the effect of the supports on the plasma-catalytic dry reforming process is firstly investigated. The catalyst supports were selected based on their abundant usage in the conventional thermal catalytic dry reforming process. 10 wt.% Ni supported catalysts are combined with DBD plasma to evaluate the plasma-catalytic activity based on the conversions of reactants, the yield and selectivity of target products and the carbon deposition as well as the EC and the FPE.

Plasma-catalytic dry reforming of CH_4 is a complex and challenging process involving a large number of physical and chemical reactions. The reaction performance (conversions of CO_2 and CH_4, yields and selectivities of products, as well as energy efficiency) is dependent on a wide range of plasma processing parameters such as the discharge power, frequency, total gas flow rate, CO_2/CH_4 molar ratio in the input gas stream and reactor configuration, as well as the catalyst components [144]. It is often of primary interest to explore the relationships between these key independent input variables and the output performance of the plasma process.

Standard experiments are designed to look at one of these parameters in isolation from the others and so screening a large number of processing parameters is time-consuming and costly due to the large numbers of experiments which need to be performed. This type of experimentation requires large quantities of resources to obtain a limited amount of information about the process. A fundamental understanding of the importance of different processing parameters, especially the combined effects of these parameters on the performance of plasma dry reforming of CH_4, is very limited and not clear, which makes it difficult to determine the set of processing parameters that will optimise the performance of the plasma process. Plasma chemical modelling offers an alternative route for solving this problem. De Bie et al. developed a one-dimensional (1D) fluid model to investigate the effect of

different plasma process conditions on the plasma decomposition of CH_4 in a DBD reactor [245]. The model consisted of 36 species (electrons, atoms, ions, molecules) and 367 gas phase reactions. This model was recently extended to simulate plasma methane conversion in CH_4/CO_2 and CH_4/O_2 mixtures [251]. Snoeckx et al. developed a zero-dimensional (0D) kinetics model to understand the influence of different processing parameters (gas mixture ratio, discharge power, residence time and frequency) on the conversion and energy efficiency of plasma dry reforming of CO_2 and CH_4 in a similar DBD reactor, and to investigate which of these parameters lead to the most promising results [144, 244]. However, although model calculations can be fast depending on the type of model, the development of a comprehensive model takes time and is thus not always useful for fast and cost-effective optimisation of highly complex plasma chemical processes.

Design of experiments (DoE) is a powerful tool for process optimisation as it allows multiple input factors to be manipulated, determining their individual and combined effects on the process performance in the form of one or more output responses, whilst significantly reducing the number of experiments compared to conventional methods that just focus on one factor at a time [252]. Response surface methodology (RSM) is one of the most useful experimental designing methodologies for building the relationship between the multiple input parameters and the output responses, which enables us to get a better understanding of the effect of individual factors and their interactions on the responses by three-dimensional and contour interpretations. Central composite design (CCD), a commonly used approach for experimental design in RSM, is an efficient five-level design developed for fitting quadratic response surfaces [253]. CCD has been widely used in areas of energy [254], environment [255] and chemistry [253]. Until now, the applications of the DoE method have mainly focused on material fabrication and treatment [256, 257]. Recently, the use of DoE for quick optimisation of plasma chemical reactions, such as CO_2 conversion and utilisation, has been demonstrated in our previous work [229].

In the second part of this chapter, upon determining the most suitable catalyst support (γ-Al_2O_3), RSM based on CCD has been used to establish the relationship between the key plasma processing parameters (discharge power, total feed flow rate, CO_2/CH_4 molar ratio and Ni loading) and the process performance, and to optimise the performance of the plasma-catalytic dry reforming reaction in terms of reactant conversions, product yields and FPE. The influence of these different processing parameters and their interactions on the reaction performance has been investigated and discussed in detail.

6.2 Effect of Supports on the Performance of Plasma-Catalytic Dry Reforming of CH_4 using Ni-based Catalysts

6.2.1 Experimental section

The Ni catalysts on different supports (γ-Al_2O_3, MgO, SiO_2, and TiO_2) with a Ni loading of 10 wt.% were prepared by the conventional wetness impregnation method using $Ni(NO_3)_2{\cdot}6H_2O$ as the metal precursor. All of the support pellets have a diameter of ~ 1 mm. The detailed procedure for the preparation of these catalysts has been described in Section 2.2. The obtained samples are denoted as Ni/M (M=Al, Mg, Si and Ti). To understand the surface structures and properties of the catalysts, as well as their effect on the performance of the plasma-catalytic dry reforming of CH_4, the N_2 physisorption is used to measure the pore size and the specific surface area of the catalysts; the crystal phases of the calcined catalysts are identified through the XRD; the CO_2-TPD measurements are performed to evaluate the amount of basic sites on the Ni catalyst. The coke deposition on the spent catalysts is analysed by TGA in air atmosphere.

Plasma-catalytic dry reforming of CH_4 over the supported Ni catalysts is performed in a coaxial DBD reactor. The experimental setup is the same as those in Section 5.3.1. Prior to the plasma-catalytic dry reforming reaction, 0.5 g of the Ni catalyst is placed at the bottom of the reactor and then reduced in an Ar-H_2 discharge at a discharge power of 50 W and a total flow rate of 50 ml/min with 20 vol.% H_2 for 30 min in the same DBD reactor. The reforming process is then conducted once the reduced catalyst has cooled down to room temperature in the Ar atmosphere. CO_2 and CH_4 are used as feed gases with a total flow rate of 50 ml/min and a CO_2/CH_4 molar ratio of 1:1. The experiments are performed using a discharge power in the range of 30-60 W.

6.2.2 Experimental results

6.2.2.1 Catalyst properties

(1) Surface structure of the catalysts

The physicochemical properties of the fresh Ni catalysts are listed in **Table 6.1**. Clearly, a wide-ranged surface area and pore distribution are detected in the Ni catalysts. The Ni/Al catalyst has the maximum surface area and pore volume, followed by the Ni/Mg, Ni/Si and Ni/Ti catalysts. The specific surface area of the Ni/Al catalyst is more than twice that of the Ni/Ti catalyst.

Table 6.1 Physicochemical properties of the Ni catalysts on different supports.

Sample	S_{BET} (m^2/g)	Pore volume (cm^3/g)	Pore diameter (nm)
Ni/Al	268.0	0.39	3.80
Ni/Mg	193.8	0.36	4.25
Ni/Si	166.4	0.33	6.73
Ni/Ti	103.6	0.26	7.84

The XRD patterns of the fresh catalysts are shown in **Figure 6.1**. For the Ni/Al, Ni/Si and Ni/Ti catalysts, the NiO peaks are clearly demonstrated in their XRD spectra. For the Ni/Mg catalyst, it is well known that both NiO and MgO oxides have a NaCl-lattice structure; it is difficult to distinguish the NiO peaks from the MgO peaks to the similar dimensions of their respective unit cells [258]. However, on the catalysts calcined at a lower temperature (e.g. 400 ^{o}C or 500 ^{o}C), only a part of NiO could be incorporated into the lattice of the MgO support, and the remainder of NiO still exists in the form of free NiO [259]. The lower calcination temperature (400 ^{o}C) in this study can ensure the existence of the NiO phase on the Ni/Mg catalyst. It has been demonstrated that the formed NiO in the supported catalysts can be reduced in the low temperature Ar-H_2 plasma [166, 260]. Compared with the diffraction peaks of NiO in the Ni/Mg, Ni/Si and Ni/Ti catalysts, the NiO peaks in the Ni/Al catalyst are weaker and broader, indicating that the high dispersion and small size of the NiO particles are obtained on the Ni/Al catalyst.

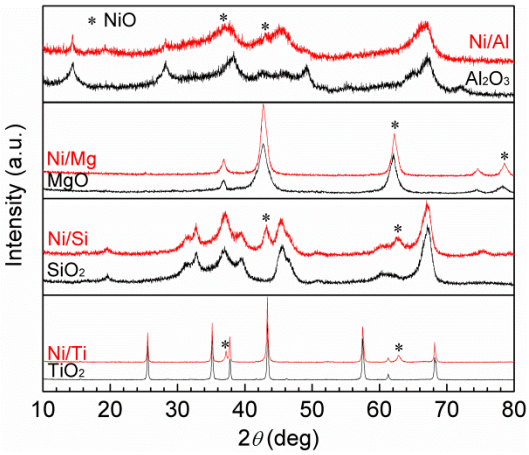

Figure 6.1 XRD patterns of catalyst supports and fresh catalysts on the different supports.

(2) CO_2-TPD

Figure 6.2 shows the CO_2-TPD patterns of the fresh Ni catalysts on different supports. It has been reported that CO_2 adsorbed on weak basic sites is desorbed at low temperatures and CO_2 adsorbed on strong basic sites is desorbed at high temperatures; the weak, intermediate, strong and very strong basic sites of the

catalysts are within the temperature ranges of 20-150, 150-300, 300-450 and > 450 ^{o}C, respectively [261]. The amount of the basic sites is estimated from the area under their CO_2-TPD curves [261]. Clearly, the Ni/Al, Ni/Mg and Ni/Si catalysts show three CO_2 desorption peaks: the first two peaks are centred at lower temperatures (around 50-100 ^{o}C and 120-200 ^{o}C, respectively) and the third peak is centred at higher temperatures (around 300-500 ^{o}C). Therefore, the first two desorption peaks on these three catalysts are assigned to weak basic sites, while the third one is attributed to strong basic sites. The peak area of the strong basic sites on the Ni/Al catalyst is much larger than that of the Ni/Mg and Ni/Si catalysts. It is interesting to note that the amount of the basic sites on the Ni/Ti catalyst is quite different from that of the other catalysts: only a small CO_2 desorption peak centred at low temperatures (around 50-100 ^{o}C) is observed. It therefore can be concluded that the Ni/Al catalyst has the highest amount of the strong basic sites, followed by the Ni/Mg, Ni/Si and Ni/Ti catalysts. Catalysts with larger amount of strong basic sites can supply surface oxygen through acidic CO_2 to inhibit coke formation on the catalyst surface [262, 263]. Thus, it could be expected that the Ni/Al catalyst will have higher coke resistance than the other catalysts.

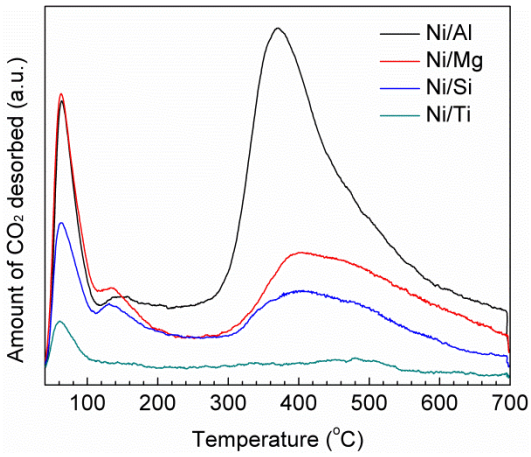

Figure 6.2 CO_2-TPD patterns of the Ni catalysts.

6.2.2.2 Reactant conversions

The effect of the catalyst supports on the conversion of CO_2 and CH_4 as a function of discharge power is shown in **Figure 6.3**. Clearly, both CO_2 and CH_4 conversions are increased by increasing the discharge power no matter whether the catalysts are used or not. In this study, the increase in the discharge power is obtained by increasing the applied voltage at a fixed frequency. As discussed in Section 3.3.2.2, increasing the discharge power enhances the formation of reaction channels and electrons, which is beneficial in improving the conversions of CO_2 and CH_4. Similar dependence of CO_2 and CH_4 conversion on discharge power have been demonstrated in previous studies [107]. In the plasma-catalytic reaction, the

combination of plasma with the Ni/Al catalyst leads to the highest reaction performance. The maximum CO_2 conversion of 26.2% is obtained with the presence of the Ni/Al catalyst at a discharge power of 60 W, followed by those achieved with the Ni/Mg, Ni/Si and Ni/Ti catalysts. Correspondingly, the activity of these catalysts for CH_4 conversion has the same order, Ni/Al > Ni/Mg > Ni/Si > Ni/Ti. A maximum CH_4 conversion of 44.1% is obtained when the Ni/Al catalyst is used. The above maximum conversions of CO_2 and CH_4 are increased by 10.1% and 5.7%, respectively, compared to the results obtained in the plasma-only process at the same discharge power.

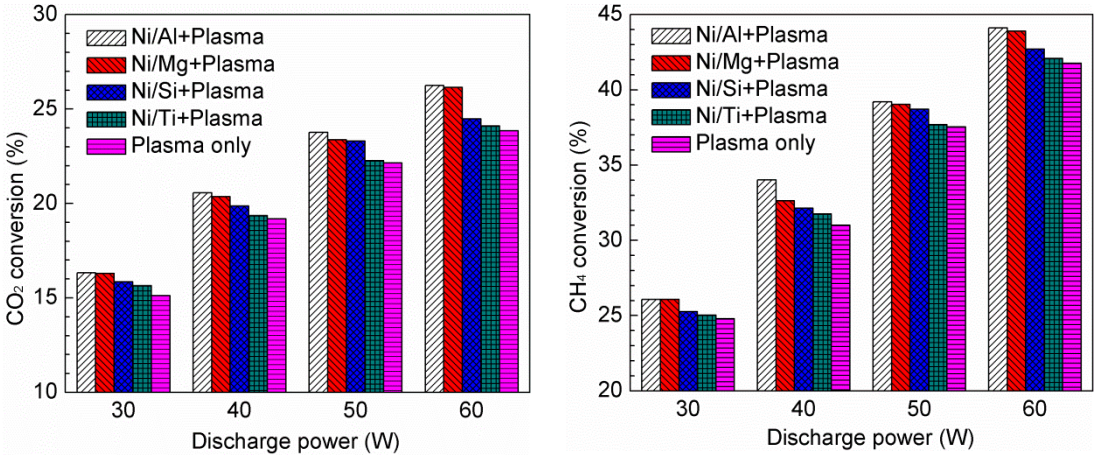

(a) (b)

Figure 6.3 Effect of the supports on (a) CO_2 conversion and (b) CH_4 conversion as a function of discharge power (total feed flow rate: 50 ml/min; CO_2/CH_4 molar ratio: 1:1).

Generally, the catalysts with higher specific surface area could provide larger contact area and more active sites for the catalytic reaction, and consequently result in higher reaction activity [264, 265]. The smaller particle size of the active phase also plays an important role in enhancing the reaction performance and reducing coke deposition on the catalysts [234, 265]. The physicochemical properties of these catalysts reveals that the large specific surface area and the smaller NiO crystalline size are obtained in the Ni/Al catalyst, which make it possible to exhibit higher catalytic performance in the plasma dry reforming process. In the dry reforming process, CO_2 molecules in the reactant gas stream are activated and reduced to CO while releasing O, which helps the oxidation of the surface carbon formed from CH_4 activation [48]. The catalysts with a larger amount of strong basic sites can improve the adsorption of CO_2; the adsorbed CO_2 then is decomposed to supply a greater amount of oxygen species on the catalyst surface for gasification of intermediate carbonaceous species from CH_4 decomposition, and consequently enhance the carbon resistance of the catalyst [264]; in addition, more reactive oxygen-containing

radicals (e.g. oxygen radicals) from CO_2 are generated in the plasma conditions to enhance the dissociation of CH_4 [41], all of which contribute to the promotion in the conversions of CO_2 and CH_4. Therefore, the larger amount of strong basic sites on the Ni/Al catalyst might be another reason for the higher conversion of CO_2 and CH_4, compared with that in other catalysts. The catalytic activity of these Ni catalysts for CO_2 and CH_4 conversion is in accordance with their amount of basic sites.

In the conventional thermal catalytic CO_2 reforming of CH_4, these catalysts are normally activated at higher temperature (around 800 ^oC) [259, 266]. The combination of plasma and catalyst can shift the catalyst activation temperature downwards. In this study, the measured temperature inside the reactor is lower than 230 ^oC in the plasma-catalytic reaction under our experimental conditions. The thermodynamic equilibrium calculation for dry reforming of CH_4 (see Chapter 5) has confirmed that the conversion of CO_2 and CH_4 is very low (<1%) at low temperatures (e.g. 300 ^oC), which suggests that extremely low CO_2 and CH_4 conversions can be obtained using thermal catalytic dry reforming reaction at low temperatures (< 300 ^oC). These results indicate the formation of a synergistic effect by combining plasma with different catalysts at low temperatures. Moreover, NiO phase detected on all of the catalysts (see **Figure 6.1**), can be reduced to the active Ni metal in the low-temperature Ar-H_2 plasma [166, 260].

We can therefore conclude that the higher catalytic activity for CO_2 and CH_4 conversion observed in the Ni/Al catalyst is mainly ascribed to the higher specific surface area, higher dispersion and smaller particle size of NiO and larger amount of the strong basic sites. The synergistic effect generated by the combination of plasma and catalyst also cannot be ruled out.

6.2.2.3 Production of syngas and C_2-C_4 hydrocarbons

Figure 6.4 shows the variation of the syngas production in the plasma catalytic dry reforming process as a function of the discharge power. Clearly, under all the experimental conditions, the yield of CO and H_2 is increased by increasing the discharge power. At a specified discharge power, the introduction of Ni catalysts into the plasma system enhances the yield of CO and H_2. The maximum yield of CO and H_2 is achieved in the presence of the Ni/Al catalyst, followed by the Ni/Mg, Ni/Si and Ni/Ti catalysts, which is in accordance with their activity for conversion of CO_2 and CH_4. With the presence of the Ni/Al catalyst in the DBD reactor, the maximum yield of CO and H_2 is 16.8% and 15.2%, respectively, at a discharge power of 60 W. This maximum yield of CO and H_2 is increased by 9.9% and 15.9%, compared with that obtained in the plasma-only process.

The combination of plasma with the Ni catalysts increases the selectivity of CO and H_2. This effect is different from the previous results reported by Song et al. in a DBD reactor [168]. They found that the use of Ni/Al_2O_3 slightly decreased the

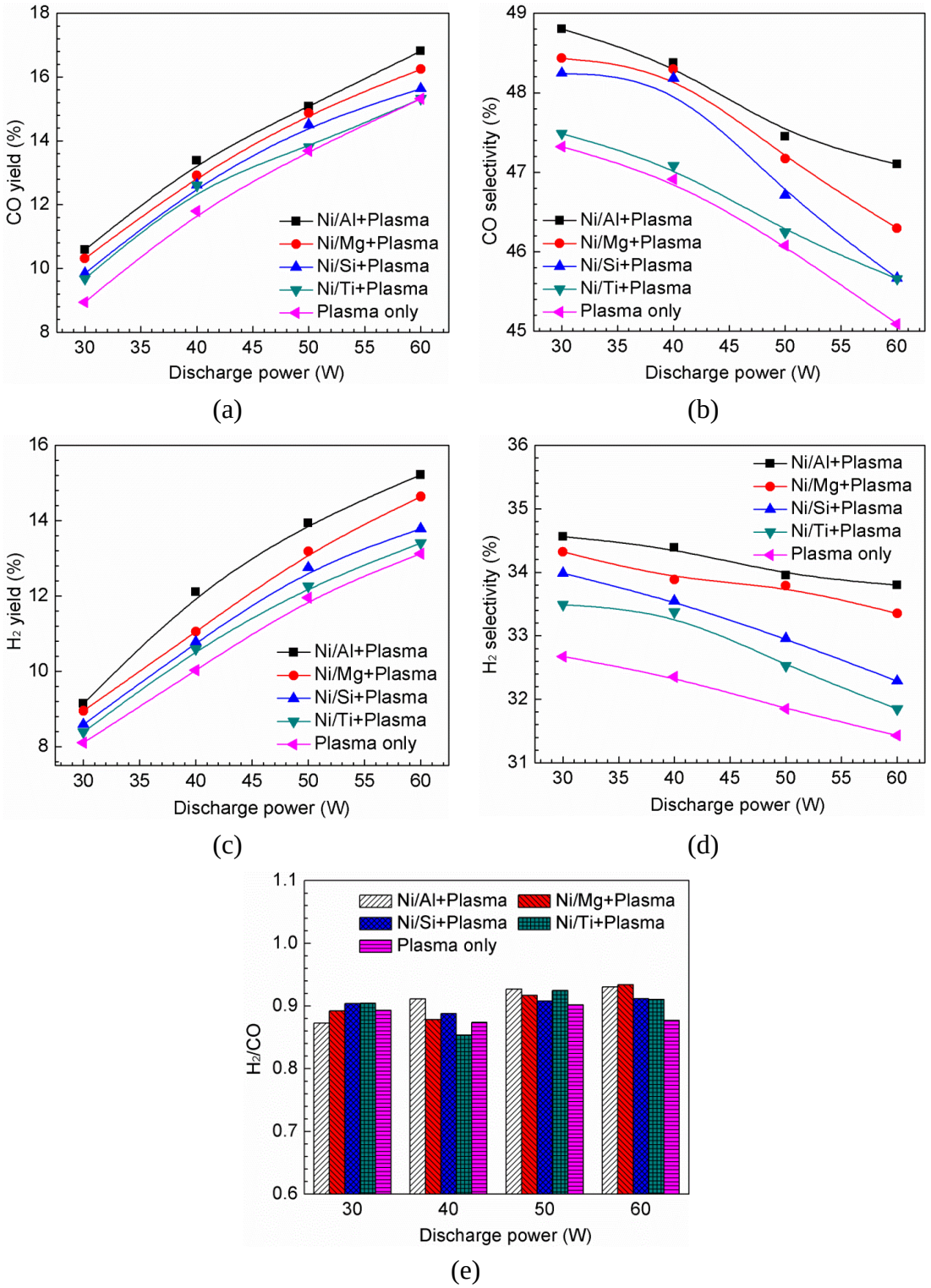

Figure 6.4 Effect of the supports on the syngas production as a function of discharge power: (a) CO yield; (b) CO selectivity; (c) H_2 yield; (d) H_2 selectivity; (e) H_2/CO molar ratio (total feed flow rate: 50 ml/min; CO_2/CH_4 molar ratio: 1:1).

selectivity of H_2 and increased the selectivity of CO during the dry reforming process at a discharge power of 130 W, compared to the plasma-only process. In this study, the effect of the catalysts on the selectivity of CO and H_2, from low to high, is in the

order of Ni/Ti < Ni/Si < Ni/Mg < Ni/Al, which is in consistent with their effect on the yield of CO and H_2 at a specified discharge power. The maximum selectivity of CO and H_2 is 48.8 % and 34.6%, respectively, when the Ni/Al catalyst is used at a discharge power of 30 W. Increasing the discharge power always decreases the selectivity of CO and H_2, regardless of the catalysts. The formation of carbon deposition and higher hydrocarbons by increasing discharge power might be the reason for the decreases in the CO selectivity; whilst the formation of higher hydrocarbons and H_2O might account for the decline in the H_2 selectivity. Similar variation in the selectivity of CO and H_2 with discharge power was also observed in previous studies. Jiang et al. also reported that the selectivity of CO and H_2 was decreased from 50.8% and 52.2% to 42.8% and 23.2%, respectively, by increasing the input power from 100 to 500 W in the plasma-catalytic dry reforming reaction over a zeolite A catalyst at a total feed flow rate of 200 ml/min with a CO_2/CH_4 molar ratio of 1:1 [160].

Figure 6.4 (e) shows that the molar ratio of H_2/CO in the gas product is lower than unity. This may be attributed to the occurrence of the RWGS reaction (Equation (5-2)), in which CO_2 reacts with the generated H_2 to form more CO. The variation of the molar ratio of H_2/CO is independent of the catalysts used in this study. Discharge power in the plasma-catalytic reforming process also plays an irregular role in the H_2/CO molar ratio, which is similar to the results of the plasma process without catalyst, as discussed in Section 5.3.2.1.

The effect of Ni catalyst supports on the selectivity of C_2-C_4 hydrocarbons as a function of discharge power is shown in **Figure 6.5**. The selectivity towards C_3H_8 and C_4H_{10} is increased by increasing the discharge power. In contrast, increasing the discharge power decreases the selectivity towards C_2H_6. The results suggest that a higher discharge power is favourable for the dissociation of the produced C_2H_6 to form other hydrocarbons.

The highest selectivity towards C_3H_8 and C_4H_{10} is achieved when the Ni/Al catalyst is combined with the DBD at a specified discharge power, while the selectivity to C_2H_6 reaches its maximum value in the plasma-only process. In this study, the maximum selectivity towards C_3H_8 and C_4H_{10} are 5.6% and 4.4%, respectively, obtained in the presence of the Ni/Al catalyst at a discharge power of 60 W, while a maximum selectivity of 22.2% towards C_2H_6 is obtained in the absence of any catalyst at a discharge power of 30 W.

6.2.2.4 Carbon balance

Figure 6.6 shows the carbon balance in the gas stream of plasma-catalytic reaction using different Ni catalysts as a function of the discharge power. The carbon balance is below 100% under all the experimental conditions and decreased by increasing discharge power. This is possibly due to carbon deposition occurring to a

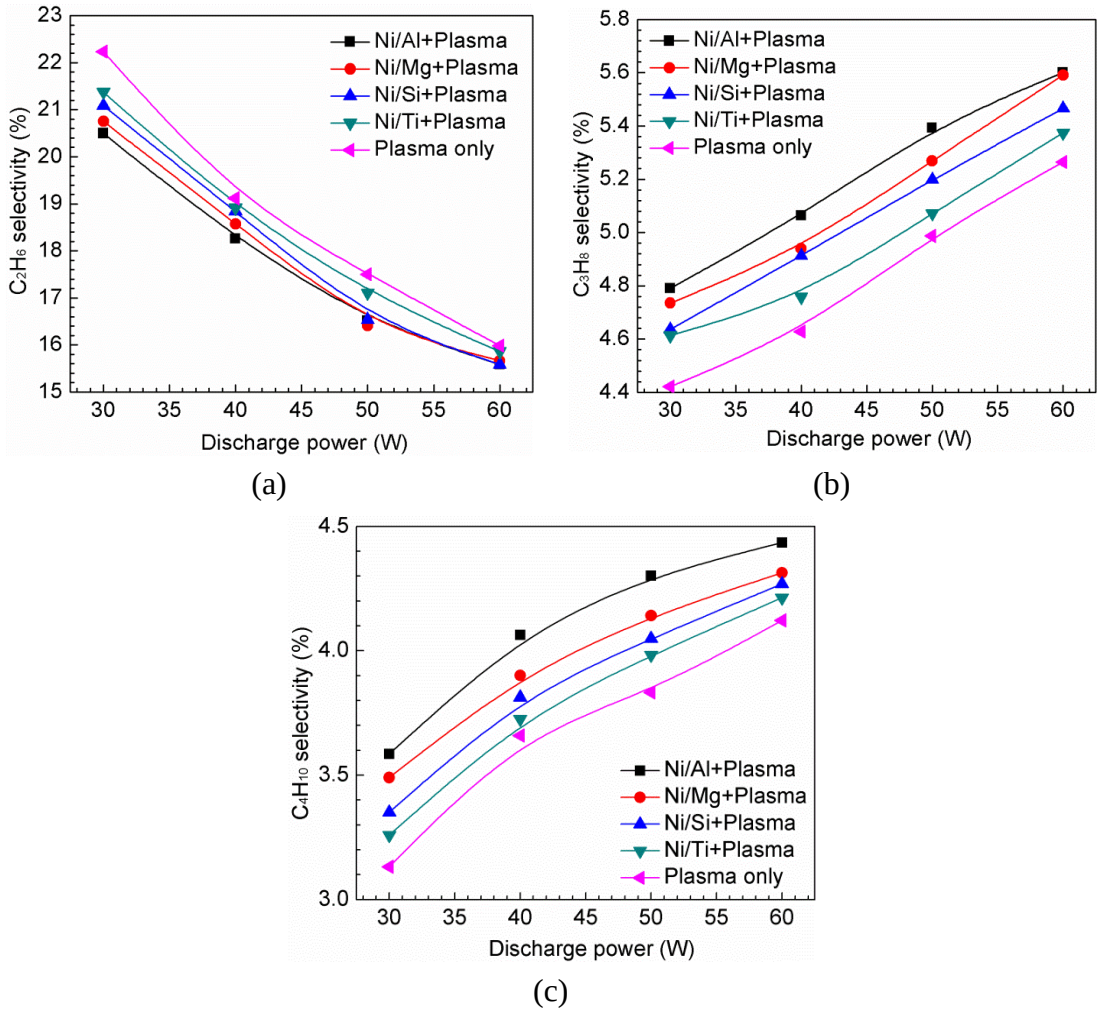

Figure 6.5 Effect of the supports on the selectivity to C_2-C_4 hydrocarbons (a) C_2H_6; (b) C_3H_8; (c) C_4H_{10} (total feed flow rate: 50 ml/min; CO_2/CH_4 molar ratio: 1:1).

greater extent in the plasma-catalytic reaction with higher discharge power [138, 149]. The higher hydrocarbons and oxygenates that are generated in the plasma process with high discharge power but cannot be identified by the GC, may be another reason for the decrease in the carbon balance. The plasma-catalytic reforming process using the Ni/Al catalyst shows the maximum carbon balance, followed by that using the Ni/Mg, Ni/Si and Ni/Ti catalyst at a specified discharge power. In this study, a maximum carbon balance of 96.4% is achieved when the Ni/Al catalyst is used in the plasma-catalytic reforming process at a discharge power of 30 W. At the same discharge power, the carbon balance in the gas stream of plasma-catalytic reaction using the Ni/Mg, Ni/Si and Ni/Ti catalyst is 96.2%, 95.9% and 95.7%, respectively.

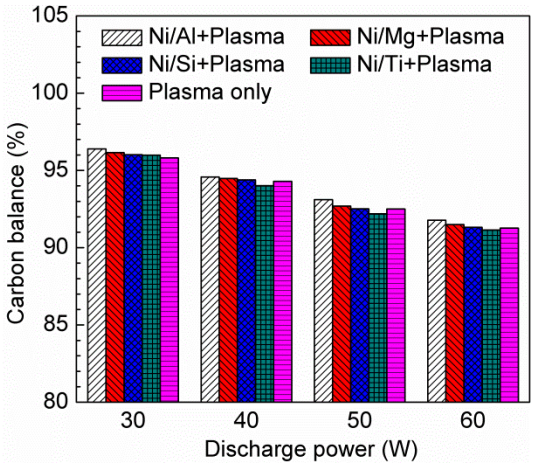

Figure 6.6 Effect of the supports on the carbon balance of the plasma-catalytic dry reforming process as a function of discharge power (total feed flow rate: 50 ml/min; CO_2/CH_4 molar ratio: 1:1).

The TG results of the Ni catalysts after the plasma-catalytic reaction at a discharge power of 50 W for 150 min are shown in **Figure 6.7**. The type of carbon deposition on these spent catalyst are quite similar, mainly the active carbonaceous species (C_α) and the less active carbonaceous species (C_β) [267]. The details of the carbon deposition will be discussed in Section 7.3.3.4. The total amount of carbon deposition formed on the surface of Ni/Ti catalyst is up to 5.3%, while it is 4.9% for the Ni/Si catalyst, 4.2% for the Ni/Mg catalyst and only 3.8% for the Ni/Al catalyst. These amounts of carbon deposition are not only lower than those detected in the conventional thermal catalytic dry reforming of CH_4 [267-270], but also lower than the carbon deposition in the previous plasma-catalytic dry reforming of CH_4 in a DBD reactor [163, 164]. Wang et al. reported that the carbon deposition was 5.4% and 11.5% when reduced and unreduced Ni/γ-Al_2O_3 catalysts were used in the plasma-catalytic dry reforming of CH_4 in a DBD reactor [163].

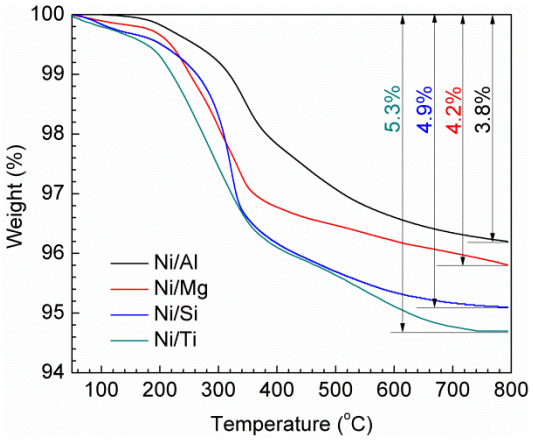

Figure 6.7 TG results of different supported Ni catalysts after reaction at a discharge power of 50 W for 150 min.

The carbon deposition in the conventional thermal-catalytic dry reforming of CH_4 can originate from either CH_4 decomposition (Equation (1-8)) or CO disproportionation (Equation (1-9)) [271]. In the plasma-catalytic dry reforming process, Li et al. stated that the carbon deposition mainly originated from CH_4 decomposition [272]. Catalysts with a larger amount of the strong basic sites have a high affinity to chemically adsorb the CO_2 molecules; this will improve the oxygen content on the catalyst surface and thus reduce the carbon deposition by carbon gasification. The larger amount of the strong basic sites on the Ni/Al catalyst therefore enables it to have high carbon resistance.

The relationship between the carbon deposition and the active metal particle size has been thoroughly discussed and several critical Ni particle sizes have been reported, below which the carbon deposition can be inhibited. For example, Tang et al. stated that this critical size was 10 nm for metallic nickel particle to inhibit the carbon deposition [273]. Kim et al. reported that a critical size of 7 nm for nickel particles to suppress the carbon formation during the dry reforming process [274]. The larger specific surface area in the Ni/Al catalyst results in higher dispersion of the Ni particles and thus smaller Ni particle size, which contributes to the reduced carbon deposition on the Ni/Al catalyst.

Therefore, we can conclude that the large surface area and larger amount of the strong basic sites on the Ni/Al catalyst contribute to the lower carbon deposition on this catalyst in comparison to the other catalysts. In addition, it is worthy to note that the carbon deposition on the catalysts in the plasma-catalytic dry reforming process is much lower compared with that in the conventional thermal catalytic dry reforming reaction using similar catalysts [275].

6.2.2.5 Energy efficiency

Figure 6.8 shows the effect of the different catalyst supports on the EC and FPE of the plasma reforming reaction at a discharge power of 30 W. The EC for CO_2 conversion is higher than that for CH_4 conversion in the plasma reaction both with and without catalysts. This result is mainly due to the higher conversion of CH_4 than that of CO_2, which have more CH_4 converted at the same discharge power. The introduction of the Ni catalysts decreases the EC for reactant conversion by differing amounts. When the Ni/Al catalyst is used, the minimum EC for CO_2 conversion, CH_4 conversion and total carbon conversion is 9.9 MJ/mol, 6.2 MJ/mol and 3.8 MJ/mol, which is decreased by 7.4%, 4.9% and 5.7%, respectively, compared with those values obtained in the plasma-only process. The Ni/Al catalyst also leads to minimum EC for H_2 and syngas production.

The FPE of the plasma reforming process is also enhanced by combining Ni catalysts with the plasma system. The maximum FPE (10.4%) is achieved when the Ni/Al catalyst is packed in the plasma region, followed by the Ni/Mg, Ni/Si and

Ni/Ti catalysts. This maximum FPE is increased by 6.1%, compared with that obtained in the plasma dry reforming process without catalyst.

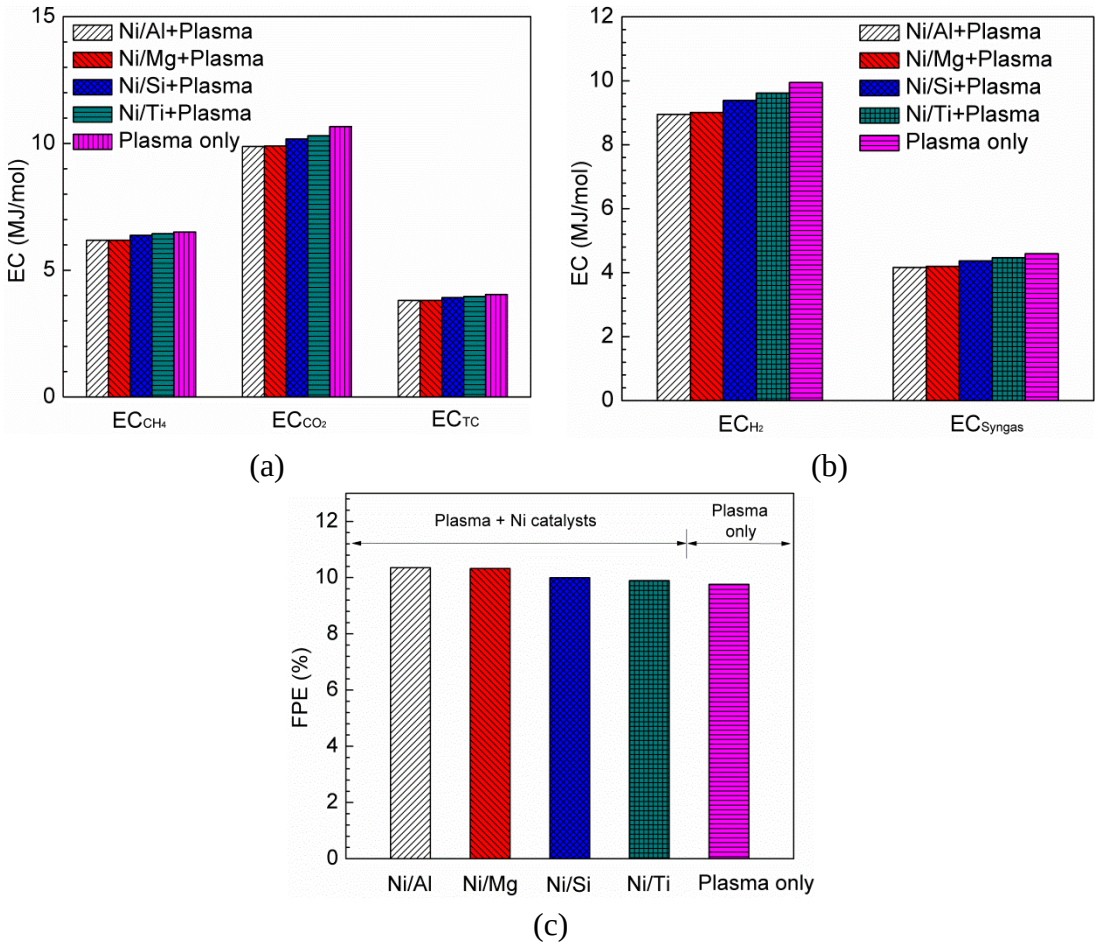

Figure 6.8 Effect of the supports on (a) the EC for CH_4 conversion, CO_2 conversion and total carbon conversion; (b) the EC for H_2 and syngas production; (c) the FPE (discharge power: 30 W; total feed flow rate: 50 ml/min; CO_2/CH_4 molar ratio: 1:1).

6.3 Optimisation of Plasma-Catalytic Dry Reforming of CH_4 using Design of Experiments

6.3.1 Experimental section

The Ni/γ-Al_2O_3 catalysts with different Ni loadings (5 wt.%, 7.5 wt.%, 10 wt.%, 12.5 wt.% and 15 wt.%) are prepared by the conventional wetness impregnation method using $Ni(NO_3)_2{\cdot}6H_2O$ as the metal precursor. The preparation procedure is the same as that in Section 2.2. The obtained samples are denoted as *x*Ni (*x* = 5, 7.5, 10, 12.5 and 15). The characterisation methods used to reveal the catalyst properties are similar to those in Section 6.2.1.

The plasma-catalytic dry reforming of CH_4 using Ni/γ-Al_2O_3 catalysts with different Ni loadings are performed in a coaxial DBD reactor. The experimental

system and procedure are the same as those in Section 6.2.1. In this section, the processing parameters of the plasma process include discharge power, total flow rate, CO_2/CH_4 molar ratio in the feed gas and the Ni loading in the Ni/γ-Al_2O_3 catalyst. The range of these plasma processing parameters is setup by design of experiments (DoE).

6.3.2 DoE

In this study, a four-factor and five-level CCD based RSM is used to investigate the effects of each independent factor and their interactions on the reaction performance of the plasma-catalytic dry reforming process. Based on the results of our previous work and other papers [91, 162], discharge power (*A*), total flow rate (*B*), CO_2/CH_4 molar ratio (*C*), and Ni loading (*D*) have been identified as the four most important independent parameters affecting the plasma-catalytic dry reforming process and thus have been chosen as the independent variables for the design, while CO_2 conversion (Y_1), CH_4 conversion (Y_2), CO yield (Y_3) , H_2 yield (Y_4) and FPE (Y_5) are identified as the responses. The coded and actual levels of the independent variables are given in **Table 6.2**.

Table 6.2 Experimental independent variables: coded and real values in CCD.

Parameter	Unit	Code	Level and range (coded)				
			-2	-1	0	+1	+2
Discharge power	W	*A*	20	30	40	50	60
Total flow rate	ml/min	*B*	25	50	75	100	125
CO_2/CH_4	-	*C*	0.5	0.75	1	1.25	1.5
Ni loading	wt.%	*D*	5	7.5	10	12.5	15

In the CCD design, the response variables will be fitted into a second-order model in order to correlate the response variables to the independent variables once the experiments are performed. The general form of the second-order polynomial equation is defined as follows [252]:

$$Y = \beta_0 + \sum_{i=1}^{3} \beta_i X_i + \sum_{i=1}^{3} \beta_{ii} X_{ii}^{\ 2} + \sum_{i=1}^{2} \sum_{j=i+1}^{3} \beta_{ij} X_i X_j \qquad (6\text{-}1)$$

where Y is the response, β_0 is a constant coefficient, β_i and β_{ii} are linear and quadratic coefficients for the term X_i and X_{ii}, respectively. β_{ij} are the coefficients representing the interactions of X_i and X_j. This model can be used to predict the reaction performance under different process conditions.

The analysis of variance (ANOVA) is used to evaluate the adequacy and fitness of the models. The statistical significance of the models and each term in the models can be identified by the *F*-test and adequacy measures such as the coefficient

of determination R^2, adjusted R^2 and predicted R^2. The difference between the predicted R^2 and adjusted R^2 should be within 0.2 for a well-developed model [252]. The above analysis is conducted using a regression analysis program coupled with ANOVA analysis at 5% significance level incorporated in Design Expert software version 9, trial version [276].

6.3.3 Experimental results

6.3.3.1 Catalyst properties

(1) Surface structures of the catalysts

The physicochemical properties of the Ni/γ-Al_2O_3 catalysts, such as specific surface area, pore volume and average pore diameter are summarised in **Table 6.3**. The specific surface area gradually decreases from 294.0 m^2/g to 223.9 m^2/g with the increase of the Ni loading. Similarly, the pore volume of the catalysts also decreases from 0.43 cm^3/g to 0.34 cm^3/g when increasing the Ni content. In contrast, an increase in average pore diameter from 3.63 to 3.84 nm on the Ni/γ-Al_2O_3 catalysts is observed when increasing the Ni loading from 5 wt.% to 15 wt.%.

Table 6.3 Physicochemical properties of the fresh catalysts with different Ni loadings.

Sample	S_{BET} (m^2/g)	Pore volume (cm^3/g)	Pore diameter (nm)
5Ni	294.0	0.43	3.63
7.5Ni	274.9	0.42	3.75
10Ni	268.0	0.39	3.80
12.5Ni	249.9	0.35	3.83
15Ni	223.9	0.34	3.84

Figure 6.9 shows the XRD patterns of the fresh catalyst samples with different Ni loadings. The XRD pattern of the γ-Al_2O_3 support shows five major diffraction peaks, which are in accordance with those of the γ-Al_2O_3 crystalline with cubic structure (2θ =14.5°, 28.3°, 38.5 °, 49.7 ° and 67.1°, PDF # 52-0803). The diffraction peaks of NiO are detected in the impregnated Ni catalysts (2θ = 37.2°, 43.3°, PDF # 44-1159). Obviously, the NiO peak at 2θ = 43.3° is intensified with increasing Ni loading. This reflects the formation of the larger NiO particle in the catalyst, which is due to the increased aggregation of Ni particles at a higher concentration of nickel. This phenomenon has been reported in previous studies [268].

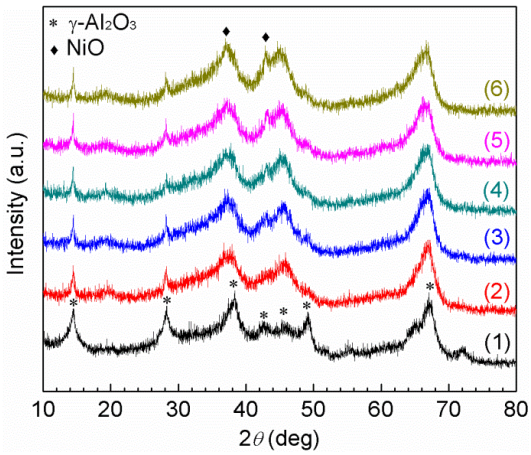

Figure 6.9 XRD patterns of catalyst support and fresh Ni/Al_2O_3 catalyst with different Ni loadings: (1) γ-Al_2O_3; (2) 5Ni; (3) 7.5Ni; (4) 10Ni; (5) 12.5Ni; (6) 15Ni.

6.3.3.2 Statistical model analysis

In this study, the total number of the experimental samples required for the CCD design is 30, including six replicated experimental runs using the processing parameters at the centre points (No. 7, 11, 13, 19, 23 and 27), shown in **Table 6.4**.

(1) Effect of operating variables on CO_2 conversion (Y_1)

The quadratic model for CO_2 conversion in terms of coded and actual factors is presented in Equations (6-2) and (6-3), where *P*, *F*, *R* and *N* account for discharge power, total flow rate, CO_2/CH_4 molar ratio and Ni loading, respectively.

Model in terms of coded factors:

$$\begin{aligned} Y_1 &: \mathrm{CO_2\ conversion\,(\%)} \\ &= +20.45 + 2.93\times A - 5.15\times B - 1.88\times C - 0.22\times D - 0.74\times AB \\ &\quad - 0.30\times AC - 0.042\times AD + 0.31\times BC + 0.073\times BD + 0.029\times CD \\ &\quad + 0.16\times A^2 + 0.051\times B^2 - 0.22\times C^2 - 0.55\times D^2 \end{aligned} \tag{6-2}$$

Model in terms of actual factors:

$$\begin{aligned} Y_1 &: \mathrm{CO_2\ conversion\,(\%)} \\ &= +14.047 + 0.525\times P - 0.161\times F - 9.416\times 10^{-3}\times R + 1.597\times N \\ &\quad - 2.979\times 10^{-3}\times PF - 0.118\times PR - 1.688\times 10^{-3}\times PN + 0.0499\times FR \\ &\quad + 1.167\times 10^{-3}\times FN + 0.046\times RN + 1.580\times 10^{-3}\times P^2 \\ &\quad + 8.106\times 10^{-5}\times F^2 - 3.493\times R^2 - 0.087\times N^2 \end{aligned} \tag{6-3}$$

Table 6.5 presents the ANOVA analysis for CO_2 conversion. Based on the 95% confidence level, the model is significant as the *F*-value (1432.55) is much higher than the critical value (2.43 in this case) [252] and the *p*-value is less than 0.05, indicating that the model is adequate to predict CO_2 conversion within the range of independent variables. This can also be evidenced by a good agreement (R^2 close to 1) between the experimental data and the simulated values from the regression model. In addition, the value of the predicted R^2 is in agreement with that

of the adjusted R^2, which also demonstrates the stability and validity of the established model for CO_2 conversion.

Table 6.4 Experiment matrix of four-factor and five-level CCD and results.

Exp. order	Factors				Y_1	Y_2	Y_3	Y_4	Y_5
	P[a)] (W)	F[b)] (ml/min)	R[c)]	N[d)] (wt.%)	C_{CO2} (%)	C_{CH4} (%)	Y_{CO} (%)	Y_{H2} (%)	*FPE* (%)
1	40	75	1	15	18.1	25.4	11.0	9.0	7.5
2	20	75	1	10	15.5	21.0	9.8	7.3	11.3
3	40	75	1.5	10	16.3	37.2	15.9	13.0	9.4
4	40	75	0.5	10	23.1	20.2	8.5	6.9	6.6
5	30	100	1.25	7.5	11.2	22.2	9.7	7.5	10.0
6	50	100	1.25	12.5	19.1	33.1	14.2	12.0	8.2
7[e)]	40	75	1	10	20.3	28.7	12.8	10.1	8.3
8	30	100	0.75	7.5	14.0	14.3	6.6	4.6	7.7
9	50	50	1.25	7.5	26.5	48.1	20.3	17.4	7.3
10	40	75	1	5	18.7	26.9	11.4	9.4	7.7
11[f)]	40	75	1	10	20.5	29.3	12.6	10.2	8.2
12	50	100	0.75	12.5	18.6	21.9	8.4	6.8	6.5
13[g)]	40	75	1	10	20.5	29.2	12.7	10.3	8.3
14	50	100	0.75	7.5	19.1	21.8	8.6	7.0	6.7
15	50	50	0.75	7.5	31.7	36.6	16.3	13.9	6.6
16	50	100	1.25	7.5	15.1	31.4	11.8	9.7	7.9
17	40	25	1	10	31.0	44.0	19.1	16.6	5.4
18	50	100	1.25	12.5	14.8	30.5	11.5	9.3	7.8
19[h)]	40	75	1	10	20.6	29.3	12.4	10.2	8.1
20	30	100	0.75	12.5	13.6	14.2	6.5	4.5	7.6
21	30	100	1.25	12.5	11.0	20.7	9.4	7.2	9.8
22	50	50	0.75	12.5	30.9	35.5	15.9	13.5	6.5
23[i)]	40	75	1	10	20.4	29.4	12.9	10.2	8.5
24	40	125	1	10	10.5	17.5	7.1	4.8	7.3
25	30	50	0.75	7.5	23.6	25.6	11.0	9.4	7.2
26	30	50	1.25	7.5	19.6	38.4	14.6	12.5	8.2
27[j)]	40	75	1	10	20.4	29.8	12.4	10.3	8.2
28	60	75	1	10	27.0	41.2	18.4	14.6	8.1
29	50	50	1.25	12.5	25.8	46.0	19.8	16.9	7.1
30	30	50	0.75	12.5	23.0	24.2	10.7	9.1	7.1

a)-d) P: discharge power; F: total flow rate; R: CO_2/CH_4; N: Ni loading;

e)-g) Replicated experimental runs (run order: 7, 11, 13, 19, 23 and 27).

Table 6.5 ANOVA for response surface quadratic model of CO_2 conversion.

Model terms	Sum of squares	Degree of freedom	Mean square	*F*-value	*p*-value
Model Equation (6-2)	952.08	14	68.01	1432.55	<0.0001
A	*206.18*	*1*	*206.18*	*4343.27*	*<0.0001*
B	*636.96*	*1*	*636.96*	*13417.53*	*<0.0001*
C	*84.89*	*1*	*84.89*	*1788.16*	*<0.0001*
D	*1.12*	*1*	*1.12*	*23.55*	*0.0002*
AB	*8.88*	*1*	*8.88*	*186.98*	*<0.0001*
AC	*1.40*	*1*	*1.40*	*29.51*	*<0.0001*
AD	*0.03*	*1*	*0.03*	*0.60*	*0.4505*
BC	*1.56*	*1*	*1.56*	*32.84*	*<0.0001*
BD	*0.09*	*1*	*0.09*	*1.79*	*0.2007*
CD	*0.01*	*1*	*0.01*	*0.28*	*0.6047*
A^2	*0.68*	*1*	*0.68*	*14.42*	*0.0018*
B^2	*0.07*	*1*	*0.07*	*1.48*	*0.2421*
C^2	*1.31*	*1*	*1.31*	*27.53*	*<0.0001*
D^2	*8.20*	*1*	*8.20*	*172.63*	*<0.0001*
Residual	0.71	15	0.047	-	-
Total	952.80	29	-	-	-

R^2: 0.9993; adjusted R^2: 0.9886; predicted R^2: 0.9862.

In order to determine the significant terms in the model for further analysis, the *p*-value of each term is estimated. If the *p*-value of a term (individual factor or interaction of two factors) is below the critical value 0.05 (level of significance), the corresponding term is considered to have a significant impact on the process performance. In this study, *A*, *B*, *C*, *D*, *AB*, *AC*, *BC*, A^2, C^2 and D^2 are identified as the significant terms, while terms *AD*, *BD*, *CD* and B^2 play a weak role in CO_2 conversion. However, the insignificant terms are not eliminated in the model Equation (6-2) in order to obtain a hierarchy model. The relative importance of a term is determined by its *F*-value. Total flow rate has the most significant impact on CO_2 conversion compared with the other factors due to the highest *F*-value of 13417.53.

Response surface plots provide a method to study the effects of different processing parameters and their interactions on each response systematically and efficiently in the form of a three dimensional response surface and corresponding projected contour derived from the regression equations. If there is no or weak interaction between two processing parameters, the fitted response surface will be a plane or a regular curved surface (e.g. contour lines will either straight, or parallel

with each other, or symmetrical about a specified line). In contrast, if two different processing parameters strongly interact, the fitted response surface will be distorted, while the contour produced by the second-order model will exhibit an elliptical or saddle nature [277]. This phenomenon is also reflected from the gradient of the response with respect to one of these processing parameters. If two processing parameters have a significant interaction effect, the gradient of the response to one processing parameter can be significantly different when changing the other parameter.

Figure 6.10 shows the combined effect of discharge power and total feed flow rate on CO_2 conversion in the form of three dimensional response surface and projected contour derived from regression Equation (6-3) at a CO_2/CH_4 molar ratio of 1:1 and a Ni loading of 10 wt.%. The maximum CO_2 conversion (around 40%) can be achieved at the highest discharge power (60 W) and the lowest total feed flow rate (25 ml/min). The conversion of CO_2 increases with the increase of discharge power from 20 W to 60 W and the increasing trend is more remarkable at the low total feed flow rate (e.g. 25 ml/min), which is reflected by the larger gradient of CO_2 conversion with respect to discharge power at the lower total feed flow rate, as plotted in **Figure 6.10** (b). This suggests that the interaction effect of discharge power and total feed flow rate plays a significant role, as confirmed by the small *p*-value (< 0.0001) of the term *AB*. In the plasma-catalytic dry reforming process, packing the Ni catalysts along the bottom of the plasma reactor shows strong filamentary discharge due to the large void fraction in the discharge gap, which significantly enhances the physical and chemical interactions between the plasma and catalyst. This phenomenon has also been observed in the previous study [91]. In this study, discharge power is changed by adjusting the applied voltage at a fixed frequency. Increasing the discharge power by only increasing the applied voltage leads to an increase in the number of microdischarges and the current intensity in the CO_2/CH_4 DBD; this is similar to our experimental work on CO_2 decomposition (see Chapter 3). Thus, more reaction channels and energetic electrons are formed in the plasma for the initiation and propagation of both physical and chemical reactions, which enhance the conversion of CO_2 and CH_4 (the conversion of CH_4 will be discussed in the next section). Moreover, a lower total feed flow rate is beneficial for improving the conversion of reactants due to the longer residence time of reactants in the plasma volume. In this study, the residence time is increased from 7.35 s to 36.73 s when the total flow rate decreases from 125 ml/min to 25 ml/min. Increasing the residence time of the reactants in the discharge region increases the possibility of activating the reactant molecules through collisions with energetic electrons and reactive species, thereby enhancing their conversions.

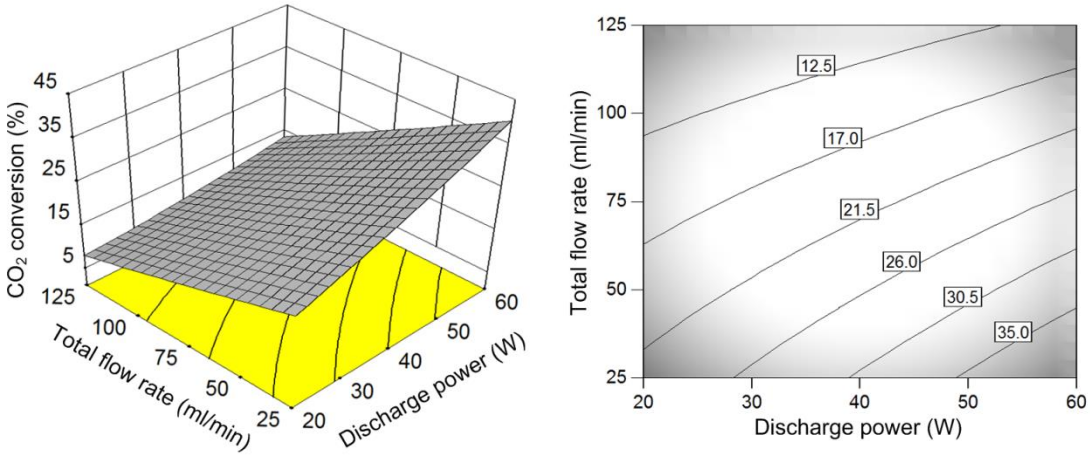

(a) (b)

Figure 6.10 Effect of discharge power, total feed flow rate and their interaction on CO_2 conversion at a CO_2/CH_4 molar ratio of 1:1 and a Ni loading of 10 wt.%: (a) 3D surface plot; (b) projected contour plot.

The combined effect of discharge power and CO_2/CH_4 molar ratio on CO_2 conversion is shown in **Figure 6.11**. The maximum CO_2 conversion (around 31%) is achieved at the lowest CO_2/CH_4 molar ratio (1:2) and the highest discharge power (60 W). Increasing CO_2/CH_4 molar ratio decreases the conversion of CO_2. This phenomenon is similar to that in the plasma dry reforming of CH_4 without catalyst [116]. Moreover, the effect of CO_2/CH_4 molar ratio on the conversion of CO_2 is dependent on discharge power, which is reflected by the gradient of CO_2 conversion with respect to CO_2/CH_4 molar ratio at different discharge powers as plotted in **Figure 6.11** (b). The gradient of CO_2 conversion with respect to CO_2/CH_4 molar ratio is only -5.2% at the discharge power of 20 W, whilst it is increased to -9.9% at the discharge power of 60 W. This suggests that the interaction between discharge power and CO_2/CH_4 molar ratio has a significant effect on CO_2 conversion, confirmed by the *p*-value (< 0.0001) of the term *AC*.

In addition, the conversion of CO_2 is slightly more sensitive to the effect of CO_2/CH_4 molar ratio at a lower total feed flow rate than that at a higher total feed flow rate, as shown in **Figure 6.12** (b). The gradient of CO_2 conversion with respect to CO_2/CH_4 molar ratio is -10.0% at a total feed flow rate of 25 ml/min, higher than that (-5.0%) obtained at a higher total feed flow rate of 125 ml/min. This shows that the interaction between total feed flow rate and CO_2/CH_4 molar ratio is significant, which is in consistent with the low *p*-value (< 0.0001) of the term *BC*, as listed in **Table 6.5**.

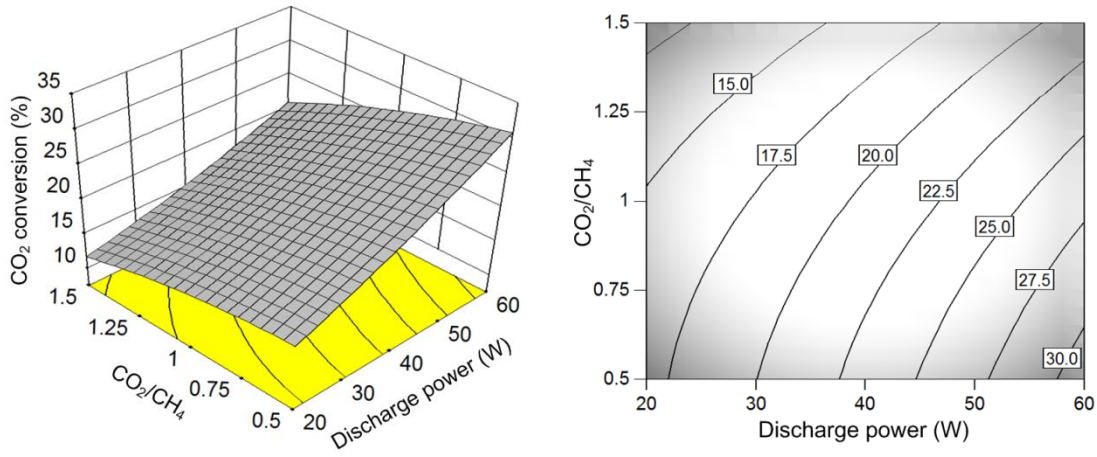

(a) (b)

Figure 6.11 Effect of discharge power, CO_2/CH_4 molar ratio and their interaction on CO_2 conversion at a total flow rate of 75 ml/min and a Ni loading of 10 wt.%: (a) 3D surface plot; (b) projected contour plot.

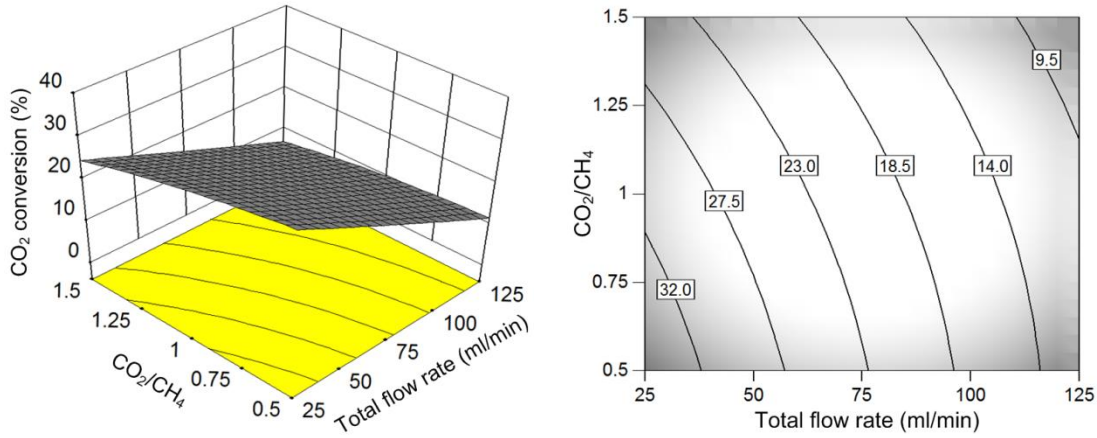

(a) (b)

Figure 6.12 Effect of total flow rate, CO_2/CH_4 molar ratio and their interaction on CO_2 conversion at a discharge power of 40 W and a Ni loading of 10 wt.%: (a) 3D surface plot; (b) projected contour plot.

Figure 6.13 shows the combined effect of discharge power and Ni loading on CO_2 conversion. Clearly, there exists an optimum Ni loading to obtain a high CO_2 conversion, regardless of the discharge power. Although a larger specific surface area is obtained at the lower Ni loading, fewer active sites are available on the catalyst surface to obtain higher reactant conversion. Therefore, CO_2 conversion initially increases by increasing the Ni loading. However, increasing the Ni loading leads to the aggregation of the active metal particles, and thus the specific surface area and metal dispersion are decreased [268]. All of these variations in the catalyst properties result in negative effects on the conversion of reactants. At a specified discharge power, the maximum CO_2 conversion is obtained at a moderate Ni loading,

which suggests that there exists an optimum Ni loading for higher reaction performance. The optimum Ni loading is near 10% at the low discharge power (20 W). Similar phenomenon has been observed in the work of Mahammadunnisa et al. [162]. They used similar Ni/Al_2O_3 catalysts with different Ni loadings (10 wt.%, 20 wt.% and 30 wt.%) for the plasma-catalytic dry reforming of CH_4 in a DBD reactor. Their results showed that maximum CO_2 and CH_4 conversions were obtained when the Ni/Al_2O_3 catalyst with the moderate Ni loading (20 wt.% Ni/Al_2O_3) was used.

Increasing discharge power from 20 W to 60 W slightly lowers the optimum Ni loading for high CO_2 conversion; however, the contour lines of CO_2 conversion are almost parallel to each other, which makes the gradient of CO_2 conversion with respect to discharge power almost constant regardless of Ni loading (see **Figure 6.13** (b)). This suggests the insignificant role of the interaction between discharge power and Ni loading on CO_2 conversion. **Table 6.5** also shows that the *p*-value (0.4776) of the term *AD* is much higher than the level of significance (0.05).

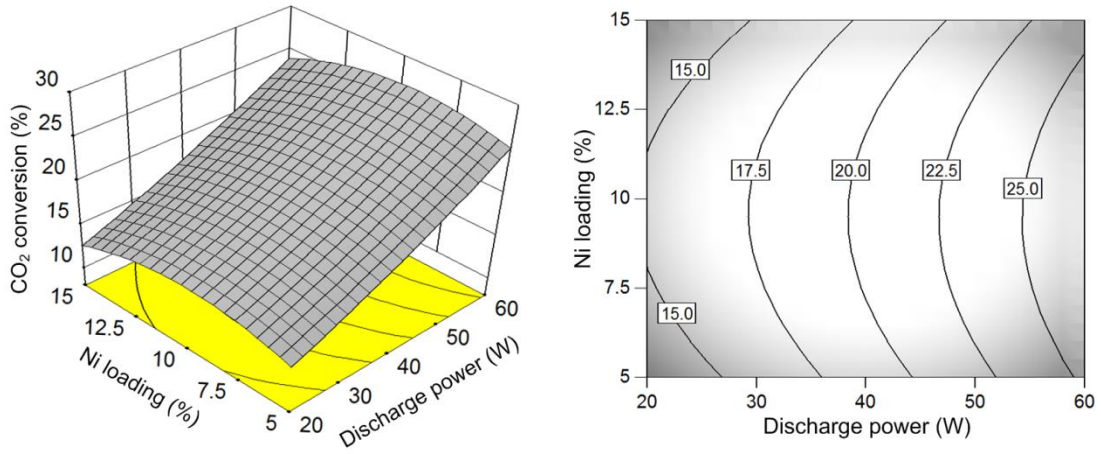

(a) (b)

Figure 6.13 Effect of discharge power, Ni loading and their interaction on CO_2 conversion at a total flow rate of 75 ml/min and a CO_2/CH_4 molar ratio of 1:1: (a) 3D surface plot; (b) projected contour plot.

(2) Effect of operating variables on CH_4 conversion (Y_2)

For the conversion of CH_4, the quadratic model in terms of coded and actual factors is expressed as follows.

Model in terms of coded factors:

$$\begin{aligned} Y_2 : \mathrm{CH_4}\ \text{conversion}\,(\%) &= +29.28 + 5.00\times A - 6.83\times B + 4.59\times C - 0.65\times D - 0.65\times AB \\ &\quad + 0.25\times AC + 0.27\times AD - 0.68\times BC + 0.46\times BD - 0.46\times CD \\ &\quad + 0.42\times A^2 + 0.34\times B^2 - 0.17\times C^2 - 0.80\times D^2 \end{aligned} \tag{6-4}$$

Model in terms of actual factors:

$$
\begin{aligned}
Y_2 : \mathrm{CH_4}\ \text{conversion}\,(\%) \\
&= -1.328 + 0.149\times P - 0.214\times F + 35.403\times R + 2.057\times N \\
&\quad - 2.613\times 10^{-3}\times PF + 0.099\times PR + 0.011\times PN - 0.110\times FR \\
&\quad + 7.342\times 10^{-3}\times FN - 0.730\times RN + 4.234\times 10^{-3}\times P^2 \\
&\quad + 5.422\times 10^{-4}\times F^2 - 2.737\times R^2 - 0.129\times N^2
\end{aligned}
\tag{6-5}
$$

The effect of the individual plasma processing parameter and their interactions on CH_4 conversion is shown in **Table 6.6**. The high *F*-value (403.39) from the *F*-test indicates that the quadratic model (Equation (6-4)) is significant for CH_4 conversion at a 95% level of confidence. *A*, *B*, *C*, *D*, *AB*, *BC*, *BD*, *CD*, A^2, B^2 and D^2 are identified as the significant model terms for the response of CH_4 conversion, due to their respective low *p*-value (< 0.05). Additionally, a high R^2 of 0.9874 and a small difference of 0.0206 between the predicted R^2 and the adjusted R^2 indicate that the quadratic model for CH_4 conversion is well developed and accurate to fit the experimental data. Total feed flow rate is also found to be the most significant term affecting the conversion of CH_4 with the highest *F*-value of 2760.71.

Table 6.6 ANOVA for response surface quadratic model of CH_4 conversion.

Model terms	Sum of squares	Degree of freedom	Mean square	*F*-value	*p*-value
Model Equation (6-4)	2287.19	14	163.37	403.39	< 0.0001
A	*598.91*	*1*	*598.91*	*1478.82*	*< 0.0001*
B	*1118.07*	*1*	*1118.07*	*2760.71*	*< 0.0001*
C	*506.13*	*1*	*506.13*	*1249.72*	*< 0.0001*
D	*10.02*	*1*	*10.02*	*24.75*	*0.0002*
AB	*6.83*	*1*	*6.83*	*16.86*	*0.0009*
AC	*0.98*	*1*	*0.98*	*2.41*	*0.1412*
AD	*1.18*	*1*	*1.18*	*2.91*	*0.1084*
BC	*7.50*	*1*	*7.50*	*18.51*	*0.0006*
BD	*3.37*	*1*	*3.37*	*8.32*	*0.0113*
CD	*3.33*	*1*	*3.33*	*8.22*	*0.0118*
A^2	*4.92*	*1*	*4.92*	*12.14*	*0.0033*
B^2	*3.15*	*1*	*3.15*	*7.78*	*0.0138*
C^2	*0.80*	*1*	*0.80*	*1.98*	*0.1795*
D^2	*17.71*	*1*	*17.71*	*43.73*	*< 0.0001*
Residual	6.07	15	0.40	-	-
Total	2293.26	29	-	-	-

R^2: 0.9874; adjusted R^2: 0.9849; predicted R^2: 0.9643.

Figure 6.14 shows the interaction effect between discharge power and total feed flow rate on CH_4 conversion. Similar with their effects on CO_2 conversion, higher discharge power and lower total flow rate contribute to the higher conversion of CH_4. The maximum CH_4 conversion almost reaches 60%, predicted by the three-dimensional response surface derived from the quadratic model Equation (6-5) at a discharge power of 60 W and a total flow rate of 25 ml/min. The small *p*-vale of 0.0009 for the model term *AB* (listed in **Table 6.6**) suggests the significant role of the interaction between discharge power and total flow rate on the response of CH_4 conversion. This is also reflected by the higher gradient of CH_4 conversion with respect to discharge power at the lower total feed flow rate than that at the higher total feed flow rate (0.63%/W at the total feed flow rate of 25 ml/min and 0.37%/W at the total feed flow rate of 125 ml/min), as illustrated by **Figure 6.14** (b). Compared with the data in **Figure 6.10**, the conversions of CH_4 are higher than those of CO_2 at the same experimental condition, which is similar to the results obtained in the plasma-only process. As mentioned above, the initial conversion reaction step of CO_2 and CH_4 in the plasma dry reforming of CH_4 is primarily controlled by electron-impact dissociation. More reaction pathways exist for CH_4 conversion than for CO_2 conversion. Although the conversions of CO_2 and CH_4 can promote each other when they are co-fed into the plasma system, the rate coefficient of the promotion reaction for CH_4 conversion is much higher than that of the promotion reaction for CO_2 conversion (see Section 5.3.2.1). All of these factors contribute to the higher conversion of CH_4 in comparison to that of CO_2.

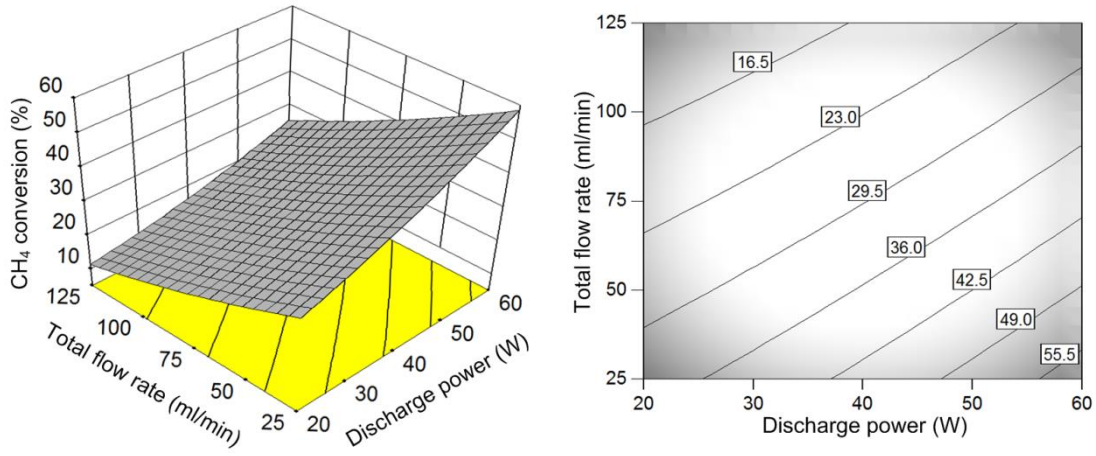

(a) (b)

Figure 6.14 Effect of discharge power, total flow rate and their interaction on CH_4 conversion at a CO_2/CH_4 molar ratio of 1:1 and a Ni loading of 10%: (a) 3D surface plot; (b) projected contour plot.

Figure 6.15 shows the combined effect of total feed flow rate and CO_2/CH_4 molar ratio on CH_4 conversion. A maximum CH_4 conversion (around 55%) is

achieved at the lowest total feed flow rate of 25 ml/min with a CO_2/CH_4 molar ratio of 3:2. Different from the effect of CO_2/CH_4 molar ratio on CO_2 conversion (see **Figure 6.11**), increasing the CO_2/CH_4 molar ratio is favourable to obtain higher CH_4 conversion. More oxygen can be supplied through CO_2 decomposition by increasing CO_2/CH_4 molar ratio, which contributes to the enhancement in CH_4 conversion by Equation (5-12). At the lowest total feed flow rate of 25 ml/min, CH_4 conversion increases from 31.7% to 55.5% when CO_2/CH_4 molar ratio rises from 1:2 to 3:2, whereas CH_4 conversion is enhanced by nearly a factor of 1.3 with the same increase in CO_2/CH_4 molar ratio at the highest total feed flow rate of 125 ml/min. This means that the gradient of CH_4 conversion with respect to CO_2/CH_4 molar ratio is dependent on total feed flow rate, as shown in **Figure 6.15** (b). These results indicate that the interaction between total feed flow rate and CO_2/CH_4 molar ratio has a significant effect on CH_4 conversion, confirmed by the small *p*-value for the term *BC* (0.0006).

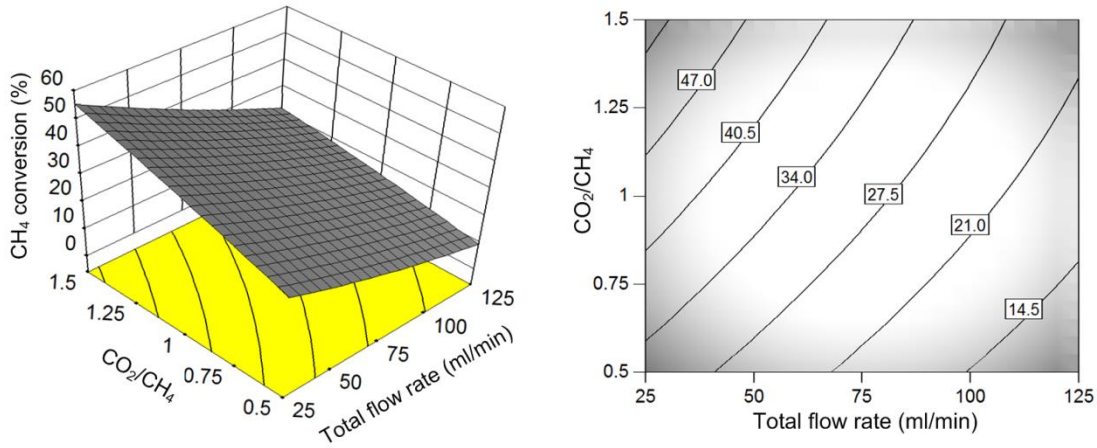

(a) (b)

Figure 6.15 Effect of total flow rate, CO_2/CH_4 molar ratio and their interaction on CH_4 conversion at a discharge power of 40 W and a Ni loading of 10 wt.%: (a) 3D surface plot; (b) projected contour plot.

Figure 6.16 shows the interaction effect of total flow rate and Ni loading on CH_4 conversion. Similar to the effect of the Ni loading on CO_2 conversion, there also exists an optimum Ni loading for higher CH_4 conversion. This optimum Ni loading is around 7.5 wt.% at the low total flow rate of 25 ml/min, and is gradually increased to a level slightly higher than 10 wt.% when the total flow rate increases to 125 ml/min. Moreover, the Ni loading significantly affects the gradient of CH_4 conversion with respect to total feed flow rate, which is 0.31%/(ml/min) at a Ni loading of 5 wt.%, and decreases to 0.23%/(ml/min) when the Ni loading increases to 15 wt.%. These results suggest that there is a significant interaction between the total feed flow rate and Ni loading on CH_4 conversion, which is confirmed by the *p*-value of 0.0113 for the term *BD*, shown in **Table 6.6**.

The optimum Ni loading for higher CH_4 conversion is also dependent on CO_2/CH_4 molar ratio, as shown in **Figure 6.17**. At the lowest CO_2/CH_4 molar ratio of 1:2, the optimum Ni loading is slightly higher than 10 wt.%, whereas it is decreased to around 7.5 wt.% when CO_2/CH_4 molar ratio is increased to 3:2. Additionally, the variation in Ni loading leads to different effect of the CO_2/CH_4 molar ratio on CH_4 conversion. At a Ni loading of 5 wt.%, CH_4 conversion is increased by a factor of 1.4 when CO_2/CH_4 molar ratio increases from 1:2 to 3:2, whilst it is only increased by 88.0% with the change of CO_2/CH_4 molar ratio at a higher Ni loading of 15 wt.%. This suggests that the interaction between CO_2/CH_4 molar ratio and Ni loading have a significant effect on CH_4 conversion, confirmed by the low *p*-value (0.0118) of the term *CD*.

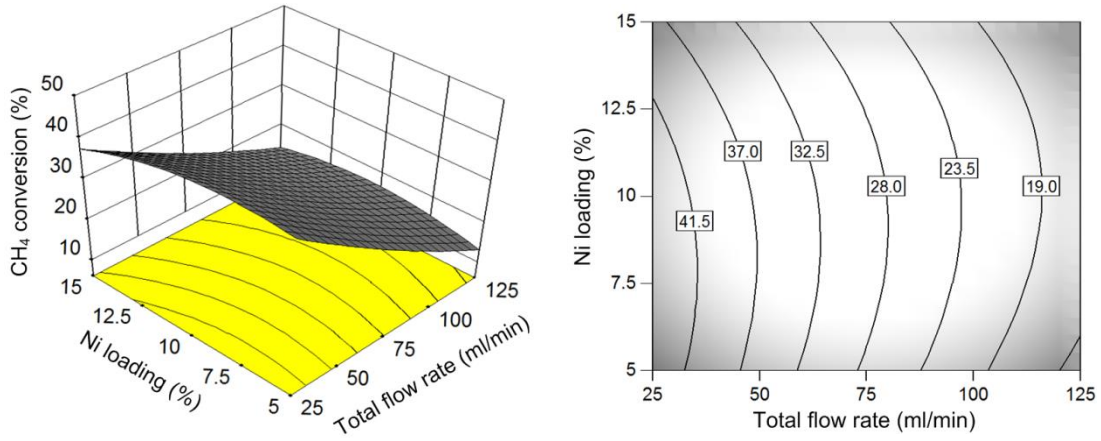

(a) (b)

Figure 6.16 Effect of total flow rate, Ni loading and their interaction on CH_4 conversion at a discharge power of 40 W and a CO_2/CH_4 molar ratio of 1:1: (a) 3D surface plot; (b) projected contour plot.

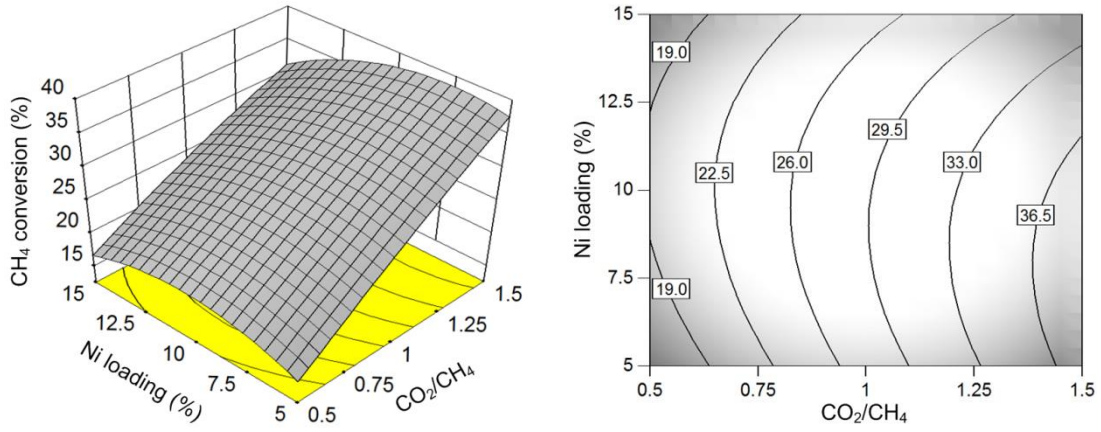

(a) (b)

Figure 6.17 Effect of CO_2/CH_4 molar ratio, Ni loading and their interaction on CH_4 conversion at a total flow rate of 75 ml/min and a discharge power of 40 W: (a) 3D surface plot; (b) projected contour plot.

(3) Effect of operating variables on CO yield (Y_3)

The quadratic model for CO yield based on the coded and actual factors is presented in Equations (6-6) and (6-7).

Model in terms of coded factors:

$$\begin{aligned} Y_3 &: \text{CO yield}(\%) \\ &= +12.61 + 1.97\times A - 3.11\times B + 1.76\times C - 0.14\times D - 0.86\times AB \\ &\quad + 0.081\times AC - 0.017\times AD - 0.16\times BC + 0.038\times BD - 0.031\times CD \\ &\quad + 0.30\times A^2 + 0.054\times B^2 - 0.18\times C^2 - 0.43\times D^2 \end{aligned} \tag{6-6}$$

Model in terms of actual factors:

$$\begin{aligned} Y_3 &: \text{CO yield}(\%) \\ &= -8.132 + 0.188\times P + 0.019\times F + 13.894\times R + 1.358\times N \\ &\quad - 3.432\times 10^{-3}\times PF + 0.033\times PR - 6.836\times 10^{-4}\times PN - 0.026\times FR \\ &\quad + 6.007\times 10^{-4}\times FN - 0.050\times RN + 3.000\times 10^{-3}\times P^2 \\ &\quad + 8.629\times 10^{-5}\times F^2 - 2.865\times R^2 - 0.069\times N^2 \end{aligned} \tag{6-7}$$

The ANOVA analysis for CO yield is listed in **Table 6.7**. The quadratic model (Equation (6-6)) is tested to be significant for CO yield at a 95% confidence level due to the high *F*-value of 231.52, which indicates that the model is adequate to predict the yield of CO. Additionally, a high value of 0.9954 for R^2 also shows the accuracy of the model. The model terms of *A*, *B*, *C*, *AB*, A^2, C^2 and D^2 are considered to be significant based on their *p*-value being lower than 0.05.

Figure 6.18 shows the combined effect of discharge power and total feed flow rate on CO yield. The distorted-quadrangle response surface for CO yield indicates that the higher discharge power and lower total flow rate favours the higher CO yield. The maximum CO yield of 27.6% is obtained at the highest discharge power of 60 W and the lowest total feed flow rate of 25 ml/min. At the total feed flow rate of 25 ml/min, CO yield is enhanced by over 110% when discharge power increases from 20 to 60 W, while it only increases from 7.3% to 8.3% with the change of discharge power at the total feed flow rate of 125 ml/min. Similarly, the gradient of CO yield with respect to total feed flow rate is much higher at a high discharge power (e.g. 60 W) compared to that at a lower discharge power (e.g. 20 W). These phenomena suggest that the interaction between discharge power and total feed flow rate play an important role in the yield of CO, which can be confirmed by the presence of the contour lines in **Figure 6.18** (b) and the low *p*-value (< 0.0001) for the term *AB* in **Table 6.7**.

Table 6.7 ANOVA for response surface quadratic model of CO yield.

Model terms	Sum of squares	Degree of freedom	Mean square	*F*-value	*p*-value
Model Equation (6-6)	422.20	14	30.16	231.52	< 0.0001
A	*92.95*	*1*	*92.95*	*713.62*	*< 0.0001*
B	*232.58*	*1*	*232.58*	*1785.56*	*< 0.0001*
C	*74.13*	*1*	*74.13*	*569.09*	*< 0.0001*
D	*0.45*	*1*	*0.45*	*3.47*	*0.0820*
AB	*11.78*	*1*	*11.78*	*90.41*	*< 0.0001*
AC	*0.11*	*1*	*0.11*	*0.81*	*0.3815*
AD	*4.673E-003*	*1*	*4.673E-003*	*0.04*	*0.8523*
BC	*0.42*	*1*	*0.42*	*3.20*	*0.0940*
BD	*0.02*	*1*	*0.02*	*0.17*	*0.6832*
CD	*0.02*	*1*	*0.02*	*0.12*	*0.7333*
A^2	*2.47*	*1*	*2.47*	*18.95*	*0.0006*
B^2	*0.08*	*1*	*0.08*	*0.61*	*0.4460*
C^2	*0.88*	*1*	*0.88*	*6.75*	*0.0202*
D^2	*5.10*	*1*	*5.10*	*39.18*	*< 0.0001*
Residual	1.95	15	0.13	-	-
Total	424.80	29	-	-	-

R^2: 0.9954; adjusted R^2: 0.9841; predicted R^2: 0.9756.

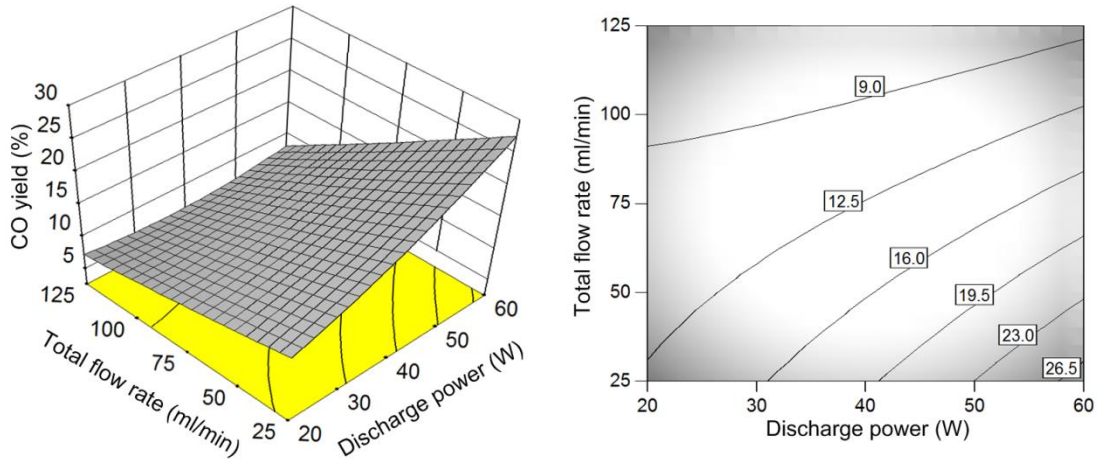

(a) (b)

Figure 6.18 Effect of discharge power, total flow rate and their interaction on CO yield at a CO_2/CH_4 molar ratio of 1:1 and a Ni loading of 10 wt.%: (a) 3D surface plot; (b) projected contour plot.

The effect of CO_2/CH_4 molar ratio and Ni loading as well as their interaction on CO yield is shown in **Figure 6.19**. An optimum Ni loading also exists to obtain the higher yield of CO. This optimum Ni loading is slightly lower than 10 wt.%, regardless of CO_2/CH_4 molar ratio. The yield of CO increases with the increase of CO_2/CH_4 molar ratio from 1:2 to 3:2, regardless of the Ni loading. This can also be reflected by a weak variation in the gradient of CO yield with respect to CO_2/CH_4 molar ratio at different Ni loadings, as plotted in **Figure 6.19** (b). The gradient of CO yield with respect to CO_2/CH_4 molar ratio is 7.3%, 7.0% and 6.8%, respectively, at a Ni loading of 5 wt.%, 10 wt.% and 15 wt.%. The *p*-value (0.7333) of the term related to the interaction of these two parameters is much higher than the critical value (0.05). These results clearly show that the interaction between CO_2/CH_4 molar ratio and Ni loading on CO yield is insignificant.

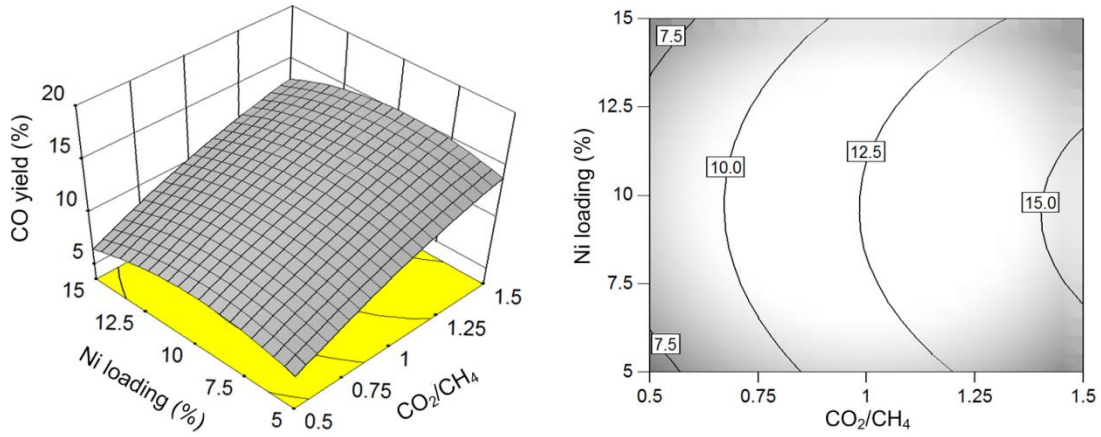

(a) (b)

Figure 6.19 Effect of CO_2/CH_4 molar ratio, Ni loading and their interaction on CO yield at a discharge power of 40 W and a total flow rate of 75 ml/min: (a) 3D surface plot; (b) projected contour plot.

(4) Effect of operating variables on H_2 selectivity (Y_4)

Equations (6-8) and (6-9) present the quadratic model for the response of H_2 yield in terms of coded and actual factors, respectively. The quadratic model is tested to be significant at 95% level of confidence based on the *F*-value of 1309.88 shown in the ANOVA analysis for the yield of H_2 (**Table 6.8**). In addition, the accuracy of the model is also confirmed by the high value of R^2 (0.9993) and the small difference between adjusted R^2 and predicted R^2 (0.0326). Clearly from **Table 6.8**, *A*, *B*, *C*, *D*, *AB*, *BC*, A^2, B^2, C^2 and D^2 are identified as the significant model terms for the response of H_2 yield, due to their small *p*-value (< 0.5).

Model in terms of coded factors:

$$
\begin{aligned}
&Y_4: \mathrm{H_2\ yield\,(\%)} \\
&= +10.22 + 1.77\times A - 2.99\times B + 1.49\times C - 0.14\times D - 0.61\times AB \\
&\quad + 0.030\times AC - 0.026\times AD - 0.14\times BC + 0.050\times BD - 0.033\times CD \\
&\quad + 0.17\times A^2 + 0.097\times B^2 - 0.091\times C^2 - 0.27\times D^2
\end{aligned}
\tag{6-8}
$$

Model in terms of actual factors:

$$
\begin{aligned}
&Y_4: \mathrm{H_2\ yield\,(\%)} \\
&= -4.463 + 0.226\times P - 0.030\times F + 10.619\times R + 0.850\times N \\
&\quad - 2.440\times 10^{-3}\times PF + 0.012\times PR - 1.035\times 10^{-3}\times PN - 0.023\times FR \\
&\quad + 8.012\times 10^{-4}\times FN - 0.053\times RN + 1.656\times 10^{-3}\times P^2 \\
&\quad + 1.556\times 10^{-4}\times F^2 - 1.449\times R^2 - 0.044\times N^2
\end{aligned}
\tag{6-9}
$$

Table 6.8 ANOVA for response surface quadratic model of H_2 yield.

Model terms	Sum of squares	Degree of freedom	Mean square	*F*-value	*p*-value
Model Equation (6-8)	353.41	14	25.24	1309.88	< 0.0001
A	*75.22*	*1*	*75.22*	*3903.1*	*< 0.0001*
B	*214.44*	*1*	*214.44*	*11127.16*	*< 0.0001*
C	*53.09*	*1*	*53.09*	*2754.87*	*< 0.0001*
D	*0.5*	*1*	*0.5*	*25.95*	*0.0001*
AB	*5.96*	*1*	*5.96*	*309.05*	*< 0.0001*
AC	*0.014*	*1*	*0.014*	*0.74*	*0.4037*
AD	*0.011*	*1*	*0.011*	*0.56*	*0.4673*
BC	*0.33*	*1*	*0.33*	*17.05*	*0.0009*
BD	*0.04*	*1*	*0.04*	*2.08*	*0.1696*
CD	*0.018*	*1*	*0.018*	*0.91*	*0.3545*
A^2	*0.75*	*1*	*0.75*	*39.02*	*< 0.0001*
B^2	*0.26*	*1*	*0.26*	*13.46*	*0.0023*
C^2	*0.22*	*1*	*0.22*	*11.66*	*0.0038*
D^2	*2.04*	*1*	*2.04*	*105.99*	*< 0.0001*
Residual	0.29	15	0.019	-	-
Total	353.70	29	-	-	-

R^2: 0.9913; adjusted R^2: 0.9884; predicted R^2: 0.9658.

Figure 6.20 shows the combined effect of discharge power and total feed flow rate on the yield of H_2 at a CO_2/CH_4 molar ratio of 1:1 and a Ni loading of 10 wt.%. The maximum H_2 yield of 23.2% is achieved at the highest discharge power of 60 W and the lowest total feed flow rate of 25 ml/min. The yield of H_2 at a higher discharge power (e.g. 60 W) is more sensitive to total feed flow rate than that at a

lower discharge power (e.g. 20 W), as plotted in **Figure 6.20** (b). In addition, the gradient of H_2 yield with respect to discharge power at the lower total feed flow rate is much higher than that at the higher total feed flow rate (0.30%/W at total feed flow rate of 25 ml/min, while only 0.06%/W at total feed flow rate of 125 ml/min). This suggests that there is a significant interaction between discharge power and total feed flow rate on the yield of H_2, which can also be confirmed by the low *p*-value (< 0.0001) of the term related to the interaction of these two parameters, as listed in **Table 6.8**.

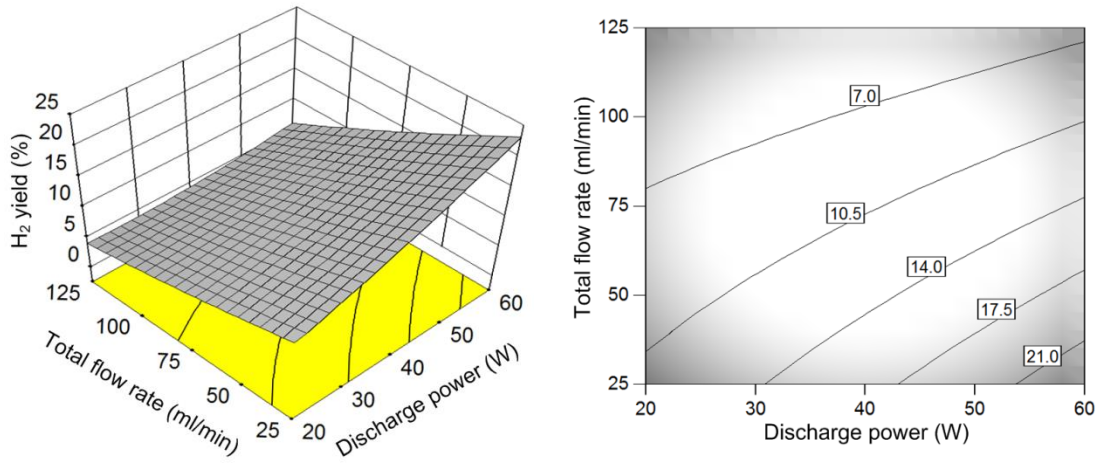

(a) (b)

Figure 6.20 Effect of discharge power, total flow rate and their interaction on H_2 yield at a CO_2/CH_4 molar ratio of 1:1 and a Ni loading of 10 wt.%: (a) 3D surface plot; (b) projected contour plot.

The small *p*-value of 0.0009 for the model term *BC* indicates that the effect of the interaction between total feed flow rate and CO_2/CH_4 molar ratio on the response of H_2 yield is significant. This can be reflected by the contour lines plotted in **Figure 6.21** (b), which shows that the H_2 yield at the higher CO_2/CH_4 molar ratio (e.g. 3:2) is more sensitive to total feed flow rate than that at the lower CO_2/CH_4 molar ratio (e.g. 1:2). In addition, at the low total feed flow rate of 25 ml/min, the gradient of H_2 yield with respect to CO_2/CH_4 molar ratio (7.1%) is higher than that (5.8%) obtained at the higher total feed flow rate of 125 ml/min. Compared with the data in **Figure 6.18**, the yield of H_2 is lower than that of CO at the same experimental condition. This mainly results from the occurrence of the RWGS reaction (Equation (5-2)), in which H_2 reacts with CO_2 to produce CO and H_2O.

The effect of discharge power and Ni loading as well as their interaction on the yield of H_2 is shown in **Figure 6.22**. There exists an optimum Ni loading for higher H_2 yield, which is similar to the effect of Ni loading on the yield of CO (see **Figure 6.19**). The optimum Ni loading is slightly lower than 10 wt.%, and is independent of discharge power. Increasing discharge power results in an increase in

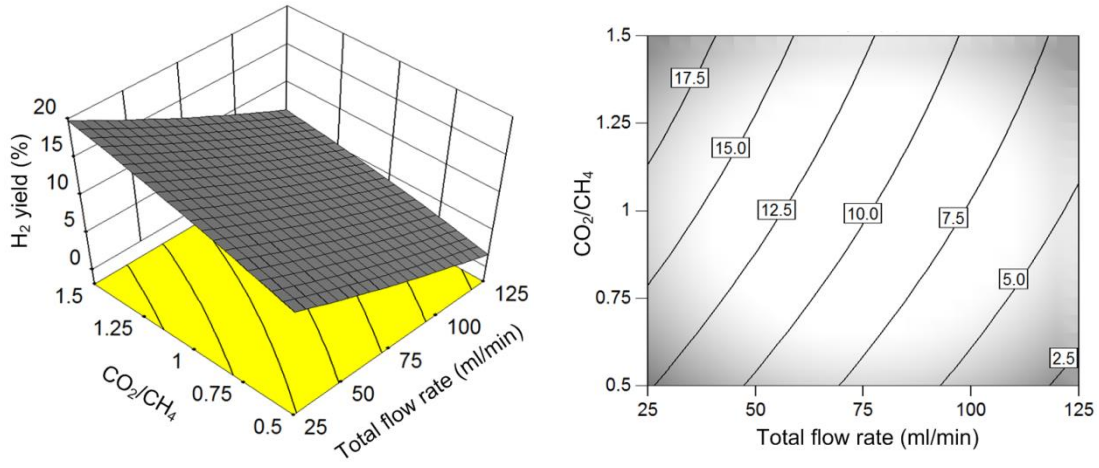

(a) (b)

Figure 6.21 Effect of total flow rate, CO_2/CH_4 molar ratio and their interaction on H_2 yield at a discharge power of 40 W and a Ni loading of 10 wt.%: (a) 3D surface plot; (b) projected contour plot.

the yield of H_2, regardless of the Ni loading; this is reflected by a nearly constant gradient of H_2 yield with respect to discharge power. This suggests that the effect of the interaction between the discharge power and Ni loading on H_2 yield is insignificant, confirmed by the high *p*-value (0.4673) of the model term *AD*.

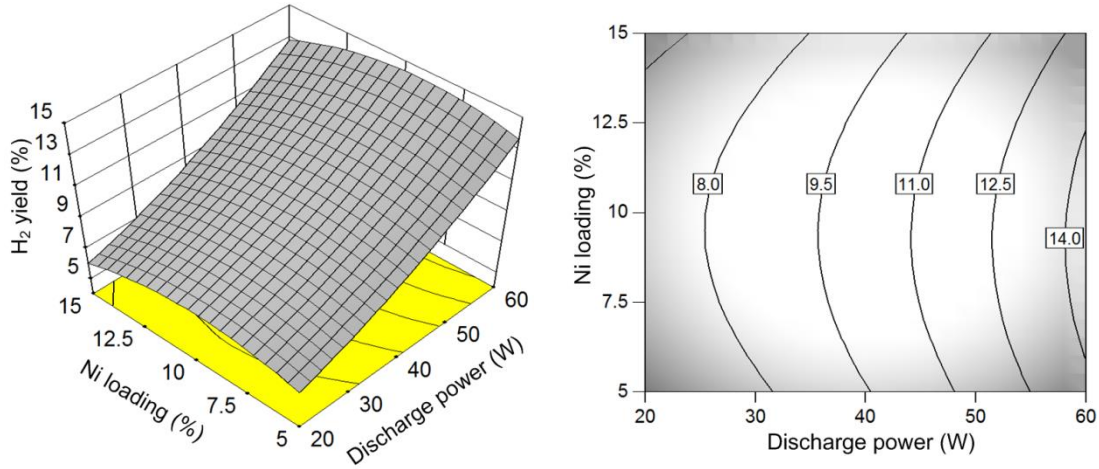

(a) (b)

Figure 6.22 Effect of discharge power, Ni loading and their interaction on H_2 yield at a total flow rate of 75 ml/min and a CO_2/CH_4 molar ratio of 1:1: (a) 3D surface plot; (b) projected contour plot.

(5) Effect of operating variables on FPE (Y_5)

The quadratic model for the response of FPE in terms of coded and actual factors is presented in Equations (6-10) and (6-11), respectively.

Model in terms of coded factors:

$$
\begin{aligned}
&Y_5: \text{FPE}(\%) \\
&= +8.26 - 0.66\times A + 0.43\times B + 0.67\times C - 0.065\times D - 0.20\times AB \\
&\quad - 0.17\times AC - 2.68\times 10^{-3}\times AD + 0.22\times BC - 0.012\times BD \\
&\quad - 2.206\times 10^{-3}\times CD + 0.31\times A^2 - 0.56\times B^2 - 0.10\times C^2 - 0.21\times D^2
\end{aligned}
\tag{6-10}
$$

Model in terms of actual factors:

$$
\begin{aligned}
&Y_5: \text{FPE}(\%) \\
&= -0.644 - 0.185\times P + 0.149\times F + 6.186\times R + 0.675\times N \\
&\quad - 7.946\times 10^{-4}\times PF - 0.070\times PR - 1.072\times 10^{-4}\times PN + 0.035\times FR \\
&\quad - 1.930\times 10^{-4}\times FN - 3.530\times 10^{-3}\times RN + 3.114\times 10^{-3}\times P^2 \\
&\quad - 8.881\times 10^{-4}\times F^2 - 1.659\times R^2 - 0.034\times N^2
\end{aligned}
\tag{6-11}
$$

The ANOVA analysis of the FPE is shown in

Table 6.9. The *F*-value for the regression model of FPE (Equation (6-10)) is 48.66, higher than the critical value of 2.43, suggesting that this model is statistically significant to represent the correlation between the plasma processing parameters and the FPE. This can also be validated by the higher value of R^2 (0.9785) and the small difference between adjusted R^2 and predicted R^2 (0.0326). Due to their small *p*-values (< 0.5) listed in **Table 6.9**, *A*, *B*, *C*, *AB*, *AC*, *BC*, A^2, B^2, C^2 and D^2 are identified as the significant model terms for the response of the FPE.

Figure 6.23 shows the combined effect of discharge power and total feed flow rate on the FPE. At a constant discharge power, an optimum total feed flow rate is observed for high FPE. This optimum total feed flow rate is around 100 ml/min at a discharge power of 20 W, and gradually decreases to 75 ml/min when the discharge power increases to 60 W. At the low and high total feed flow rates, the FPE decreases with the increase of discharge power initially and reaches a minimum value at a certain discharge power, beyond which the FPE starts to increase gradually. The discharge power related to the minimum FPE, is dependent on total feed flow rate (around 45 W at a total feed flow rate of 25 ml/min, while nearly 60 W at a total feed flow rate of 125 ml/min). Whilst at the moderate range of total feed flow rate (50 ml/min to 100 ml/min), the FPE is initially decreased by increasing discharge power and stabilised when discharge power is higher than 45 W. The maximum FPE is obtained at a discharge power of 20 W and a total feed flow rate of around 100 ml/min. The contour lines in the shape of a saddle (see **Figure 6.23** (b)) indicate that there is a significant role of the interaction between the discharge power and total feed flow rate on the FPE, which can be confirmed by the low *p*-value (0.0057) of the term *AB* listed in **Table 6.9**.

Table 6.9 ANOVA for response surface quadratic model of the FPE.

Model terms	Sum of squares	Degree of freedom	Mean square	*F*-value	*p*-value
Model Equation (6-10)	41.4	14	2.96	48.66	< 0.0001
A	*10.45*	*1*	*10.45*	*172*	*< 0.0001*
B	*4.51*	*1*	*4.51*	*74.21*	*< 0.0001*
C	*10.7*	*1*	*10.7*	*176.02*	*< 0.0001*
D	*0.1*	*1*	*0.1*	*1.67*	*0.2152*
AB	*0.63*	*1*	*0.63*	*10.39*	*0.0057*
AC	*0.49*	*1*	*0.49*	*8.03*	*0.0126*
AD	*1.15E-04*	*1*	*1.15E-04*	*1.89E-03*	*0.9659*
BC	*0.77*	*1*	*0.77*	*12.66*	*0.0029*
BD	*2.33E-03*	*1*	*2.33E-03*	*0.038*	*0.8474*
CD	*7.79E-05*	*1*	*7.79E-05*	*1.28E-03*	*0.9719*
A^2	*2.66*	*1*	*2.66*	*43.77*	*< 0.0001*
B^2	*8.45*	*1*	*8.45*	*139.06*	*< 0.0001*
C^2	*0.29*	*1*	*0.29*	*4.85*	*0.0437*
D^2	*1.23*	*1*	*1.23*	*20.31*	*0.0004*
Residual	0.91	15	0.061	-	-
Total	42.31	29	-	-	-

R^2: 0.9785; adjusted R^2: 0.9583; predicted R^2: 0.9154.

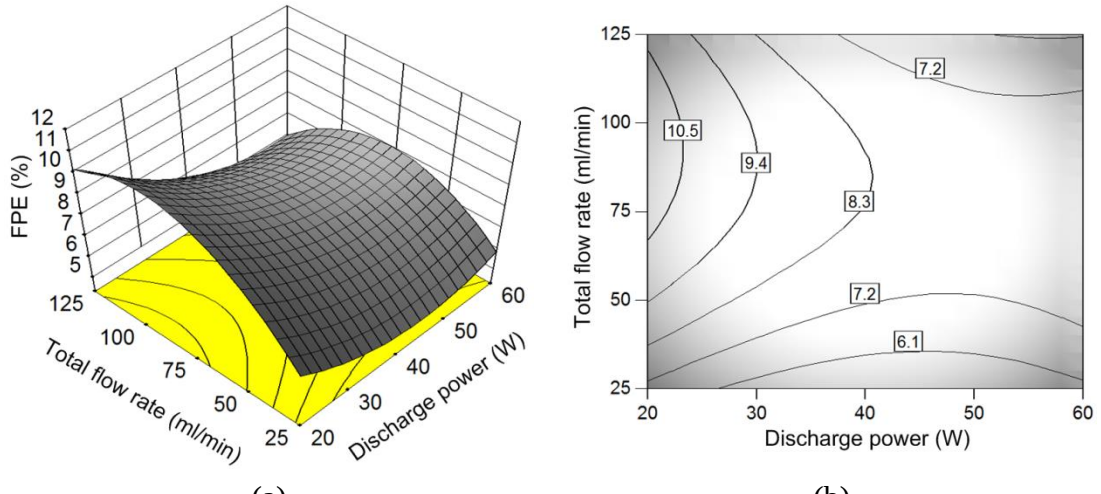

(a) (b)

Figure 6.23 Effect of discharge power, total flow rate and their interaction on the FPE at a CO_2/CH_4 molar ratio 1:1 and a Ni loading of 10 wt.%: (a) 3D surface plot; (b) projected contour plot.

The effect of discharge power and CO_2/CH_4 molar ratio as well as their interaction on the FPE at a total flow rate of 75 ml/min and a Ni loading of 10 wt.% is shown in **Figure 6.24**. The maximum FPE of around 12.4% is achieved at the lowest discharge power and the highest CO_2/CH_4 molar ratio. At low values of CO_2/CH_4 molar ratio, there exists a certain discharge power to achieve the minimum FPE. The discharge power corresponding to the minimum FPE is shifted to a higher value when CO_2/CH_4 molar ratio increases from 1:2 to 5:4. When CO_2/CH_4 molar ratio is larger than 5:4, the FPE decreases with discharge power to a minimum value and then remains stable. In addition, the FPE at a low discharge power is more sensitive to CO_2/CH_4 molar ratio than that at a high discharge power, confirmed by the large difference in the gradient of FPE with respect to CO_2/CH_4 molar ratio at different discharge power levels (-4.1% at a discharge power of 20 W, but -1.3% at a discharge power of 60 W). **Table 6.9** shows that the *p*-value of the term *AC* (0.0126) is lower than the level of significance (0.05). These results indicate that the interaction between discharge power and CO_2/CH_4 molar ratio plays a significant role in the FPE.

The presence of the contour lines (part of ellipse, see **Figure 6.25**) for the interaction of total feed flow rate and CO_2/CH_4 molar ratio demonstrates that there is also a significant interaction between the effects of these two processing parameters on the FPE, which can be confirmed by the low *p*-value of the term *BC* (0.0029) listed in **Table 6.9**. Additionally, increasing CO_2/CH_4 molar ratio increases the optimum total feed flow rate for high FPE (e.g. around 75 ml/min at a CO_2/CH_4 molar ratio of 1:2, while nearly 100 ml/min at a CO_2/CH_4 molar ratio of 3:2).

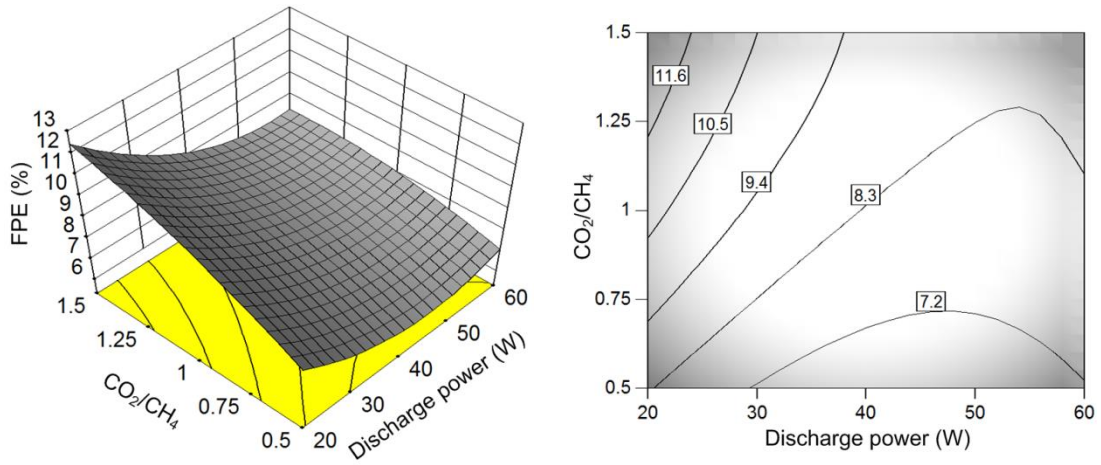

(a) (b)

Figure 6.24 Effect of discharge power, CO_2/CH_4 molar ratio and their interaction on the FPE at a total flow rate of 50 ml/min and a Ni loading of 10 wt.%: (a) 3D surface plot; (b) projected contour plot.

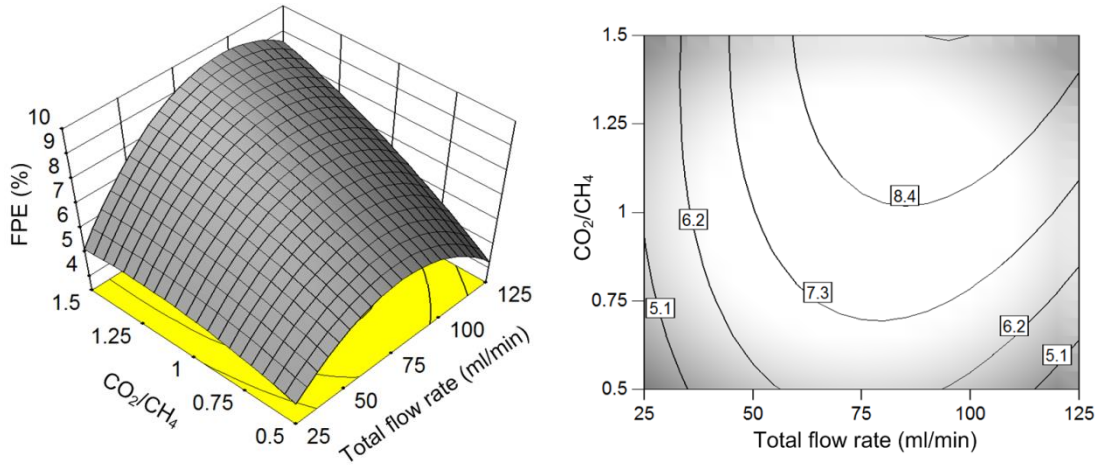

(a) (b)

Figure 6.25 Effect of total flow rate, CO_2/CH_4 molar ratio and their interaction on the FPE at a discharge power of 40 W and a Ni loading of 10 wt.%: (a) 3D surface plot; (b) projected contour plot.

Figure 6.26 shows the combined effect of discharge power and Ni loading on the FPE. Similar to the relationship shown in **Figure 6.23**, the FPE decreases with discharge power until it reaches a minimum value, and then starts to increase slightly at a constant Ni loading. The discharge power for the minimum FPE is independent on Ni loading (50 W at all the Ni loading conditions). Moreover, an optimum Ni loading (slightly less than 10 wt.%) is observed for high FPE, regardless of the change of discharge power. The maximum FPE is achieved at the lowest discharge power of 20 W with a Ni loading slightly lower than 10 wt.%. The contour lines (see in **Figure 6.26** (b)) are symmetrical about the line through the optimum Ni loading and parallel to the x-axis for discharge power. These results suggest that the interaction between discharge power and Ni loading is very weak in terms of FPE, which can also be confirmed by the high *p*-value (0.9659) of the term *AD*, listed in **Table 6.9.**

6.3.3.3 Optimisation of the processing variables

From the above analysis, we find that the reactant conversion and product yield follow the same trend with respect to the processing parameters. However, the FPE and reactant conversion (and also product yield) cannot reach their maximum values simultaneously under the same plasma operating conditions. For example, higher discharge power results in higher reactant conversion and higher product yield but lower FPE when the other processing parameters are fixed. In contrast, higher total feed flow rate leads to higher FPE but significantly decreases the conversion of reactants. Therefore, increasing discharge power and total feed flow rate has an opposite effect on reactant conversion (product yield) and FPE, indicating that there exists a trade-off between reactant conversion (product yield) and FPE. The SED is

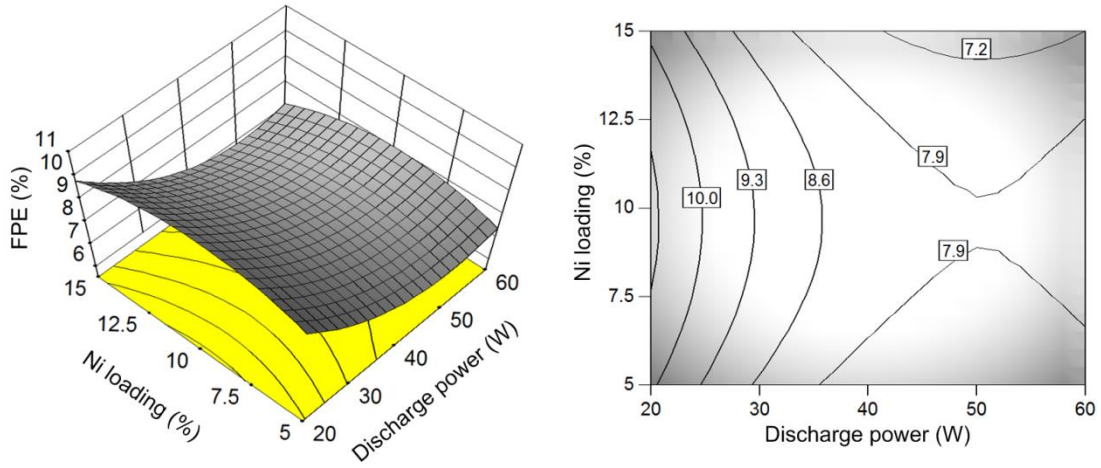

(a) (b)

Figure 6.26 Effect of discharge power, Ni loading and their interaction on the FPE at a total flow rate of 75 ml/min and a CO_2/CH_4 molar ratio of 1:1: (a) 3D surface plot; (b) projected contour plot.

introduced to further investigate the effect of discharge power and total feed flow rate on the performance of the plasma dry reforming process. **Figure 6.27** shows the effect of the SED on reactant conversions, product yields and FPE. Clearly, both the reactant conversions (including the conversion of CO_2 and CH_4 and the total carbon conversion) and the yield of CO and H_2 is increased by increasing the SED, but the increase in the SED leads to a decline in the FPE.

Similar trade-off has been observed in previous studies related to plasma dry reforming of CH_4 both with and without catalyst. **Figure 6.28** shows a comparison of the total carbon conversion and the FPE as a function of the SED in different atmospheric non-thermal plasma reactors. For reasonable comparison, the plasma reforming processes with a CO_2/CH_4 molar ratio of 1:1 are selected. In the plasma-only process, Wang et al. reported a maximum total carbon conversion of 66.1% with a CO_2 conversion of 52.7% and a CH_4 conversion of 79.5% in a DBD reactor at a SED of 533 kJ/l (discharge power: 177.8 W; total feed flow rate: 20 ml/min), corresponding to a FPE of 2.7% [154]. They claimed that a maximum FPE of 7.7% was achieved at the expense of relatively low total carbon conversion (31.0%) [154]. In a similar coaxial DBD reactor, Goujard et al. found that a maximum total carbon conversion of 19.3% can be obtained at a SED of 60 kJ/l with a discharge power of 9 W and a total feed flow rate of 9 ml/min [278]. However, the maximum FPE of the plasma process (8.0%) was not achieved at the same operating conditions, but at a much lower SED of 15 kJ/l [278]. Similarly, in the work of Kim et al., the maximum total carbon conversion of 73.0% was obtained at a SED of 1500 kJ/l with an electrical power of 500 W and a total feed flow rate of 20 ml/min, while the maximum FPE (2.6%) was achieved at a much lower SED of 176.5 kJ/l [238]. Gliding arc discharge has been used for plasma dry reforming of CH_4 and offers a

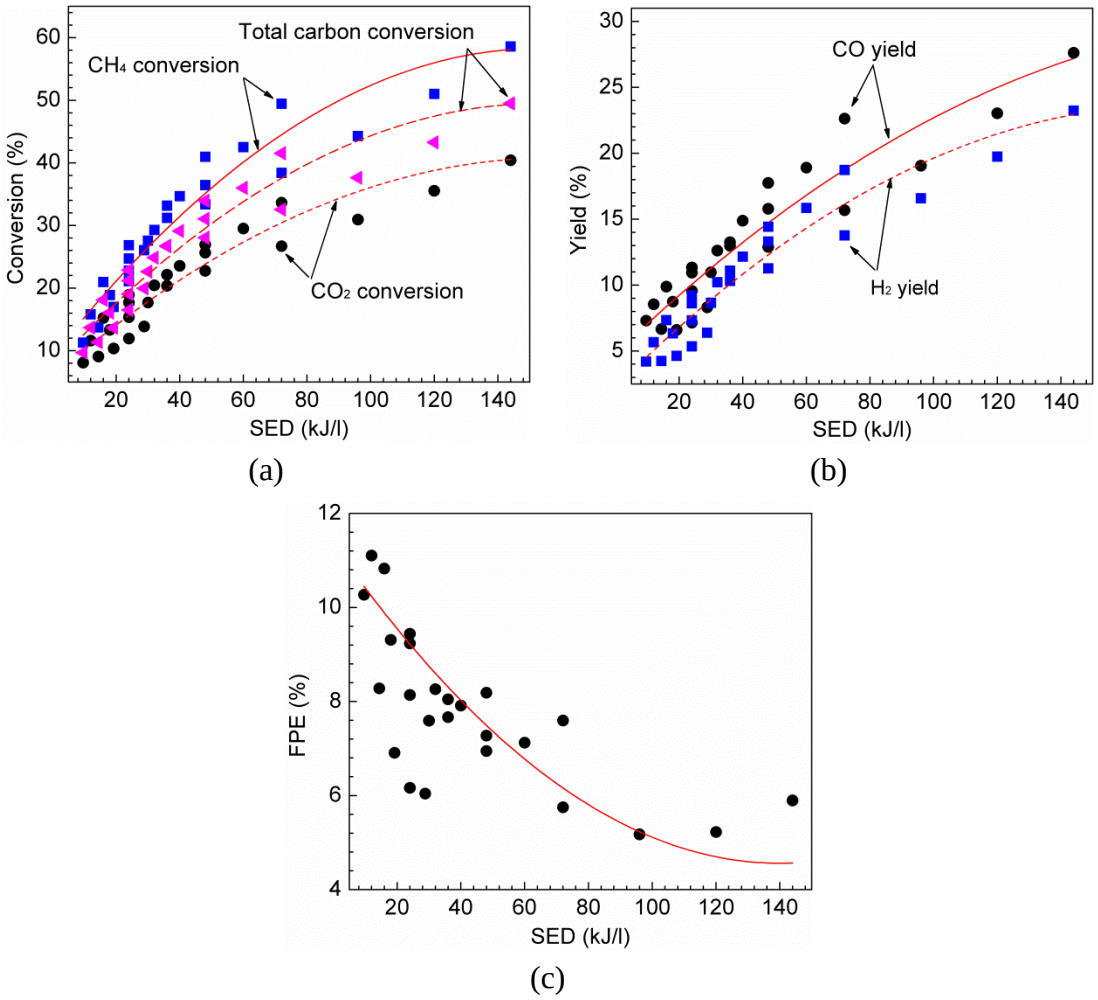

Figure 6.27 Effect of SED on reactant conversion, product yield and FPE at a CO_2/CH_4 molar ratio of 1:1 and a Ni loading of 10 wt.%.

high flexibility to work in a relatively high reactant gas flow rate [143]. A maximum FPE of 47.2% was obtained at a SED of 1.32 kJ/l with an electrical power of 165 W and a total feed flow rate of 7500 ml/min, which corresponds to a relatively low total carbon conversion (9.8%), compared to the maximum CO_2 conversion of 13.8% obtained in their work [143]. For the plasma-catalytic dry reforming processes, Eliasson et al. investigated the effect of zeolite NaX on the performance in the plasma process [158]. They reported that a maximum total carbon conversion of 55.0% was obtained at an electric power of 500 W and a total feed flow rate of 150 ml/min (a SED of 200 kJ/l), which corresponds to a low FPE of 2.8%; while the highest FPE of 6.4% was achieved at a much lower SED of 37.5 kJ/l with a much higher total feed flow rate of 800 ml/min, which led to a lower total carbon conversion of 17.7% [158]. A similar effect of the SED on total carbon conversion and FPE has also been observed when other zeolite catalysts were used in the plasma-catalytic dry reforming process, such as zeolite NaY [42], zeolite HY [159], and zeolite A [160]. Zheng et al. prepared the silica-coated $LaNiO_3$ nanoparticles

($LaNiO_3$@ SiO_2 NPs) for the production of syngas from dry reforming of CH_4 in a DBD reactor [174]. The maximum total carbon conversion of 63.3% was obtained at an electrical power of 160 W and a total feed flow rate of 50 ml/min (a SED of 192 kJ/l), which corresponds to a relatively low FPE (5.9%), compared with the maximum FPE of 6.3% obtained at a lower SED of 120 kJ/l with a higher total feed flow rate of 80 ml/min [174].

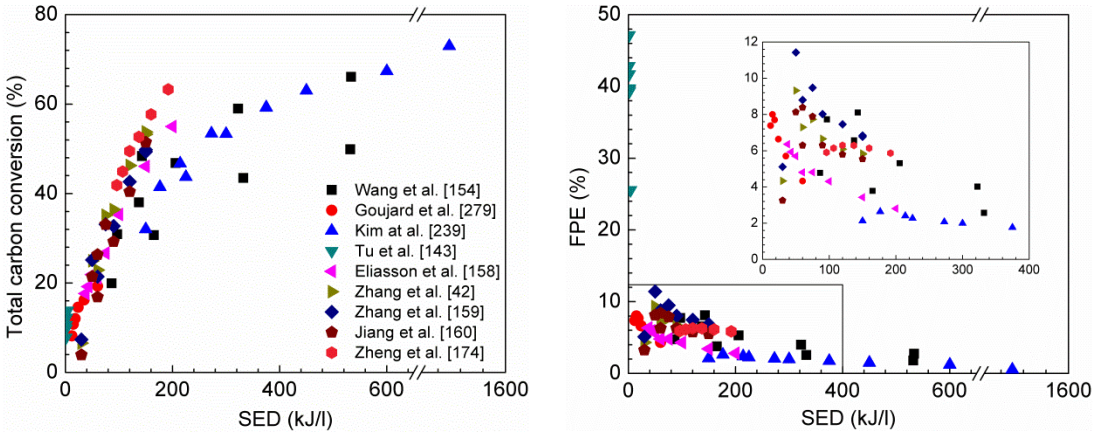

(a) (b)

Figure 6.28 Comparison of total carbon conversion and FPE vs. SED of the plasma reforming process in different atmospheric non-thermal plasma reactors at a CO_2/CH_4 molar ratio of 1:1, collected from literature.

Apart from the trade-off between the reactant conversion and FPE, the trade-off between the conversion of CO_2 and CH_4 is also observed when changing CO_2/CH_4 molar ratio in the feed gas and fixing the other processing parameters. **Figure 6.29** shows the comparison of reactant conversion vs. CO_2/CH_4 molar ratio of the plasma reforming process in different atmospheric non-thermal plasma reactors. In our study, increasing CO_2/CH_4 molar ratio from 1:2 to 3:2 results in a decrease in CO_2 conversion from 23.3% to 15.8% but an increase in CH_4 conversion from 19.4% to 37.8%; the corresponding total carbon conversion increases slightly and peaks at a CO_2/CH_4 molar ratio of 5:4, and then starts to decline gradually. Similar behaviours of reactant conversions with changing CO_2/CH_4 molar ratio have been also observed in previous studies. Wang et al. found that CO_2 conversion decreased from 43.6% to 27.1%, while CH_4 conversion increased by 81.8% when CO_2/CH_4 molar ratio increased from 1:5 to 5:1 [154]. The reactant conversions in their work were higher than our results, due to the higher SED in their work (71.5 kJ/l) than that in this study (32 kJ/l). Ozkan et al. used a new geometry of DBD reactor with multi-electrodes for dry reforming of CH_4; however, the reported reactant conversions were lower compared to the results in our studies due to their lower SED (22.5 kJ/l) [157].

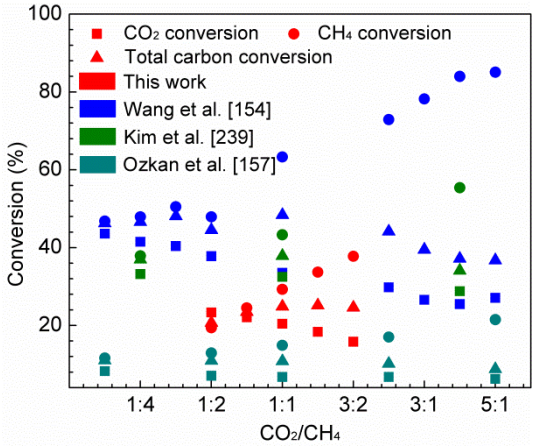

Figure 6.29 Comparison of reactant conversion vs. CO_2/CH_4 molar ratio of the plasma reforming process in different atmospheric non-thermal plasma reactors.

The overall performance of the plasma dry reforming of CH_4 strongly depends on a wide range of plasma operating conditions. In addition, a balance between the reactant conversions and FPE as well as a balance between CO_2 and CH_4 conversion is of significant importance for the development of an efficient plasma process for dry reforming of CH_4. Therefore, it is essential to optimise the plasma dry reforming process using multiple inputs and multiple responses. The aim of the process optimisation in this study is to find a combination of the plasma processing parameters (different factors) that maximise the reactant conversions (product yields) and FPE (different responses) simultaneously. RSM coupled with function maximisation technique is applied to determine the optimum process operating conditions in the plasma-catalytic dry reforming. The response surface method is embedded in the regression analysis program (Design Expert 9 software, trial version) [276]. A global desirability function (D) has been introduced as a key parameter to identify the optimal processing parameters and performance in the plasma-catalytic process. This function can be calculated from the product of individual desirability function (d_i) for each response, as shown in the following equation: [279, 280]

$$D = \left(d_1 \times d_2 \times \mathrm{L} \times d_n\right)^{\frac{1}{n}} = \left(\prod_{i=1}^{n} d_i\right)^{\frac{1}{n}} \tag{6-13}$$

where n is the number of the response in the experiment (n = 4 in this work) and d_i is in the range between 0 (least desirable) and 1 (most desirable). The optimal processing parameters can be achieved when the highest value D is found.

Table 6.10 shows the different values of global desirability for the plasma-catalytic dry reforming reaction in the process optimisation. The optimal process performance - CO_2 conversion (31.7%), CH_4 conversion (48.1%), CO yield (21.7%), H_2 yield (17.9%) and FPE (7.9%) - is achieved at a discharge power of 60.0 W, a total feed flow rate of 56.1 ml/min, a CO_2/CH_4 molar ratio of 1.03 and a Ni loading

of 9.5 wt.% as the highest global desirability of 0.854 is obtained at these input values. To validate this predicted result, five additional experimental runs are carried out using the optimal processing parameters. The results show a fairly good agreement between the experimental results and the predicted ones with a relative error of less than 10% for all of the five responses. The reproducible results confirm that DoE can be used to optimise the plasma-catalytic dry reforming of CH_4 process.

Table 6.10 Process optimisation for plasma-catalytic dry reforming of CH_4 by RSM.

Opt.	*P* (W)	*F* (ml/min)	*R*	*N* (wt.%)	C_{CO2} (%)	C_{CH4} (%)	Y_{CO} (%)	Y_{H2} (%)	FPE (%)	*D*
1	60.0	56.1	1.03	9.5	31.7	48.1	21.7	17.9	7.9	0.854
2	59.9	55.8	1.04	9.6	31.7	48.1	21.7	17.9	7.9	0.852
3	59.9	55.6	1.04	10.2	31.7	48.1	21.8	17.9	7.8	0.851
4	59.6	55.5	1.04	9.3	31.7	48.1	21.7	17.9	7.8	0.850
5	60.0	53.9	1.09	10.0	31.6	50.2	22.6	18.7	7.8	0.848

6.4 Conclusions

In this chapter, the plasma-catalytic dry reforming of CH_4 using Ni-based catalysts are performed in a coaxial DBD plasma reactor. The effect of different supports on the plasma dry reforming performance is investigated in terms of reactant conversion, product yield and selectivity and the carbon deposition on the spent catalysts, as well as the EC and FPE of plasma-catalytic process. In the prepared Ni catalysts, NiO phases are formed, which are reduced to the active Ni metal for the dry reforming process. Due to its high specific surface area and larger amount of strong basic sites, the Ni/Al catalysts shows the maximum conversion of CO_2 and CH_4, followed by (in decreasing order) the Ni/Mg, Ni/Si and Ni/Ti catalysts. Furthermore, the maximum carbon-resistance is also obtained from the Ni/Al catalyst with a minimum carbon deposition of 3.8% after the reaction was performed at a discharge power of 50 W for 150 min. The variation of carbon resistance in these catalysts is found to be in accordance with that of the carbon balance. Because of the lower specific surface area and much smaller amount of the basic sites, the Ni/Ti catalyst is observed to have the minimum carbon resistance, demonstrated by the low carbon balance.

After determining the support with the highest performance, the effects of the processing parameters (discharge power, total feed flow rate, CO_2/CH_4 molar ratio and Ni loading in the γ-Al_2O_3 supported Ni catalyst) and their combined effect on the plasma-catalytic dry reforming process are studied through RSM based on CCD. Regression models have been developed to describe the relationships between the plasma processing parameters and the reaction performance. The significance and adequacy of the models for each response (CO_2 conversion, CH_4 conversion, CO

yield, H_2 yield and FPE) have been verified by ANOVA. Based on the optimum process operating conditions determined by the optimisation module, the optimum plasma-catalytic dry reforming performance with maximum reactant conversion (CO_2 conversion of 31.7%, CH_4 conversion of 48.1%) and product yield (CO yield of 21.7 %, H_2 yield of 17.9%), as well as the maximum FPE (7.9%) is achieved at a discharge power of 60.0 W, a total flow rate of 56.1 ml/min, a CO_2/CH_4 molar ratio of 1.03 and a Ni loading of 9.5 wt.% to balance the trade-off between the reactant conversion and FPE as well as that between CO_2 conversion and CH_4 conversion. The reproducible experimental results obtained when using the theoretical optimal conditions have demonstrated the capability and reliability of the DoE method as a way of better understanding the role of different processing parameters and their interactions for process optimisation of the plasma-catalytic dry reforming of CH_4.

CHAPTER SEVEN APPLICATION OF NI-BASED BIMETALLIC CATALYSTS IN PLASMA-CATALYTIC DRY REFORMING OF METHANE

7.1 Introduction

As mentioned in Chapter 6, introducing active metal additives to form Ni-based bimetallic catalyst is one approach to improve their catalytic activity and stability in the dry reforming process. Previous studies have reported the beneficial effect of the noble metal addition (e.g. Pd, Rh, Ru and Pt) to the Ni-based monometallic catalyst in the conventional thermal catalytic dry reforming process [247, 281-283]. From the economic point of view, the addition of non-noble metals is more preferable. In this respect, active additives such as K, Mo, Mn, Cu, and Co are of great interest [46, 284-289]. In the plasma-catalytic dry reforming process, Zhang et al. used a Ni-Cu bimetallic catalyst in a DBD reactor to enhance the dry reforming reaction performance and a synergistic effect, generated by combining the plasma with the bimetallic catalyst, was observed [116]. However, no further related work has been reported and the understanding on the effect of the bimetallic catalysts in the plasma-catalytic dry reforming process is limited. Therefore, further investigations are required to reveal the synergistic effect resulting from the combination of plasma and bimetallic catalysts.

In this chapter, Co, Cu and Mn are incorporated into the Ni catalysts supported on γ-Al_2O_3 to form bimetallic catalysts for the plasma-catalytic dry reforming process. In Chapter 6, the optimum Ni loading for high reforming performance is around 7.5 wt.% to 10 wt.% under different experimental conditions; therefore, the Ni loading in the bimetallic catalysts is fixed at 10 wt.%. The effects of the active metal additives on the performance of the plasma-catalytic dry reforming of CH_4 are investigated and discussed in terms of the reactant conversions, product yields, carbon resistance of these bimetallic catalysts and FPE in the plasma process.

The effect of the Co loading in the Ni-Co bimetallic catalysts on the performance of the dry reforming process is investigated when the optimal bimetallic catalyst (Ni-Co) is determined. The relationships between the reforming performance and the catalyst characters are discussed. Moreover, a comparison of the plasma dry reforming performance using different plasma systems with and without catalysts are performed with respect to the total carbon conversion, the EC for H_2 production and the FPE of the plasma process.

7.2 Plasma-Catalytic Dry Reforming of CH_4 over Ni-M/γ-Al_2O_3 Bimetallic Catalysts (M= Co, Cu and Mn)

7.2.1 Experimental section

The 10 wt.% Ni/γ-Al_2O_3 catalyst (denoted as 10Ni) is prepared by the wetness impregnation method using $Ni(NO_3)_2{\cdot}6H_2O$, as described in Section 2.2. The 10 wt.% Ni - 3wt.% M/γ-Al_2O_3 (M = Co, Cu and Mn) bimetallic catalysts are prepared by co-impregnation of the nitrate salts of Ni and Co, Cu or Mn using the same procedure. The obtained bimetallic catalysts are denoted as 10Ni3M (M = Co, Cu and Mn). The characterisation methods used to reveal the catalyst properties are the same as those in Section 6.2.1. The plasma-catalytic dry reforming of CH_4 with Ni-based bimetallic catalysts is performed in a coaxial DBD reactor. The experimental system and procedure are the same as those used in Section 6.2.1

7.2.2 Experimental results

7.2.2.1 Catalyst properties

(1) Surface structure of the catalysts

Table 7.1 shows the physicochemical properties of the supported Ni catalysts. Compared with the 10Ni catalyst, introducing 3 wt.% metal additive decreases the specific surface area of the catalysts. The specific surface area of the 10Ni3Co catalyst is decreased by 6.6%, followed by larger decreases in this property for the 10Ni3Mn and 10Ni3Cu catalysts. In addition, these catalysts have a similar pore volume and an average pore diameter. The variations in the physicochemical properties of the catalysts can be attributed to doping with the metal additives, which have also been observed in previous studies [290].

Table 7.1 Physicochemical properties of the fresh Ni-based catalysts with different metal additives.

Sample	S_{BET} (m^2/g)	Pore volume (cm^3/g)	Pore diameter (nm)
10Ni	268.0	0.39	3.80
10Ni3Co	250.4	0.38	3.83
10Ni3Cu	231.8	0.35	3.86
10Ni3Mn	245.2	0.37	3.84

Figure 7.1 shows the XRD patterns of the fresh catalyst and support. All the catalysts show a clear γ-Al_2O_3 structure at 2θ =14.5°, 28.3°, 38.5°, 49.7 ° and 67.1° (PDF # 52-0803). Profiles of all samples contain NiO peaks at 2θ = 37.2° and 43.3° (PDF # 44-1159). It is interesting to note that the NiO peaks are weak and broad,

indicating that the high dispersion and small particle size of the active species are achieved on the catalysts. In addition, the diffraction peaks related to the oxide phase of the metal additives are also detected in the corresponding bimetallic catalysts, namely: Co_3O_4 (2θ = 19.1°, 31.2°, 36.5°, 44.8°, 55.6°, 59.3° and 65.2°: PDF# 42-1467), CuO (2θ = 35.5° and 48.7°: PDF # 45-0937) and Mn_2O_3 (2θ = 38.2°, 45.2° and 55.2°: PDF # 41-1442) in the catalysts of 10Ni3Co, 10Ni3Cu and 10Ni3Mn, respectively. These oxides in the supported catalysts can be reduced in the low temperature Ar-H_2 plasma, which has been demonstrated in previous studies [166].

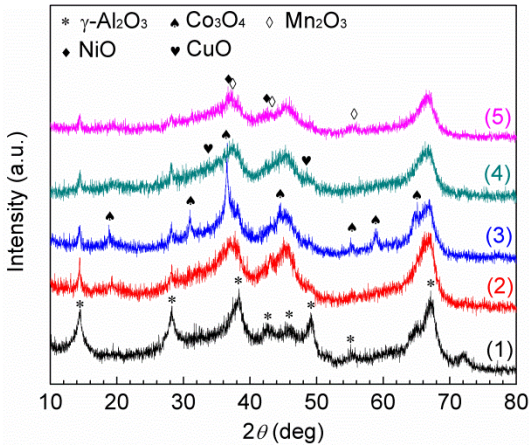

Figure 7.1 XRD patterns of catalyst support and different fresh Ni catalysts: (1) γ-Al_2O_3; (2) 10Ni; (3) 10Ni3Co; (4) 10Ni3Cu; (5) 10Ni3Mn.

(2) CO_2-TPD

The CO_2-TPD patterns of the Ni catalysts are displayed in **Figure 7.2**. For all the catalysts, two obvious CO_2 adsorption peaks at around 75 °C and 370 °C as well as one weak and broad peak at around 150 °C are observed. As mentioned in Section 6.2.2.1, the two CO_2 adsorption peaks at lower temperatures are assigned to the weak basic sites, and the peak at the higher temperature is attributed to the strong basic site. Compared with the 10Ni catalyst, the central temperature of CO_2 desorption peaks in the 10Ni3Co and 10Ni3Mn catalysts are shifted to a higher temperature by 21.5 °C and 4.2 °C, respectively; whereas the temperature of the CO_2 desorption peak in the 10Ni3Cu catalyst is reduced by 6.0 °C. It has been reported that the amount and strength of the basic sites on the catalysts significantly affects the performance of the dry reforming [291]. Moreover, CO_2 molecules can be more easily adsorbed on stronger basic sites, which could favour the gasification of the deposited carbon and thus inhibit the carbon formation [262, 263]. We therefore can expect that the 10Ni3Co catalyst might give the highest performance among all the catalysts in the plasma-catalytic dry reforming reaction from the perspective of strong basic sites.

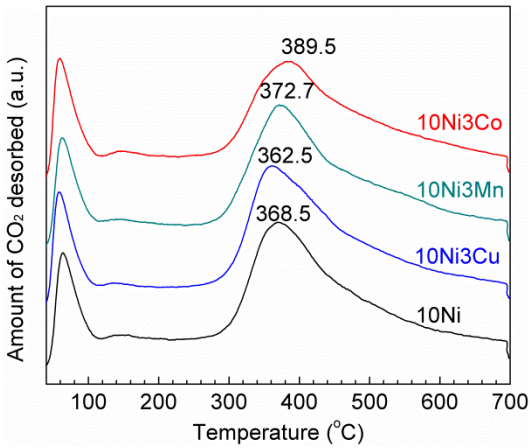

Figure 7.2 CO_2-TPD patterns of the fresh Ni catalysts.

7.2.2.2 Reactant conversion

Figure 7.3 shows the conversion of CO_2 and CH_4 in the plasma dry reforming of CH_4 as a function of discharge power. As discussed in Chapter 6, both CO_2 conversion and CH_4 conversion are increased by increasing the discharge power regardless of whether the catalysts are used or not. Increasing the discharge power contributes to the increased number of microdischarges, which implies that more reaction channels and energetic electrons are generated to enhance the plasma dry reforming process. Compared to the plasma reforming reaction without a catalyst, the combination of plasma with the 10Ni catalyst can improve the conversion of the reactants. For example, CO_2 conversion is increased from 23.8% to 26.2% when the 10Ni catalyst is used at a discharge power of 60 W; the corresponding CH_4 conversion is increased by 5.6% (from 41.8% to 44.1%). The conversions of CO_2 and CH_4 are further enhanced by introducing the active metal additives into the 10Ni catalyst. At a discharge power of 60 W, the presence of the 10Ni3Co catalyst in the DBD reactor leads a maximum CO_2 conversion of 29.8%, which is increased by 25.0% compared with that obtained in the plasma-only process. The corresponding conversion of CH_4 is increased by 17.5%. Zhang et al. reported similar enhancement in reactant conversions when bimetallic catalyst was used for plasma dry reforming of CH_4 [116]. The conversions of CO_2 and CH_4 were increased by 212.5% and 130.0%, respectively, when a 12 wt.% Cu-12 wt.% Ni/γ-Al_2O_3 catalyst was used in a DBD reactor at a discharge power of 60 W. In their work, Ar was used as the dilution gas and the plasma-catalytic reforming reaction was performed using extra thermal heating (at 450 ^oC), which may contribute to the much greater enhancement in their reactant conversions than these in our study. Similar improvement in the conversions of CO_2 and CH_4 due to metal additives has also been reported in previous studies of the thermal catalytic dry reforming of CH_4 using Ni-based bimetallic catalysts [292].

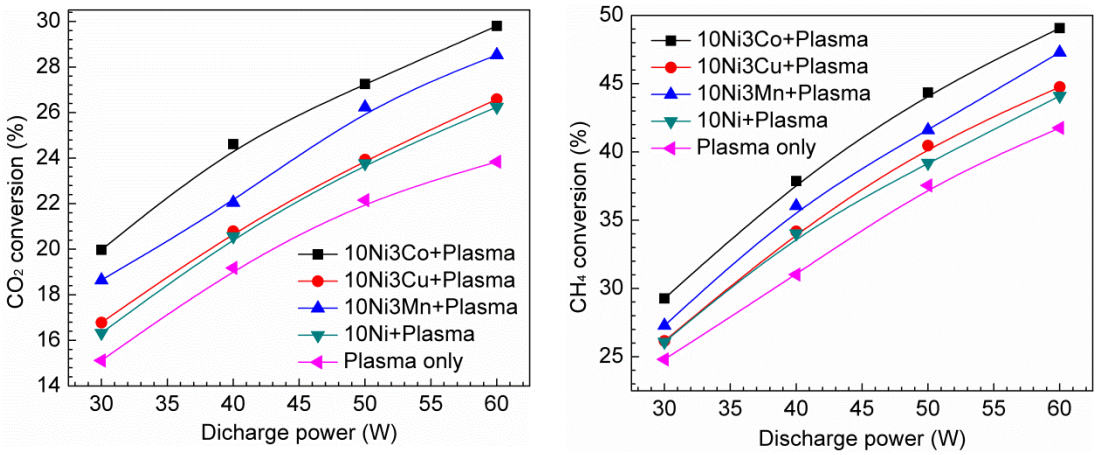

(a) (b)

Figure 7.3 Effect of bimetallic catalysts on (a) CO_2 conversion and (b) CH_4 conversion as a function of discharge power (total feed flow rate: 50 ml/min; CO_2/CH_4 molar ratio: 1:1).

The positive effect of the metal additives on promotion in the conversion of CO_2 and CH_4 is related to the interaction between the metal additive and Ni in the individual catalyst. In the 10Ni3Co catalyst, the simultaneous presence of Ni and Co on the γ-Al_2O_3 support increases the reducibility of the Ni-Co bimetallic catalyst. Co catalyst shows higher activity for CH_4 decomposition, which generates more H_2 to be used as a reducing agent to reduce the metal oxides during the dry reforming process [292-294]. In addition, the adjacent Ni and Co sites on the Ni-Co bimetallic catalyst will hinder the deactivation of the Co single sites [293]. Moreover, cobalt has a high ability to oxidise the deposited carbon to avoid the deactivation of the catalyst, thus maintaining the high catalytic performance [295, 296].

For the 10Ni3Mn catalyst, it was reported that the performance of the catalytic dry reforming is still enhanced when the Ni-Mn bimetallic catalyst is used, although patches of partially-reduced manganese oxide species MnO_x cover part of the active nickel surface [284, 297]. Two major factors could be responsible for this observation. Firstly, the decoration of Ni by the MnO_x species acts as a control of the metal ensemble size on the nickel surfaces, as it has been reported that smaller nickel particles were obtained in the Ni-based catalyst with Mn additive [297]. Secondly, as a basic oxide, MnO_x can increase the adsorption of CO_2 on the bimetallic catalyst; with the increase in CO_2 concentration, carbon deposition can be reduced through CO disproportionation by shifting the equilibrium concentration [298]. Moreover, with the adsorbed CO_2, MnO_x can form reactive carbonate species to react with the carbon deposition from CH_4 decomposition, thereby improve the conversion of CO_2 and CH_4 [299].

In the 10Ni3Cu catalyst, the Cu additive stabilises the structure of the active sites on the Ni surface for CH_4 decomposition, which will inhibit the deactivation of

the Ni catalyst resulting from sintering or loss of Ni crystallites. Moreover, the co-existence of Ni and Cu can adjust the catalytic activity to balance the CH_4 decomposition and carbon gasification by CO_2, thereby preventing carbon deposition on the Ni particle and maintaining the catalytic activity [300]. However, the sintering of the Cu particles leads to lower catalytic activity than other Ni-based bimetallic catalysts, which has been reported in a previous study [301]. This may be the main reason for the weak enhancement in the performance of the plasma-catalytic reforming when the 10Ni3Cu catalyst is used.

Compared to the plasma reforming reaction without catalyst, the combination of plasma with the 10Ni3Co catalyst leads to the maximum enhancement in both conversion of CO_2 and CH_4, followed by the catalysts of 10Ni3Mn and 10Ni3Cu. The active metal oxides in the catalysts (see **Figure 7.1**) can be reduced to the active species for the dry reforming process in the low-temperature Ar-H_2 plasma [166]. As mentioned in Section 6.2, these reduced catalysts favour the low temperature conversion of CO_2 and CH_4 due to the synergistic effect resulting from the combination of plasma and catalyst. In addition to the unique characteristics of each catalyst, the difference in the physicochemical properties and the basic sites between these catalysts also leads to the disparity in their activities in the plasma dry reforming process. The higher specific surface area can enhance the contact area for the reactants with the active sites, and consequently results in higher conversion of reactants [302]. Although introducing metal additives into the Ni catalysts leads to a slight decrease of the specific surface area, this negative influence is compensated by the promotional effect of the metal additives, confirmed by the enhancement in the conversion of CO_2 and CH_4 when using these bimetallic catalysts. Among the three Ni-based bimetallic catalysts, the 10Ni3Co catalyst shows the largest specific surface area, and therefore the highest plasma-catalytic reaction performance is achieved when it is combined with plasma. Moreover, the effect of the stronger basic sites on the 10Ni3Co catalyst should not be ruled out. In addition, the synergy between Ni and Co - the formation of Ni-Co alloy, which will be discussed in Section 7.3 in detail - is another important contributor to its high catalytic performance.

7.2.2.3 Production of syngas and C_2-C_4 hydrocarbons

Figure 7.4 shows the variation of syngas production in the plasma catalytic dry reforming of CH_4. Similar to the results obtained in Section 6.2.2.3, the yield of CO and H_2 increases with increase in the discharge power under all the experimental conditions. At a specific discharge power, introducing the bimetallic catalysts leads to an enhancement in the yield of syngas. The maximum yield of CO and H_2 is obtained when the 10Ni3Co catalyst is used, followed by the 10Ni3Mn, 10Ni3Cu and 10Ni catalyst. Interestingly, only a slight difference in the yield of syngas is observed when the 10Ni3Cu and 10Ni catalysts are combined with the

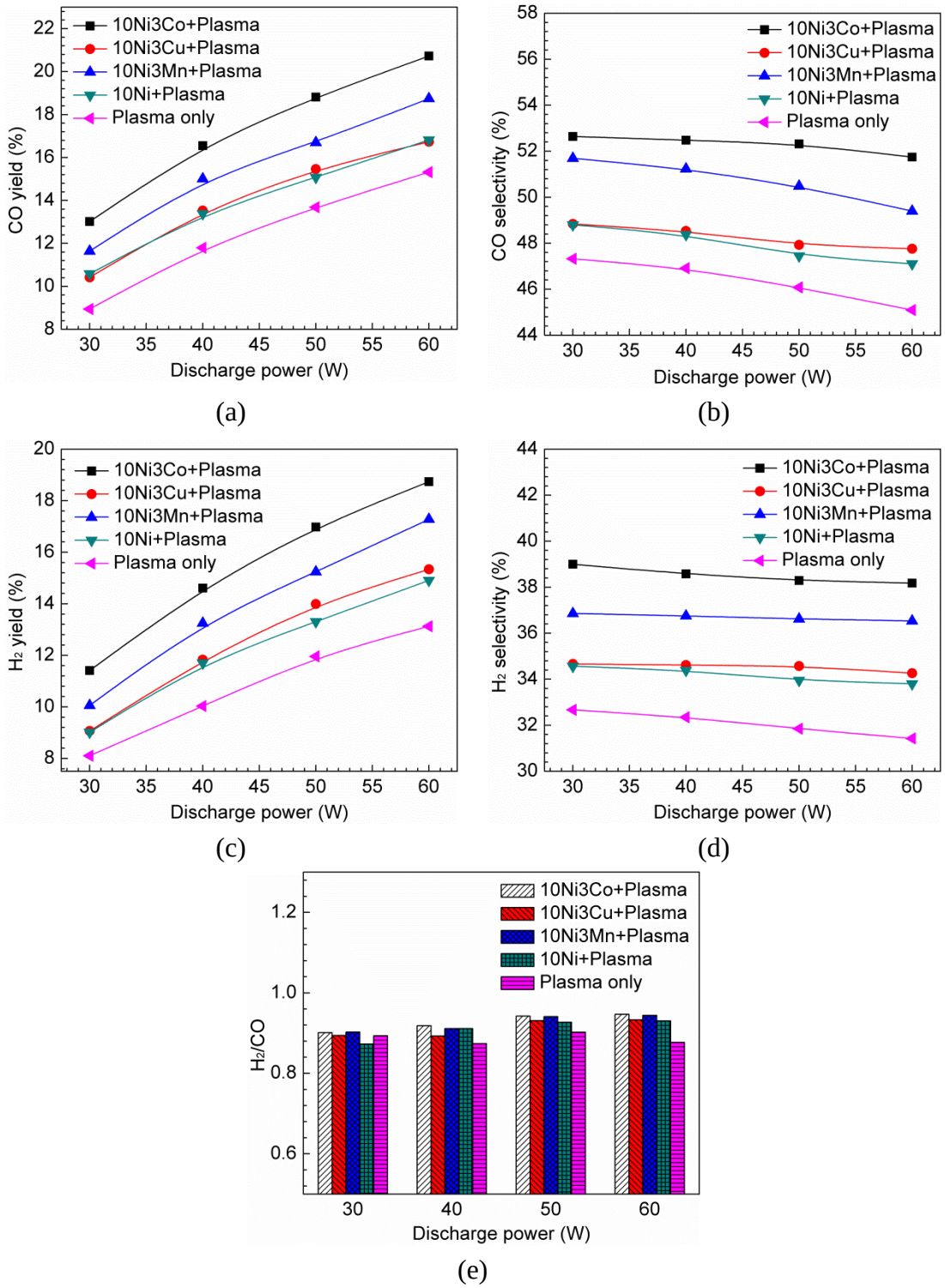

Figure 7.4 Effect of bimetallic catalysts on the syngas production as a function of discharge power: (a) CO yield; (b) CO selectivity; (c) H_2 yield; (d) H_2 selectivity; (e) H_2/CO molar ratio (total feed flow rate: 50 ml/min; CO_2/CH_4 molar ratio: 1:1).

plasma system. This phenomenon is similar to the difference in the reactant conversions when the 10Ni3Cu and 10Ni catalysts are used (see **Figure 7.3**). When the 10Ni3Co catalyst is used, the maximum yield of CO and H_2 is 20.7% and 18.7%, respectively, at a discharge power of 60 W. In addition, the combination of plasma

with bimetallic catalysts also increases the selectivity of syngas. The selectivity of CO and H_2 reaches its peak of 52.6% and 39.0%, respectively, in the plasma-catalytic dry reforming over the 10Ni3Co catalyst at a discharge power of 30 W. However, the selectivity is decreased by increasing the discharge power due to the formation of other hydrocarbons, similar to the results obtained in Section 6.2.2.3.

Figure 7.4 (e) shows the variation of the H_2/CO molar ratio in the gas product. Higher discharge power leads to a higher H_2/CO molar ratio. At a specified discharge power, the effect of these bimetallic catalysts on the H_2/CO molar ratio is in consistent with that on the reactant conversions. Additionally, all the H_2/CO molar ratios are less than unity, regardless of the catalysts; this is partly due to the occurrence of the reverse water gas shift reaction. The decrease in the selectivity of H_2 and CO due to the formation of C_2-C_4 hydrocarbons and carbon deposition might be another possible reason.

The selectivity of the hydrocarbons C_2H_6, C_3H_8, and C_4H_{10} produced in the plasma process is presented in **Figure 7.5**. At a fixed discharge power, the introduction of these bimetallic catalysts into the DBD reactor increases the selectivity of C_3H_8 and C_4H_{10}, and the maximum selectivity is obtained when the 10Ni3Co catalyst is used. This is in accordance with their catalytic activity for reactant conversions. Additionally, increasing discharge power increases the selectivity of C_3H_8 and C_4H_{10}. By contrast, the selectivity of C_2H_6 is decreased by increasing discharge power, and is further reduced by the introduction of the bimetallic catalysts. The maximum selectivity of C_3H_8 and C_4H_{10} (6.2% and 5.3%) is achieved when the 10Ni3Co catalyst is used at a discharge power of 60 W, whilst the selectivity of C_2H_6 reaches its minimum value of 13.8% under the same condition.

7.2.2.4 Carbon balance

The carbon balance in the gas stream of plasma-catalytic reaction using different Ni-based bimetallic catalysts is shown in **Figure 7.6**. The variation of the carbon balance with these bimetallic catalysts is consistent with their catalytic ability. In this study, the maximum carbon balance of 97.2% is obtained with the 10Ni3Co catalyst at a discharge power of 30 W. From the TG analysis shown in **Figure 7.7**, the carbon deposition amounts formed on the catalyst surface are within the range of 2.9% - 3.9% after the plasma-catalytic reaction at a discharge power of 50 W for 150 min. Compared to that of the 10Ni catalyst, the higher carbon resistance of the bimetallic catalysts (except the 10Ni3Cu catalyst) is partly ascribed to the increased amount of strong basic sites on the catalysts caused by the metal additives. The smaller particle size resulting from the larger specific surface area also contributes to the higher carbon resistance. The higher amount of the strong basic sites and the larger specific surface area in the 10Ni3Co catalyst contribute to its maximum carbon resistance in comparison to the other catalysts.

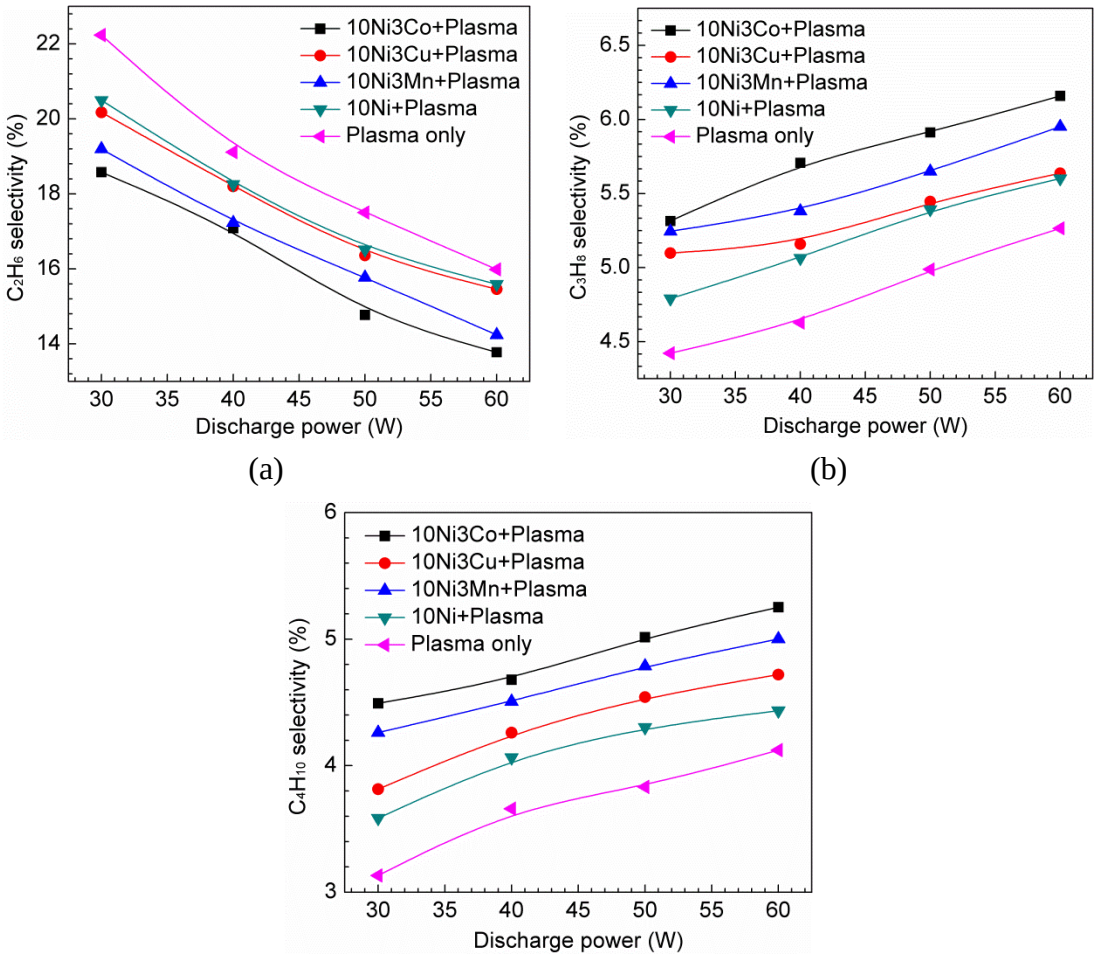

Figure 7.5 Effect of bimetallic catalysts on the selectivity of C_2-C_4 hydrocarbons (a) C_2H_6; (b) C_3H_8; (c) C_4H_{10} (total feed flow rate: 50 ml/min; CO_2/CH_4 molar ratio: 1:1).

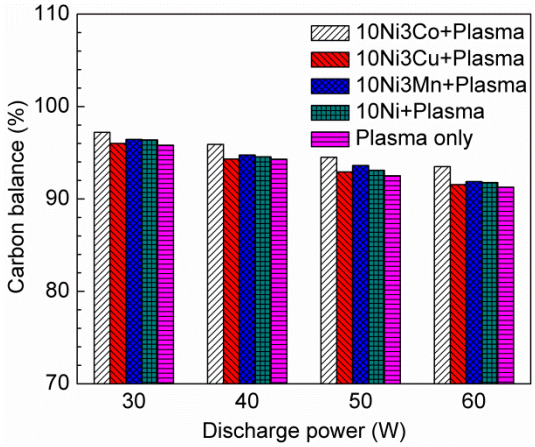

Figure 7.6 Effect of bimetallic catalysts on the carbon balance as a function of discharge power (total feed flow rate: 50 ml/min; CO_2/CH_4 molar ratio: 1:1).

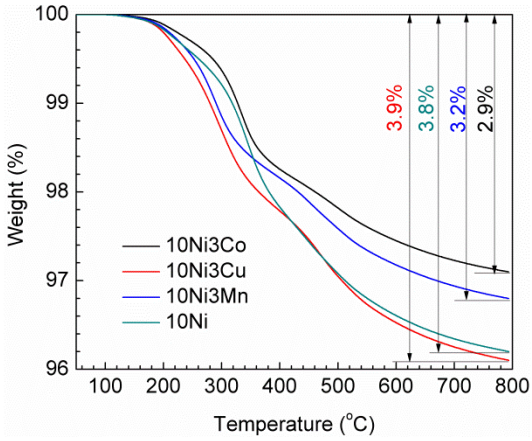

Figure 7.7 TG results of bimetallic catalysts after reaction at a discharge power of 50 W for 150 min.

7.2.2.5 Energy efficiency

The effect of the Ni catalysts on the EC and FPE of the plasma dry reforming process at a discharge power of 30 W is shown in **Figure 7.8**. The use of the different bimetallic catalysts decreases the EC for reactant conversion. The combination of the 10Ni3Co catalyst with the DBD decreases the EC for CO_2 conversion, CH_4 conversion and total carbon conversion by 24.4%, 15.2% and 18.9%, respectively, compared with that obtained in the plasma-only process. Correspondingly, the EC for H_2 and syngas is decreased by 29.4% and 27.9%, respectively. The presence of the 10Ni3Co catalyst in the DBD reactor improves the FPE by 25.8%. It is worthy to note that little differences in the EC and FPE are observed when the 10Ni3Cu and 10Ni catalysts are used.

7.3 Effect of Co Loading on Plasma-Catalytic Dry Reforming of CH_4 using Ni-Co Bimetallic Catalysts

7.3.1 Experimental section

Wetness impregnation method is used to prepare the 10 wt.% Ni/γ-Al_2O_3 catalyst (denoted as 10Ni) by impregnating $Ni(NO_3)_2{\cdot}6H_2O$, as described in Section 6.2.1. The 10 wt.%Ni - *x* wt.%Co/γ-Al_2O_3 bimetallic catalysts with different Co loadings (*x* = 1, 3, 5, 7.5 and 10) are prepared by co-impregnation of nitrate salts of the Ni and Co using the same procedure. The obtained samples are denoted as 10Ni*x*Co (*x*=0 stands for the 10Ni catalyst). The characterisation methods used to reveal the catalyst properties are the same as those used in Section 6.2.1. The plasma-catalytic dry reforming of CH_4 using the Ni-Co bimetallic catalysts are performed in a coaxial DBD reactor. The experimental system and procedure are the same as those in Section 6.2.1.

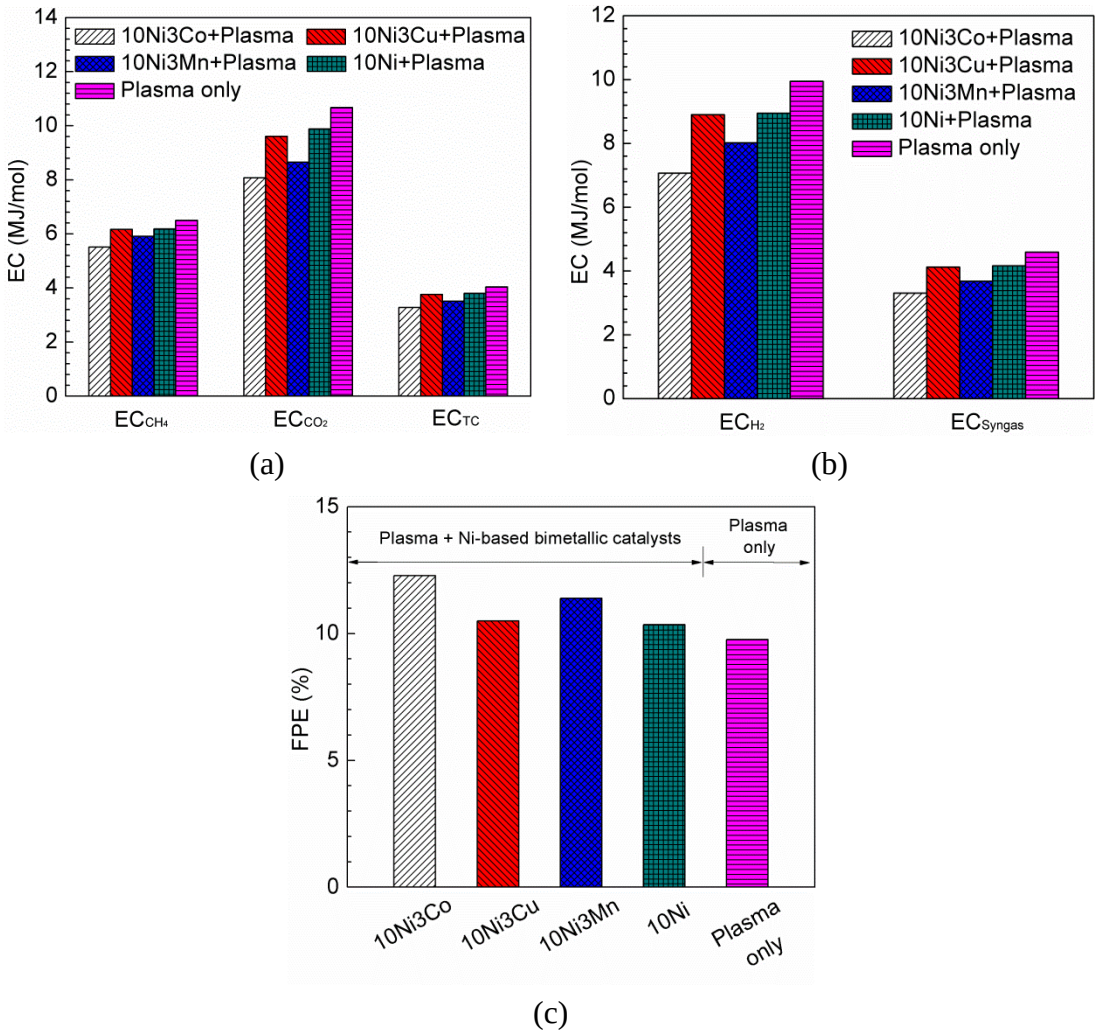

Figure 7.8 Effect of bimetallic catalysts on (a) the EC for CH_4 conversion, CO_2 conversion and total carbon conversion; (b) the EC for H_2 and syngas production; (c) the FPE of the plasma-catalytic process (discharge power: 30 W; total feed flow rate: 50 ml/min; CO_2/CH_4 molar ratio: 1:1).

7.3.2 Experimental results

7.3.2.1 Catalyst properties

(1) Surface structure of the prepared catalysts

Table 7.2 summarises the physicochemical properties of the Ni-Co/γ-Al_2O_3 bimetallic catalysts with different Co loadings. With the increase of the Co loading, the specific surface area of the catalysts gradually decreases from 268.0 m^2/g (without Co loading) to 221.3 m^2/g in the 10Ni10Co catalyst; the corresponding pore volume also slightly decreases from 0.39 to 0.31 cm^3/g. This phenomenon could be attributed to the deposition of the metal particles inside γ-Al_2O_3 pores or the partial blocking of pores [303]. In addition, these catalysts have similar average pore diameter.

Table 7.2 Physicochemical properties of the Ni-Co/γ-Al_2O_3 bimetallic catalysts with different Co loadings.

Sample	S_{BET} (m^2/g)	Pore volume (cm^3/g)	Pore diameter (nm)
10Ni	268.0	0.39	3.80
10Ni1Co	256.0	0.39	3.81
10Ni3Co	250.4	0.36	3.82
10Ni5Co	246.5	0.35	3.83
10Ni7.5Co	228.7	0.33	3.84
10Ni10Co	221.3	0.31	3.86

Figure 7.9 (a) shows the XRD patterns of the catalyst support and fresh catalysts. The XRD spectrum of the support shows five diffraction peaks at 2θ =14.5°, 28.3°, 38.5 °, 49.7 ° and 67.1°, which are assigned to the cubic structure of γ-Al_2O_3 crystalline (PDF # 52-0803). These peaks can also be observed in the XRD patterns of the Ni-Co bimetallic catalysts with different Co loadings.

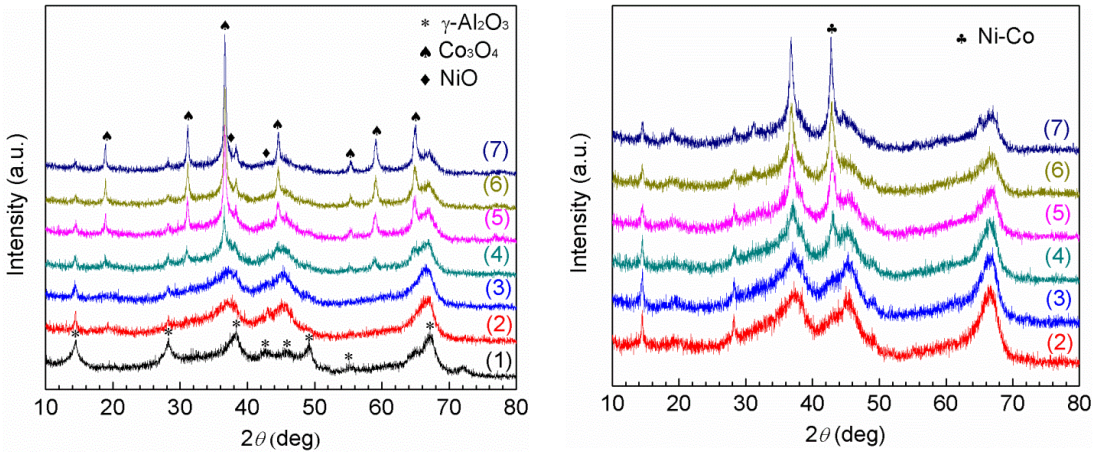

(a) (b)

Figure 7.9 XRD patterns of (a) the fresh and (b) the reacted catalysts (1) γ-Al_2O_3; (2) 10Ni; (3) 10Ni1Co; (4) 10Ni3Co; (5) 10Ni5Co; (6) 10Ni7.5Co; (7) 10Ni10Co.

The XRD patterns of the bimetallic catalysts show diffraction peaks of Co_3O_4 at 2θ = 19.1 º, 31.2 º, 36.5 º, 44.8 º, 55.6 º, 59.3 ºand 65.2 º(PDF# 42-1467), while weak peaks of NiO (PDF# 44-1159) are identified at 2θ = 37.2° and 43.3° (PDF # 44-1159). In the bimetallic catalysts, obvious peak narrowing is observed at Co_3O_4 peaks with the increase in Co loading, which may indicate the increase of the crystalline size of Co_3O_4 or the crystallinity of the catalysts. In this study, the interaction between the catalyst support and the active metal phase is relatively weak under the low calcination temperature (400 °C), which favours the formation of metal oxides in the catalyst preparation process [91]. It has been demonstrated that these metal oxides can be reduced in the low temperature Ar-H_2 plasma [166]. **Figure 7.9**

(b) shows the XRD patterns of the spent catalysts after the plasma catalytic dry reforming process at a discharge power of 50 W for 150 min. The details will be explained in the following section.

(2) CO_2-TPD

The CO_2-TPD patterns for the Ni-Co bimetallic catalysts with different Co loadings are presented in **Figure 7.10**. Obviously, the 10Ni catalyst shows three CO_2 adsorption peaks centred around 75 ^oC, 150 ^oC and 370 ^oC. The former two peaks are assigned to the weak (20-150 ^oC) basic sites, while the third one is ascribed to the strong (300-450 ^oC) basic sites [261]. Compared with the 10Ni catalyst, all the Ni-Co bimetallic catalysts have similar CO_2 adsorption peaks. However, the peaks corresponding to the strong basic sites are shifted to a higher temperature by increasing the Co loading, and the area under the CO_2-TPD curve is also gradually increased, especially when the Co loading is higher than 5 wt.%. These phenomena indicate that the amount of the strong basic sites on the Ni-Co bimetallic catalysts is increased by increasing the Co loading. As mentioned before, catalysts with more strong basic sites can improve the adsorption of CO_2, which will provide more surface oxygen for the gasification of coke during the dry reforming reaction, and consequently reduce coke deposition on the catalysts. The oxygen species from CO_2 decomposition also contributes to the enhancement in the CH_4 conversion.

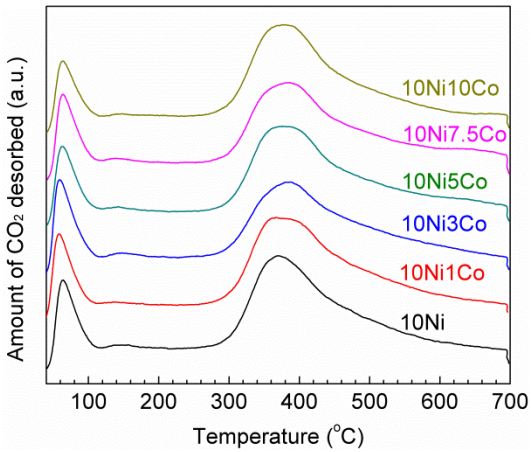

Figure 7.10 CO_2-TPD patterns of the fresh catalysts with different Co loadings.

7.3.2.2 Reactant conversion

Figure 7.11 presents the effect of different Co loadings on the conversion of CO_2 and CH_4 in the plasma catalytic dry reforming of CH_4. Compared to the plasma dry reforming reaction without catalyst, the combination of the plasma with these catalysts results in significant enhancement in the conversions of CO_2 and CH_4; and an optimum Co loading for maximum CO_2 and CH_4 conversion is observed. For example, when the discharge power is fixed at 60 W, CO_2 conversion increases

gradually by increasing the Co loading, and peaks (30.9%) at a Co loading of 5 wt.%, beyond which CO_2 conversion decreases slowly. A CO_2 conversion of 26.0% is obtained when the Co loading is increased to 10 wt.%; this value is still higher than that obtained in the plasma process without catalyst. Similarly, the corresponding maximum CH_4 conversion (50.7%) is also achieved at the Co loading of 5 wt.%. This maximum conversion of CO_2 and CH_4 is increased by 29.4% and 21.5%, respectively, compared with that obtained in the plasma-only process. Zhang et al. also reported that there existed an optimum loading of the metal additive in the bimetallic catalyst to obtain high reactants conversion in the plasma-catalytic dry reforming of CH_4 [116]. In their study, Cu with different loadings (1 wt.%, 5 wt.%, 12 wt.% and 16 wt.%) was added to the 12 wt.% Ni/γ-Al_2O_3 catalyst to form the Ni-Cu bimetallic catalysts for the plasma-catalytic dry reforming in a DBD reactor. Their results indicated that the presence of the 12 wt.% Ni-12 wt.% Cu/γ-Al_2O_3 catalyst in the DBD reactor showed the highest conversion of reactants. The similar enhancement in CH_4 and CO_2 conversion over the Ni-Co bimetallic catalysts have been previously reported in thermal catalytic dry reforming processes, and various optimum Co loadings have been proposed [292, 295, 302-304]. Sengupta et al. stated that the Ni-Co bimetallic catalyst with a Ni/Co weight ratio of 3:1 (total loading: 15 wt.%) exhibited a better catalytic activity than other catalysts in the CO_2 reforming of CH_4 [292]. Chen et al. found that the Ni-Co bimetallic catalyst with a Ni/Co weight ratio of 1:1 and 7:3 (total loading: 10 wt.%) had a similar activity in terms of CH_4 conversion, and CH_4 conversion with these two catalysts was higher than that obtained when using the Ni-Co bimetallic catalyst with a lower Ni/Co weight ratio (3:7) [295]. The excellent performance of the Ni-Co bimetallic catalysts in the dry reforming of CH_4 is closely related to the synergy between nickel and cobalt, e.g. the formation of the Ni-Co alloy [304]. In this study, the characteristic diffraction peaks of the active Ni-Co alloy can be clearly identified on the spent catalysts (**Figure 7.9** (b)), and the alloy size is enlarged by increasing the Co loading, which is demonstrated by the narrowing in the characteristic peaks of the Ni-Co alloys at 2θ = 43.8^o. The 10Ni5Co catalyst exhibits the highest activity in terms of CO_2 and CH_4 conversion, compared with the other catalysts. This variation in the catalytic activity for the Ni-Co bimetallic catalysts could be ascribed to the difference in the surface structures and the amount of the basic sites on the catalysts. The catalysts with high specific surface area can supply the reactants with a large contact area, which leads to a high reaction activity [302]. In this study, increasing the Co loading in the bimetallic catalysts results in the decrease in the specific surface area and the increase in the particle size, and consequently lowers the catalyst activity for reactant conversion in the plasma dry reforming process. However, the amount of strong basic sites on the bimetallic catalyst is enhanced by increasing the Co loading, which contributes to the improvement in the reactant conversions. These results suggest that

the compromise between the surface structure and the amount of the strong basic sites of the Ni-Co bimetallic catalysts has been achieved and enables the 10Ni5Co catalyst to show the highest activity for reactant conversion.

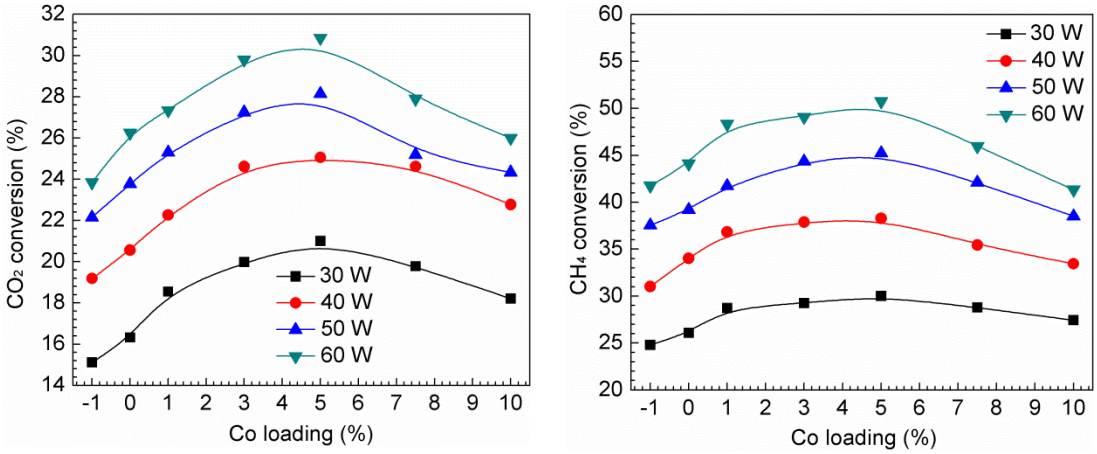

(a) (b)

Figure 7.11 Effect of Co loadings on (a) CO_2 conversion and (b) CH_4 conversion as a function of discharge power (total feed flow rate: 50 ml/min; CO_2/CH_4 molar ratio: 1:1; -1 in the x-coordinate stands for the case in the absence of the catalyst).

7.3.2.3 Production of syngas and C_2-C_4 hydrocarbons

Figure 7.12 shows the effect of the Co loadings on the production of syngas as a function of discharge power. In the plasma process without catalyst, increasing the discharge power increases the yield of CO and H_2, but decreases their selectivity. The presence of the 10Ni catalysts leads to an increment in both the yield and selectivity of syngas. This phenomenon has also been reported in previous studies, where a similar Ni/γ-Al_2O_3 catalyst was used in the DBD plasma catalytic dry reforming of CH_4 [91]. The use of Ni-Co bimetallic catalysts further increase the yield and selectivity of syngas until the Co loading reaches the optimum value for maximum CO_2 and CH_4 conversions. For example, the highest yield of CO and H_2 is 21.2% and 19.1% when the 10Ni5Co catalyst is used at a discharge power of 60 W; their corresponding maximum selectivity is 51.9% and 37.6%, respectively.

It is clear to see in **Figure 7.12** (e) that the effect of Co loadings on the molar ratio of H_2/CO is consistent with that on the yield and selectivity of H_2 and CO. A H_2/CO molar ratio close to 1 is obtained when the Co loading approaches its optimum value. As mentioned before, the syngas with a H_2/CO molar ratio close to 1 is favourable for the synthesis of higher hydrocarbons [305]. In this study, the maximum H_2/CO molar ratio of 0.96 is obtained when the 10Ni5Co catalyst is used in the plasma-catalytic dry reforming reaction at a discharge power of 50 W.

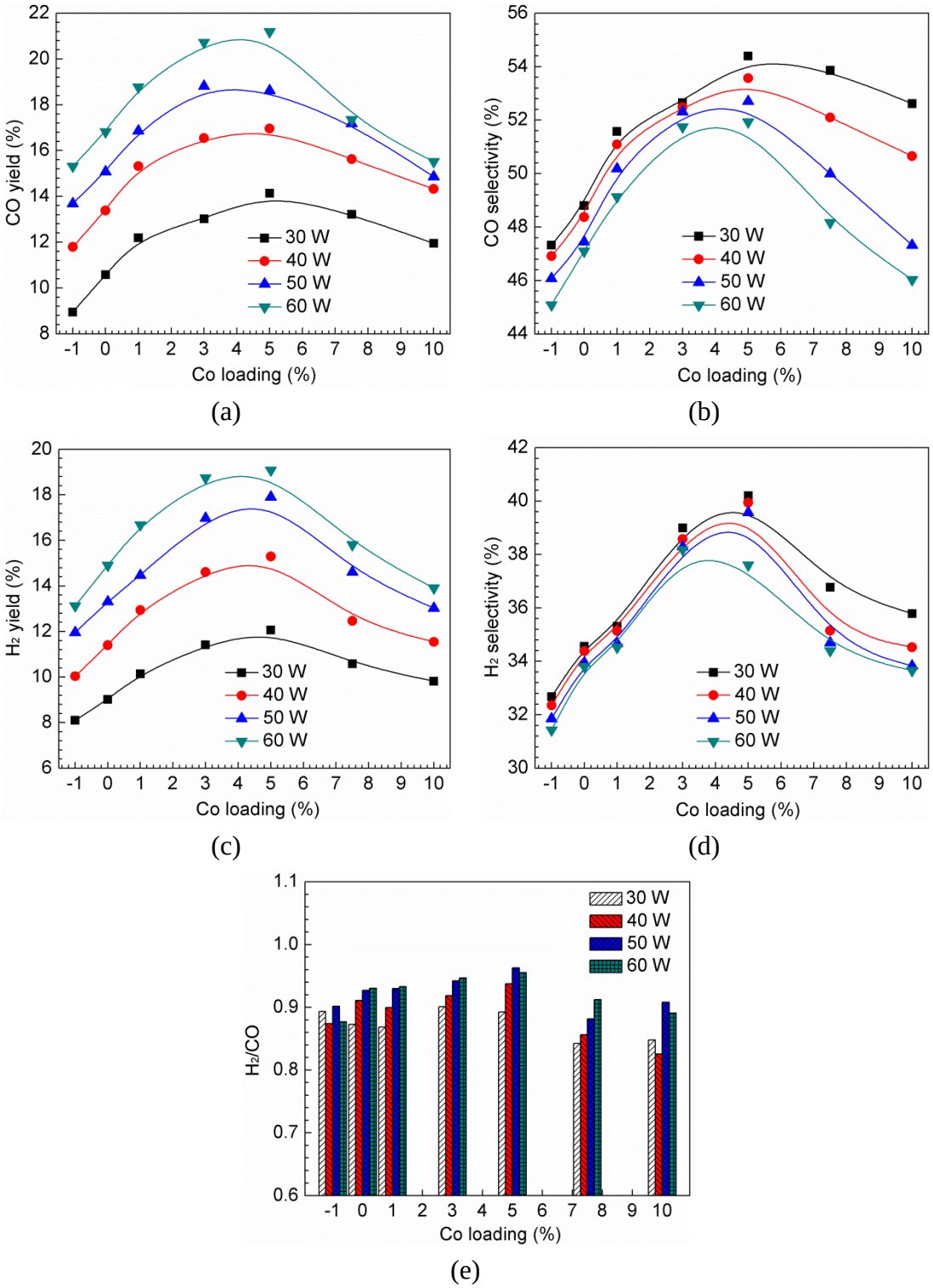

Figure 7.12 Effect of Co loadings on the production of syngas as a function of discharge power: (a) CO yield; (b) CO selectivity; (c) H_2 yield; (d) H_2 selectivity; (e) H_2/CO molar ratio (total feed flow rate: 50 ml/min; CO_2/CH_4 molar ratio: 1:1; -1 in the x-coordinate stands for the case in the absence of the catalyst).

The influence of Co loadings on the selectivity of C_2-C_4 hydrocarbons is illustrated in **Figure 7.13**. Different to the variation of selectivity towards CO and

H_2, the optimum Co loading for syngas production leads to the minimum selectivity to C_2H_6. In the plasma reaction system, Ni-Co bimetallic catalyst with appropriate Co loading favours the dissociation of the produced C_2H_6 to further form higher hydrocarbons. This can be confirmed by the maximum selectivity towards C_3H_8 and C_4H_{10} achieved for the catalyst with the optimum Co loading, as shown in **Figure 7.13** (b) and (c).

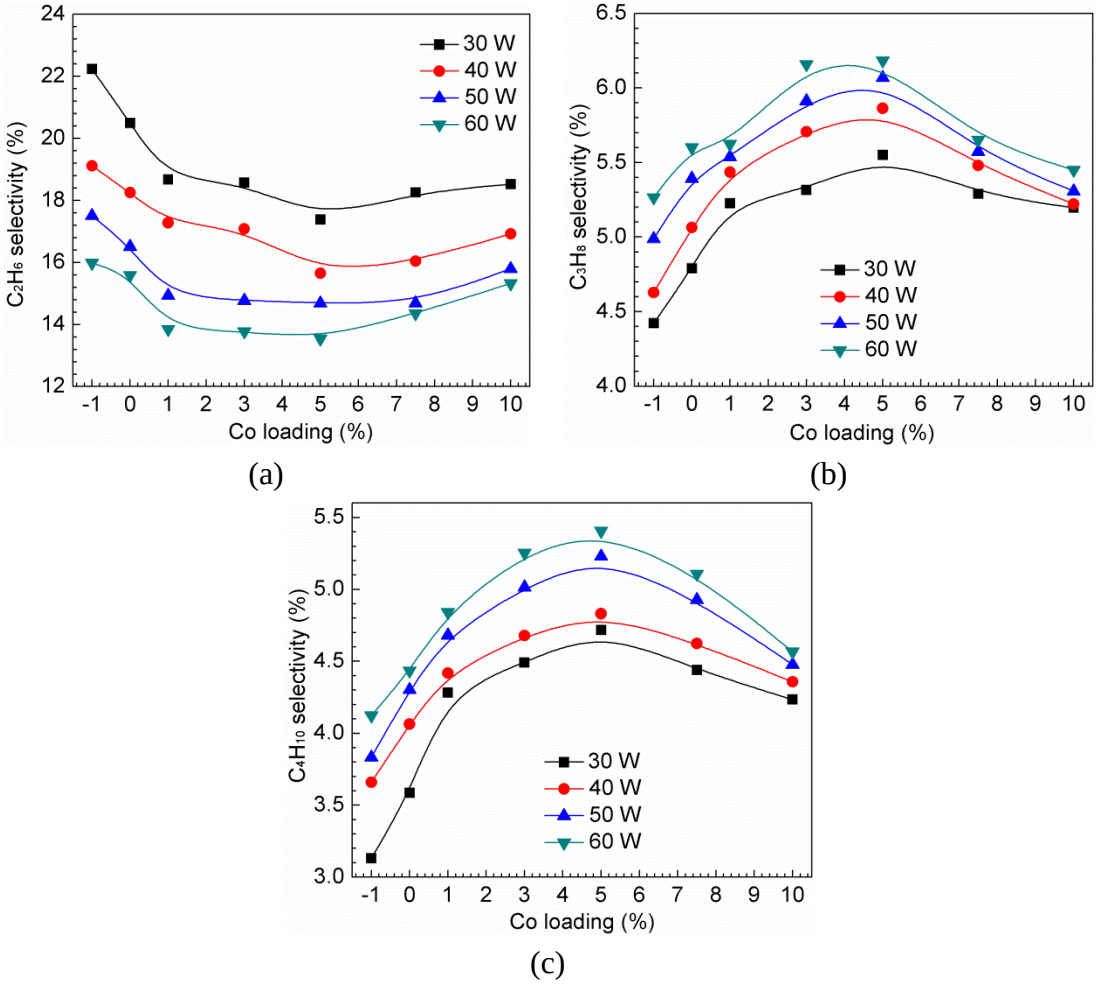

Figure 7.13 Effect of Co loadings on the selectivity to C_2-C_4 hydrocarbons (a) C_2H_6; (b) C_3H_8; (c) C_4H_{10} (total feed flow rate: 50 ml/min; CO_2/CH_4 molar ratio: 1:1; -1 in the x-coordinate stands for the case in the absence of a catalyst).

In the plasma-catalytic reforming reaction, the temperature inside the reactor is within the range of 160-230 ^oC, slightly higher than the temperature measured in the plasma reforming process without catalysts (150 ^oC to 225 ^oC, see in Section 5.3.2.1). Our thermodynamic equilibrium analysis for dry reforming of CH_4 has demonstrated that the conversions of both gases are very low (< 1%) at such low temperatures (160-230 ^oC). Moreover, much higher temperatures (e.g. > 600 ^oC) are required in thermal catalytic CO_2 reforming of CH_4 in order to obtain favourable conversion of CO_2 and CH_4 and yield of CO and H_2 [306, 307]. Therefore, we can

conclude that only extremely low conversions of the feed gases can be obtained in the conventional thermal catalytic dry reforming of CH_4 when carried out at low temperatures within the temperature range in our plasma-catalytic reaction. These results clearly indicate the generation of a synergistic effect resulting from the combination of plasma and the Ni-Co bimetallic catalyst at low temperature (without extra heating), in which the performance of plasma-catalytic reaction is much higher than the sum of results in the plasma-only and the catalysis only processes. This synergistic effect is closely related to the balance between the change in the discharge behaviour produced by packing the catalysts in the discharge gap and the catalytic activity of the catalyst generated by the plasma [91, 92]. In this case, the synergy is believed to be attributed to the strong plasma-catalyst interaction due to the filamentary discharge resulting from the large discharge volume when the catalysts are partially packed along the bottom of the reactor and the high activity of the Ni-Co bimetallic catalyst with appropriate Co loadings.

7.3.3.4 Catalyst characterisation after reaction

The carbon balance in the gas stream of plasma-catalytic reaction using different Ni-Co bimetallic catalysts is shown in **Figure 7.14**. A maximum carbon balance of 97.4% is achieved when the 10Ni5Co catalyst is used at a discharge power of 30 W.

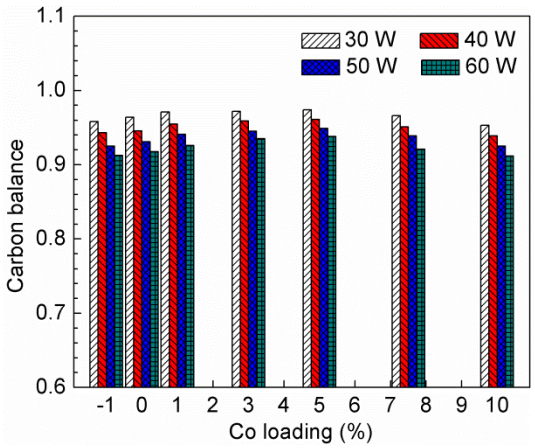

Figure 7.14 Effect of Co loadings on the carbon balance as a function of discharge power (total feed flow rate: 50 ml/min; CO_2/CH_4 molar ratio: 1:1; -1 in the x-coordinate stands for the case in the absence of the catalyst).

The amount of carbon deposition on the catalysts is analysed using TG-DTG and the results are presented in **Figure 7.15** and **Table 7.3**. TG analysis of the Ni catalysts shows a weight loss within the range of 2.1%-3.8%. The TGA profile of the 10Ni10Co catalyst indicates that two different carbonaceous species are formed on the catalysts, as shown in **Figure 7.15**. The peak at around 320 ^oC is assigned to the

formation of active carbonaceous species (C_α), which are easily oxidisable amorphous carbon and often regarded as the intermediate for CO formation. The higher temperature (around 520 ^oC) peak corresponds to the less active carbonaceous species (C_β), which may be between amorphous carbon and graphitic carbon [267]. Both carbonaceous species are formed in all of the spent catalysts, as shown in **Table 7.3**. The graphitic carbon species (shown by a peak above 650 ^oC) is responsible for the deactivation of the catalysts. It can be found that no such carbon species is formed on the catalysts used in the plasma dry reforming process. This can be confirmed by the stability of the CO_2 and CH_4 conversion, and the CO and H_2 selectivity when the catalysts participate in the plasma reaction for 150 min. The variation of carbon deposition with the Co loading, as given in **Table 7.3**, indicates the least amount of carbon (2.1%) is formed on the 10Ni5Co catalyst, which exhibits the highest carbon resistance; whereas the largest amount of carbon (3.8%) is formed on the 10Ni catalyst (without Co additive). In the conventional thermal catalytic dry reforming of CH_4 using similar Ni-Co bimetallic catalysts, Sengupta et al. used Al_2O_3 supported Ni-Co bimetallic catalysts containing 15 wt.% metal for the dry reforming of CH_4 at a high temperature of 600 ^oC. They found that the bimetallic catalyst 25Ni75Co (3.75 wt.%/11.25 wt.%) had a minimum carbon deposition of 3%; while the maximum amount of carbon (20%) was deposited on the 75Ni25Co catalyst (11.25 wt.%/3.75 wt.%) [292]. Son et al. reported a high carbon deposition of 16% when the Ni-Co/Al_2O_3 catalyst was used in the thermal-catalytic dry reforming of CH_4 performed at the temperature between 700 ^oC to 850 ^oC [308]. This phenomenon indicates that the combination of plasma and the Ni-Co bimetallic catalysts in our study can further suppress the carbon deposition.

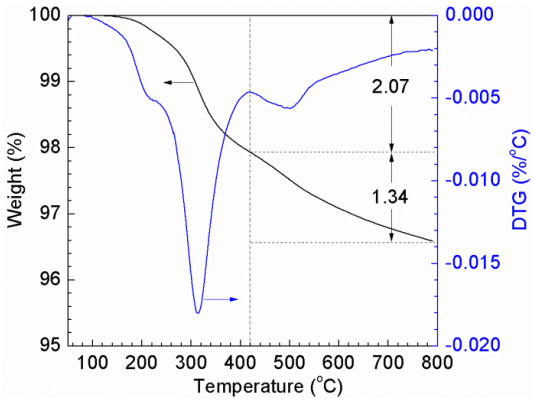

Figure 7.15 TG and DTG results for the 10Ni10Co catalyst after reaction at a discharge power of 50 W for 150 min.

Table 7.3 Comparison of carbon deposition of different catalysts at a discharge power of 50 W for 150 min.

Sample	Carbonaceous species /%		
	C_α	C_β	Total
10Ni	2.6	1.2	3.8
10Ni1Co	1.9	1.1	3.0
10Ni3Co	1.8	1.1	2.9
10Ni5Co	1.1	1.0	2.1
10Ni7.5Co	1.7	1.1	2.8
10Ni10Co	2.1	1.3	3.4

The introduction of the Ni-Co bimetallic catalysts in the dry reforming process is mainly motivated by the high catalytic activity of Ni catalysts and the high carbon resistance of Co catalysts. Ni catalysts show high catalytic activity in the dry reforming of CH_4; however, during the reforming process, a large amount of carbon species are formed on the catalyst surface, which need to be removed to proceed with the reforming reaction [309]. Cobalt is a good oxidative agent for soot, which can decrease the coke formation rate by transforming the surface carbon to CO and/or CO_2 [296]. Previous studies have reported that increasing the Co loading in the Ni-Co bimetallic catalyst would result in a significant decrease of coke in the reforming process [309, 310]. This is possibly due to the fact that increasing the Co loading could effectively control the activity of CH_4 decomposition to balance carbon formation and elimination, thereby achieving a higher carbon resistance [309]. Moreover, the contribution of the larger amount of strong basic sites on the catalyst to its high carbon resistance cannot be ruled out [284].

The geometric effect is another important factor influencing the carbon resistance of the Ni-Co bimetallic catalysts. A large ensemble of adjacent sites is a prerequisite for carbon growth during the carbon deposition process; and there exists a critical size of the metal particles below which carbon formation can be significantly reduced in the reforming process. In the thermal-catalytic dry reforming of CH_4 using Ni-Co bimetallic catalysts, Zhang et al. found that the metal particle size less than 10 nm is critical to avoid carbon formation [302]. In this study, the metal particle size is enlarged by increasing the Co loading in the Ni-Co bimetallic catalysts. It is clear from **Table 7.3** that the carbon deposition is enhanced when the Co loading is higher than 5 wt.%, therefore we may conclude that the metal particle size is beyond the critical size for inhibiting carbon formation by increasing the Co loading to higher than 5 wt.%. In this study, the lowest carbon deposition is achieved when the 10Ni5Co catalyst is used in the plasma dry reforming process, indicating that the formation of the Ni-Co alloy and the variation in its size are the main driving forces that control the carbon resistance of the Ni-Co bimetallic catalysts.

7.3.3.5 Energy efficiency

Figure 7.16 shows the EC and FPE of the plasma catalytic dry reforming process using different NI-Co bimetallic catalysts at a discharge power of 30 W. A minimum EC of 7.7, 5.4 and 3.2 MJ/mol for CO_2 conversion, CH_4 conversion and total carbon conversion, respectively, is achieved when the 10Ni5Co catalyst is combined with the DBD plasma; this value is decreased by 28.0%, 17.4% and 21.8%, compared to the respective values in the plasma-only process. Correspondingly, introducing the 10Ni5Co catalyst into the plasma reaction decreases the EC for H_2 and syngas production by 32.9% and 32.2%. In addition, the combination of the 10Ni5Co catalyst with the DBD reactor leads to a maximum FPE of 12.7%, which is increased by 30.4% compared to that obtained in the plasma-only process at the same condition.

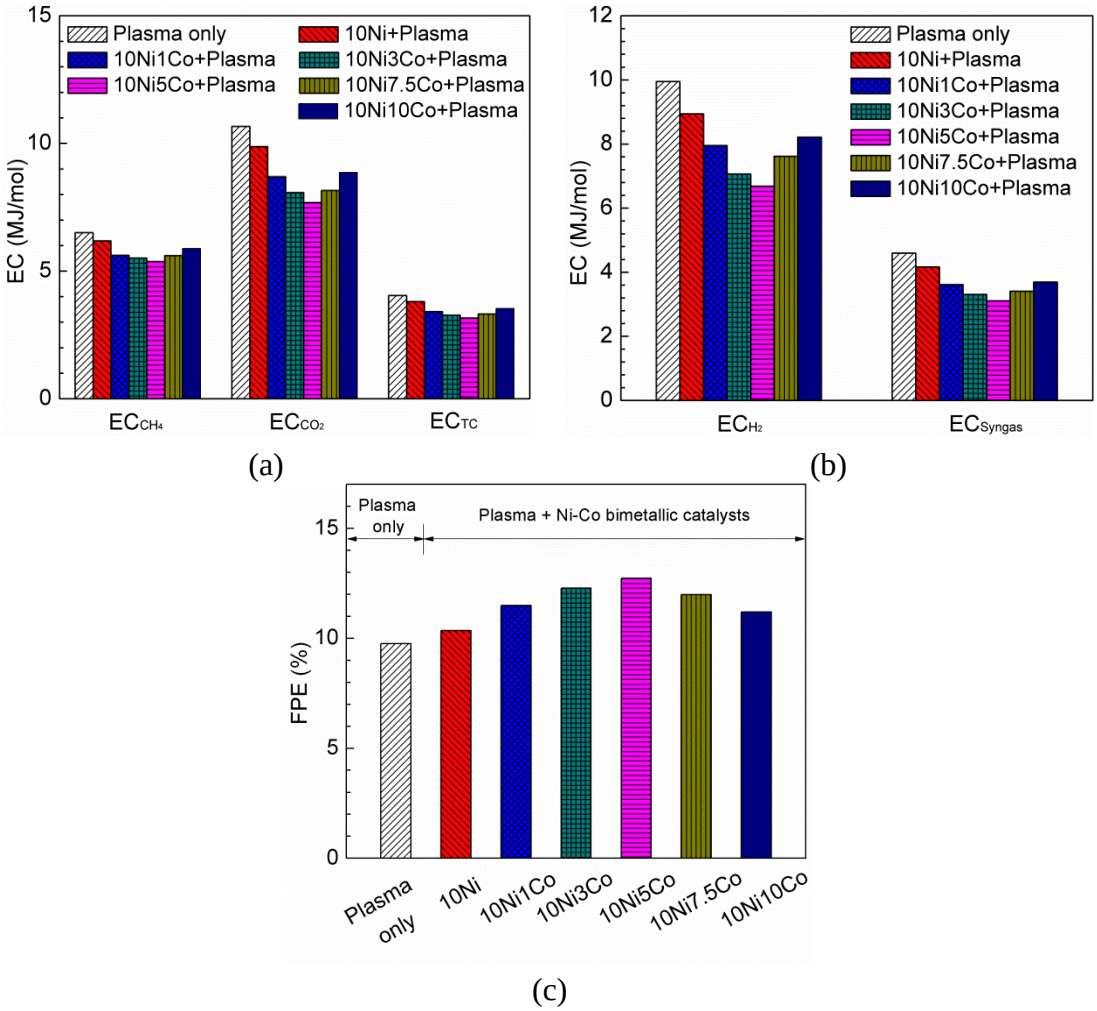

Figure 7.16 Effect of Co loadings on (a) the EC for CH_4 conversion, CO_2 conversion and total carbon conversion; (b) the EC for H_2 and syngas production; (c) the FPE (discharge power: 30 W; total feed flow rate: 50 ml/min; CO_2/CH_4 molar ratio: 1:1).

7.4 Comparison of Reaction and Energy Performance for Different Non-thermal Plasma Dry Reforming Reactors

In order to evaluate the effectiveness of the DBD reactor for the plasma dry reforming of CH_4, we compare the performance of our DBD reactor with that of other non-thermal plasma reactors. Reactant conversion and energy efficiency are the most important performance parameters for the plasma process [144]. In this work, we also compare the EC for H_2 production, as H_2 is a promising alternative to fossil fuels and its production cost is one of the main issues for its large scale application.

Table 7.4 lists various atmospheric pressure non-thermal plasma systems for comparison along with their different specific processing parameters, including discharge form, frequency, power, total flow rate, CO_2/CH_4 molar ratio in the feed gas as well as any catalysts used. In addition to the DBD reactors, one DC pulsed plasma reactor, two GA reactors, and a pulsed corona reactor, are also selected.

7.4.1 Performance comparison for plasma dry reforming of CH_4 without catalyst

In this section, the performance comparison for the dry reforming of CH_4 in the plasma-only process is performed in terms of the maximum total carbon conversion, the minimum EC for H_2 production and the maximum FPE.

Table 7.5 shows the maximum total carbon conversion in our study and that obtained from literature. Other parameters, such as product selectivity, EC for H_2 production and FPE, are also included. The effect of SED on the maximum total carbon conversion is illustrated in **Figure 7.17**. Generally, the maximum total carbon conversion is enhanced by increasing SED. Similar phenomenon has been observed in other plasma gas reactions, such as removal of VOC and CO_2 decomposition [234, 311].

It is clear from **Table 7.4** and **Table 7.5** that most of the reactors produce their maximum total carbon conversion at the lower limit of the total feed flow rate, which indicates that a lower total feed flow rate is beneficial for the conversion of reactants. Decreasing the total feed flow rate increases the residence time of the reactant molecules in the discharge region, which will increase the possibility of collisions between the reactant molecules and the highly energetic electrons as well as active species, therefore enhancing the conversion. The maximum total carbon conversion in our study (42.3%) is obtained at a SED of 120 kJ/l and a total feed flow of 25 ml/min with a CO_2/CH_4 molar ratio of 1:1. Due to the relatively low SED, this maximum total carbon conversion is smaller than that obtained in most of the other reactors, but it is comparable to that obtained in reactors which have a similar SED to ours, such as the DBD reactor of Tu et al. (No 15) [91] and Mahammadunnisa et al. (No 16) [162]. The DBD reactor of Zhang et al. had the

Table 7.4 Experimental conditions of the atmospheric non-thermal plasma reactors for dry reforming of CH_4.

Plasma reactor		Frequency (kHz)	Power (W)	Total feed flow rate (ml/min)	CO_2/CH_4 molar ratio	Catalyst	Ref
No	Type						
1	DBD	5 – 20	20 – 60	25 – 150	1:4 – 4:1	Ni-based catalysts	This work
2	DBD	30	200 – 700	150, 500	1:4 – 4:1	–	[151]
3	DBD	25	100	40	17.2:82.8 – 66:34	–	[312]
4	DBD	5 – 20	23.0 – 178.5	16, 20, 30	1:5 – 5:1	–	[154]
5	DBD	30	200 – 500	20 – 200	1:4 – 4:1	–	[238]
6	DBD	0.3	9	4.5 – 45	1:1	–	[278]
7	DBD	10 – 40	24 – 147	30	1:1	–	[313]
8	DC pulse	0 - 700	9.2 – 34.8	45, 90	1:1	–	[314]
9	Gliding arc	0.05	205.3 – 544.0	12700	1:2 – 2:1	–	[142]
10	Gliding arc	0.05	95 – 165	2500 - 7500	3:7 – 7:3	–	[143]
11	DBD	30	200 – 700	150 – 800	1:5 – 4:1	Zeolite NaX	[158]
12	DBD	30	500	200 – 600	1:3 – 2:1	Zeolite NaX, HY, NaY	[42]
13	DBD	30	100 – 500	200 – 600	1:3 – 1:1	Zeolite A	[160]
14	DBD	20	80 – 130	10 – 40	1:4 – 2:1	(2, 5, 7, 10 wt.%) $Ni/\gamma\text{-}Al_2O_3$	[168]
15	DBD	30 – 40	30 – 60	25 – 100	1:1	10 wt.% $Ni/\gamma\text{-}Al_2O_3$	[91]
16	DBD	0.05	1.4 – 4.8	2.67, 3	1:2 – 2:1	(10, 20, 30 wt.%) $Ni/\gamma\text{-}Al_2O_3$	[162]
17	DBD	20	126	30	1:1	5 wt.% $Ni/\gamma\text{-}Al_2O_3$	[165]
18	DBD	30 – 40	70.5 – 97.3	50	1:1	26 wt.% Ni/Al_2O_3	[107]
19	DBD	30	25 – 75	30 – 75	2:3 – 3:1	$Ni/\gamma\text{-}Al_2O_3$, $Cu/\gamma\text{-}Al_2O_3$, $Cu\text{-}Ni/\gamma\text{-}Al_2O_3$, $Ni\text{-}Cu/\gamma\text{-}Al_2O_3$	[116]
20	DBD	5 – 100	150	40	1:1	Ni/SiO_2, $LaNiO_3$, $LaNiO_3/SiO_2$, $LaNiO_3@SiO_2$	[173]
21	DBD	–	2.8 – 25.4	11.3 – 45	2:3 – 10:7	Perovskite $LaNiO_3$	[315]
22	Corona	–	18 – 42	60	2:1	$Ni/\gamma\text{-}Al_2O_3$, Zeolite HZSM-5	[272]

same SED as that in this study and presented a more promising total carbon conversion than ours [116], but FPE in their reactor is relatively lower. From the perspective of industrial applications, higher reactant conversions with large treatment capacity are desired. Although the total feed flow rates in the GA reactors (e.g. plasma reactor No 9 and 10) were typically higher than that in the DBD reactors, the reactant conversions in the GA reactors is relatively low. Therefore, how to increase the treatment capacity when maintaining the high reactant conversion should be a research topic in the future.

Table 7.5 Comparison of the maximum total carbon conversion in different plasma-only systems.

Plasma reactor		SED (kJ/l)	Total feed flow rate (ml/min)	CO_2/ CH_4 molar ratio	Conversion (%)			Selectivity (%)		EC_{H2} (MJ/ mol)	FPE (%)	Ref
No	Type				CH_4	CO_2	C_{TC}	H_2	CO			
1	DBD	120	25	1:1	50.5	34.1	42.3	35.8	52.0	14.9	5.8	This work
2	DBD	280	150	1:2	72.4	63.0	69.3	46.8	34.2	13.9	3.9	[151]
3	DBD	150	40	1:3	52.5	41.9	49.8	37.4	24.6	11.4	5.1	[312]
4	DBD	533.4	20	1:1	79.5	52.7	66.1	75.7	84.9	19.9	2.7	[154]
5	DBD	1500	20	1:1	78.1	67.9	73.0	46.2	47.2	93.1	0.5	[238]
6	DBD	60	9	1:1	21.1	17.5	19.3	50.3	57.5	12.7	4.3	[278]
7	DBD	282	30	1:1	65.7	38.7	52.2	46.2	53.8	20.8	3.2	[313]
8	DC pulse	46.4	45	1:1	52.7	42.7	47.7	75.0	70.8	2.6	15.3	[314]
9	GA	2.46	12700	2:1	41.0	36.4	38.0	38.4	55.0	0.5	64.7	[142]
10	GA	3.96	2500	7:3	19.3	11.5	13.8	25.8	63.0	3.0	25.6	[143]
11	DBD	200	150	1:2	64.3	55.4	61.3	40.5	33.3	12.9	4.7	[158]
14	DBD	780	10	1:1	74.1	49.2	61.7	66.0	73.8	35.8	1.5	[168]
15	DBD	144	25	1:1	50.6	30.5	40.6	33.4	53.8	19.1	3.0	[91]
16	DBD	90.0	2.7	1:1	45.8	39.0	42.4	32.5	38.6	13.5	3.7	[162]
19	DBD	120	30	1:1	59.6	37.0	48.3	43.5	43.5	10.4	4.2	[116]
21	DBD	62.6	11.5	2:3	30.7	22.0	27.2	33.9	35.3	11.2	6.3	[315]

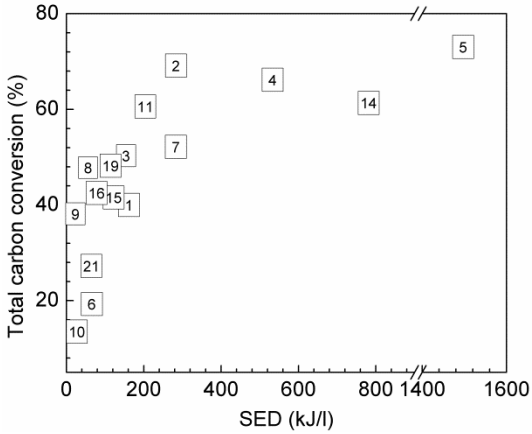

Figure 7.17 Comparison of the maximum total carbon conversion in the plasma-only dry reforming of CH_4 as a function of SED (each squared number refers to the plasma reactor No listed in **Table 7.4**).

The minimum EC for H_2 production in our DBD plasma reactor and that obtained from literature is shown in **Table 7.6** and **Figure 7.18**. Similar to the maximum total carbon conversion, the minimum EC for H_2 production is also increased by increasing the SED. From **Table 7.6**, the selectivity towards H_2 is another important parameter controlling the EC for H_2 production. The EC for H_2 production can be significantly decreased when higher selectivity of H_2 is obtained. In the DBD reactor of Wang et al. [154], the higher selectivity of H_2 resulted in the deviation of the minimum EC for H_2 production from its general trend with SED (see **Figure 7.18**). Compared with the DBD reactors, the DC pulsed wire-to-plate reactor (No 8) and GA reactor (No 9 and 10) show a much lower minimum EC for H_2 production together with a much higher FPE. As mentioned above, Ar was used as the carrier gas in plasma reactor No 8 to enhance the reactant conversion. However, the cost of the carrier gas is not considered in our comparison, thus the actual EC for H_2 production in plasma reactor No 8 could be much higher. For the GA reactors (No 9 and 10), the lower minimum EC for H_2 production and higher FPE were obtained at the expense of lower reactant conversions. For example, in the plasma reactor No 10, the minimum EC for H_2 and the corresponding FPE are 1.2 MJ/mol and 47.2%, obtained at a SED of 1.32 kJ/l and a CO_2/CH_4 molar ratio of 3:7, but the total carbon conversion is only 9.8% at the same condition. A large amount of unconverted reactant in the product stream would increase the cost of separating the products for further application. Among the DBD plasma reactor, a minimum EC for H_2 production of 7.5 MJ/mol is obtained in this study at a SED of 24 kJ/l and a CO_2/CH_4 molar ratio of 1:1 with a total flow rate of 50 ml/min, which is comparable to other DBD plasma reactors due to the combination of the low SED and relatively high selectivity of H_2.

Table 7.6 Comparison of the minimum EC for H_2 production in different atmospheric non-thermal plasma-only systems.

Plasma reactor		SED (kJ/l)	Total feed flow rate (ml/min)	CO_2/ CH_4 molar ratio	Conversion (%)			Selectivity (%)		EC_{H2} (MJ/ mol)	FPE (%)	Ref
No	Type				CH_4	CO_2	C_{TC}	H_2	CO			
1	DBD	24	50	1:1	21.2	14.3	17.7	33.7	47.8	7.5	13.0	This work
2	DBD	160	150	1:2	58.4	49.7	55.5	36.6	33.3	12.6	5.3	[151]
3	DBD	150	40	1:3	52.5	41.9	49.8	37.4	24.6	11.4	5.1	[312]
4	DBD	143	30	1:1	63.3	33.5	48.4	89.9	94.7	5.6	8.1	[154]
5	DBD	150	200	1:4	37.9	33.2	37.0	36.4	25.4	15.2	2.2	[238]
6	DBD	15	36	1:1	12.7	8.9	10.8	46.2	39.9	5.7	8.0	[278]
7	DBD	70	30	1:1	24.4	16.1	20.3	45.9	53.2	14.0	5.2	[313]
8	DC pulse	12.3	45	1:1	29.0	21.0	25.0	65.8	61.9	1.4	23.2	[314]
9	GA	1.0	12700	1:2	12.3	8.1	10.9	72.8	26.4	0.2	87.9	[142]
10	GA	1.32	7500	3:7	13.3	8.4	9.8	31.6	69.5	1.2	47.2	[143]
11	DBD	200	150	1:2	64.3	55.4	61.3	40.5	33.3	12.9	4.7	[158]
14	DBD	260	30	1:3	42.6	29.0	39.2	54.1	25.5	16.8	2.7	[168]
15	DBD	18	100	1:1	15.5	6.3	10.9	21.6	37.4	12.0	4.2	[91]
16	DBD	28.2	3	1:2	22.0	10.3	18.1	33.9	36.8	6.4	5.7	[162]
19	DBD	25	60	1:1	17.5	12.3	14.9	58.3	59.1	5.5	7.9	[116]
21	DBD	36.5	22.5	2:3	17.0	12.5	15.2	57.6	37.3	7.0	8.3	[315]

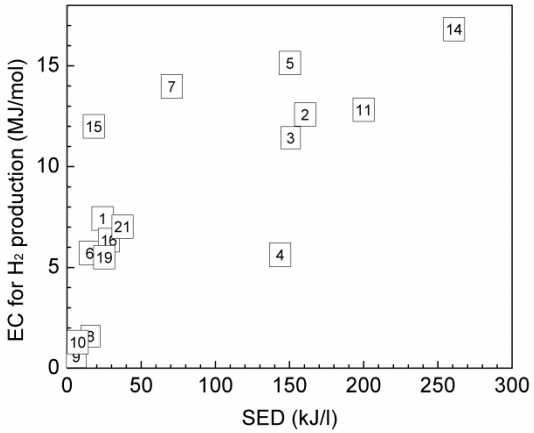

Figure 7.18 Comparison of the minimum EC for H_2 production in the plasma-only dry reforming of CH_4 as a function of SED.

Table 7.7 and **Figure 7.19** show the comparison of the FPE in different plasma-only systems for dry reforming of CH_4. Obviously, a lower SED is favourable for a higher FPE in the plasma dry reforming process. It can be seen from **Table 7.4** and **Table 7.7** that the majority of the maximum FPE are obtained near the upper limit of the total feed flow rate, which suggests that a higher total feed flow

rate is preferred for higher FPE. From the definition of the SED (Equation (2-1)), a higher total feed flow rate leads to a lower SED when maintaining or reducing discharge power, thereby increasing the FPE as discussed above. This phenomenon has been reported in our previous study [229]. A maximum FPE of 13.0% is obtained at a SED of 24 kJ/l. It is interesting to note that the maximum FPE is obtained at the same experimental condition as that for the minimum EC for H_2 production in our study. The same results were also obtained in plasma reactors No 4, 6, 8, 9, 10, 16 and 19, which implies that similar experimental conditions are required to obtain both lower EC for H_2 production and higher FPE. Apart from the maximum FPE obtained in plasma reactor No 8 (with the aid of the carrier gas Ar) and that in the plasma reactors No 9 and 10 (obtained at the expense of reactant conversion), the maximum FPE in our DBD reactor is higher than that in other DBD reactors from the published literature. Comparing **Table 7.5** with **Table 7.7**, it can be found that the FPE corresponding to the maximum total carbon conversion is relatively low, and vice versa. This suggests that further optimisation is necessary in the future work to enhance the reactant conversion and the FPE simultaneously.

Table 7.7 Comparison of the FPE in different plasma-only processes for dry reforming of CH_4.

Plasma reactor		SED (kJ/l)	Total feed flow rate (ml/min)	CO_2/ CH_4 molar ratio	Conversion (%)			Selectivity (%)		EC_{H2} (MJ/ mol)	FPE (%)	Ref
No	Type				CH_4	CO_2	C_{TC}	H_2	CO			
1	DBD	24	50	1:1	21.2	14.3	17.7	33.7	47.8	7.5	13.0	This work
2	DBD	80	150	1:2	34.1	30.2	32.8	19.7	31.4	20.0	5.9	[151]
3	DBD	150	40	1:2	54.0	37.4	48.6	40.3	31.8	11.4	5.2	[312]
4	DBD	143	30	1:1	63.3	33.5	48.4	89.9	94.7	5.6	8.1	[154]
5	DBD	150	200	1:1	43.3	32.5	37.9	42.6	55.4	18.2	2.9	[238]
6	DBD	15	36	1:1	12.7	8.9	10.8	46.2	39.9	5.7	8.0	[278]
7	DBD	86	30	1:1	27.0	16.7	21.9	50.8	61.5	14.0	5.3	[313]
8	DC pulse	12.3	45	1:1	29.0	21.0	25.0	65.8	61.9	1.4	23.2	[314]
9	GA	1.0	12700	1:2	12.3	8.1	10.9	72.8	26.4	0.2	87.9	[142]
10	GA	1.32	7500	7:3	13.3	8.4	9.8	31.6	69.5	1.2	47.2	[143]
11	DBD	60	500	1:2	36.3	27.8	33.5	11.9	43.1	23.3	6.7	[158]
14	DBD	160	30	1:2	39.3	20.4	29.9	53.8	54.6	17.0	3.5	[168]
15	DBD	36	50	1:1	20.2	13.1	16.7	29.0	42.4	13.8	9.6	[91]
16	DBD	28.2	3	1:2	22.0	10.3	18.1	33.9	36.8	6.4	5.7	[162]
19	DBD	25	60	1:1	17.5	12.3	14.9	58.3	59.1	5.5	7.9	[116]
21	DBD	16.0	44.9	2:3	10.7	8.3	9.7	35.0	33.0	8.0	9.6	[315]

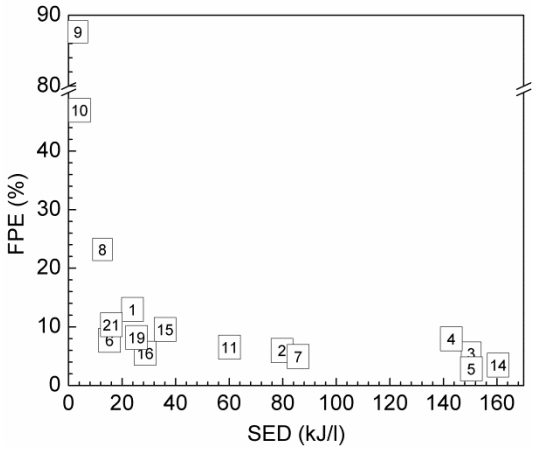

Figure 7.19 Comparison of the maximum FPE in the plasma-only dry reforming of CH_4 as a function of SED.

7.4.2 Performance comparison for plasma-catalytic dry reforming of CH_4

A comparison of the FPE in the different plasma-catalytic processes for dry reforming of CH_4 is shown in **Table 7.8**. Most research has focused on the DBD reactor, which reflects the potential of this reactor for the dry reforming process. In the early stages, zeolites were used in the plasma-catalytic reforming process. Later, some new catalysts, such as $LaNiO_3@SiO_2$, were applied as well as the common Ni/γ-Al_2O_3 catalyst. **Figure 7.20** shows the variation of the maximum FPE as a function of the SED in the plasma-catalytic processes. Similar to the phenomenon in the plasma-only process, the maximum FPE in the plasma-catalytic process is also decreased by increasing SED. The DBD reactor of Lee et al. showed very high reactant conversions and product selectivities when the 5% Ni/γ-Al_2O_3 catalyst was used [165]; however, they were obtained at a higher SED of 252 kJ/l and by using thermal heating at 573 K, both of which increase EC for H_2 production and decrease the FPE. The cost of the thermal heating is not considered in this comparison; thus the FPE in their DBD reactor would be lower than the stated value of 8.4%. Similarly, in the DBD reactor of Zheng et al., the core-shell structured $LaNiO_3@SiO_2$ nano-particle catalysts were introduced to obtain high reactant conversion and product selectivity [173]; however, the reactions were performed at a high SED of 225 kJ/l, resulting in a low FPE of 7.3%. Zhang et al. reported that high reactant conversion and product selectivity were obtained at a relatively low SED of 120 kJ/l when the 12 wt.%Ni-12 wt.% Cu/γ-Al_2O_3 catalyst was used in a DBD reactor [116] but the promotional effect of the carrier gas Ar and the thermal heating (at 450 ^oC) should not be ruled out, which would decrease FPE from its current value of 8.5%. In the DBD reactor of Mahammadunnisa et al., relatively high FPE (12.0%) and low EC for H_2 production (2.3 MJ/mol) were obtained over the 20 wt.% Ni/γ-Al_2O_3 catalyst at a SED of 28 kJ/l [162], but the reactants were balanced with Ar and the effective total flow rate was very low (only 3 ml/min), which is unsuitable for practical application.

Table 7.8 Comparison of the FPE in different plasma-catalytic systems

Plasma reactor		SED (kJ/l)	Total feed flow rate (ml/min)	CO_2/CH_4 molar ratio	Catalyst	Conversion (%)			Selectivity (%)		EC_{H2} (MJ/mol)	FPE (%)	Ref
No	Type					CH_4	CO_2	Total	H_2	CO			
1	DBD	36	50	1:1	10 wt.% Ni-5 wt.% Co/γ-Al_2O_3	30.0	21.0	25.5	40.2	54.4	6.7	12.7	This work
11	DBD	37.5	800	1:1	Zeolite NaX	20.1	15.3	17.7		40.1		6.4	[158]
12	DBD	50	600	1:1	Zeolite NaY	34.7	15.2	25.0	23.2	45.0	13.9	9.3	[42]
13	DBD	150	200	1:3	Zeolite A	54.8	25.3	47.4	48.1	26.8	8.5	8.6	[160]
14	DBD	260	30	1:1	7 wt.% Ni/γ-Al_2O_3	55.5	32.6	44.0	53.5	63.9	19.6	3.2	[168]
15	DBD	60	50	1:1	10 wt.%Ni/γ-Al_2O_3	56.4	30.2	43.3	31.0	52.4	7.7	16.4	[91]
16	DBD	28	3	1:2	20 wt.% Ni/γ-Al_2O_3	35.9	20.0	30.6	57.1	37.0	2.3	12.0	[162]
17	DBD	252	30	1:1	5 wt.% Ni/ γ-Al_2O_3	97.0	99.8	98.4	100.0	97.0	5.8	8.4	[165]
18	DBD	116.9	50	1:1	26 wt.% Ni/γ-Al_2O_3	18.0	12.4	15.2	45.5	23.8	32.0	1.3	[107]
19	DBD	120	30	1:1	12 wt.%Ni-12 wt.% Cu/γ-Al_2O_3	69.8	75.3	72.6	56.6	76.0	6.8	8.5	[116]
20	DBD	225	40	1:1	$LaNiO_3$@SiO_2	88.3	77.8	83.0	83.7	92.4	6.8	7.3	[173]
21	DBD	66.7	22.5	2:3	Perovskite $LaNiO_3$	54.5	73.0	61.9	38.2	50.4	6.0	8.5	[315]
22	Corona	18	60	2:1	Ni/Al_2O_3	43.8	35.5	38.2	74.9	89.6	1.8	28.8	[272]

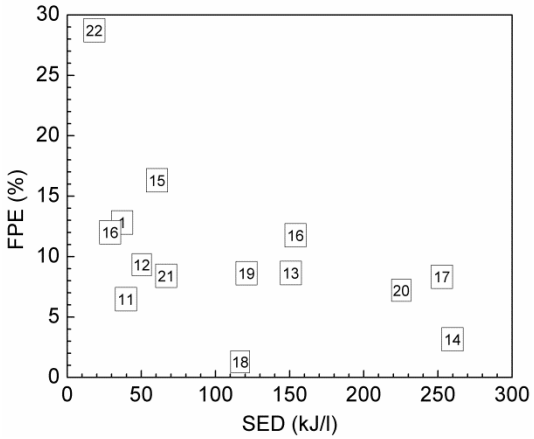

Figure 7.20 Comparison of the maximum FPE in the plasma-catalytic dry reforming of CH_4 as a function of SED.

In this study, the plasma-catalytic dry reforming of CH_4 using Ni-based catalysts is performed at low temperatures and atmospheric pressure (without extra heating). Compared with simple catalysts in the previous studies, the suitable supports for the Ni-based catalysts have been screened and the optimal Ni loading on the suitable support for high reaction performance have also been determined. The Ni-based bimetallic catalysts are further developed to improve their plasma-catalytic activity and stability, and to decrease the carbon deposition on the spent catalysts. The optimised Ni-Co bimetallic catalyst has shown the stronger carbon resistance than that in both conventional thermal-catalytic and previous plasma-catalytic dry reforming of CH_4. The highest FPE of 12.7% is achieved in the presence of the 10Ni5Co catalyst at a SED of 36 kJ/l and CO_2/CH_4 molar ratio of 1:1 with a total feed flow rate of 50 ml/min, which is comparable to the results obtained in the published non-thermal plasma reactors, except that reported in the corona reactor (28.8% in reactor No 22) [272]. Nevertheless, characterised by the localised breakdown, corona discharge may not have a very large treatment capacity for the plasma-catalytic dry reforming of CH_4 due to the limited reaction volume [147]. Contrarily, the DBD reactor can effectively utilise the entire electrode area for plasma reactions and a large scale DBD reactor can be obtained by integrating a number of coaxial tubular reactors, which has been demonstrated in the large scale water treatment using DBD reactors at water purification plants [316]. This enables DBD reactors to treat gases at a high flow rate and results in their high potential for industrial scale application. The research related to the Ni catalysts contributes to the exploration of the feasible catalysts for the plasma-catalytic dry reforming process and the further development of the plasma-catalysis system. In addition, renewable energy (e.g. solar and wind energy) is witnessing rapid development worldwide, and the renewable energy plants are generally established in remote areas. Its compactness and fast start-up and switch-off enable the plasma system to be easily

established in those areas and integrated with the renewable energy sources. The utilisation of the plasma-catalytic process supplied by energy from renewable sources will provide a promising approach for storage and transportation, in the chemical form, of the electricity produced during peak periods; in this way, the operating cost of the plasma-catalytic process will be significantly reduced. Moreover, no more CO_2 will be emitted into the atmosphere in this process, thus achieving carbon neutrality.

7.5 Conclusions

In this chapter, the Ni-based bimetallic catalysts are introduced into the coaxial DBD reactor for the plasma-catalytic dry reforming of CH_4. The combination of plasma with the bimetallic catalysts improves the performance of the plasma-catalytic reforming reaction, regardless of the discharge power. Among the three Ni-based bimetallic catalysts - 10Ni3Co, 10Ni3Cu, 10Ni3Mn - the 10Ni3Co catalyst shows the best catalytic performance due to its large amount of the strong basic sites, the interaction between Ni and Co, as well as the relative high specific surface area.

For the Ni-Co bimetallic catalysts with different Co loadings, it is found that the 10Ni5Co catalyst gives the highest catalytic performance, with the highest CO_2 conversion of 30.9% and CH_4 conversion of 50.8% at the discharge power of 60 W and a total feed flow rate of 50 ml/min. In addition, it was found that the carbon resistance is firstly enhanced by increasing the Co loading and then is decreased when the Co loading is beyond its optimal value. This is possibly due to the variation of physicochemical properties (i.e. metal particle size and specific surface area) and the amount of the basic sites on these catalysts. The 10Ni5Co catalyst shows the highest carbon resistance, which is higher than that in the thermal-catalytic reforming process using a similar Ni-Co bimetallic catalyst.

Considering the reaction performance, reasonable total carbon conversion, EC for H_2 production and FPE of the plasma-only process are obtained in this study, compared with those values available from literature related to the dry reforming of CH_4 in atmospheric pressure non-thermal plasma reactors. For the plasma-catalytic dry reforming process, the maximum FPE is obtained with a promising EC for H_2 production, which is comparable to those in the published works. It is expected that the integration of the plasma-catalytic process with renewable energy sources will give it high potential for use on an industrial scale.

CHAPTER EIGHT CONCLUSIONS AND FUTURE WORK

8.1 Conclusions

Climate change due to greenhouse gas emission has attracted worldwide attention, along with the need to find new methods of producing clean and sustainable energy. Carbon dioxide utilisation will benefit humans from the perspectives of energy utilisation and environmental protection. In this thesis, worldwide energy consumption and greenhouse gas emission are firstly described, followed by current strategies for CO_2 remediation and utilisation, including policy and technological efforts. As an attractive and promising alternative to the thermal catalytic route for the conversion of CO_2 into value-added fuels and chemicals, the non-thermal plasma technology is employed. Specifically, direct CO_2 decomposition and dry reforming of CH_4 are performed in a coaxial DBD reactor. The pursuit of suitable catalysts for the plasma-catalytic processed of these two reactions is also carried out to enhance the energy efficiency of the plasma process. The main conclusions are summarised as follows:

(1) In the plasma decomposition of CO_2, the effects of the processing parameters - frequency, discharge power, feed flow rate, discharge length, discharge gap and dielectric thickness - on the performance of CO_2 decomposition (CO_2 conversion and energy efficiency) are systematically investigated. Empirical equations relating the CO_2 decomposition performance and processing parameters are established for sensitivity analysis. It is found that CO_2 is stoichiometrically decomposed into CO and O_2 and no carbon deposition is observed. The discharge gap plays the most important role in CO_2 conversion, whilst discharge power most significantly affects the energy efficiency.

(2) The enhancement in the performance of the plasma CO_2 decomposition is achieved by introducing a screw-type inner electrode and an Al foil outer electrode. The local electric field near the inner electrode surface is enhanced by the sharp edge of the screw electrode, whilst the larger effective cover area is obtained by using the Al foil outer electrode, all of these factors contribute to the intensification of the filamentary discharges and the generation of more energetic electrons and reactive species, and consequently lead to higher CO_2 conversion and energy efficiency. With the screw-type inner electrode and the Al foil outer electrode, CO_2 conversion and energy efficiency is increased by 21.3% and 21.4%, respectively, at a SED of 120 kJ/l.

(3) In the plasma-photocatalytic conversion of CO_2 using $BaTiO_3$ and TiO_2 as photocatalysts, the gas temperature of the plasma (almost the same as the temperature on the surface of the photocatalysts) is increased by 6-11 ^oC compared to

that in the CO_2 discharge in the absence of a catalyst at a SED of 28 kJ/l. A synergistic effect is generated from the combination of non-thermal plasma with photocatalysts in the plasma-catalytic CO_2 decomposition. CO_2 conversion and energy efficiency are both increased by a factor of 2.5 compared to the plasma reaction in the absence of a catalyst. This phenomenon is mainly attributed to both the physical effect (enhancement in the electric field and the mean electron energy) induced by the presence of the photocatalysts in the discharge volume and the photocatalytic surface reactions driven by the non-thermal plasma (energetic electrons and reactive species generated in the discharge contribute to the chemical reactions). It is suggested that the highly energetic electrons generated by plasma is the main driving force to activate the photocatalysts for CO_2 conversion.

(4) In the packed-bed DBD reactor, by integrating the packing pellets ($BaTiO_3$ and glass beads) into the DBD reactor to form a packed-bed, the discharge behaviour changes from a typical filamentary discharge with no packing to a combination of filamentary discharge and surface discharge at a constant discharge power. An enhancement in CO_2 conversion and energy efficiency in the packed-bed DBD reactor are also achieved due to the increase in the electric field and mean electron energy resulting from the presence of the packing pellets. For $BaTiO_3$, the effect of its photocatalytic properties to the enhanced conversion of CO_2 is also considered. A maximum CO_2 conversion of 28.2% is obtained when $BaTiO_3$ is used at a SED of 60 kJ/l.

(5) For the dry reforming of CH_4, different reaction mechanisms are found to exist in the thermal-catalytic and the plasma reforming processes. This can be ascertained by comparing the reaction performance of these two processes using the thermodynamic equilibrium calculation and the experiments of dry reforming of CH_4 in the plasma-only process. In the thermal dry reforming process, pyrolysis is the main reaction mechanism; while in the plasma process, reactions related to electrons, radicals and reactive species are of great importance.

(6) The synergistic effects in the plasma-catalytic dry reforming of CH_4 are observed when the Ni-based catalysts are placed in the DBD plasma reactor. Due to the higher specific surface area and larger amount of basic sites compared with other catalysts (Ni/Mg, Ni/Si and Ni/Ti), the Ni/Al catalyst shows the highest conversion of reactants, the highest yield and selectivity of desired products and the lowest carbon deposition. The maximum conversions of CO_2 and CH_4 are increased by 10.1% and 5.7% when the Ni/Al catalyst is used compared to these obtained in the plasma-only process at a discharge power of 60 W.

(7) The optimum Ni loading in the Ni/γ-Al_2O_3 catalyst for the plasma-catalytic dry reforming of CH_4 in different operating conditions is found to be around 10 wt.% through ANOVA in the CCD based RSM. The effect of the processing parameters (e.g. discharge power, total feed flow rate, CO_2/CH_4 molar ratio and Ni

loading) and their interactions on the performance of the dry reforming process is also analysed. Based on the optimisation of the processing variables, the optimum processing parameter setting for the highest reactant conversion, product yield and FPE is as follows: A discharge power of 60 W, a total flow rate of 56.1 ml/min, a CO_2/CH_4 molar ratio of 1.03 and a Ni loading of 9.5 wt.%.

(8) Further enhancement of the plasma-catalytic reforming performance is achieved by introducing Ni-based bimetallic catalysts into the DBD reactor. The 10Ni3Co catalyst shows the highest plasma-catalytic ability, with maximum reactant conversions and target product yields and selectivities due to the interaction between Ni and Co. The highest carbon resistance is also observed in the 10Ni3Co catalyst compared with the other bimetallic catalysts (10Ni3Cu, 10Ni3Mn and 10Ni). In addition, an optimum Co loading (10Ni5Co) is detected in the Ni-Co bimetallic catalyst, which gives the best plasma-catalytic performance. The maximum CO_2 and CH_4 conversion is 30.9% and 50.7% when the 10Ni5Co catalyst is used at a discharge power of 60W. This optimum bimetallic catalyst also shows the maximum carbon resistance, reflected by the minimum carbon deposition value of 2.1% when the catalyst is involved in the plasma dry reforming reaction at a discharge power of 50 W for 150 min. This minimum carbon deposition is lower than that in the conventional thermal catalytic reforming of CH_4 using similar Ni-Co bimetallic catalysts at higher temperatures.

(9) The maximum FPE for the plasma-catalytic dry reforming of CH_4 is 12.7%, higher than most of the previous results obtained in atmospheric non-thermal plasma reactors. The integration of the non-thermal plasma-catalytic process with renewable energy sources (e.g. solar and wind energy) is expected to be a promising approach to transport and store the surplus energy from renewable energy sources in a chemical form.

8.3 Future work

This thesis is mainly aimed at investigating the performance of the direct decomposition of CO_2 into CO and O_2 and dry reforming of CH_4, to produce syngas and other value-added fuels and chemicals, in a plasma-catalytic reactor in order to pursue a cost-effective and environmentally-friendly method of controlling greenhouse gas emissions. There is still much room for improvement when it comes to the efficiency of the plasma-catalytic process.

(1) Currently, the detailed mechanism of the plasma-catalysis process in the plasma-catalytic reforming reaction is still unclear. Much work is required to reveal the interaction between the plasma and catalyst and to gain a complete understanding of the fundamental mechanisms leading to the synergy. It is suggested that more detailed catalyst characterisation should be performed based on the work in this

thesis, such as transmission electron microscopy (TEM), H_2-temperature programmed reduction (H_2-TPR), etc.

(2) New nanocatalysts (e.g. $LaNiO_3@SiO_2$) have been used in the previous plasma-catalytic dry reforming of CH_4, but the energy efficiency is still relatively low. Further investigations are required to develop suitable catalysts for plasma-catalysis process, including study on the effective promoters, preparation methods, calcination approaches, reducing environment as well as the selection of plasma reactor and the interaction between plasma and catalysts. Several important factors should be paid attention to during this process, such as high catalytic activity towards the desired reactions, inhibition of processes that lead to undesired by-products, high surface area of the active species to enhance reaction rates, high activity and stability at the low temperature related to that in the plasma reactor, etc.

(3) For the decomposition of CO_2, the effective catalysts for the plasma process are very limited, so the exploration of catalysts with high redox ability and low-temperature activity should be emphasised; for the plasma-catalytic dry reforming of CH_4, the catalysts used are mainly the same as those for the thermal-catalytic process. It would therefore be useful to develop the special catalysts for the plasma-assisted conversion of CO_2 and other plasma processes. This research into new catalysts for plasma processes should consider the catalysts' dielectric properties, size and porosity, which have substantial influence on the plasma physical properties. Additionally, the stability of the catalysts in the plasma processes should also be taken into consideration.

(4) In this thesis, only the pure reactant gases are considered in the experiments, while in practical applications, other gases in differing amounts (such as air, O_2, N_2, C_2-C_{4+} hydrocarbons and H_2S) are generally present in the feed mixture. The effects of these gases on the plasma process and the effectiveness of the catalysts should be taken into consideration in future experiments.

REFERENCES

[1] International Energy Outlook 2013, U.S. Energy Information Administration, 2013.

[2] World Energy Resources 2013 Survey, World Energy Council, 2013.

[3] Renewables 2014 Global Status Report, REN 21 Steering Committee, 2014.

[4] World Energy Outlool 2014 Executive Summary, International Energy Agency, 2014.

[5] Climate Change 2014 Synthesis Report, Intergovernmental Panel on Climate Change, 2015.

[6] N.S. Spinner, J.A. Vega, W.E. Mustain, Recent progress in the electrochemical conversion and utilization of CO_2, Catalysis Science & Technology, 2 (2012) 19-28.

[7] Global Biodiversity Outlook 3, Convention on Biological Diversity, 2010.

[8] A. Shah, Climate Change and Global Warming Introduction http://www.globalissues.org/article/233/climate-change-and-global-warming-introduction, 2015.

[9] United Nations Framework Convention on Climate Change - Status of Ratification of the Convention https://unfccc.int/essential_background/convention/status_of_ratification/items/2631.php.

[10] 7.a Kyoto Protocol to the United Nations Framework Convention on Climate Change https://treaties.un.org/pages/ViewDetails.aspx?src=TREATY&mtdsg_no=XXVII-7-a&chapter=27&lang=en, 2015.

[11] Report of the Conference of the Parties on its thirteenth session, held in Bali from 3 to 15 December 2007. Addendum. Part Two: Action taken by the Conference of the Parties at its thirteenth session., 2008.

[12] Report of the Conference of the Parties on its fifteenth session, held in Copenhagen from 7 to 19 December 2009. Addendum. Part Two: Action taken by the Conference of the Parties at its fifteenth session, 2010.

[13] Report of the Conference of the Parties on its sixteenth session, held in Cancun from 29 November to 10 December 2010. Addendum. Part two: Action taken by the Conference of the Parties at its sixteenth session., 2011.

[14] Report of the Conference of the Parties on its seventeenth session, held in Durban from 28 November to 11 December 2011. Addendum. Part two: Action taken by the Conference of the Parties at its seventeenth session., 2012.

[15] 2012 United Nations Climate Change Conference, http://en.wikipedia.org/wiki/2012_United_Nations_Climate_Change_Conference#cite_note-8.

[16] 2015 United Nations Climate Change Conference http://en.wikipedia.org/wiki/2015_United_Nations_Climate_Change_Conference#cite_note-NYT-20150525-1.

[17] President Obama Sets a Target for Cutting U.S. Greenhouse Gas Emissions http://apps1.eere.energy.gov/news/news_detail.cfm/news_id=15650, Energy Efficiency & Renewable Energy, EERE Network News, 2009.

[18] FACT SHEET: U.S.-China Joint Announcement on Climate Change and Clean Energy Cooperation https://www.whitehouse.gov/the-press-office/2014/11/11/fact-sheet-us-china-joint-announcement-climate-change-and-clean-energy-c, 2014.

[19] Climate Change Legislation in the EU https://www.theccc.org.uk/tackling-climate-change/the-legal-landscape/european-union-legislation/.

[20] Climate Change Act 2008 http://www.legislation.gov.uk/ukpga/2008/27/contents, legislation.gov.uk, 2008.

[21] China makes carbon pledge ahead of Paris climate change summit http://www.theguardian.com/environment/2015/jun/30/china-carbon-emissions-2030-premier-li-keqiang-un-paris-climate-change-summit, 2015.

[22] U.K. Mirza, N. Ahmad, K. Harijan, T. Majeed, Identifying and addressing barriers to renewable energy development in Pakistan, Renewable & Sustainable Energy Reviews, 13 (2009) 927-931.
[23] S. Bachu, CO_2 storage in geological media: Role, means, status and barriers to deployment, Progress in Energy and Combustion Science, 34 (2008) 254-273.
[24] W.G. Tu, Y. Zhou, Z.G. Zou, Photocatalytic conversion of CO_2 into renewable hydrocarbon fuels: State-of-the-art accomplishment, challenges, and prospects, Advanced Materials, 26 (2014) 4607-4626.
[25] T. Inoue, A. Fujishima, S. Konishi, K. Honda, Photoelectrocatalytic reduction of carbon dioxide in aqueous suspensions of semiconductor powders, Nature, 277 (1979) 637-638.
[26] M. Tahir, N.S. Amin, Recycling of carbon dioxide to renewable fuels by photocatalysis: Prospects and challenges, Renewable and Sustainable Energy Reviews, 25 (2013) 560-579.
[27] K.F. Li, X.Q. An, K.H. Park, M. Khraisheh, J.W. Tang, A critical review of CO_2 photoconversion: Catalysts and reactors, Catalysis Today, 224 (2014) 3-12.
[28] E.V. Kondratenko, G. Mul, J. Baltrusaitis, G.O. Larrazábal, J. Pérez-Ramírez, Status and perspectives of CO_2 conversion into fuels and chemicals by catalytic, photocatalytic and electrocatalytic processes, Energy & Environmental Science, 6 (2013) 3112-3135.
[29] M. Bevilacqua, J. Filippi, H.A. Miller, F. Vizza, Recent technological progress in CO_2 electroreduction to fuels and energy carriers in aqueous environments, Energy Technology, 3 (2015) 197-210.
[30] J. Qiao, Y. Liu, F. Hong, J. Zhang, A review of catalysts for the electroreduction of carbon dioxide to produce low-carbon fuels, Chemical Society Reviews, 43 (2014) 631-675.
[31] J. Lee, Y. Tak, Electrocatalytic activity of Cu electrode in electroreduction of CO_2, Electrochimica Acta, 46 (2001) 3015-3022.
[32] A. Dibenedetto, A. Angelini, P. Stufano, Use of carbon dioxide as feedstock for chemicals and fuels: homogeneous and heterogeneous catalysis, Journal of Chemical Technology and Biotechnology, 89 (2014) 334-353.
[33] B. Maeda, Y. Miyazaki, T. Ema, Recent progress in catalytic conversions of carbon dioxide, Catalysis Science & Technology, 4 (2014) 1482-1497.
[34] W. Wang, S.P. Wang, X.B. Ma, J.L. Gong, Recent advances in catalytic hydrogenation of carbon dioxide, Chemical Society reviews, 40 (2011) 3703-3727.
[35] Y. Tamaura, M. Tabata, Complete reduction of carbon-dioxide to carbon using cation-excess magnetite, Nature, 346 (1990) 255-256.
[36] C. Nordhei, K. Mathisen, I. Bezverkhyy, D. Nicholson, Decomposition of carbon dioxide over the putative cubic spinel nanophase cobalt, nickel, and zinc ferrites, Journal of Physical Chemistry C, 112 (2008) 6531-6537.
[37] K.S. Lin, A.K. Adhikari, Z.Y. Tsai, Y.P. Chen, T.T. Chien, H.B. Tsai, Synthesis and characterization of nickel ferrite nanocatalysts for CO_2 decomposition, Catalysis Today, 174 (2011) 88-96.
[38] L.J. Ma, R. Wu, H.D. Liu, W.J. Xu, L.S. Chen, S.Y. Chen, Studies on CO2 decomposition over H-2-reduced MFe2O4 (M = Ni, Cu, Co, Zn), Solid State Sciences, 13 (2011) 2172-2176.
[39] J. Hunt, A. Ferrari, A. Lita, M. Crosswhite, B. Ashley, A.E. Stiegman, Microwave-specific enhancement of the carbon-carbon dioxide (boudouard) reaction, Journal of Physical Chemistry C, 117 (2013) 26871-26880.
[40] W.C. Chueh, C. Falter, M. Abbott, D. Scipio, P. Furler, S.M. Haile, A. Steinfeld, High-flux solar-driven thermochemical dissociation of CO_2 and H_2O using nonstoichiometric ceria, Science, 330 (2010) 1797-1801.

[41] H.J. Gallon, Dry reforming of methane using non-thermal plasma-catalysis, Faculty of Engineering and Physical Sciences, PhD Thesis, The University of Manchester, Manchester, 2010.
[42] K. Zhang, U. Kogelschatz, B. Eliasson, Conversion of greenhouse gases to synthesis gas and higher hydrocarbons, Energy & Fuels, 15 (2001) 395-402.
[43] X.P. Song, Z.C. Guo, Technologies for direct production of flexible H_2/CO synthesis gas, Energy Conversion and Management, 47 (2006) 560-569.
[44] L.M. Zhou, B. Xue, U. Kogelschatz, B. Eliasson, Nonequilibrium plasma reforming of greenhouse gases to synthesis gas, Energy & Fuels, 12 (1998) 1191-1199.
[45] M.S. Fan, A.Z. Abdullah, S. Bhatia, Catalytic technology for carbon dioxide reforming of methane to synthesis gas, Chemcatchem, 1 (2009) 192-208.
[46] M. Usman, W.M.A.W. Daud, H.F. Abbas, Dry reforming of methane: Influence of process parameters-A review, Renewable & Sustainable Energy Reviews, 45 (2015) 710-744.
[47] C.J. Liu, J.Y. Ye, J.J. Jiang, Y.X. Pan, Progresses in the preparation of coke resistant Ni-based catalyst for steam and CO_2 reforming of methane, Chemcatchem, 3 (2011) 529-541.
[48] Pakhare, J. Spivey, A review of dry (CO_2) reforming of methane over noble metal catalysts, Chemical Society Reviews, 43 (2014) 7813-7837.
[49] C.J. Liu, G.H. Xu, T.M. Wang, Non-thermal plasma approaches in CO_2 utilization, Fuel Processing Technology, 58 (1999) 119-134.
[50] A. Indarto, J.W. Choi, H. Lee, H.K. Song, Decomposition of greenhouse gases by plasma, Environmental Chemistry Letters, 6 (2008) 215-222.
[51] M.P.K. Srivastava, Akira, Carbon dioxide decomposition by plasma methods and application of high energy and high density plasma in material processing and nanostructures, Transaction of JWRI, 39 (2010) 11-25.
[52] A. Lebouvier, S.A. Iwarere, P. d'Argenlieu, D. Ramjugernath, L. Fulcheri, Assessment of carbon dioxide dissociation as a new route for syngas production: A comparative review and potential of plasma-based technologies, Energy & Fuels, 27 (2013) 2712-2722.
[53] Plasma- The fourth state of matter: http://www.plasmatreat.com/plasma-technology/what-is-plasma.html.
[54] L. Bardos, H. Barankova, Cold atmospheric plasma: Sources, processes, and applications, Thin Solid Films, 518 (2010) 6705-6713.
[55] H. Conrads, M. Schmidt, Plasma generation and plasma sources, Plasma Sources Science and Technology, 9 (2000) 441-454.
[56] D.H. Lee, K.T. Kim, Y.H. Song, W.S. Kang, S. Jo, Mapping plasma chemistry in hydrocarbon fuel processing processes, Plasma Chemistry and Plasma Processing, 33 (2013) 249-269.
[57] Tendero, C. Tixier, P. Tristant, J. Desmaison, P. Leprince, Atmospheric pressure plasmas: A review, Spectrochimica Acta Part B, 61 (2006) 2-30.
[58] W. Elenbaas, Light Sources, The Macmillan Press Ltd., London, 1972.
[59] A. Fridman,, Plasma Chemistry, Cambridge University Press, England, 2008.
[60] U. Kogelschatz, B. Eliasson, W. Egli, From ozone generators to flat television screens: history and future potential of dielectric-barrier discharges, Pure and Applied Chemistry, 71 (1999) 1819-1828.
[61] A. Fridman, L.A. Kennedy, Plasma Physics and Engineering, CRC Press, 2011.
[62] Y.P. Raizer, Gas Discharge Physics, Springer, 1991.
[63] Tatarova, N. Bundaleska, J.P. Sarrette, C.M. Ferreira, Plasmas for environmental issues: from hydrogen production to 2D materials assembly, Plasma Sources Science and Technology, 23 (2014) 063002.
[64] L. Bromberg, D.R. Cohn, A. Rabinovich, A. N., Hydrogen manufacturing using low current, non-thermal plasma boosted fuel converters, Symposium on Energy for the 21st century: hydrogen energy, San Diego, CA, 2001.

[65] B. Eliasson, U. Kogelschatz, Nonequilibrium volume plasma chemical-processing, IEEE Transactions on Plasma Science, 19 (1991) 1063-1077.
[66] Thevenet, L. Sivachandiran, O. Guaitella, C. Barakat, A. Rousseau, Plasma-catalyst coupling for volatile organic compound removal and indoor air treatment: a review, Journal of Physics D: Applied Physics, 47 (2014) 224011.
[67] P. Talebizadeh, M. Babaie, R. Brown, H. Rahimzadeh, Z. Ristovski, M. Arai, The role of non-thermal plasma technique in NO_x treatment: A review, Renewable & Sustainable Energy Reviews, 40 (2014) 886-901.
[68] J. Foster, B.S. Sommers, S.N. Gucker, I.M. Blankson, G. Adamovsky, Perspectives on the interaction of plasmas with liquid water for water purification, IEEE Transactions on Plasma Science, 40 (2012) 1311-1323.
[69] C.M. Du, J.M. Mo, H.X. Li, Renewable hydrogen production by alcohols reforming using plasma and plasma-catalytic technologies: Challenges and opportunities, Chemical Reviews, 115 (2015) 1503-1542.
[70] H.E. Wagner, R. Brandenburg, K.V. Kozlov, A. Sonnenfeld, P. Michel, J.F. Behnke, The barrier discharge: basic properties and applications to surface treatment, Vacuum, 71 (2003) 417-436.
[71] T. Witvrouwen, S. Paulussen, B. Sels, The use of non-equilibrium plasmas for the synthesis of heterogeneous catalysts, Plasma Processes and Polymer, 9 (2012) 750-760.
[72] J.S. Chang, P.A. Lawless, T. Yamamoto, Corona Discharge Processes, IEEE Transactions on Plasma Science, 19 (1991) 1152-1166.
[73] A. Fridman, A. Chirokov, A. Gutsol, Non-thermal atmospheric pressure discharges, Journal of Physics D: Applied Physics, 38 (2005) R1-R24.
[74] J. Ehlbeck, U. Schnabel, M. Polak, J. Winter, T. von Woedtke, R. Brandenburg, T. von dem Hagen, K.D. Weltmann, Low temperature atmospheric pressure plasma sources for microbial decontamination, Journal of Physics D: Applied Physics, 44 (2011) 013002.
[75] H.S. Uhm, Y.C. Hong, D.H. Shin, A microwave plasma torch and its applications, Plasma Sources Science and Technology, 15 (2006) S26-S34.
[76] M.J. Gallagher Jr., A. Fridman, Plasma reforming for H_2-rich synthesis gas, in: D. Shekhawat, J.J. Spivey, D. Berry (Editors.) Fuel Cells: Technologies for Fuel Processing, Elsevier, (2011), 223-259.
[77] A. Czernichowski, Gliding arc - Applications to engineering and environment control, Pure and Applied Chemistry, 66 (1994) 1301-1310.
[78] Z. Bo, Fundamental Research of the Treatment of Volatile Organic Compounds with Gliding Arc Discharge Plasma, PhD Thesis, Zhejiang University, Hangzhou, Zhejiang, 2008.
[79] D.H. Lee, K.T. Kim, M.S. Cha, Y.H. Song, Plasma-controlled chemistry in plasma reforming of methane, International Journal of Hydrogen Energy, 35 (2010) 10967-10976.
[80] S.P. Gangoli, A.F. Gutsol, A.A. Fridman, A non-equilibrium plasma source: magnetically stabilized gliding arc discharge: I. Design and diagnostics, Plasma Sources Science and Technology, 19 (2010) 065003.
[81] C.S. Kalra, Y.I. Cho, A. Gutsol, A. Fridman, T.S. Rufael, Gliding arc in tornado using a reverse vortex flow, Review of Scientific Instruments, 76 (2005) 025110.
[82] Istadi, N.A.S. Amin, Co-generation of synthesis gas and C_{2+} hydrocarbons from methane and carbon dioxide in a hybrid catalytic-plasma reactor: A review, Fuel, 85 (2006) 577-592.
[83] U. Kogelschatz, Dielectric-barrier discharges: Their history, discharge physics, and industrial applications, Plasma Chemistry and Plasma Processing, 23 (2003) 1-46.
[84] A.M. Vandenbroucke, R. Morent, N. De Geyter, C. Leys, Non-thermal plasmas for non-catalytic and catalytic VOC abatement, Journal of Hazardous Materials, 195 (2011) 30-54.

[85] U. Kogelschatz, Filamentary, patterned, and diffuse barrier discharges, IEEE Transactions on Plasma Science, 30 (2002) 1400-1408.
[86] G.J. Pietsch, Peculiarities of dielectric barrier discharges, Contributions to Plasma Physics, 41 (2001) 620-628..
[87] H.H. Kim, Nonthermal plasma processing for air-pollution control: A historical review, current issues, and future prospects, Plasma Processes and Polymers, 1 (2004) 91-110.
[88] H.L. Chen, H.M. Lee, S.H. Chen, M.B. Chang, Review of packed-bed plasma reactor for ozone generation and air pollution control, Industrial & Engineering Chemistry Research, 47 (2008) 2122-2130.
[89] J.C. Whitehead, Plasma catalysis: A solution for environmental problems, Pure and Applied Chemistry, 82 (2010) 1329-1336.
[90] J. Van Durme, J. Dewulf, C. Leys, H. Van Langenhove, Combining non-thermal plasma with heterogeneous catalysis in waste gas treatment: A review, Applied Catalysis B: Environmental, 78 (2008) 324-333.
[91] X. Tu, J.C. Whitehead, Plasma-catalytic dry reforming of methane in an atmospheric dielectric barrier discharge: Understanding the synergistic effect at low temperature, Applied Catalysis B: Environmental, 125 (2012) 439-448.
[92] H.L. Chen, H.M. Lee, S.H. Chen, Y. Chao, M.B. Chang, Review of plasma catalysis on hydrocarbon reforming for hydrogen production-Interaction, integration, and prospects, Applied Catalysis B: Environmental, 85 (2008) 1-9.
[93] M.G. Sobacchi, A.V. Saveliev, A.A. Fridman, L.A. Kennedy, S. Ahmed, T. Krause, Experimental assessment of a combined plasma/catalytic system for hydrogen production via partial oxidation of hydrocarbon fuels, International Journal of Hydrogen Energy, 27 (2002) 635-642.
[94] H.L. Chen, H.M. Lee, S.H. Chen, M.B. Chang, S.J. Yu, S.N. Li, Removal of volatile organic compounds by single-stage and two-stage plasma catalysis systems: A review of the performance enhancement mechanisms, current status, and suitable applications, Environmental Science & Technology, 43 (2009) 2216-2227.
[95] E.C. Neyts, B. A, Understanding plasma catalysis through modelling and simulation-a review, Journal of Physics D: Applied Physics, 47 (2014) 224010
[96] M. Laroussi, Nonthermal decontamination of biological media by atmospheric-pressure plasmas: Review, analysis, and prospects, IEEE Transcations on Plasma Science, 30 (2002) 1409-1415.
[97] Holzer, F.D. Kopinke, U. Roland, Influence of ferroelectric materials and catalysts on the performance of non-thermal plasma (NTP) for the removal of air pollutants, Plasma Chemistry and Plasma Processing, 25 (2005) 595-611.
[98] K. Hensel, V. Martisovit, Z. Machala, M. Janda, M. Lestinsky, P. Tardiveau, A. Mizuno, Electrical and optical properties of AC microdischarges in porous ceramics, Plasma Processes and Polymers, 4 (2007) 682-693.
[99] K. Hensel, Microdischarges in ceramic foams and honeycombs, European Physical Journal D, 54 (2009) 141-148.
[100] M.A. Malik, Y. Minamitani, K.H. Schoenbach, Comparison of catalytic activity of aluminum oxide and silica gel for decomposition of volatile organic compounds (VOCs) in a plasmacatalytic reactor, IEEE Transactions on Plasma Science, 33 (2005) 50-56.
[101] N. Blin-Simiand, P. Tardiveau, A. Risacher, F. Jorand, S. Pasquiers, Removal of 2-heptanone by dielectric barrier discharges - The effect of a catalyst support, Plasma Processes and Polymers, 2 (2005) 256-262.
[102] J.P. Hong, W. Chu, P.A. Chernavskii, A.Y. Khodakov, Cobalt species and cobalt-support interaction in glow discharge plasma-assisted Fischer-Tropsch catalysts, Journal of Catalysis, 273 (2010) 9-17.

[103] Y.F. Guo, D.Q. Ye, K.F. Chen, J.C. He, W.L. Chen, Toluene decomposition using a wire-plate dielectric barrier discharge reactor with manganese oxide catalyst in situ, J Journal of Molecular Catalysis A: Chemical, 245 (2006) 93-100.
[104] K. Ostrikov, E.C. Neyts, M. Meyyappan, Plasma nanoscience: from nano-solids in plasmas to nano-plasmas in solids, Advances in Physics, 62 (2013) 113-224.
[105] R. Martinez, E. Romero, C. Guimon, R. Bilbao, CO_2 reforming of methane over coprecipitated Ni-Al catalysts modified with lanthanum, Applied Catalysis A: General, 274 (2004) 139-149.
[106] A.I. Pylinina, I.I. Mikhalenko, Activation of Cu-, Ag-, Au/ZrO_2 catalysts for dehydrogenation of alcohols by low-temperature oxygen and hydrogen plasma, Theoretical and Experimental Chemistry, 49 (2013) 65-69.
[107] X. Tu, H.J. Gallon, M.V. Twigg, P.A. Gorry, J.C. Whitehead, Dry reforming of methane over a Ni/Al_2O_3 catalyst in a coaxial dielectric barrier discharge reactor, Journal of Physics D: Applied Physics, 44 (2011) 274007.
[108] S.Y. Shang, G.H. Liu, X.Y. Chai, X.M. Tao, X. Li, M.G. Bai, W. Chu, X.Y. Dai, Y.X. Zhao, Y.X. Yin, Research on Ni/γ-Al_2O_3 catalyst for CO_2 reforming of CH_4 prepared by atmospheric pressure glow discharge plasma jet, Catalysis Today, 148 (2009) 268-274.
[109] C.J. Liu, R. Mallinson, L. Lobban, Nonoxidative met177hane conversion to acetylene over zeolite in a low temperature plasma, Journal of Catalysis, 179 (1998) 326-334.
[110] C.C. Wu, C.I. Wu, J.C. Sturm, A. Kahn, Surface modification of indium tin oxide by plasma treatment: An effective method to improve the efficiency, brightness, and reliability of organic light emitting devices, Applied Physics Letters, 70 (1997) 1348-1350.
[111] J. Poppe, S. Volkening, A. Schaak, E. Schutz, J. Janek, R. Imbihl, Electrochemical promotion of catalytic CO oxidation on Pt/YSZ catalysts under low pressure conditions, Physical Chemistry Chemical Physics, 1 (1999) 5241-5249.
[112] H.H. Kim, A. Ogata, S. Futamura, Atmospheric plasma-driven catalysis for the low temperature decomposition of dilute aromatic compounds, Journal of Physics D: Applied Physics, 38 (2005) 1292-1300.
[113] V. Demidyuk, J.C. Whitehead, Influence of temperature on gas-phase toluene decomposition in plasma-catalytic system, Plasma Chemistry and Plasma Processing, 27 (2007) 85-94.
[114] S. Futamura, H. Einaga, H. Kabashima, L.Y. Hwan, Synergistic effect of silent discharge plasma and catalysts on benzene decomposition, Catalysis Today, 89 (2004) 89-95.
[115] T. Mizushima, K. Matsumoto, J. Sugoh, H. Ohkita, N. Kakuta, Tubular membrane-like catalyst for reactor with dielectric-barrier-discharge plasma and its performance in ammonia synthesis, Applied Catalysis A: General, 265 (2004) 53-59.
[116] A.-J. Zhang, A.-M. Zhu, J. Guo, Y. Xu, C. Shi, Conversion of greenhouse gases into syngas via combined effects of discharge activation and catalysis, Chemical Engineering Journal, 156 (2010) 601-606.
[117] A. Vesel, M. Mozetic, A. Drenik, M. Balat-Pichelin, Dissociation of CO_2 molecules in microwave plasma, Chemical Physics, 382 (2011) 127-131.
[118] L.F. Spencer, A.D. Gallimore, Efficiency of CO_2 dissociation in a radio-frequency discharge, Plasma Chemistry and Plasma Processing, 31 (2011) 79-89.
[119] Maezono, J.-s. Chang, Reduction of CO_2 from combustion gases by DC corona torches, IEEE Transactions on Industry Applications, 26 (1990) 651-655.
[120] T. Mikoviny, M. Kocan, S. Matejcik, N.J. Mason, J.D. Skalny, Experimental study of negative corona discharge in pure carbon dioxide and its mixtures with oxygen, Journal of Physics D: Applied Physics, 37 (2004) 64-73.
[121] W. Xu, M.W. Li, G.H. Xu, Y.L. Tian, Decomposition of CO_2 using DC corona discharge at atmospheric pressure, Japanese Journal of Applied Physics, 43 (2004) 8310-8311.

[122] G. Horvath, J.D. Skalny, N.J. Mason, FTIR study of decomposition of carbon dioxide in dc corona discharges, Journal of Physics D: Applied Physics, 41 (2008) 225207.
[123] S. Paulussen, B. Verheyde, X. Tu, C. De Bie, T. Martens, D. Petrovic, A. Bogaerts, B. Sels, Conversion of carbon dioxide to value-added chemicals in atmospheric pressure dielectric barrier discharges, Plasma Sources Science and Technology, 19 (2010) 034015.
[124] R. Aerts, W. Somers, A. Bogaerts, Carbon dioxide splitting in a dielectric barrier discharge plasma: a combined experimental and computational study, ChemSusChem, 8 (2015) 702-716.
[125] F. Brehmer, S. Welzel, M.C.M. van de Sanden, R. Engeln, CO and byproduct formation during CO_2 reduction in dielectric barrier discharges, Journal of Applied Physics, 116 (2014) 123303.
[126] T.G. Nunnally, K.; Rabinovich, A.; Fridman, A.; Gutsol, A.; Kemoun, A., Dissociation of CO_2 in a low current gliding arc plasmatron, Journal of Physics D: Applied Physics, 44 (2011) 274009.
[127] A. Indarto, D.R. Yang, J.W. Choi, H. Lee, H.K. Song, Gliding arc plasma processing of CO_2 conversion, Journal of Hazardous Materials, 146 (2007) 309-315.
[128] Matsumoto, S. Tanabe, K. Okitsu, Y. Hayashi, S.L. Suib, Profiles of carbon dioxide decomposition in a dielectric-barrier discharge-plasma system, Bulletin of the Chemical Society of Japan, 72 (1999) 2567-2571.
[129] S.L. Brock, M. Marquez, S.L. Suib, Y. Hayashi, H. Matsumoto, Plasma decomposition of CO_2 in the presence of metal catalysts, Journal of Catalysis, 180 (1998) 225-233.
[130] Y.Z. Wen, X.Z. Jiang, Decomposition of CO_2 using pulsed corona discharges combined with catalyst, Plasma Chemistry and Plasma Processing, 21 (2001) 665-678.
[131] Q.Q. Yu, M. Kong, T. Liu, J.H. Fei, X.M. Zheng, Characteristics of the decomposition of CO_2 in a dielectric packed-bed plasma reactor, Plasma Chemistry and Plasma Processing, 32 (2012) 153-163.
[132] X.F. Duan, Z.Y. Hu, Y.P. Li, B.W. Wang, Effect of dielectric packing materials on the decomposition of carbon dioxide using DBD microplasma reactor, AIChE Journal, 61 (2015) 898-903.
[133] R.X. Li, Q. Tang, S. Yin, T. Sato, Preparation and application of $Ca_{0.8}Sr_{0.2}TiO_3$ for plasma activation of CO_2, Plasma Chemistry and Plasma Processing, 26 (2006) 267-276.
[134] G. Liu, W. Chu, H. Long, X. Dai, Y. Yin, A novel reduction method for Ni/γ-Al_2O_3 catalyst by a high frequency cold plasma jet at atmospheric pressure, Chinese Journal of Catalysis, 28 (2007) 582-584.
[135] S. Wang, Y. Zhang, X. Liu, X. Wang, Enhancement of CO_2 conversion rate and conversion efficiency by homogeneous discharges, Plasma Chemistry and Plasma Processing, 32 (2012) 979-989.
[136] A.M. Ghorbanzadeh, H. Modarresi, Carbon dioxide reforming of methane by pulsed glow discharge at atmospheric pressure: The effect of pulse compression, Journal of Applied Physics, 101 (2007) 123303.
[137] D. Li, X. Li, M. Bai, X. Tao, S. Shang, X. Dai, Y. Yin, CO_2 reforming of CH_4 by atmospheric pressure glow discharge plasma: A high conversion ability, International Journal of Hydrogen Energy, 34 (2009) 308-313.
[138] M.-W. Li, Y.-L. Tian, G.-H. Xu, Characteristics of carbon dioxide reforming of methane via alternating current (AC) corona plasma reactions, Energy & Fuels, 21 (2007) 2335-2339.
[139] M.A. Malik, X.Z. Jiang, The CO_2 reforming of natural gas in a pulsed corona discharge reactor, Plasma Chemistry and Plasma Processing, 19 (1999) 505-512.
[140] M. Jasinski, D. Czylkowski, B. Hrycak, M. Dors, J. Mizeraczyk, Atmospheric pressure microwave plasma source for hydrogen production, International Journal of Hydrogen Energy, 38 (2013) 11473-11483.

[141] J.Q. Zhang, J.S. Zhang, Y.J. Yang, Q. Liu, Oxidative coupling and reforming of methane with carbon dioxide using a pulsed microwave plasma under atmospheric pressure, Energy & Fuels, 17 (2003) 54-59.
[142] Z. Bo, J.H. Yan, X.D. Li, Y. Chi, K.F. Cen, Plasma assisted dry methane reforming using gliding arc gas discharge: Effect of feed gases proportion, International Journal of Hydrogen Energy, 33 (2008) 5545-5553.
[143] X. Tu, J.C. Whitehead, Plasma dry reforming of methane in an atmospheric pressure AC gliding arc discharge: Co-generation of syngas and carbon nanomaterials, International Journal of Hydrogen Energy, 39 (2014) 9658-9669.
[144] R. Snoeckx, Y.X. Zeng, X. Tu, A. Bogaerts, Plasma-based dry reforming: improving the conversion and energy efficiency in a dielectric barrier discharge, RSC Advances, 5 (2015) 29799-29808.
[145] G. Scarduelli, G. Guella, D. Ascenzi, P. Tosi, Synthesis of liquid organic compounds from CH_4 and CO_2 in a dielectric barrier discharge operating at atmospheric pressure, Plasma Processes and Polymers, 8 (2011) 25-31.
[146] A.M. Ghorbanzadeh, S. Norouzi, T. Mohammadi, High energy efficiency in syngas and hydrocarbon production from dissociation of CH_4-CO_2 mixture in a non-equilibrium pulsed plasma, Journal of Physics D: Applied Physics, 38 (2005) 3804-3811.
[147] X. Tao, M. Bai, X. Li, H. Long, S. Shang, Y. Yin, X. Dai, CH_4-CO_2 reforming by plasma - challenges and opportunities, Progress in Energy and Combustion Science, 37 (2011) 113-124.
[148] B. Dai, X.L. Zhang, W.M. Gong, R. He, Study on the methane coupling under pulse corona plasma by using CO_2 as oxidant, Plasma Science and Technology, 2 (2000) 577-580.
[149] M.W. Li, G.H. Xu, Y.L. Tian, L. Chen, H.F. Fu, Carbon dioxide reforming of methane using DC corona discharge plasma reaction, Journal of Physical Chemistry A, 108 (2004) 1687-1693.
[150] H.D. Gesser, N.R. Hunter, D. Probawono, The CO_2 reforming of natural gas in a silent discharge reactor, Plasma Chemistry and Plasma Processing, 18 (1998) 241-245.
[151] C.J. Liu, B.Z. Xue, B. Eliasson, F. He, Y. Li, G.H. Xu, Methane conversion to higher hydrocarbons in the presence of carbon dioxide using dielectric-barrier discharge plasmas, Plasma Chemistry and Plasma Processing, 21 (2001) 301-310.
[152] Y. Li, C.J. Liu, B. Eliasson, Y. Wang, Synthesis of oxygenates and higher hydrocarbons directly from methane and carbon dioxide using dielectric-barrier discharges: Product distribution, Energy & Fuels, 16 (2002) 864-870.
[153] Y.P. Zhang, Y. Li, Y. Wang, C.J. Liu, B. Eliasson, Plasma methane conversion in the presence of carbon dioxide using dielectric-barrier discharges, Fuel Processing Technology, 83 (2003) 101-109.
[154] Q. Wang, B.H. Yan, Y. Jin, Y. Cheng, Investigation of dry reforming of methane in a dielectric barrier discharge reactor, Plasma Chemistry and Plasma Processing, 29 (2009) 217-228.
[155] V.J. Rico, J.L. Hueso, J. Cotrino, A.R. Gonzalez-Elipe, Evaluation of different dielectric barrier discharge plasma configurations as an alternative technology for green C_1 chemistry in the carbon dioxide reforming of methane and the direct decomposition of methanol, Journal of Physical Chemistry A, 114 (2010) 4009-4016.
[156] H.J. Gallon, X. Tu, J.C. Whitehead, Effects of reactor packing materials on H_2 production by CO_2 reforming of CH_4 in a dielectric barrier discharge, Plasma Processes and Polymers, 9 (2012) 90-97.
[157] A. Ozkan, T. Dufour, G. Arnoult, P. De Keyzer, A. Bogaerts, F. Reniers, CO_2-CH_4 conversion and syngas formation at atmospheric pressure using a multi-electrode dielectric barrier discharge, Journal of CO_2 Utilization, 9 (2015) 74-81.

[158] B. Eliasson, C.J. Liu, U. Kogelschatz, Direct conversion of methane and carbon dioxide to higher hydrocarbons using catalytic dielectric-barrier discharges with zeolites, Industrial & Engineering Chemistry Research, 39 (2000) 1221-1227.
[159] Zhang, B. Eliasson, U. Kogelschatz, Direct conversion of greenhouse gases to synthesis gas and C_4 hydrocarbons over zeolite HY promoted by a dielectric-barrier discharge, Industrial & Engineering Chemistry Research, 41 (2002) 1462-1468.
[160] T. Jiang, Y. Li, C.J. Liu, G.H. Xu, B. Eliasson, B.Z. Xue, Plasma methane conversion using dielectric-barrier discharges with zeolite A, Catalysis Today, 72 (2002) 229-235.
[161] Y. Li, G.H. Xu, C.J. Liu, B. Eliasson, B.Z. Xue, Co-generation of syngas and higher hydrocarbons from CO_2 and CH_4 using dielectric-barrier discharge: Effect of electrode materials, Energy & Fuels, 15 (2001) 299-302.
[162] S. Mahammadunnisa, P.M.K. Reddy, B. Ramaraju, C. Subrahmanyam, Catalytic nonthermal plasma reactor for dry reforming of methane, Energy & Fuels, 27 (2013) 4441-4447.
[163] Q. Wang, B.-H. Yan, Y. Jin, Y. Cheng, Dry reforming of methane in a dielectric barrier discharge reactor with Ni/Al_2O_3 catalyst: Interaction of catalyst and plasma, Energy & Fuels, 23 (2009) 4196-4201.
[164] Q. Wang, Y. Cheng, Y. Jin, Dry reforming of methane in an atmospheric pressure plasma fluidized bed with Ni/γ-Al_2O_3 catalyst, Catalysis Today, 148 (2009) 275-282.
[165] H. Lee, H.K. Song, B.R. Min, Heating effect of plasma catalytic reaction on the CH_4 reforming of CO_2 over Ni/γ-Al_2O_3 catalyst in dielectric-barrier discharge reactor, Chemistry Letters, 35 (2006) 646-647.
[166] Y.X. Zeng, X.B. Zhu, D.H. Mei, B. Ashford, X. Tu, Plasma-catalytic dry reforming of methane over γ -Al_2O_3 supported metal catalysts, Catalysis Today, 256 (2015) 80-87.
[167] Q. Wang, H.L. Shi, B.H. Yan, Y. Jin, Y. Cheng, Steam enhanced carbon dioxide reforming of methane in DBD plasma reactor, International Journal of Hydrogen Energy, 36 (2011) 8301-8306.
[168] H.K. Song, J.W. Choi, S.H. Yue, H. Lee, B.K. Na, Synthesis gas production via dielectric barrier discharge over Ni/γ-Al_2O_3 catalyst, Catalysis Today, 89 (2004) 27-33.
[169] Sentek, K. Krawczyk, M. Mlotek, M. Kalczewska, T. Kroker, T. Kolb, A. Schenk, K.-H. Gericke, K. Schmidt-Szalowski, Plasma-catalytic methane conversion with carbon dioxide in dielectric barrier discharges, Applied Catalysis B: Environmental, 94 (2010) 19-26.
[170] T. Kroker, T. Kolb, A. Schenk, K. Krawczyk, M. Mlotek, K.H. Gericke, Catalytic conversion of simulated biogas mixtures to synthesis gas in a fluidized bed reactor supported by a DBD, Plasma Chemistry and Plasma Processing, 32 (2012) 565-582.
[171] Krawczyk, M. Mlotek, B. Ulejczyk, K. Schmidt-Szalowski, Methane conversion with carbon dioxide in plasma-catalytic system, Fuel, 117 (2014) 608-617.
[172] M.H. Pham, V. Goujard, J.M. Tatibouet, C. Batiot-Dupeyrat, Activation of methane and carbon dioxide in a dielectric-barrier discharge-plasma reactor to produce hydrocarbons-Influence of La_2O_3/γ-Al_2O_3 catalyst, Catalysis Today, 171 (2011) 67-71.
[173] X. Zheng, S. Tan, L. Dong, S. Li, H. Chen, $LaNiO_3@SiO_2$ core-shell nano-particles for the dry reforming of CH_4 in the dielectric barrier discharge plasma, International Journal of Hydrogen Energy, 39 (2014) 11360-11367.
[174] X.G. Zheng, S.Y. Tan, L.C. Dong, S.B. Li, H.M. Chen, Silica-coated $LaNiO_3$ nanoparticles for non-thermal plasma assisted dry reforming of methane: Experimental and kinetic studies, Chemical Engineering Journal, 265 (2015) 147-156.
[175] V. Goujard, J.M. Tatibouet, C. Batiot-Dupeyrat, Influence of the plasma power supply nature on the plasma-catalyst synergism for the carbon dioxide reforming of methane, IEEE Transactions on Plasma Science, 37 (2009) 2342-2346.
[176] T.C. Manley, The electric characteristics of the ozonator discharge, Journal of the Electrochemical Society, 84 (1943) 83-96.

[177] T. Yamamoto, M. Okubo, Nonthermal Plasma Technology, in: L.K. Wang, N.C. Pereira, Y.-T. Hung (Editors.) Handbook of Environmental Engineering, Humana Press, (2007) 135-293.
[178] D.H. Mei, X.B. Zhu, Y.L. He, J.D. Yan, X. Tu, Plasma-assisted conversion of CO_2 in a dielectric barrier discharge reactor: understanding the effect of packing materials, Plasma Sources Science and Technology, 24 (2015) 015011.
[179] R. Valdivia-Barrientos, J. Pacheco-Sotelo, M. Pacheco-Pacheco, J.S. Benitez-Read, R. Lopez-Callejas, Analysis and electrical modelling of a cylindrical DBD configuration at different operating frequencies, Plasma Sources Science and Technology, 15 (2006) 237-245.
[180] K.P. Francke, R. Rudolph, H. Miessner, Design and operating characteristics of a simple and reliable DBD reactor for use with atmospheric air, Plasma Chemistry and Plasma Processing, 23 (2003) 47-57.
[181] Z. Falkenstein, J.J. Coogan, Microdischarge behaviour in the silent discharge of nitrogen-oxygen and water-air mixtures, Journal of Physics D: Applied Physics, 30 (1997) 817-825.
[182] Y.H. Tee, J. Zou, W.S.W. Ho, CO_2-selective membranes containing dimethylglycine mobile carriers and polyethylenimine fixed carrier, Journal of The Chinese Institute Chemical Engineers, 37 (2006) 37-47.
[183] C. Hammond, The Basics of Crystallography and Diffraction, Oxford University Press, New York, 2009.
[184] A. Chorkendorff, J.W. Niemantsverdriet, Concepts of Modern Catalysis and Kinetics, WILEY-VCH Verlag GmbH & Co. KGaA, Weinheim, 2003.
[185] X. Tu, H.J. Gallon, J.C. Whitehead, Electrical and spectroscopic diagnostics of a single-stage plasma-catalysis system: effect of packing with TiO_2, Journal of Physics D: Applied Physics, 44 (2011) 482003.
[186] B. Stock, C.B.F. Rice, Chromatographic Methods, Chapman and Hall Ltd, London, 1967.
[187] G. Centi, E.A. Quadrelli, S. Perathoner, Catalysis for CO_2 conversion: a key technology for rapid introduction of renewable energy in the value chain of chemical industries, Energy & Environmental Science, 6 (2013) 1711-1731.
[188] F.Q. Chen, X.Y. Huang, D.G. Cheng, X.L. Zhan, Hydrogen production from alcohols and ethers cold plasma: A review, International Journal of Hydrogen Energy, 39 (2014) 9036-9046.
[189] B.R. Locke, K.Y. Shih, Review of the methods to form hydrogen peroxide in electrical discharge plasma with liquid water, Plasma Sources Science and Technology, 20 (2011) 034006.
[190] T. Nozaki, K. Okazaki, Innovative methane conversion technology using atmospheric pressure non-thermal plasma, Journal of the Japan Petroleum Institute, 54 (2011) 146-158.
[191] M.K. Nikoo, N.A.S. Amin, Thermodynamic analysis of carbon dioxide reforming of methane in view of solid carbon formation, Fuel Processing Technology, 92 (2011) 678-691.
[192] J.J. Gao, Y.L. Wang, Y. Ping, D.C. Hu, G.W. Xu, F.N. Gu, F.B. Su, A thermodynamic analysis of methanation reactions of carbon oxides for the production of synthetic natural gas, RSC Advances, 2 (2012) 2358-2368.
[193] S.Y. Liu, D.H. Mei, Z. Shen, X. Tu, Nonoxidative conversion of methane in a dielectric barrier discharge reactor: prediction of reaction performance based on neural network model, Journal of Physical Chemistry C, 118 (2014) 10686-10693.
[194] X. Tu, B. Verheyde, S. Corthals, S. Paulussen, B.F. Sels, Effect of packing solid material on characteristics of helium dielectric barrier discharge at atmospheric pressure, Physics of Plasmas, 18 (2011) 080702.

[195] H.H. Kim, A. Ogata, Nonthermal plasma activates catalyst: from current understanding and future prospects, European Physical Journal Applied Physics, 55 (2011) 13806.
[196] L.F. Dong, X.C. Li, Z.Q. Yin, S.F. Qian, J.T. Ouyang, L. Wang, Self-organized filaments in dielectric barrier discharge in air at atmospheric pressure, Chinese Physics Letters, 18 (2001) 1380-1382.
[197] A. Meiners, M. Leck, B. Abel, Efficiency enhancement of a dielectric barrier plasma discharge by dielectric barrier optimization, Review of Scientific Instruments, 81 (2010) 113507.
[198] B.W. Wang, W.J. Yan, W.J. Ge, X.F. Duan, Methane conversion into higher hydrocarbons with dielectric barrier discharge micro-plasma reactor, Journal of Energy Chemistry, 22 (2013) 876-882.
[199] Jiang, N. Lu, K.F. Shang, J. Li, Y. Wu, Effects of electrode geometry on the performance of dielectric barrier/packed-bed discharge plasmas in benzene degradation, Journal of Hazardous Materials, 262 (2013) 387-393.
[200] H.H. Kim, A. Ogata, S. Futamura, Effect of different catalysts on the decomposition of VOC_S using flow-type plasma-driven catalysis, IEEE Transactions on Plasma Science, 34 (2006) 984-995.
[201] T. Hammer, T. Kappes, M. Baldauf, Plasma catalytic hybrid processes: gas discharge initiation and plasma activation of catalytic processes, Catalysis Today, 89 (2004) 5-14.
[202] H.J. Gallon, H.H. Kim, X. Tu, J.C. Whitehead, Microscope-ICCD imaging of an atmospheric pressure CH_4 and CO_2 dielectric barrier discharge, IEEE Transactions on Plasma Science, 39 (2011) 2176-2177.
[203] X. Tu, H.J. Gallon, J.C. Whitehead, Transition behavior of packed-bed dielectric barrier discharge in argon, EEE Transactions on Plasma Science, 39 (2011) 2172-2173.
[204] W.S. Kang, J.M. Park, Y. Kim, S.H. Hong, Numerical study on influences of barrier arrangements on dielectric barrier discharge characteristics, EEE Transactions on Plasma Science, 31 (2003) 504-510.
[205] Zaka-ul-Islam, K. Van Laer, A. Bogaerts, Fluid modelling of a packed bed plasma reactor, 31th International Conference on Phenomena in Ionized GasesGranada, Spain, 2013.
[206] A. Guaitella, L. Gatilova, A. Rousseau, Plasma-photocatalyst interaction: Production of oxygen atoms in a low pressure discharge, Applied Physics Letters, 86 (2005) 151502.
[207] X.B. Zhu, X. Gao, C.H. Zheng, Z.H. Wang, M.J. Ni, X. Tu, Plasma-catalytic removal of a low concentration of acetone in humid conditions, RSC Advances, 4 (2014) 37796-37805.
[208] L.G. Devi, G. Krishnamurthy, TiO_2- and $BaTiO_3$-assisted photocatalytic degradation of selected chloroorganic compounds in aqueous medium: Correlation of reactivity/orientation effects of substituent groups of the pollutant molecule on the degradation rate, Journal of Physical Chemistry A, 115 (2011) 460-469.
[209] C. Subrahmanyam, M. Magureanu, D. Laub, A. Renken, L. Kiwi-Minsker, Nonthermal plasma abatement of trichloroethylene enhanced by photocatalysis, Journal of Physical Chemistry C, 111 (2007) 4315-4318.
[210] A. Guaitella, F. Thevenet, E. Puzenat, C. Guillard, A. Rousseau, C_2H_2 oxidation by plasma/TiO_2 combination: Influence of the porosity, and photocatalytic mechanisms under plasma exposure, Applied Catalysis B: Environmental, 80 (2008) 296-305.
[211] B. Cybula, M. Klein, A. Zaleska, Methane formation over TiO_2-based photocatalysts: Reaction pathways, Applied Catalysis B: Environmental, 164 (2015) 433-442.
[212] S. Xie, Y. Wang, Q. Zhang, W. Deng, Y. Wang, MgO- and Pt-promoted TiO_2 as an efficient photocatalyst for the preferential reduction of carbon dioxide in the presence of water, ACS Catalysis, 4 (2014) 3644-3653.

[213] A.A. Assadi, A. Bouzaza, S. Merabet, D. Wolbert, Modeling and simulation of VOCs removal by nonthermal plasma discharge with photocatalysis in a continuous reactor: Synergetic effect and mass transfer, Chemical Engineering Journal, 258 (2014) 119-127.

[214] A.A. Assadi, J. Palau, A. Bouzaza, J. Penya-Roja, V. Martinez-Soriac, D. Wolbert, Abatement of 3-methylbutanal and trimethylamine with combined plasma and photocatalysis in a continuous planar reactor, Journal of Photochemistry and Photobiology A: Chemistry, 282 (2014) 1-8.

[215] T. Sano, N. Negishi, E. Sakai, S. Matsuzawa, Contributions of photocatalytic/catalytic activities of TiO_2 and γ-Al_2O_3 in nonthermal plasma on oxidation of acetaldehyde and CO, Journal of Molecular Catalysis A: Chemical, 245 (2006) 235-241.

[216] A.E. Wallis, J.C. Whitehead, K. Zhang, Plasma-assisted catalysis for the destruction of CFC-12 in atmospheric pressure gas streams using TiO_2, Catalysis Letter, 113 (2007) 29-33.

[217] Nakamura, N. Negishi, S. Kutsuna, T. Ihara, S. Sugihara, E. Takeuchi, Role of oxygen vacancy in the plasma-treated TiO_2 photocatalyst with visible light activity for NO removal, Journal of Molecular Catalysis A: Chemical, 161 (2000) 205-212.

[218] L.J. Liu, Y. Li, Understanding the reaction mechanism of photocatalytic reduction of CO_2 with H_2O on TiO_2-based photocatalysts: A review, Aerosol and Air Quality, 14 (2014) 453-469.

[219] X.Y. Pan, M.Q. Yang, X.Z. Fu, N. Zhang, Y.J. Xu, Defective TiO_2 with oxygen vacancies: synthesis, properties and photocatalytic applications, Nanoscale, 5 (2013) 3601-3614.

[220] N.A. Deskins, R. Rousseau, M. Dupuis, Distribution of Ti^{3+} Surface Sites in Reduced TiO_2, Journal of Physical Chemistry C, 115 (2011) 7562-7572.

[221] L.J. Liu, C.Y. Zhao, Y. Li, Spontaneous dissociation of CO_2 to CO on defective surface of Cu(I)/TiO_{2-x} nanoparticles at room temperature, Journal of Physical Chemistry C, 116 (2012) 7904-7912.

[222] A. Mizuno, Y. Kisanuki, M. Noguchi, S. Katsura, S.H. Lee, U.K. Hong, S.Y. Shin, J.H. Kang, Indoor air cleaning using a pulsed discharge plasma, Ieee Transactions on Industry Applications, 35 (1999) 1284-1288.

[223] W. Pipornpong, R. Wanbayor, V. Ruangpornvisuti, Adsorption CO_2 on the perfect and oxygen vacancy defect surfaces of anatase TiO_2 and its photocatalytic mechanism of conversion to CO, Applied Surface Science, 257 (2011) 10322-10328.

[224] L.B. Xiong, J.L. Li, B. Yang, Y. Yu, Ti^{3+} in the surface of titanium dioxide: Generation, properties and photocatalytic application, Journal of Nanomaterials, (2012) 831524.

[225] A. Fujishima, T.N. Rao, D.A. Tryk, Titanium dioxide photocatalysis, Journal of Photochemistry and Photobiology C: Photochemistry Reviews, 1 (2000) 1-21.

[226] R.X. Li, Q. Tang, S. Yin, T. Sato, Investigation of dielectric barrier discharge dependence on permittivity of barrier materials, Applied Physics Letter, 90 (2007) 131502.

[227] H.M. Lee, S.H. Chen, H.L. Chen, Influence of packing materials on the electric fields of packed-bed dielectric barrier discharge reactors, 18th International Symposium on Plasma Chemistry, Japan, 2007.

[228] G.J.M. Hagelaar, L.C. Pitchford, Solving the Boltzmann equation to obtain electron transport coefficients and rate coefficients for fluid models, Plasma Sources Science and Technology, 14 (2005) 722-733.

[229] D. Mei, Y.-L. He, S. Liu, J.D. Yan, X. Tu, Optimization of CO_2 conversion in a cylindrical dielectric barrier discharge reactor using design of experiments, Plasma Processes and Polymers, 13 (2016): 544-556.

[230] R.X. Li, Q. Tang, S. Yin, T. Sato, Performance of $Ca_{1-x}Sr_xTiO_3$ as barriers in dielectric barrier discharges with different Sr content, Journal of Physics D: Applied Physics, 40 (2007) 5187-5191.

[231] G.Y. Zheng, J.M. Jiang, Y.P. Wu, R.X. Zhang, H.Q. Hou, The mutual conversion of CO_2 and CO in dielectric barrier discharge (DBD), Plasma Chemistry and Plasma Processing, 23 (2003) 59-68.
[232] J.Y. Wang, G.G. Xia, A.M. Huang, S.L. Suib, Y. Hayashi, H. Matsumoto, CO_2 decomposition using glow discharge plasmas, Journal of Catalysis, 185 (1999) 152-159.
[233] S.L. Brock, T. Shimojo, M. Marquez, C. Marun, S.L. Suib, H. Matsumoto, Y. Hayashi, Factors influencing the decomposition of CO_2 in AC fan-type plasma reactors: Frequency, waveform, and concentration effects, Journal of Catalysis, 184 (1999) 123-133.
[234] X.B. Zhu, X. Gao, R. Qin, Y.X. Zeng, R.Y. Qu, C.H. Zheng, X. Tu, Plasma-catalytic removal of formaldehyde over Cu-Ce catalysts in a dielectric barrier discharge reactor, Applied Catalysis B: Environmental, 170 (2015) 293-300.
[235] A.E. Wallis, J.C. Whitehead, K. Zhang, The removal of dichloromethane from atmospheric pressure nitrogen gas streams using plasma-assisted catalysis, Applied Catalysis B: Environmental, 74 (2007) 111-116.
[236] A.E. Wallis, J.C. Whitehead, K. Zhang, The removal of dichloromethane from atmospheric pressure air streams using plasma-assisted catalysis, Applied Catalysis B: Environmental, 72 (2007) 282-288.
[237] C. Nordhei, K. Mathisen, O. Safonova, W. van Beek, D.G. Nicholson, Decomposition of carbon dioxide at 500 ℃ over reduced iron, cobalt, nickel, and zinc ferrites: A combined XANES-XRD study, Journal of Physical Chemistry C, 113 (2009) 19568-19577.
[238] T.K. Kim, W.G. Lee, Reaction between methane and carbon dioxide to produce syngas in dielectric barrier discharge system, Journal of Industrial and Engineering Chemistry, 18 (2012) 1710-1714.
[239] K.S. Lin, A.K. Adhikari, C.Y. Wang, P.J. Hsu, H.Y. Chan, Synthesis and characterization of nickel and zinc ferrite nanocatalysts for decomposition of CO_2 greenhouse effect gas, Journal of Nanoscience and Nanotechnology, 13 (2013) 2538-2548.
[240] T. Martens, A. Bogaerts, J. van Dijk, Pulse shape influence on the atmospheric barrier discharge, Applied Physics Letter, 96 (2010) 131503.
[241] L. Yuliati, H. Yoshida, Photocatalytic conversion of methane, Chemical Society Reviews, 37 (2008) 1592-1602.
[242] V. Havran, M.P. Dudukovic, C.S. Lo, Conversion of methane and carbon dioxide to higher value products, Industrial & Engineering Chemistry Research, 50 (2011) 7089-7100.
[243] A. Aziznia, H.R. Bozorgzadeh, N. Seyed-Matin, M. Baghalha, A. Mohamadalizadeh, Comparison of dry reforming of methane in low temperature hybrid plasma-catalytic corona with thermal catalytic reactor over Ni/γ-Al_2O_3, Journal of Natural Gas Chemistry, 21 (2012) 466-475.
[244] R. Snoeckx, R. Aerts, X. Tu, A. Bogaerts, Plasma-based dry reforming: A computational study ranging from the nanoseconds to secondstime scale, Journal of Physical Chemistry C, 117 (2013) 4957-4970.
[245] C. De Bie, B. Verheyde, T. Martens, J. van Dijk, S. Paulussen, A. Bogaerts, Fluid modeling of the conversion of methane into higher hydrocarbons in an atmospheric pressure dielectric barrier discharge, Plasma Processes and Polymers, 8 (2011) 1033-1058.
[246] Y. Yang, Methane conversion and reforming by nonthermal plasma on pins, Industrial & Engineering Chemistry Research, 41 (2002) 5918-5926.
[247] J. Gao, Z. Hou, H. Lou, X. Zheng, Dry (CO_2) reforming, in: D. Shekhawat, J.J. Spivey, D.A. Berry (Editors), Fuel Cells: Technologies for Fuel Processing, Elsevier (2011) 191-221.

[248] L.L. Xu, H.L. Song, L.J. Chou, Carbon dioxide reforming of methane over ordered mesoporous NiO-Al_2O_3 composite oxides, Catalysis Science & Technology, 1 (2011) 1032-1042.
[249] L.L. Xu, Z.C. Miao, H.L. Song, W. Chen, L.J. Chou, Significant roles of mesostructure and basic modifier for ordered mesoporous Ni/CaO-Al_2O_3 catalyst towards CO_2 reforming of CH_4, Catalysis Science & Technology, 4 (2014) 1759-1770.
[250] A. Fouskas, M. Kollia, A. Kambolis, C. Papadopoulou, H. Matralis, Boron-modified Ni/Al_2O_3 catalysts for reduced carbon deposition during dry reforming of methane, Applied Catalysis A: General, 474 (2014) 125-134.
[251] B. De Bie, J. van Dijk, A. Bogaerts, The dominant pathways for the conversion of methane into oxygenates and syngas in an atmospheric pressure dielectric barrier discharge, Journal of Physical Chemistry C, 119 (2015) 22331-22350.
[252] D.C. Montgomery, Design and Analysis of Experiments, Wiley, New York, 2012.
[253] M.A. Bezerra, R.E. Santelli, E.P. Oliveira, L.S. Villar, L.A. Escaleira, Response surface methodology (RSM) as a tool for optimization in analytical chemistry, Talanta, 76 (2008) 965-977.
[254] Noshadi, N.A.S. Amin, R.S. Parnas, Continuous production of biodiesel from waste cooking oil in a reactive distillation column catalyzed by solid heteropolyacid: Optimization using response surface methodology (RSM), Fuel, 94 (2012) 156-164.
[255] A.R. Khataee, M. Fathinia, S. Aber, M. Zarei, Optimization of photocatalytic treatment of dye solution on supported TiO_2 nanoparticles by central composite design: Intermediates identification, Journal of Hazardous Materials, 181 (2010) 886-897.
[256] K.S. Prasad, C.S. Rao, D.N. Rao, Application of design of experiments to plasma arc welding process: A review, Journal of the Brazilian Society of Mechanical Sciences and Engineering, 34 (2012) 75-81.
[257] C.S. Ramachandran, V. Balasubramanian, P.V. Ananthapadmanabhan, Multiobjective optimization of atmospheric plasma spray process parameters to deposit yttria-stabilized zirconia coatings using response surface methodology, Journal of Thermal Spray Technology, 20 (2011) 590-607.
[258] Feng, Y. Ding, Y. Guo, X. Li, W. Li, Calcination temperature effect on the adsorption and hydrogenated dissociation of CO2 over the NiO/MgO catalyst, Fuel, 109 (2013) 110-115.
[259] Y.-H. Wang, H.-M. Liu, B.-Q. Xu, Durable Ni/MgO catalysts for CO_2 reforming of methane: Activity and metal-support interaction, Journal of Molecular Catalysis A-Chemical, 299 (2009) 44-52.
[260] X. Tu, H.J. Gallon, J.C. Whitehead, Plasma-assisted reduction of a NiO/Al_2O_3 catalyst in atmospheric pressure H_2/Ar dielectric barrier discharge, Catalysis Today, 211 (2013) 120-125.
[261] Pino, A. Vita, F. Cipiti, M. Lagana, V. Recupero, Hydrogen production by methane tri-reforming process over Ni-ceria catalysts: Effect of La-doping, Applied Catalysis B: Environmental, 104 (2011) 64-73.
[262] S.B. Wang, G.Q.M. Lu, Effects of promoters on catalytic activity and carbon deposition of Ni/γ-Al_2O_3 catalysts in CO_2 reforming of CH_4, Journal of Chemical Technology and Biotechnology, 75 (2000) 589-595.
[263] T. Horiuchi, K. Sakuma, T. Fukui, Y. Kubo, T. Osaki, T. Mori, Suppression of carbon deposition in the CO_2-reforming of CH_4 by adding basic metal oxides to a Ni/Al_2O_3 catalyst, Applied Catalysis A: General, 144 (1996) 111-120.
[264] M.A. Naeem, A.S. Al-Fatesh, A.E. Abasaeed, A.H. Fakeeha, Activities of Ni-based nano catalysts for CO_2-CH_4 reforming prepared by polyol process, Fuel Processing Technology, 122 (2014) 141-152.
[265] Q. Zhang, T. Wu, P. Zhang, R.J. Qi, R. Huang, X.F. Song, L. Gao, Facile synthesis of hollow hierarchical Ni/γ-Al_2O_3 nanocomposites for methane dry reforming catalysis, RSC Advances, 4 (2014) 51184-51193.

[266] S.B. Wang, G.Q. Lu, Catalytic activities and coking characteristics of oxides-supported Ni catalysts for CH_4 reforming with carbon dioxide, Energy & Fuels, 12 (1998) 248-256.
[267] Y.K. Han, C.-I. Ahn, J.-W. Bae, A.R. Kim, G.Y. Han, Effects of carbon formation on catalytic performance for CO_2 reforming with methane on Ni/Al_2O_3 catalyst: Comparison of fixed-bed with fluidized-bed reactors, Industrial & Engineering Chemistry Research, 52 (2013) 13288-13296.
[268] L.M. Zhang, L. Li, Y.H. Zhang, Y.X. Zhao, J.L. Li, Nickel catalysts supported on MgO with different specific surface area for carbon dioxide reforming of methane, Journal of Energy Chemistry, 23 (2014) 66-72.
[269] S. Zhang, J. Wang, H. Liu, X. Wang, One-pot synthesis of Ni-nanoparticle-embedded mesoporous titania/silica catalyst and its application for CO_2-reforming of methane, Catalysis Communications, 9 (2008) 995-1000.
[270] Tao, L. Shi, Q. Ma, D. Wang, C. Zeng, C. Kong, M. Wu, L. Chen, S. Zhou, Y. Hu, N. Tsubaki, Methane reforming with carbon dioxide over mesoporous nickel-alumina composite catalyst, Chemical Engineering Journal, 221 (2013) 25-31.
[271] S. Damyanova, B. Pawelec, K. Arishtirova, J.L.G. Fierro, Ni-based catalysts for reforming of methane with CO_2, International Journal of Hydrogen Energy, 37 (2012) 15966-15975.
[272] M.W. Li, C.P. Liu, Y.L. Tian, G.H. Xu, F.C. Zhang, Y.Q. Wang, Effects of catalysts in carbon dioxide reforming of methane via corona plasma reactions, Energy & Fuel, 20 (2006) 1033-1038.
[273] S. Tang, L. Ji, J. Lin, H.C. Zeng, K.L. Tan, K. Li, CO_2 reforming of methane to synthesis gas over Sol-Gel-made $Ni/\gamma\text{-}Al_2O_3$ catalysts from organometallic precursors, Journal of Catalysis, 194 (2000) 424-430.
[274] J.H. Kim, D.J. Suh, T.J. Park, K.L. Kim, Effect of metal particle size on coking during CO_2 reforming of CH_4 over Ni-alumina aerogel catalysts, Applied Catalysis A: General, 197 (2000) 191-200.
[275] S.B. Wang, G.Q.M. Lu, CO_2 reforming of methane on Ni catalysts: Effects of the support phase and preparation technique, Applied Catalysis B: Environmental, 16 (1998) 269-277.
[276] Design-Expert® Software Version 9: http://www.statease.com/dx9.html.
[277] H.L. Liu, Y.R. Chiou, Optimal decolorization efficiency of Reactive Red 239 by UV/TiO_2 photocatalytic process coupled with response surface methodology, Chemical Engineering Journal, 112 (2005) 173-179.
[278] V. Goujard, J.-M. Tatibouet, C. Batiot-Dupeyrat, Carbon dioxide reforming of methane using a dielectric barrier discharge reactor: effect of helium dilution and kinetic model, Plasma Chemistry and Plasma Processing, 31 (2011) 315-325.
[279] G. Derringer, R. Suich, Simultaneous optimization of several response variables, Journal of Quality Technology, 12 (1980) 214-219.
[280] N.R. Costa, J. Lourenco, Z.L. Pereira, Desirability function approach: A review and performance evaluation in adverse conditions, Chemometrics and Intelligent Laboratory Systems, 107 (2011) 234-244.
[281] S. Ozkara-Aydinoglu, A.E. Aksoylu, A comparative study on the kinetics of carbon dioxide reforming of methane over $Pt\text{-}Ni/Al_2O_3$ catalyst: Effect of Pt/Ni ratio, Chemical Engineering Journal, 215 (2013) 542-549.
[282] W.J. Cai, L.P. Qian, B. Yue, H.Y. He, Rh doping effect on coking resistance of Ni/SBA-15 catalysts in dry reforming of methane, Chinese Chemical Letters, 25 (2014) 1411-1415.
[283] Y.G. Chen, K. Tomishige, K. Yokoyama, K. Fujimoto, Promoting effect of Pt, Pd and Rh noble metals to the $Ni_{0.03}Mg_{0.97}O$ solid solution catalysts for the reforming of CH_4 with CO_2, Applied Catalysis A: General, 165 (1997) 335-347.

[284] A.H. Fakeeha, M.A. Naeenn, W.U. Khan, A.E. Abasaeed, A.S. Al-Fatesh, Reforming of methane by CO_2 over bimetallic Ni-Mn/γ-Al_2O_3 catalyst, Chinese Journal of Chemical Physics, 27 (2014) 214-220.
[285] Khzouz, J. Wood, B. Pollet, W. Bujalski, Characterization and activity test of commercial Ni/Al_2O_3, Cu/ZnO/Al_2O_3 and prepared Ni-Cu/Al_2O_3 catalysts for hydrogen production from methane and methanol fuels, International Journal of Hydrogen Energy, 38 (2013) 1664-1675.
[286] Djinovic, I.G.O. Crnivec, B. Erjavec, A. Pintar, Influence of active metal loading and oxygen mobility on coke-free dry reforming of Ni-Co bimetallic catalysts, Applied Catalysis B: Environmental, 125 (2012) 259-270.
[287] K.Y. Koo, H.-S. Roh, U.H. Jung, W.L. Yoon, Combined H_2O and CO_2 reforming of CH_4 over Ce-promoted Ni/Al_2O_3 catalyst for gas to liquid (GTL) process: Enhancement of Ni-CeO_2 interaction, Catalysis Today, 185 (2012) 126-130.
[288] J. Juan-Juan, M.C. Roman-Martinez, M.J. Illan-Gomez, Effect of potassium content in the activity of K-promoted Ni/Al_2O_3 catalysts for the dry reforming of methane, Applied Catalysis A: General, 301 (2006) 9-15.
[289] A. Siahvashi, A.A. Adesina, Synthesis gas production via propane dry (CO_2) reforming: Influence of potassium promotion on bimetallic Mo-Ni/Al_2O_3, Catalysis Today, 214 (2013) 30-41.
[290] C. Shi, P. Zhang, Effect of a second metal (Y, K, Ca, Mn or Cu) addition on the carbon dioxide reforming of methane over nanostructured palladium catalysts, Applied Catalysis B: Environmental, 115 (2012) 190-200.
[291] V.R. Choudhary, S.A.R. Mulla, B.S. Uphade, Oxidative coupling of methane over alkaline earth oxides deposited on commercial support precoated with rare earth oxides, Fuel, 78 (1999) 427-437.
[292] S. Sengupta, K. Ray, G. Deo, Effects of modifying Ni/Al_2O_3 catalyst with cobalt on the reforming of CH_4 with CO_2 and cracking of CH_4 reactions, International Journal of Hydrogen Energy, 39 (2014) 11462-11472.
[293] V.M. Gonzalez-delaCruz, R. Pereniguez, F. Ternero, J.P. Holgado, A. Caballero, In situ XAS study of synergic effects on Ni-Co/ZrO_2 methane reforming catalysts, Journal of Physical Chemistry C, 116 (2012) 2919-2926.
[294] D. San-Jose-Alonso, J. Juan-Juan, M.J. Illan-Gomez, M.C. Roman-Martinez, Ni, Co and bimetallic Ni-Co catalysts for the dry reforming of methane, Applied Catalysis A: General, 371 (2009) 54-59.
[295] L. Chen, Q. Zhu, R. Wu, Effect of Co-Ni ratio on the activity and stability of Co-Ni bimetallic aerogel catalyst for methane Oxy-CO_2 reforming, International Journal of Hydrogen Energy, 36 (2011) 2128-2136.
[296] A.C.W. Koh, L.W. Chen, W.K. Leong, B.F.G. Johnson, T. Khimyak, J.Y. Lin, Hydrogen or synthesis gas production via the partial oxidation of methane over supported nickel-cobalt catalysts, International Journal of Hydrogen Energy, 32 (2007) 725-730.
[297] S.H. Seok, S.H. Han, J.S. Lee, The role of MnO in Ni/MnO-Al_2O_3 catalysts for carbon dioxide reforming of methane, Applied Catalysis A: General, 215 (2001) 31-38.
[298] M.C.J. Bradford, M.A. Vannice, CO_2 reforming of CH_4, Catalysis Reviews, 41 (1999) 1-42.
[299] K. Tomishige, Y.G. Chen, K. Fujimoto, Studies on carbon deposition in CO_2 reforming of CH_4 over nickel-magnesia solid solution catalysts, Journal of Catalysis, 181 (1999) 91-103.
[300] H.W. Chen, C.Y. Wang, C.H. Yu, L.T. Tseng, P.H. Liao, Carbon dioxide reforming of methane reaction catalyzed by stable nickel copper catalysts, Catalysis Today, 97 (2004) 173-180.
[301] S.M. Sajjadi, M. Haghighi, A.A. Eslami, F. Rahmani, Hydrogen production via CO_2-reforming of methane over Cu and Co doped Ni/Al_2O_3 nanocatalyst: impregnation

versus sol-gel method and effect of process conditions and promoter, Journal of Sol-Gel Science and Technology, 67 (2013) 601-617.
[302] H.G. Zhang, H. Wang, A.K. Dalai, Effects of metal content on activity and stability of Ni-Co bimetallic catalysts for CO_2 reforming of CH_4, Applied Catalysis A: General, 339 (2008) 121-129.
[303] M.-S. Fan, A.Z. Abdullah, S. Bhatia, Utilization of greenhouse gases through carbon dioxide reforming of methane over Ni-Co/MgO-ZrO_2: Preparation, characterization and activity studies, Applied Catalysis B: Environmental, 100 (2010) 365-377.
[304] [J.K. Xu, W. Zhou, Z.J. Li, J.H. Wang, J.X. Ma, Biogas reforming for hydrogen production over nickel and cobalt bimetallic catalysts, International Journal of Hydrogen Energy, 34 (2009) 6646-6654.
[305] Rahemi, M. Haghighi, A.A. Babaluo, M.F. Jafari, S. Khorram, Non-thermal plasma assisted synthesis and physicochemical characterizations of Co and Cu doped Ni/Al_2O_3 nanocatalysts used for dry reforming of methane, International Journal of Hydrogen Energy, 38 (2013) 16048-16061.
[306] H. Sun, H. Wang, J. Zhang, Preparation and characterization of nickel-titanium composite xerogel catalyst for CO_2 reforming of CH_4, Applied Catalysis B: Environmental, 73 (2007) 158-165.
[307] G. Sierra Gallego, F. Mondragon, J. Barrault, J.-M. Tatibouet, C. Batiot-Dupeyrat, CO_2 reforming of CH_4 over La-Ni based perovskite precursors, Applied Catalysis A: General, 311 (2006) 164-171.
[308] I.H. Son, S.J. Lee, H.-S. Roh, Hydrogen production from carbon dioxide reforming of methane over highly active and stable MgO promoted Co-Ni/γ-Al_2O_3 catalyst, International Journal of Hydrogen Energy, 39 (2014) 3762-3770.
[309] K. Takanabe, K. Nagaoka, K. Nariai, K. Aika, Titania-supported cobalt and nickel bimetallic catalysts for carbon dioxide reforming of methane, Journal of Catalysis, 232 (2005) 268-275.
[310] K. Nagaoka, K. Takanabe, K. Aika, Modification of Co/TiO_2 for dry reforming of methane at 2 MPa by Pt, Ru or Ni, Applied Catalysis A: General, 268 (2004) 151-158.
[311] D. Mei, X. Zhu, C. Wu, B. Ashford, P.T. Williams, X. Tu, Plasma-photocatalytic conversion of CO_2 at low temperatures: Understanding the synergistic effect of plasma-catalysis, Applied Catalysis B: Environmental, 182 (2015) 525-532.
[312] C.J. Liu, Y. Li, Y.P. Zhang, Y. Wang, J.J. Zou, B. Eliasson, B.Z. Xue, Production of acetic acid directly from methane and carbon dioxide using dielectric-barrier discharges, Chemistry Letters, (2001) 1304-1305.
[313] H.K. Song, H. Lee, J.-W. Choi, B.-k. Na, Effect of electrical pulse forms on the CO_2 reforming of methane using atmospheric dielectric barrier discharge, Plasma Chemistry and Plasma Processing, 24 (2004) 57-72.
[314] Seyed-Matin, A.H. Jalili, M.H. Jenab, S.M. Zekordi, A. Afzali, C. Rasouli, A. Zamaniyan, DC-pulsed plasma for dry reforming of methane to synthesis gas, Plasma Chemistry and Plasma Processing, 30 (2010) 333-347.
[315] V. Goujard, J.M. Tatibouet, C. Batiot-Dupeyrat, Use of a non-thermal plasma for the production of synthesis gas from biogas, Applied Catalysis A: General, 353 (2009) 228-235.
[316] T. Nozaki, K. Okazaki, Plasma enhanced C_1-chemistry: towards greener methane conversion, Green Processing and Synthesis, 1 (2012) 517-523.

List of Academic Publications

- **Peer-reviewed journal papers**

[1] **Danhua Mei**, Xinbo Zhu, Chunfei Wu, Bryony Ashford, Paul Williams, Xin Tu*. Plasma-photocatalytic conversion of CO_2 at low temperatures: understanding the synergistic effect of plasma-catalysis. *Applied Catalysis B: Environmental*. 2016; 182: 525-532. (Impact Factor: 7.435)

[2] **Danhua Mei**, Ya-Ling He, Shiyun Liu, Joseph D. Yan, Xin Tu*. Optimization of CO_2 conversion in a cylindrical dielectric barrier discharge reactor using Design of Experiments. *Plasma Processes and Polymers*. 2016; 13: 544-556. (Impact Factor: 2.453)

[3] **Danhua Mei**, Xinbo Zhu, Ya-Ling He, Joseph D. Yan, Xin Tu*. Plasma-assisted conversion of CO_2 in a dielectric barrier discharge reactor: understanding the effect of packing materials. *Plasma Sources Science & Technology*. 2015; 24: 015011. (Impact Factor: 3.591; **Top ten (4th) most downloaded PSST paper in 2015, 2015 Highlights in PSST**)

[4] **Danhua Mei**, Bryony Ashford, Ya-Ling He, Xin Tu*. Plasma-catalytic reforming of biogas over supported Ni catalysts in a dielectric barrier discharge reactor: Effect of catalyst supports. *Plasma Processes and Polymers*. 2016; submitted. (Impact Factor: 2.453)

[5] Shiyun Liu, **Danhua Mei**, Ze Shen, Xin Tu*. Nonoxidative Conversion of Methane in a Dielectric Barrier Discharge Reactor: Prediction of Reaction Performance Based on Neural Network Model. *Journal of Physical Chemistry C*. 2014; 118: 10686-10693. (Impact Factor: 4.772)

[6] Dong Liu*, **Danhua Mei**, Xin Tu*. Vision-based tomographic reconstruction of emissivity distribution in asymmetric thermal plasma. *EPL*. 2013; 103: 35002. (Impact Factor: 2.095)

[7] Xinbo Zhu, Xin Tu*, **Danhua Mei**, Chenghang Zheng, Jinsong Zhou, Xiang Gao, Zhongyang Luo, Mingjiang Ni, Kefa Cen. Investigation of hybrid plasma-catalytic removal of acetone over CuO/γ-Al_2O_3 catalysts using response surface method. Chemosphere. 2016; 155: 9-17. (Impact Factor: 3.340)

[8] Yuxuan Zeng, Xinbo Zhu, **Danhua Mei**, Bryony Ashford, Xin Tu*. Plasma-catalytic dry reforming of methane over γ-Al_2O_3 supported metal catalysts. *Catalysis Today*. 2015; 256: 80-87. (Impact Factor: 3.893)

[9] Weizong Wang*, Xin Tu, **Danhua Mei**, Mingzhe Rong. Dielectric breakdown properties of hot SF_6/He mixtures predicted from basic data. *Physics of Plasmas*. 2013; 20: 113503. (Impact Factor: 2.142)

[10] Weizong Wang, Mingzhe Rong*, Yi Wu, Joseph W. Spencer, Joseph D. Yan, **Danhua Mei**. Thermodynamic and transport properties of two-temperature SF_6 plasmas. *Physics of Plasmas*. 2012; 19: 083506. (Impact Factor: 2.142)

- **Conference**

[11] **Danhua Mei**, Li Wang, Xin Tu*. Plasma-catalytic conversion of greenhouse gases over supported Ni catalysts in a coaxial dielectric barrier discharge reactor. International Symposium on Non-Thermal/Thermal Plasma Pollution Control Technology and Sustainable Energy (ISNTP-10), Florianopolis, SC, Brazil, August 1-5, 2016.

[12] **Danhua Mei**, Yuxuan Zeng, Shiyun Liu, Xin Tu*. Plasma-catalysis for energy and environmental applications. International Symposium on Non-Thermal/Thermal Plasma Pollution Control Technology and Sustainable Energy (ISNTP-10), Florianopolis, SC, Brazil, August 1-5, 2016.

[13] **Danhua Mei**, Bryony Ashford, Li Wang, Xin Tu*. Plasma-photocatalytic conversion of CO_2: Understanding the synergistic effect of plasma-catalysis at low temperatures. The 16th International Congress on Catalysis (ICC 16), Beijing, China, July 3-8, 2016.

[14] **Danhua Mei**, Li Wang, Yuan Gao, Tao Shao, Xin Tu. Plasma-catalytic dry reforming of CH_4 over Ni-Co/γ-Al_2O_3 catalysts at low temperatures. The 16th International Congress on Catalysis (ICC 16), Beijing, China, July 3-8, 2016.

[15] **Danhua Mei**, Li Wang, Yuan Gao, Tao Shao, Xin Tu. Dry reforming of methane in a plasma-catalytic hybrid reactor. UK Catalysis Conference 2016, Belfast, UK, January 6-8, 2016.

[16] **Danhua Mei**, Yuxuan Zeng, Shiyun Liu, Xin Tu*. Plasma-catalysis for energy and environmental applications. 1st Sino-Cerman Symposium on Atmospheric Pressure Gas Discharges and Plasma Applications, Beijing, China, October 11-17, 2015.

[17] **Danhua Mei**, Yuxuan Zeng, Xin Tu. Dry reforming of methane over alumina supported Ni-Co bimetallic catalysts in a non-thermal plasma reactor: Effect of the cobalt loading amount. The 42nd International Conference on Plasma Science (IEEE ICOPS 2015), Antalya, Turkey, May 24-28, 2015.

[18] **Danhua Mei**, Joseph D. Yan, Xin Tu. Plasma-catalytic conversion of CO_2 into value-added chemicals: Understanding the synergistic effect at low temperatures. The 42nd International Conference on Plasma Science (IEEE ICOPS 2015), Antalya, Turkey, May 24-28, 2015.

[19] **Danhua Mei**, Joseph D. Yan, Xin Tu. Plasma-catalytic carbon dioxide decomposition into value-added compounds in an atmospheric dielectric barrier discharge. UK Catalysis Conference 2015, Loughborough, UK, January 8-9, 2015.

[20] **Danhua Mei**, Joseph D. Yan, Xin Tu. Plasma-photocatalytic conversion of CO_2 into value-added chemicals. The 12th Technological Plasma Workshop (TPW), Coventry, UK, October 15-16, 2014.

[21] **Danhua Mei**, Joseph D. Yan, Xin Tu. Plasma-catalysis for CO_2 conversion: understanding plasma-catalyst interactions from a physical and chemical perspective. ESCAMPIG XXII, Greifswald, Germany, July 15-19, 2014.

[22] **Danhua Mei**, Yuxuan Zeng, Ze Shen, Joseph D. Yan, Xin Tu. Conversion of carbon dioxide into value-added chemicals using non-thermal plasma. The 11th Technological Plasma Workshop (TPW), York, UK, December 16-17, 2013.

[23] Shiyun Liu, **Danhua Mei**, Xin Tu. Conversion of methane into hydrogen and C2 hydrocarbons in a dielectric barrier discharge reactor. The 42nd International Conference on Plasma Science (IEEE ICOPS 2015), Antalya, Turkey, May 24-28, 2015.

[24] Yuxuan Zeng, **Danhua Mei**, Xin Tu. Plasma-catalytic reforming of methane for hydrogen production. The 12th Technological Plasma Workshop (TPW), Coventry, UK, October 15-16, 2014.

[25] Mohamad A Nahil, Shiyun Liu, **Danhua Mei**, Chunfei Wu, Xin Tu, Paul Williams. Low temperature plasma treated catalysts for steam reforming of tars from biomass gasification. UK Catalysis Conference 2016, Belfast, UK, January 6-8, 2016.